



University of HUDDERSFIELD

University of Huddersfield Repository

Townsend, Andrew

Characterisation of the Surface Topography of Additively Manufactured Parts

Original Citation

Townsend, Andrew (2018) Characterisation of the Surface Topography of Additively Manufactured Parts. Doctoral thesis, University of Huddersfield.

This version is available at <http://eprints.hud.ac.uk/id/eprint/34575/>

The University Repository is a digital collection of the research output of the University, available on Open Access. Copyright and Moral Rights for the items on this site are retained by the individual author and/or other copyright owners. Users may access full items free of charge; copies of full text items generally can be reproduced, displayed or performed and given to third parties in any format or medium for personal research or study, educational or not-for-profit purposes without prior permission or charge, provided:

- The authors, title and full bibliographic details is credited in any copy;
- A hyperlink and/or URL is included for the original metadata page; and
- The content is not changed in any way.

For more information, including our policy and submission procedure, please contact the Repository Team at: E.mailbox@hud.ac.uk.

<http://eprints.hud.ac.uk/>

**CHARACTERISATION OF THE SURFACE
TOPOGRAPHY OF ADDITIVELY MANUFACTURED
PARTS**

ANDREW PAUL TOWNSEND

A thesis submitted to the University of Huddersfield in partial fulfilment of the requirements
for the degree of Doctor of Philosophy

March 2018

Copyright statement

- i. The author of this thesis (including any appendices and/or schedules to this thesis) owns any copyright in it (the "Copyright") and s/he has given The University of Huddersfield the right to use such copyright for any administrative, promotional, educational and/or teaching purposes.
- ii. Copies of this thesis, either in full or in extracts, may be made only in accordance with the regulations of the University Library. Details of these regulations may be obtained from the Librarian. This page must form part of any such copies made.
- iii. The ownership of any patents, designs, trademarks and any and all other intellectual property rights except for the Copyright (the "Intellectual Property Rights") and any reproductions of copyright works, for example graphs and tables ("Reproductions"), which may be described in this thesis, may not be owned by the author and may be owned by third parties. Such Intellectual Property Rights and Reproductions cannot and must not be made available for use without the prior written permission of the owner(s) of the relevant Intellectual Property Rights and/or Reproductions

Abstract

Additive manufacturing (AM) techniques provide engineering design flexibility not available when manufacturing is constrained by the tool-path restrictions of conventional subtractive techniques such as turning, milling and grinding. AM techniques allow the manufacture of complex form, light weight components with optimised geometries and topographies, including internal and re-entrant features. These features may greatly enhance the components functional capability. The design flexibility may allow a reduction in assembly part count, with a corresponding reduction in assembly time. Additionally, the ability to use high performance engineering metals in the AM process, such as 316 stainless steel, titanium Ti6Al4V and cobalt chrome provide the aerospace, medical and automotive industries with a new manufacturing toolbox using familiar raw materials. These quality-driven industries are fully aware of the potential of AM and are actively engaged and invested with the AM industry and research community. The complex features and design freedom providing great potential for these industries also presents challenges for surface measurement and characterisation. Surface measurement is vital to assure compliance with designed sealing, bearing, flow and adhesion properties of the component. Parts manufactured using AM are not exempt from the stringent quality requirements applicable to other manufacturing processes and so surface texture requirements will be incorporated into drawings and design specifications, imposed by customers onto suppliers. There will need to be a common language and approved standards. Compliance verification will be mandatory. If a feature is specified on a drawing then these industries will require verification that the component complies with design requirements. Traditionally, line-of-sight measuring devices were able to follow the tool pathways to access and measure these surfaces. With the advent of additive processes, new techniques will need to be developed. X-ray computed tomography (CT) has been used successfully for dimensional and defect detection as it allows the measurement of internal and re-entrant features. Thus far, there has been little research on the application of CT for

the measurement of surface texture. This thesis reports on the development of a novel technique, detailing the first extraction of areal surface texture parameters per a recognised standard (ISO 25178-2) from CT scans of AM components. Industry will require reproducibility of measurements and so an interlaboratory comparison was performed to compare CT measurement results using this technique from four laboratories. The repeatability and accuracy of surface measurements is also vital for industrial applications and so the influence on extracted surface texture parameter values of selected CT measurement and reconstruction factors has been investigated. Extraction of true 3D data from CT requires the generation of new surface characterisation parameters to take full advantage of the technique and a new parameter has been developed to enable the true surface of re-entrant surfaces to be characterised. The additive process itself is complex and verification of consistent additive machine performance is vital for production. A series of small, inexpensive, surface-specific measurement artefacts has been developed and built to characterise the build chamber and provide production process verification. This series of inter-related experimental investigations were chosen to be industrially relevant, to be linked closely to component function and be used as practical measurement and surface characterisation techniques. This work is intended, as far as possible, to not be machine-specific, but to be applicable to all CT machines and all metal powder bed fusion (PBF) AM machines. As AM and CT machine capability improves, as it inevitably will, the techniques and applications presented here are designed to evolve with these changes.

Table of Contents

Chapter 1 Introduction.....	19
1.1 Background and motivation	19
1.2 Scope of the thesis	22
1.2.1 Aim.....	22
1.2.2 Objectives.....	22
1.3 Thesis layout	23
1.3.1 Chapter 2 Literature review	23
1.3.2 Chapter 3 Surface from CT	24
1.3.3 Chapter 4 CT-STARR (Surface Texture from Additive Round Robin)	25
1.3.4 Chapter 5 Factors affecting the accuracy of CT surface measurement	25
1.3.5 Chapter 6 CT measurement of re-entrant surfaces	26
1.3.6 Chapter 7 Surface-specific artefacts and build chamber characterisation	26
1.3.7 Chapter 8 Discussion and conclusions	27
1.3.8 Chapter 9 Future work	27
Chapter 2 Literature review	28
2.1 Additive manufacturing	28
2.1.1 Powder bed fusion.....	29
2.2 Surface texture metrology for metal AM	32
2.2.1 Surface metrology.....	32
2.2.2 Scale-of-interest	33

2.2.3	Importance of AM surfaces	36
2.2.4	Profile and areal surface measurement.....	40
2.2.5	Industrial applications, AM methods and build materials	42
2.2.6	Measurement technologies	43
2.2.7	Focus variation	44
2.2.8	Surface characterisation.....	47
2.2.9	Parameters sensitive to AM surface and component performance	48
2.2.10	Areal surface data processing.....	54
2.2.11	Conclusions	60
2.3	CT for AM metrology	61
2.3.1	Computed tomography	61
2.3.2	X-ray generation	64
2.3.3	Surface determination.....	65
2.3.4	CT for metrology	66
2.4	Literature review conclusions	69
Chapter 3 Areal surface texture data from CT.....		70
3.1	Methodology.....	71
3.1.1	Artefacts.....	72
3.1.2	Measurements	74
3.1.3	Data processing	82
3.2	Results	86
3.2.1	AM surface results.....	86
3.2.2	Dimensional artefact results.....	96

3.3	Discussion.....	98
3.4	Conclusion	99
Chapter 4 CT-STARR Stage 1		100
4.1	Introduction	100
4.1.1	Lessons learned	101
4.2	Methodology.....	103
4.3	Measurement artefacts.....	103
4.3.1	AM artefact	103
4.3.2	Dimensional artefact.....	104
4.4	CT measurement settings	105
4.5	Reconstruction.....	107
4.6	Comparative measurements	107
4.7	Results	108
4.7.1	AM surface texture artefact.....	108
4.7.2	Dimensional artefact.....	111
4.7.3	Measurement voxel size	121
4.7.4	Cone beam artefacts.....	126
4.7.5	Conclusions	127
Chapter 5 Factors affecting the accuracy of CT surface measurements		129
5.1	CT surface determination	130
5.1.1	Surface plates.....	131
5.1.2	Surface determination methods.....	131
5.1.3	CT-focus variation comparison	133

5.1.4	Analysis of results	133
5.1.5	Surface determination conclusions	138
5.2	Component magnification and voxel size	138
5.2.1	Voxel size and magnification conclusions	141
5.3	Comparison of external and internal measurement results	142
5.3.1	CT measurement.....	142
5.3.2	External/internal surface conclusions	145
5.4	Section conclusions	145
Chapter 6	CT measurement of re-entrant surfaces	147
6.1	Introduction	147
6.2	Methodology.....	149
6.2.1	CT measurements and surface extraction	149
6.2.2	Data processing and parameter generation	151
6.3	Results	155
6.3.1	Structured surface simulation	155
6.3.2	AM surfaces.....	158
6.4	Conclusions	159
Chapter 7	Surface-specific artefact design and build chamber characterisation	161
7.1	Introduction	161
7.2	Methodology.....	162
7.3	Measurement bars.....	163
7.3.1	Bar locations	164
7.3.2	Bar measurement	165

7.3.3	Data processing and analysis	168
7.3.4	Areal measurement results	168
7.3.5	Visual inspection of the bars	174
7.4	AMSA artefact analysis.....	179
7.4.1	Dimensional artefacts	179
7.4.2	The AMSA artefacts	179
7.4.3	Methodology.....	181
7.4.4	Artefact measurement	182
7.4.5	AMSA1	183
7.4.6	AMSA3	187
7.4.7	AMSA4	192
7.4.8	Artefact base deviation	195
7.4.9	AMSA series artefact discussion and conclusions	195
7.5	Build angle hemi-sphere artefact	197
7.6	Surface measurement artefacts conclusions	201
Chapter 8 Discussion and conclusions.....		203
Chapter 9 Future work		210
9.1	Automated surface-from-CT.....	210
9.2	Scaling and surface determination correction.....	211
9.3	Further CT chamber analysis.....	212
9.4	CT-STARR Stage 2	212
9.5	Re-entrant features and functional analysis.....	212
9.6	Surface-specific measurement artefacts	212

Chapter 10 References.....	214
Chapter 11 Appendices	223
Appendix 1 Chapter 2 Precision Engineering review paper	224
Appendix 2 Chapter 3 Precision Engineering surface from CT paper	238
Appendix 3 Chapter 3 ASPE 2016 conference presentation	249
Appendix 4 Chapter 4 iCT Leuven 2017 conference presentation	254
Appendix 5 Chapter 4 euspen 2017 conference paper and poster	261
Appendix 6 Chapter 5 CIRP Annals 2017 CT accuracy factors	264
Appendix 7 Chapter 6 euspen + ASPE Leuven 2018 conference.....	268
Appendix 8 Chapter 6 iCT Wels 2017 conference presentation.....	273
Appendix 9 Chapter 7 Met&Props 2017 conference presentation	275
Appendix 10 Chapter 9 euspen 2016 conference presentation	279
Appendix 11 Referenced areal surface texture parameters.....	281

List of Figures

Figure 1-1: Historical additive manufacturing.	19
Figure 1-2: Breakeven analysis.	20
Figure 1-3: Metal AM components.....	22
Figure 1-4: Moth eye and AM surface.	24
Figure 2-1: Laser-based PBF system.	30
Figure 2-2: EBM system configuration (Arcam).	31
Figure 2-3: Waviness and roughness of a machined surface.	32
Figure 2-4: As-built Ti6Al4V SLM AM surface SEM micrographs.	33
Figure 2-5: Typical machine turned component.	34
Figure 2-6: What is the correct scale of interest?	35
Figure 2-7: Visually similar surfaces.....	35
Figure 2-8: Picture of typical PBF build configuration.	38
Figure 2-9: Diagrammatic side view of 4 mm cube showing scan pattern.	39
Figure 2-10: Profile measurement extracted from a ground surface.	41
Figure 2-11: Schematic of a typical focus variation system.....	44
Figure 2-12: Alicona G4 focus variation surface measurement system.....	45
Figure 2-13: Focus variation information at a position of interest.	46
Figure 2-14: Focus variation height maps of a Ti6AL4V SLM part side surface.	50
Figure 2-15: Surface feature extraction from and SLM part top surface.	54
Figure 2-16: ISO 25178-2 Surface filtering.	55
Figure 2-17: Effect of changing L-filter nesting index on S_a value, SLM sample.	56
Figure 2-18: Effect of changing L-filter nesting index on S_a value, EBM sample.	56
Figure 2-19: Cone beam CT schematic.	62
Figure 2-20: CT reconstruction from multiple projections.	63
Figure 2-21: CT image of a Ti6AL4V AM lattice strut.	68

Figure 3-1: Images of an AlSi10Mg SLM upskin surface.....	72
Figure 3-2: Cross section of the dimensional artefact.....	73
Figure 3-3: Surface determination images of an AlSi10Mg part.	74
Figure 3-4: Focus variation test fixture used for the AM surface measurements.	75
Figure 3-5: Aluminium dimensional artefact CMM measurement locations.....	77
Figure 3-6: CAD rendering of the ABS fixture and artefacts.	77
Figure 3-7: Measurement artefact assembly mounted in the Nikon XT H 225.	78
Figure 3-8: Nikon XT H 225 electron-generation filament.	80
Figure 3-9: XT H 225 X-ray "gun" showing the assembly joint and hinge.....	80
Figure 3-10: CT AM surface measurement and characterisation sequence.....	85
Figure 3-11: False colour height maps of the AlSi10Mg AM surface.	85
Figure 3-12: Deviation analysis between two aligned Alicona measurements.....	89
Figure 3-13: Filament change areal parameter data.	91
Figure 3-14: AM surface parameter values including stage-move data.	93
Figure 3-15: ISO 25178-2 parameters, Alicona to CT comparison charts [18].	96
Figure 3-16: OD, ID and Length measurement comparisons.....	97
Figure 4-1: CAD section view of the RR CT fixture.....	101
Figure 4-2: CAD rendering of the dimensional artefact.....	102
Figure 4-3: Artefact assembly mounted in the Nikon XT H 225.....	105
Figure 4-4: Artefact assembly mounted in a Nikon MCT225.	106
Figure 4-5: False colour height maps of the RR Ti6Al4V EBM surface.....	109
Figure 4-6: RR surface texture results (a) S_a , (b) S_q , (c) S_z	110
Figure 4-7: CMM and CT dimensional results.	113
Figure 4-8: Effect of surface determination correction.....	115
Figure 4-9: Dimensional results after surface determination correction.....	116
Figure 4-10: Effect of global scaling correction.	117
Figure 4-11: Dimensional results after SD and scaling correction.....	118

Figure 4-12: Dimensional results after just scaling correction.	120
Figure 4-13: Surface texture results for HUD and NOTS.	122
Figure 4-14: Dimensional results for HUD and NOTS.	124
Figure 4-15: Dimensional results including SD and dimensional correction.	125
Figure 4-16: MCT225 dimensional artefact reconstruction.	126
Figure 4-17: Charts of cylinder dimensions (a) OD, (b) ID.	127
Figure 5-1: Microsurf Rubert 335 (casting) comparator plate.	130
Figure 5-2: Rubert 50 plate surface determination (VGStudio MAX 2.2 [136]).	133
Figure 5-3: False colour height maps of the nominal Ra 50 μm Rubert sample.	134
Figure 5-4: Percentage difference, CT to FV of nominal 50 μm Ra Rubert sample.	135
Figure 5-5: Absolute difference, CT to FV of nominal 50 μm Ra Rubert sample.	135
Figure 5-6: False colour height maps of the nominal Ra 25 μm Rubert sample.	136
Figure 5-7: Percentage difference, CT to FV of nominal 25 μm Ra Rubert sample.	137
Figure 5-8: Absolute difference, CT to FV of nominal 25 μm Ra Rubert sample.	137
Figure 5-9: Sa values for the CT SLM and EBM sample measurements.	140
Figure 5-10: Detail of Sa vs voxel size, XT H 225 CT.	141
Figure 5-11: Ti6Al4V bar (a) scan of original part, (b) after physical sectioning.	142
Figure 5-12: Internal and external measurements results.	144
Figure 6-1: SLM re-entrant surface.	147
Figure 6-2: Extracted surface of the CT SLM planar surface measurement.	150
Figure 6-3: Extracted surface of CT scan of the EBM lattice showing ROI (mm).	150
Figure 6-4: Extracted surface from the SLM planar surface (mm).	151
Figure 6-5: Detail of the SLM planar surface.	151
Figure 6-6: Extracted bar ROI from the CT lattice structure.	151
Figure 6-7: Section of unwrapped CT-measured lattice surface.	152
Figure 6-8: (a) Structured "mushroom" surface example, (b) "mushroom" "detail".	155
Figure 6-9: Height vs volume curve for a single structured mushroom.	156

Figure 6-10: Material ratio curve for a single structured mushroom.	157
Figure 6-11: Round structured surface.	157
Figure 6-12: Material ratio curve for the SLM planar surface.	158
Figure 6-13: Material ratio curve for the EBM lattice.	159
Figure 7-1: CAD rendering of the complete measurement artefact set.	162
Figure 7-2: Artefact set showing build dimensions, with the nine bars highlighted.	163
Figure 7-3: Orientation of the bars within the chamber.	164
Figure 7-4: Nine bars from batch 1 mounted in the Alicona G4 measurement fixture.	165
Figure 7-5: Batch 1 bars arranged for the first surface measurements of side 1.	166
Figure 7-6: Batch 1 bars arranged for first surface measurements of side 2.	166
Figure 7-7: Locations of the four sides for (a) corner bars, (b) cross bars.	166
Figure 7-8: Measurement sequence of the nine bars.	167
Figure 7-9: Residual plots for the 576 measurements.	169
Figure 7-10: Main effects plot.	169
Figure 7-11: Tukey pairwise comparison for builds 1-4.	170
Figure 7-12: Tukey pairwise comparison for bar side orientation.	171
Figure 7-13: Tukey pairwise comparison for bar measurement height.	172
Figure 7-14: Back-front and side facing bar sides.	173
Figure 7-15: Location of visual inconsistencies.	175
Figure 7-16: Photographs of the four sides of bar 4 from build 1 and build 2.	176
Figure 7-17: Photographs of four sides of bar 4 for build 3 and build 4.	177
Figure 7-18: False-colour height map of Build 1, measurement 24.	178
Figure 7-19: False-colour height map of Build 2, measurement 24.	178
Figure 7-20: AM measurement artefacts for form and dimensional measurements.	179
Figure 7-21: CAD rendering of the AMSA series artefacts.	179
Figure 7-22: CAD rendering of the surface-specific artefacts in blue.	181
Figure 7-23: CAD rendering of artefact AMSA1.	183

Figure 7-24: EBM AMSA1 horizontal and vertical build surfaces.	184
Figure 7-25: EBM AMSA1 artefact deviation analysis	185
Figure 7-26: Photographs of the AMSA1 horizontal artefacts (a) SLM, (b) EBM.	186
Figure 7-27: False-colour height map of the horizontal EBM flat section.	187
Figure 7-28: CAD rendering of the AMSA3 artefact set.....	187
Figure 7-29: EBM horizontal AMSA3 photographs and deviation analyses.	188
Figure 7-30: EBM vertical AMSA3 photographs and deviation analyses.	189
Figure 7-31: SEM micrographs of the AMSA3 medium Siemens Star.	190
Figure 7-32: SEM micrographs of the AMSA3 medium Siemens Star outer section.	190
Figure 7-33: Photographs of the AMSA3 artefact horizontal build.....	191
Figure 7-34: SLM AMSA3 artefact SEM micrographs.	191
Figure 7-35: CAD rendering of the AMSA4 artefact.....	192
Figure 7-36: Horizontally and vertically built EBM AMSA4 artefacts.	193
Figure 7-37: Photographs of the horizontally built AMSA4 artefact.....	194
Figure 7-38: Deviation analyses showing the underside of the EBM artefacts.	195
Figure 7-39: Proposed ASTM F42 AM measurement artefact suite,.....	197
Figure 7-40: CAD rendering of the two hemi-spheres, in blue.	198
Figure 7-41: Hemi-sphere artefact.....	198
Figure 7-42: Build 1 surface roughness (S_a) at each build angle.	199
Figure 7-43: Build 2 surface roughness (S_a) at each build angle.	200
Figure 7-44: Build 3 surface roughness (S_a) at each build angle.	200
Figure 7-45: Build 4 surface roughness (S_a) at each build angle.	200
Figure 7-46: Mean roughness (S_a) of the hemi-sphere vs build angle for four builds.	201
Figure 11-1: Areal material ratio curve and calculation of S_k and S_{mr2}	283

List of Tables

Table 1: Metal PBF AM input parameters and physical processes.	37
Table 2: Reviewed research papers for each material group.	43
Table 3: Examples of surface texture parameters used in AM research, from [15]......	51
Table 4: ISO 4288, table 1.	57
Table 5: ISO 25178-3 table 1.....	58
Table 6: ISO 25178-3 table 3.....	59
Table 7: Nikon XT H 225 measurement settings.....	78
Table 8: Master Alicona and copy ISO 25178-2 parameter values and differences.....	87
Table 9: ISO 25178-2 parameter values for the Alicona G4 ten measurements.....	88
Table 10: CT set 1 AM surface parameter mean and standard deviation values.	90
Table 11: CT set 2 AM surface parrameter mean and standard deviation values.	92
Table 12: Surface parameter and standard deviation values for the stage positioning test.	93
Table 13: CT set 3 AM surface parrameter mean and standard deviation values.	94
Table 14: Surface parameter values and percentage differences.	95
Table 15: CMM and CT artefact dimensional results.	97
Table 16: Mean CT parameter value, pre and post filament change.	98
Table 17: Round robin participants and their CT machines.....	103
Table 18: Nikon XT H 225 measurement settings for the RR measurements.....	105
Table 19: Nikon MCT225 measurement settings for the RR measurements.	106
Table 20: RR surface texture parameter mean values and sample standard deviation.....	108
Table 21: Differences between CT and Alicona mean measurements.....	108
Table 22: CMM and CT dimensional artefact mean and standard deviation results.....	112
Table 23: Surface determination correction applied to OD and ID.	115
Table 24: Voxel size and magnification for each measurement.	121
Table 25: Surface texture results.....	121

Table 26: Differences between CT mean values and FV mean values.	121
Table 27: Dimensions using all areas and selected areas.....	127
Table 28 Mean values of Alicona measurements of nominal Ra 50 μm Rubert sample.....	134
Table 29: Mean values of Alicona measurements of nominal Ra 25 μm Rubert sample....	136
Table 30: XT H 225 settings for the SLM medical implant scan.....	149
Table 31: XT H 225 settings for the EBM lattice structure scan.....	150
Table 32 Single planar mushroom extracted parameters	156
Table 33: SLM planar surface texture Sdr_{prime} mesh and grid parameters.....	158
Table 34: EBM lattice surface texture Sdr_{prime} mesh and grid parameters.....	158
Table 35: Processing parameters per ISO 25178-3.....	168
Table 36: Location of significant surface (visual) irregularities.....	174
Table 37: CT scanning parameters for the AMSA series artefacts.....	182
Table 38: AMSA1 surface Sa values.	186
Table 39: Hemi-sphere surface angles to the horizontal and number of samples.....	199

List of Equations

Equation 1	38
Equation 2	38
Equation 3	49
Equation 4	62
Equation 5	139
Equation 6	153
Equation 7	154
Equation 8	192
Equation 9	192
Equation 10	192

Acknowledgements

“If you wish to make an apple pie from scratch, you must first invent the universe.”
Carl Sagan (1934-1996)

Thanks to these exceptional people for putting a piece of the universe in place —
so I could make pie!

Thanks to Liam for making this journey a pleasure from day one.

Thanks to Jane and Paul for sage advice along the way.

To my friends at the University of Huddersfield Centre for Precision Technologies. I am especially indebted to Katie, Chris, Karl, Luca and Darshil for the support and the good times, in equal measure.

To Richard, Nicola, Petros and Adam from the University of Nottingham — to Richard for offering me authorship of the review paper and to all for making conferences so much fun.

Thanks to Bozena for being there from before day one.

Thanks to the “Algonquin gang” for all the encouragement: Jeff, Carol, John, Eileen, David, Melanie, Scott, Donna, Marty, Angela, Dave, Patti — and the families!

To Chris, Dawn, Terry, Irene, John, Sarah for the encouragement, perspective and for making the breaks so entertaining.

Thanks to Pam and Steve for being a shining example of Northern England’s friendliness and generosity.

Thanks and love to family Pete, Nid, Terry, Richard, the other Richard, Wendy, Mum and Dad and Kate. Thanks to the staff of Huddersfield Royal Infirmary, especially A&E and Ward 9, for making sure I got to the viva! Brilliant work...and thanks to Luca for making sure I got to A&E!

Sincere thank you to the UK EPSRC for funding my PhD.

Andy Townsend, March 2017.

List of abbreviations

ABS	Acrylonitrile Butadiene Styrene
AM	Additive Manufacturing
AMSA	Additive Manufacturing Surface Artefact
ANOVA	Analysis of Variance
ASTM	American Society for Testing and Materials
CAD	Computer Aided Design
CMM	Coordinate Measuring Machine
CT	X-ray Computed Tomography
DED	Directed Energy Deposition
DMLS	Direct Metal Laser Sintering
EBM	Electron Beam Melting
ELI	Extra Low Interstitial
FDM	Fused Deposition Modelling
FV	Focus Variation
ICP	Iterative Closest Point
ID	Inside Diameter
ISO	International Organization for Standardization
ITK	Insight Segmentation and Registration Toolkit
MPE	Maximum Permissible Error
NIST	National Institute of Standards and Technology
NPL	National Physical Laboratory
OD	Outside Diameter
PBF	Powder Bed Fusion
PLY	Polygon file format
ROI	Region Of Interest
RMS	Root Mean Square
RR	Round Robin
SD	Surface Determination
SDF	SDFFile format
SE	Secondary Electron
SEM	Scanning Electron Microscope
SLM	Selective Laser Melting
SLS	Selective Laser Sintering
STL	Stereo Lithography format
UV	Ultra Violet

Chapter 1 Introduction

“Additive manufacturing—a third industrial revolution.”
The Economist (2012) [1]

1.1 Background and motivation

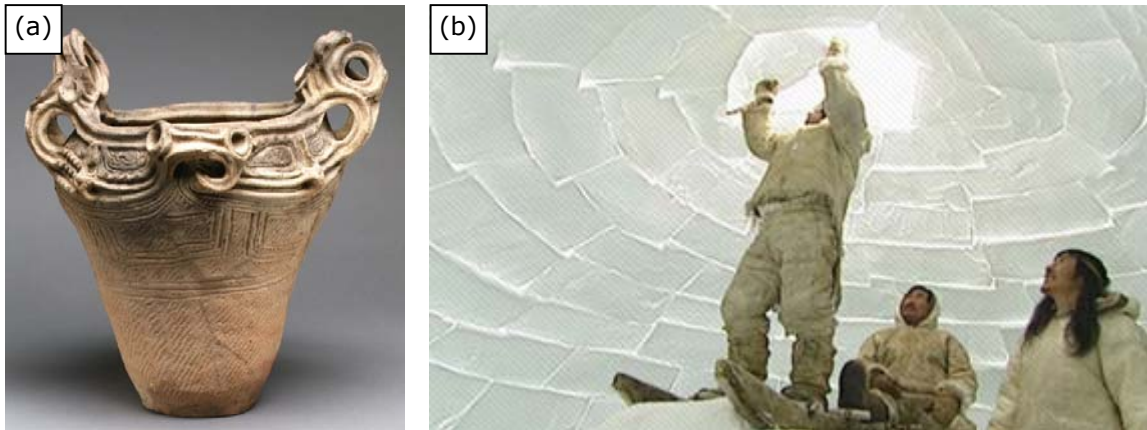


Figure 1-1: Historical additive manufacturing.
(a) Japanese Jōmon coil pot, reproduced from [2], (b) Inuit people and igloo, reproduced from [3].

Additive manufacturing techniques have existed for millennia. The Japanese, during the Jōmon period, (ca. 10,500 B.C.–ca. 300 B.C.), created intricate coil pottery, see Figure 1-1:(a) [2]. Igloos, the traditional shelter of the Inuit people, are known to have existed from at least the 16th century, see Figure 1-1:(b) [3]. These two techniques are both examples of additive manufacturing, where raw material is added piece-by-piece or layer-by-layer to produce the final product, perhaps with some post-processing to improve aesthetics or functional performance. However, additive manufacturing (AM) as referred to in the research reported in this thesis, is the production of items built in layers from a computer aided design (CAD) model. This method of additive manufacturing has a relatively short but dynamic history. Since Chuck Hull received a patent for the first commercial AM technology (1986 U.S. Patent 4,575,330 entitled “Apparatus for production of three-dimensional objects by stereo lithography”) [4] there has been a continuing evolution of AM technology and a corresponding

increase in industrial and commercial interest in applications of the technology in all its forms; with some methods having, currently, more significant commercial and industrial application than others. These processes have significant potential for the quality-driven aerospace, medical and automotive industries, where these techniques, particularly using metal raw material [5] may present significant advantages over conventional manufacturing techniques. AM processes complement, but are not a substitute for, conventional subtractive manufacturing methods, such as milling, turning and grinding. There are many applications, for example high-volume production of hydraulic pistons, where turning and milling from wrought bar stock will be more economical in terms of raw material and manufacturing costs, material traceability and consistency. AM has generally been more viable as a manufacturing technique for bespoke or small batch quantities, see Figure 1-2:, however, the costs of AM are reducing and the number of manufactured parts at the AM break even cost-point is gradually increasing.

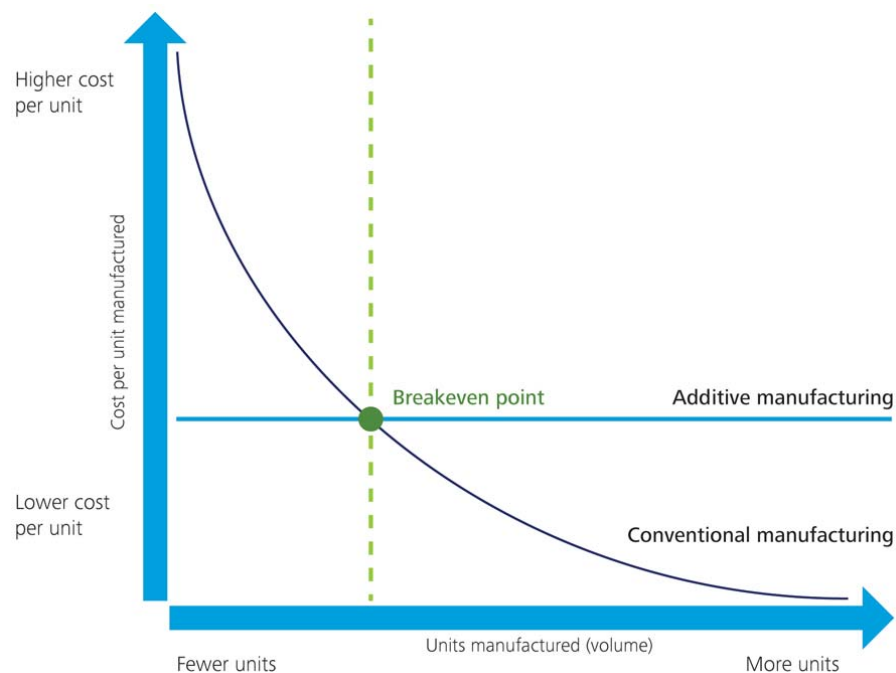


Figure 1-2: Breakeven analysis. Comparing additive and conventional manufacturing, showing conventional manufacturing techniques are more economical as the number of manufactured units increases. Reproduced from [6].

AM techniques provide another tool in the manufacturing toolbox. Importantly, AM processes, even though they are in their infancy and not as well established or understood as conventional machining process will *not* have an exemption from the stringent quality requirements of safety-critical industries such as medical or aerospace:

“Additive manufacturing may be the new “miracle process”, but there is no special dispensation from complying with the requirements of quality-driven industries such as medical or aerospace. Additionally, the old adage that “if it can’t be measured, it can’t be made” applies and therefore developing suitable traceable metrology for potentially very complex additive components is vital if the AM process is to become mainstream.”

Liam Blunt, Director, Centre for Precision Technologies, University of Huddersfield (2017)

Typical applications of AM techniques include the manufacture of components with complex geometries and internal features that are either very difficult or impossible to produce using conventional techniques. As an example, Sachs [7] reported on the manufacture of injection molding tooling using additive manufacturing. Not restricted to the straight holes produced by drilling operations, complex, curved flow channels can be manufactured using AM without the need for a multi-part mold. The primary advantage of AM is that these processes are not limited by tooling path restrictions inherent in subtractive techniques [8]. This permits novel designs to be made and by potentially reducing the number of parts in an assembly, saving on manufacturing time, assembly time, part storage and documentation, eliminating the need for elastomeric seals with potential leakage paths for example. AM is currently being used in high-value applications where customisation and complex geometries are required, such as the shells for hearing aids [8]. The UK Foresight Report (2013) [9] highlighted applications such as this: personalised but high-volume applications, as a potential game-changing technology. AM has been called *the third industrial revolution* [1]. Perhaps it is a little early to describe the technology this way, but AM does have significant enough advantages that

the technological challenges, many of which will be discussed here, will be addressed and resolved. AM is here to stay. Figure 1-3: shows three metal AM components incorporating topology optimisation, and weight-saving design features.



Figure 1-3: Metal AM components.
(a) Airbus A380 bracket. Optimised AM [front] and conventional [rear] (S. Steel). Reproduced from [10]. (b) Arup AM construction bracket (Maraging steel). Reproduced from [11]. (c) GE LEAP fuel nozzle (Cobalt Chrome) Reproduced from [12].

1.2 Scope of the thesis

1.2.1 Aim

The aim of this work is to characterise the surface texture of additively manufactured parts, introducing and verifying the robustness of novel techniques and methods that, individually or when combined, provide industry with tools for production development and process control.

1.2.2 Objectives

To meet this aim the following objectives were set:

- Develop a non-destructive technique for measuring and characterising internal surfaces of metal powder bed fusion (PBF) AM components.
- Verify reproducibility of the technique by performing an interlaboratory comparison.

- Investigate parameters that may impact the accuracy of the extracted data.
- Develop a non-destructive technique for measuring and characterising re-entrant AM surfaces.
- Develop novel surface-specific AM artefacts for industrial process verification and use these as part of an artefact measurement suite to characterise the PBF AM machine manufacturing envelope (the build chamber).

This work is not concerned with monitoring or in-situ AM metrology, discussed here [13] or with form or shape inspection, discussed here [14]. Because of its industrial importance, this work focusses on metal AM surface metrology. However, the techniques and methods specified here may have application for polymer AM measurement (and indeed application for surface measurement and characterisation outside the AM field).

1.3 Thesis layout

The thesis consists of nine chapters including the introduction, plus references and appendices. A synopsis of chapter numbers two to nine is provided here. A brief rationale for the experimental work, together with novelty, are discussed. Detailed explanations are included in the specific chapters.

1.3.1 Chapter 2 Literature review

Chapter two is a review of current literature and state-of-the-art, comprising of three sections. Section 2.1 is an overview of additive manufacturing. Section 2.2 is a review of literature pertaining to metal AM surfaces and their measurement. A review paper [15] (the author of this thesis is the first author), indicated that there had been very limited application of computed tomography (CT) for the measurement, extraction and characterisation of data from AM surfaces. This lack of research was surprising as the author had seen potential for creating CT reconstructions with useable surface texture data. During unrelated work, using

the Nikon XT H 225 CT at Huddersfield University, this author had imaged the head of a brown house moth (*hofmannophila pseudospretella*). When sectioned in the analysis software, significant detail was visible on the inside of the moth's eyes and antennae (Figure 1-4:(a)). It was realised that the scale of the surface texture was significantly less than that of standard as-built PBF AM surfaces (Figure 1-4:(b)) and so there seemed potential for the extraction of meaningful surface data from CT. This led to a literature review of the current research into the application of CT for the measurement of AM components, included here as Chapter 2.3.

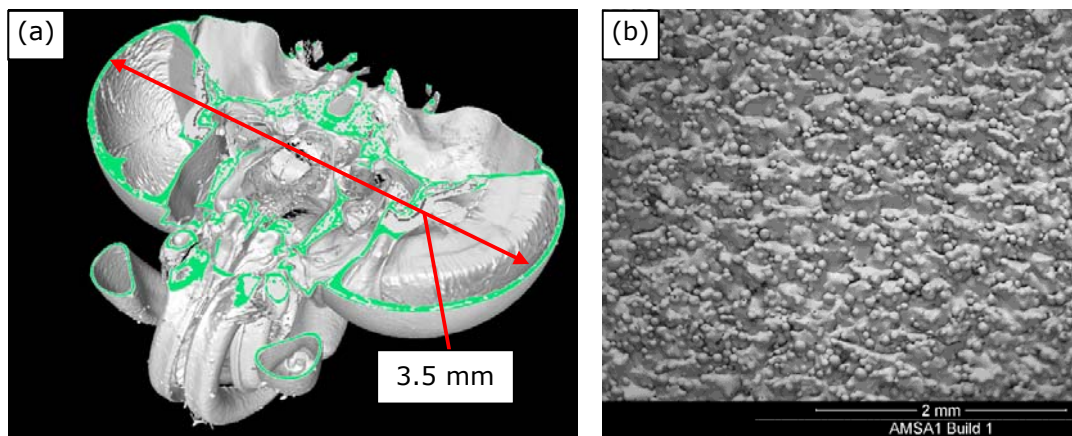


Figure 1-4: Moth eye and AM surface.
(a) Head of *Hofmannophila pseudospretella*, sectioned in VGStudio MAX 3.0. Voxel size 7.5 μm , (b) SEM image of an EBM AM as-built side surface (similar scale).

1.3.2 Chapter 3 Surface from CT

Prior to the work reported here, there had been no published areal AM surface extraction and characterisation from CT reconstructions of AM components. This chapter discusses the development of measurement artefacts, including a dimensional artefact scanned with the AM surface measurement artefact. This chapter also presents the extraction technique, the generation of areal parameter data per ISO 25178-2 [16], the evaluation of repeatability and comparison with results obtained from a focus variation instrument. The results were presented at conference [17] and a journal paper reporting this work has been published [18].

1.3.3 Chapter 4 CT-STARR (Surface Texture from Additive Round Robin)

The surface extraction technique, as presented in Chapter 3, had been shown to be robust—but the work had been performed on one CT machine, a Nikon XT H 225 at Huddersfield University. This technique, to have industrial application, would need to be applicable to other machines, so an interlaboratory comparison (round robin [RR]) was planned to evaluate reproducibility. RR evaluations of AM dimensional extraction from CT has been performed [19-21] but, as the base technique here is novel, this is the first RR investigating the extraction and characterisation of surface texture from an AM component. A multi-machine, worldwide round robin was considered, but it was decided that an initial (Stage 1) round robin, including a limited number of participants (four) using similar machines (one Nikon XT H 225 commercial machine and three Nikon MCT225 metrology machines) would be more expeditious and the lessons learned about measurement technique, sample preparation and data analysis would provide a solid foundation for an expanded Stage 2 RR with a larger cohort of CT machines and with greater machine configuration variation. The development of Stage 1 was presented at conference [22], as were the initial results [23].

1.3.4 Chapter 5 Factors affecting the accuracy of CT surface measurement

For industrial applications it is important to know the potential effect of measurement process variation. The effect of changing the electron-generation filament in the X-ray generation assembly is discussed in Chapter 3. The effects of three additional factors on the extracted surface texture parameter data are investigated in this chapter. These factors are CT surface determination, which is the computation of the location of the surface based on the grey-scale values of the re-constructed voxels. The second factor is the magnification and measurement voxel size and the third factor investigated was the influence of measuring a surface as an internal surface compared with the same surface as an external surface. The results of this study were presented at conference and published as a journal paper [24].

1.3.5 Chapter 6 CT measurement of re-entrant surfaces

The PBF additive process often produces an as-built surface with re-entrant (overhanging) features. Additionally, the process presents the opportunity to *intentionally* produce designed surfaces with overhanging or re-entrant features to improve component functionality. Measurement of these features is important, as a process verification and functional optimisation tool. These features can be imaged using the CT process. It will be shown in Chapter 5 that there is insignificant difference between CT measurements of the same surface as an external surface and as an internal surface, so the data for re-entrant surfaces should be a true representation of the surface. CT measurements generate true 3D (x,y,z) data, including internal features and surfaces. Line-of-sight measurement techniques, such as optical focus variation and mechanical stylus cannot be used to measure re-entrant features. The output of these line-of-sight processes is generally height map information: a single z value created for any given x,y coordinate. If the data from CT is processed as a height map then valuable measured data is lost. This lost data may have significant information that may relate to the required part function. This Chapter reports on the novel measurement and characterisation of re-entrant features using CT and a new surface parameter is proposed, Sdr_{prime} . The work was presented at conference [25].

1.3.6 Chapter 7 Surface-specific artefacts and build chamber characterisation

Collaborations with industrial partners have shown that AM components with functional as-built surfaces are now being used in critical applications, for example percutaneous (through-the-skin) medical implants. In addition to the requirement to measure any re-entrant surfaces correctly, as discussed in Chapter 6, these critical applications require consistent production quality across the build chamber and between successive builds. This chapter reports on the characterisation of an EBM chamber used for manufacturing medical implants, through analysis of four builds using powder with differing re-use cycles. Included in the artefacts in each build is a novel set of surface-specific measurement artefacts. Design rationale is

discussed for these artefacts and the methodology and results for the characterisation is reported. The surface-specific artefact work was presented at conference [26].

1.3.7 Chapter 8 Discussion and conclusions

The conclusions drawn from each experimental section and general conclusions are presented.

1.3.8 Chapter 9 Future work

On-going and future work are presented, together with an outlook of possible future trends and opportunities.

Chapter 2 Literature review

“Surfaces cover everything.”

Christopher A. Brown [27]

This chapter provides a review of the background literature and current state-of-the-art research applicable to this thesis. The chapter is divided into three sections: section 2.1 is an overview of AM, section 2.2 is a review of surface texture metrology for metal AM and section 2.3 is a review of the application of CT for metrology.

2.1 Additive manufacturing

The ASTM Committee F42 on Additive Manufacturing Technologies has defined seven methods of additive manufacturing [28]:

- Vat photo polymerisation

This method uses a vat of photopolymer resin that is selectively cured using ultraviolet (UV) light. The build platform is lowered by the layer thickness and the process is repeated.

- Material extrusion

This process, often called fused deposition modelling (FDM), involves the layer-by-layer deposition of material heated and extruded through a nozzle.

- Powder bed fusion

PBF techniques use a raw material powder that is spread over the build plate surface. The powder is selectively melted, the build plate is lowered by the layer thickness and then another layer is applied and selectively melted. The two most common melting processes are electron beam melting (EBM) and laser-based processes, including selective laser melting (SLM), selective laser sintering (SLS) and direct metal laser sintering (DMLS) [29]. The majority of metal powder bed processes (laser or electron beam based) involve full melting of the raw material powder [8].

- Material jetting

In this process raw material is jetted, layer by layer, onto the build plate. This process is similar to two-dimensional, single layer, ink-jet printing.

- Binder jetting

Liquid binder material is selectively jetted onto a powder bed layer. The build plate is lowered, another layer of powder is applied and a further layer of binder liquid is applied. The powder is glued by the adhesive binder to the layer below.

- Directed energy deposition

Directed energy deposition (DED) involves feeding the raw material stock (wire or powder) into the heat source (such as a laser beam) near or on the material surface. A liquid pool of molten material forms on the surface. This process is often used for repair or cladding of existing components.

- Sheet lamination

Sheet layers are positioned onto the machine bed, bonded (glue or ultrasonic welding) to the previous layers. The layer is then trimmed to the required shape and the process is repeated.

2.1.1 Powder bed fusion

The work reported in the present thesis will specifically involve research into one of these processes: powder bed fusion. This process has seen the most widespread adoption and there has been significant investment by the aerospace and medical industries in PBF AM, primarily metal AM. As an example General Electric, a company with significant involvement in both the aviation [30] and medical [31] industries has purchased a controlling share (76.1% as of January 2017 [32]) of Swedish company, Arcam, the leading EBM machine manufacturer. The PBF process involves the thermal fusion of a base material powder. Typical particle size range for metal PBF powders is 15–45 μm for laser-based systems [33] and 45–100 μm for electro-beam based systems [34]. The particle size for electron-beam systems is generally

larger to reduce the effect of particle charging and repulsion caused by the flow of electrons through the powder during e-beam application [8].

2.1.1.1 Laser-based AM

A schematic of a typical laser-based PBF system is shown in Figure 2-1: [29].

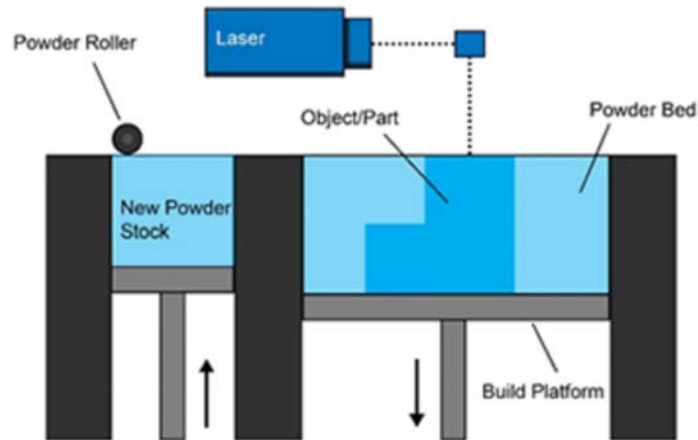


Figure 2-1: Laser-based PBF system. Reproduced from [29].

Laser-based PBF systems include a laser system to provide the thermal energy necessary to melt the powder. The laser beam is scanned across the powder surface by a mechanical galvanometer system. Between each layer the build platform is lowered by the layer thickness and the next layer of powder is applied using a blade or roller. The build chamber typically has an inert gas atmosphere (usually argon or nitrogen). This minimises oxidation of the powder [29].

2.1.1.2 Electron-beam based AM

EBM systems operate in a vacuum or partial vacuum and at high temperature. The base vacuum level in the Arcam Q10 is maintained at 1×10^{-5} mbar. Helium gas at a partial pressure of 2×10^{-3} mbar is introduced during the melting process [35]. The electron beam is scanned across the entire build after the addition of each powder layer, maintaining the entire build at

an optimal ambient temperature (dependent upon the raw material used). This process reduces the residual stresses within the finished component and reduces powder displacement due to the charge-repulsion caused by the electron flow. The build process is achieved by scanning the beam using a greater energy flux over just the areas required to be melted for that build layer. One significant advantage of EBM process is the fast scanning speed, as the electron beam is deflected using magnetic coils, similar to those incorporated in cathode ray tubes and scanning electron microscopes, see Figure 2-2:. This electronic scanning is faster than the mechanical scanning of the optical laser beam in laser PBF systems.

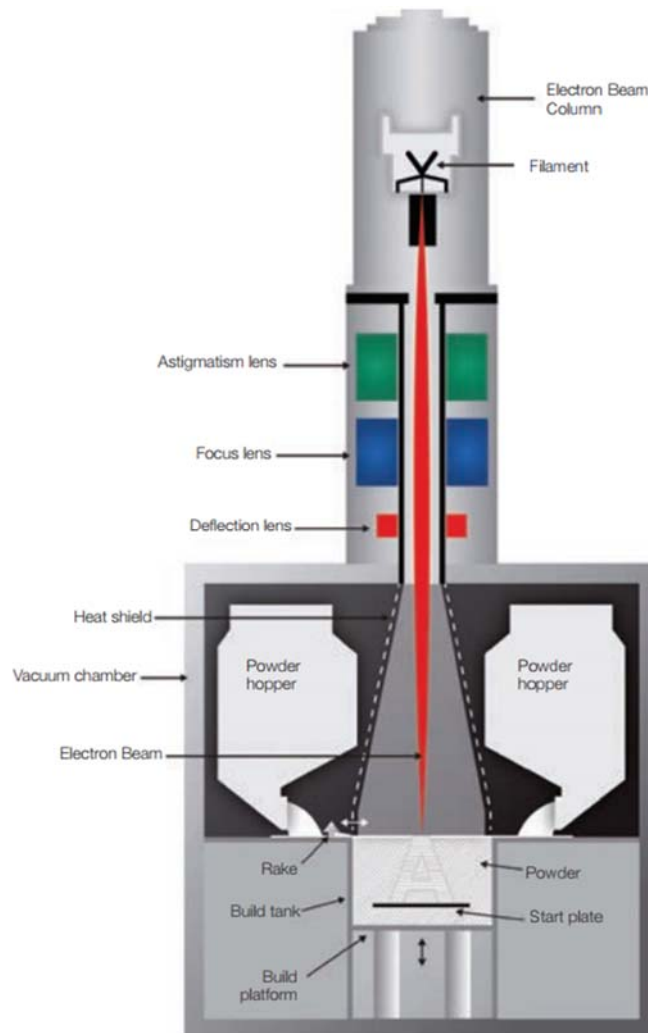


Figure 2-2: EBM system configuration (Arcam).
Reproduced from [36].

2.2 Surface texture metrology for metal AM

A review paper by Townsend et al., “Surface texture metrology for metal additive manufacturing: a review” [15] underpins this section. This review paper includes analysis of 120 references from 1997 [37] to the publication submission date: May 29, 2016. More recent references have been discussed here as applicable. A copy of the review paper is included in Appendix 1.

2.2.1 Surface metrology

Surface metrology is defined as the measurement and characterisation of surface topography [38]. The *measurement* of the surface is a separate, but inter-related, function from the surface *characterisation*. Measurement is the process of acquiring surface data. Characterisation is the process of extracting useful quantitative information from the data. The measurement process has to be configured to acquire the necessary data to allow correct characterisation of the surface. The required data may be specified by reference standards, based on the surface configuration, measurement technique and the characterisation to be performed. Measurement and characterisation will be discussed separately. The word *topography* typically describes the geometric information for the surface, at all measurement scales. This includes the surface form (shape), waviness and texture. Form is of longer wavelength than waviness, which in turn is of longer wavelength than texture. The work discussed in this review is focussed primarily on surface texture. The actual wavelengths corresponding to waviness and texture (roughness) are surface dependent, see Figure 2-3:.

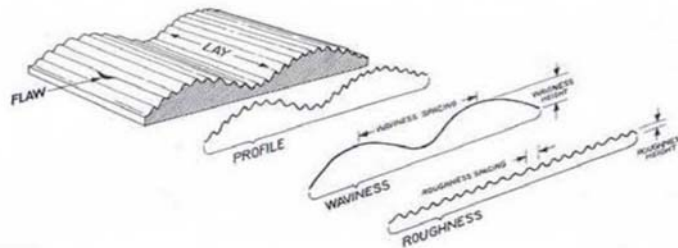


Figure 2-3: Waviness and roughness of a machined surface. Reproduced from [39].

The final scale-of-interest (wavelengths) chosen for measurement and characterisation should ideally be those that are most sensitive to component function. If, however, a relationship between function and specific wavelengths has not been developed, there are standard surface-scale values that may be generated based on the surface roughness. Interestingly, this means that an approximate value of the surface roughness needs to be known to enable correct settings for the final measurement and characterisation.

2.2.2 Scale-of-interest

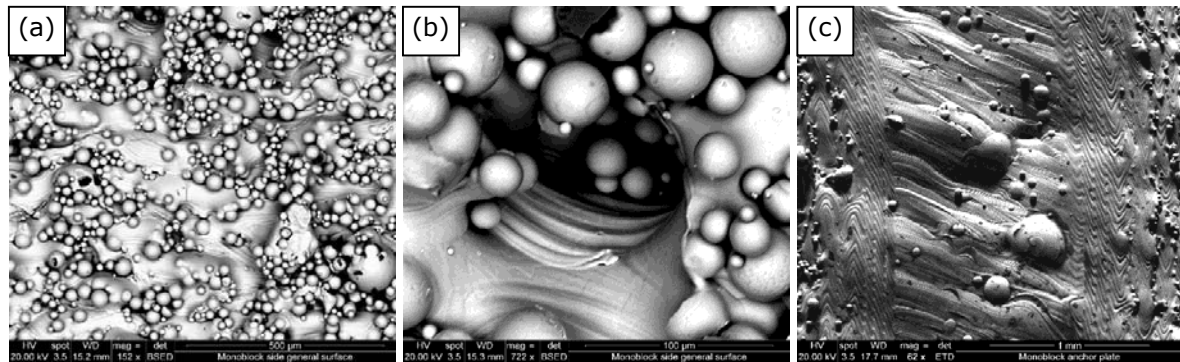


Figure 2-4: As-built Ti6Al4V SLM AM surface SEM micrographs. (a) Side surface, (b) detail of side surface, (c) top surface.

Figure 2-4:(a,b) show current work analysing a typical as-built SLM side surface (Ti6Al4V). The surface has a high degree of irregularity at different observation scales. Partially melted powder grains can be observed, together with melt flow waves and ripples. Figure 2-4:(b) shows a surface pocket. Perhaps this pocket is an indicator of internal porosity within the component: the material surrounding such pockets may not be fully re-melted during subsequent layer deposition, so creating a void that becomes embedded within the component. Figure 2-4:(c) shows the top surface of the same component. The melt path strategy is visible on the surface. There are asperities and globules on the surface that are of different configuration to those on the side surface. Figure 2-5:, by comparison shows an image of a machine-turned component. This surface is characterised by generally repeating

features of similar pitch based on the machine feeds and speeds, with smaller scale features, perhaps caused by tool edge irregularities.

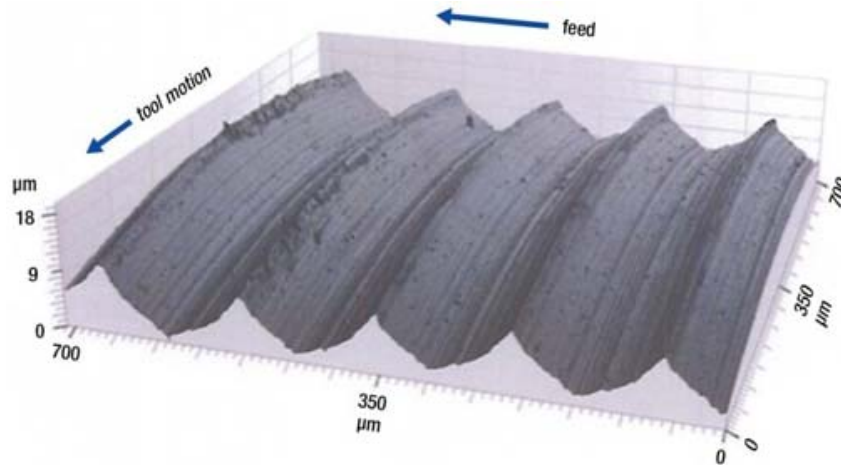
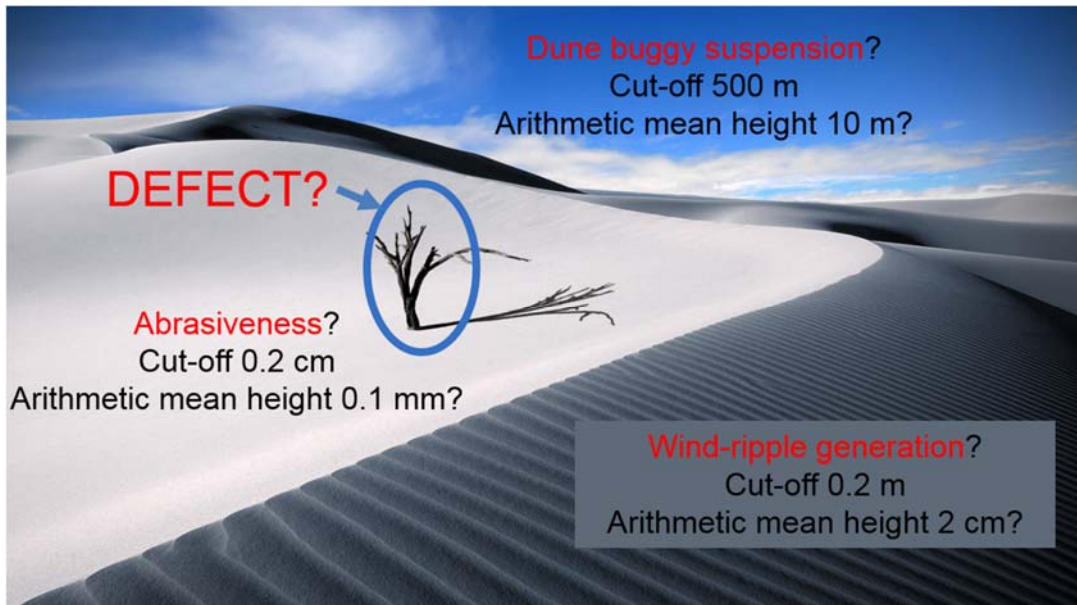


Figure 2-5: Typical machine turned component. Showing repeating features based on the machine feed rate and rotational speed, together with smaller features from tool edge irregularities. Reproduced from [40].

As has been discussed, the driving factor for the measurement scale-of-interest should be component function, which may dictate very specific measurement and characterisation parameters. A simple example to illustrate the importance of measurement scale-of-interest is shown in Figure 2-6:. This desert landscape has several distinct surface scales. If the surface is to be used as a track for dune buggies then the tuning of the car suspension may be based on large wavelengths, up to perhaps 500 m. This may give an arithmetic mean deviation of the surface of 10 m. If the interest is in the formation and characterisation of wind-induced rippling then perhaps the largest scale of interest may be 0.2 m. If all wavelengths above 0.2 m are filtered then the arithmetic mean deviation of the surface may be 2 cm. Finally, if the abrasiveness of the surface is the important function, then the maximum scale-of-interest may be 0.2 cm, which, after filtering all wavelengths above this value, may result in a roughness value of 0.1 mm. These arithmetic mean height deviation values are all for the same surface, the 10 m to 0.1 mm difference (a 100,000 : 1 ratio) is purely due to the filtering applied, which in turn is based on the scale-of-interest.



**Figure 2-6: What is the correct scale of interest?
Sand dune with features at different scales-of-interest, based on function.**

It should be noted that visual evaluation of surface may not always give an indication of the correct measurement scale. Figure 2-7: shows two images of visually, fairly similar features. However, the difference in the scale bar length is 1:1,000,000,000.

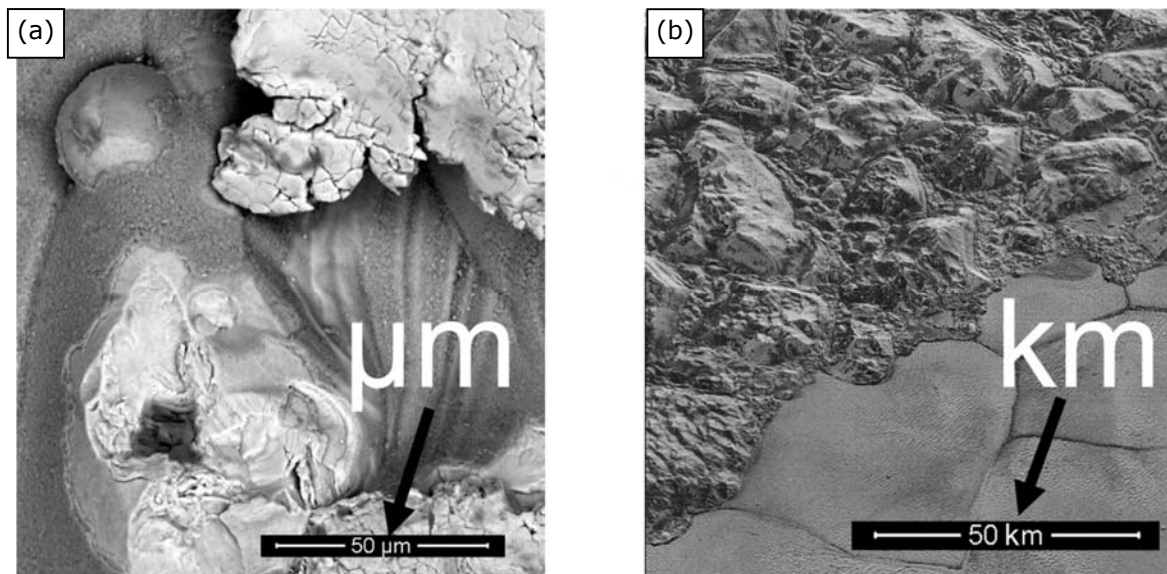


Figure 2-7: Visually similar surfaces. Approximately 1 billion times scale difference. (a) SLM AM surface (b) surface of the planet Pluto. Modified from [41].

Many surface metrology instruments can be configured to measure surfaces at a wide range of scales of interest, for example a typical focus variation instrument may have selectable objective lenses with magnifications from x2.5 to x100. The machine operator is responsible for configuring the measuring instrument system based upon the scales-of-interest, filtering and characterisation requirements.

2.2.3 Importance of AM surfaces

Subtractive manufacturing methods remove surface to create a new surface. This is not the case with PBF AM. A surface is first created and then re-melted. Surface texture may relate to the internal structure of the component. Surface defects may become embedded in the body of the component when subsequent layers are added. This may produce porosity that may reduce fatigue life and material strength. The porosity may be exposed on a critical sealing surface during later post-processing, rendering the component un-useable. Surface texture measurement, in addition to providing accept/reject data during production, may provide significant insight into the manufacturing process and, in the case of AM manufacturing, the physical phenomena occurring during the manufacturing process. There are many input parameters and physical processes in the metal PBF AM process, see Table 1. As can be seen in Figure 2-4:, there is a wealth of information at the surface to aid in process analysis and correction.

**Table 1: Metal PBF AM input parameters and physical processes.
Reproduced from [42].**

<u>Input Parameters</u>	<u>Physical Processes</u>
<ul style="list-style-type: none"> • Powder size (e.g. d10, d50, d90) • Powder packing • Material composition & properties • Laser or e-beam spot size • Pulse v CW energy deposition • Power level • Pulse spacing (if pulsed) • Scan speed • Atmosphere (air, inert gas) • Material homogeneity (variations in O₂ or alloy constituents) • Linear track separation • Vertical step height • Powder age & re-use • Part geometry, STL file characteristics • Scanning strategy (contour-fill, checker board, random) • Scan to powder-wiper orientation • Errors (e.g. motion, energy deposition) 	<ul style="list-style-type: none"> • Conduction heat transfer • Phase changes • Radiation heat transfer • Denuding effect • Balling effect • Spatter • Melt pool size (3D) • Pore formation • Hydrodynamics • Raleigh instability • Marangoni circulation • Grain Structure • Spatial variations in temperature (e.g. proximity to heat sinks) • Variations in energy deposition (e.g. variations in absorptance) • Staircase effect • Thermal expansion & Shrinkage • Residual stress

To illustrate the potential impact of the surface texture on an AM component a calculation was performed of the approximate total surface area created during the build, compared to the surface area remaining on the outside of the component after build completion.

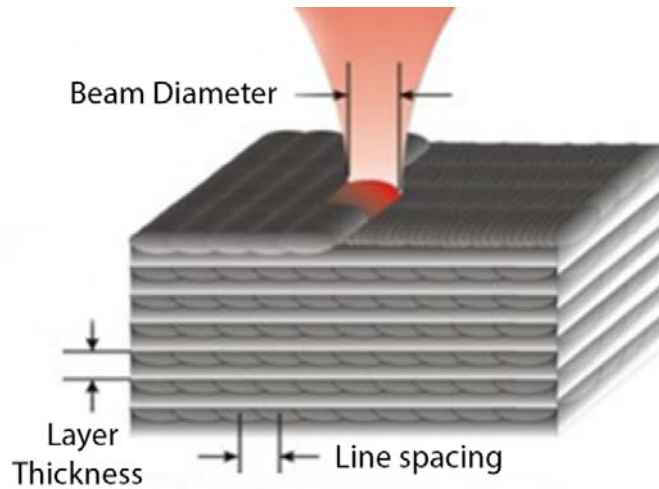


Figure 2-8: Picture of typical PBF build configuration. Showing build layers and line-spacings. Modified from [43].

Figure 2-8: shows a typical build configuration. The approximate embedded surface (S_{emb}) was calculated using Equation 1 (developed by this author). This example is for a PBF AM cube, assuming orthogonal scan pattern and rectangular (or square) bead cross section for each pass.

$$S_{emb} = L^2((M-1) + (N-1)) \quad \text{Equation 1}$$

Where:

L = Part width, length, depth

M = Laser passes on each layer

N = Number of layers

Therefore:

L^2 = the area of each embedded horizontal or vertical surface

$(M-1)$ = the number of embedded vertical surfaces

$(N-1)$ = the number of embedded horizontal surfaces

The external surface of a cube, s_{ext} , is given by:

$$s_{ext} = 6L^2 \quad \text{Equation 2}$$

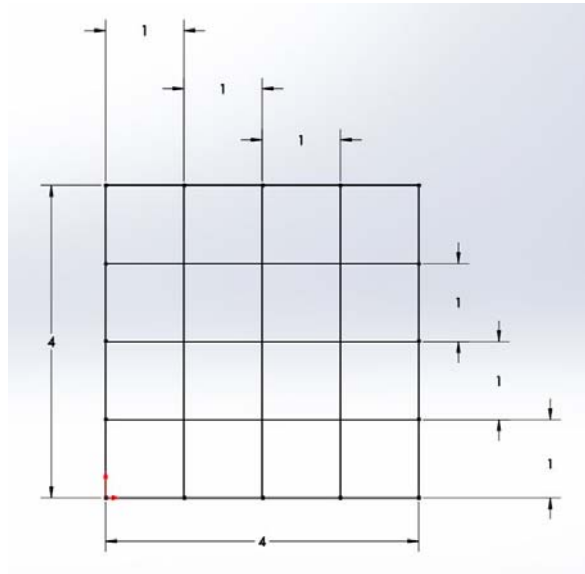


Figure 2-9: Diagrammatic side view of 4 mm cube showing scan pattern. Representing 1 mm layer thickness and 1 mm line-spacing.

For a 4 mm cube, 4 passes per layer (each pass 1 mm wide), 4 layers (each 1 mm thick):

$$\text{Embedded surface} = 4^2 \times (3+3) = 96 \text{ mm}^2$$

This is three embedded horizontal surfaces, each with an area of 4 mm x 4 mm in addition to three embedded vertical surfaces, each with an area of 4 mm x 4 mm, see Figure 2-9.

$$\text{External surface} = 6 \times 4^2 = 96 \text{ mm}^2$$

$$\text{Percentage of "total surface" remaining} = 96 / (96+96) = 50\%$$

Similarly, for a 10 mm cube, 100 passes per layer, 100 layers:

$$\text{Embedded surface} = 10^2 \times (99 + 99) = 19,800 \text{ mm}^2$$

$$\text{External surface} = 6 \times 10^2 = 600 \text{ mm}^2$$

$$\text{Percentage of "total surface" remaining} = 600 / (600+19,800) = 3\%$$

So in this example, for a 10 mm cube with 100 μm layers and 100 μm scan spacing, the final surface is less than 3% of the total surface area produced during the build. The vast majority (97%) of the surface manufactured during the build is re-melted as further layers are applied. This illustrates the possible catastrophic impact of surface defects on the internal structure of

the component. The as-built AM surface may be post-processed by machining for example. Additional material needs to be added to the design prior to the build in specific areas that will be post processed to improve sealing, bearing areas or mounting surfaces. This is similar to the allowances provided on casting drawings. Design of datums on the part should be considered to allow correct mounting and orientation prior to this machining. The depth of surface defects and possible surface distortions produced during the build is critical in deciding the additional material allowance required to ensure complete clean-up of the surface. Characterisation of the build chamber using artefacts that can be compared to the nominal CAD drawing using a deviation analysis will provide significant information on the required allowance, see 7.4.4.

2.2.4 Profile and areal surface measurement

The review paper, Townsend et al., "Surface texture for metal additive manufacturing: a review" [15], Appendix 1, contained an analysis of literature pertaining to surface texture metrology of metal additively manufactured parts. The review paper was divided into sections based on area-of-interest. The following section of the thesis are based upon those sections, with additional explanation where applicable. Industrial applications, build technology and raw materials, surface measurement and characterisation and surface texture parameters are discussed. Surface measurement and characterisation can broadly be divided into two methods: profile and areal. Profile measurement is the extraction of two-dimensional data from the surface: linear position along a straight line (x) and a corresponding surface height (z) at that position. Areal surface measurement data is generally of height map format, consisting of an (x,y) location on a plane with a corresponding height value (z). Measurement and characterisation of true 3D data (x,y,z) will be discussed in later chapters. ISO standards 4287 [44] and ISO 25178-2 define the most frequently used surface texture parameters in academia and industry. ISO 4287 defines terms, definitions and surface texture parameters for profile measurements and ISO 25178-2 defines terms, definitions and surface texture

parameters for areal measurements. While profile parameters still see more application in the reviewed research (80%), with areal parameters reported in approximately 20% of the research, areal parameters have distinct advantages over profile parameters for the characterisation of surfaces. Surfaces topography is three dimensional in nature and so analysis using profiles (two dimensional data) will not fully describe the surface and may give misleading results when taken in isolation, leading to components that may not function as required. Figure 2-10: shows a surface with an extracted profile measurement. The profile measurement may be interpreted as a pit or a scratch. The measured surface shows this is a scratch. Functionally, for fluid sealing for example, a pit may be acceptable whereas as scratch may lead to leakage.

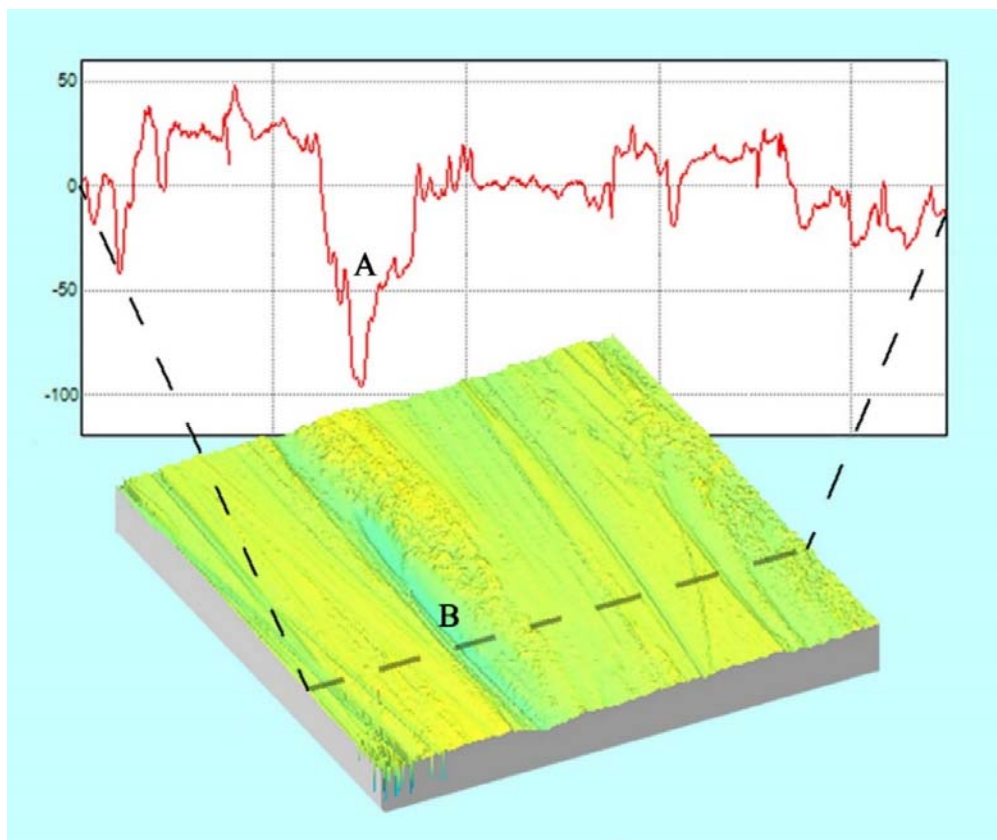


Figure 2-10: Profile measurement extracted from a ground surface. Profile trace "A" could be a pit or a scratch. "B" surface image indicates this is a scratch. Reproduced from [45].

2.2.5 Industrial applications, AM methods and build materials

The aerospace and medical industries have been early adopters of AM manufacturing [46]. In part, this interest is because of the ability to manufacture components using standard high-performance metal material types currently used in these industries, such as titanium alloys (34% of references that specified material used titanium, with Ti6Al4V and Ti6Al4V ELI comprising 95% of those references) and stainless steels (39% of references, 316L SS comprising 70% of those references). Other steels, such as alloy and maraging steels comprise 10% of the literature. Refractory materials, such as cobalt chrome and alumina, together with tool steels and copper alloys comprise only 7% of the analysed references. Nickel alloys were the subject of 5% of references (with Inconel 625 being the subject of 75% of the research). Aluminium alloys, such as AlSi10Mg were the subject of 5% of the research. At this point the metal AM build process with the greatest economic impact has been PBF [42]. As a result there has been greater research into metal PBF processes than other metal AM processes, such as DED, material extrusion and material jetting. While literature references the importance of AM surface texture for industrial applications, currently the published AM surface texture research shows limited connection to application-specific industrial applications. Generally, AM surface texture research is at an infant stage, where surface texture metrology is being used to understand the manufacturing process capability and the effect of build parameter variation. There has been some investigation into the use of bio-compatible materials, such as cobalt chrome and Ti6Al4V ELI, using AM techniques [47, 48]. The effect of AM surface roughness on electromagnetic horn antennae performance [49] and the effect of texture (as-built, machined and polished) on fatigue performance has been investigated [50].

A review of the literature indicated that, of the two most significant metal AM processes, PBF and DED, PBF was the subject of greater research, with 44 published references ([47, 48, 50-91]). There were seven published references for DED research ([92]). Table 2 shows the AM technique used for each of the material groups used in the AM surface research.

The research included in this thesis will be focussed on PBF techniques, using aerospace and medical grade materials, Ti6Al4V ELI, AISI10Mg using EBM and SLM build systems, to ensure the maximum relevance of the research.

Table 2: Reviewed research papers for each material group. Showing percentage of AM technique (EBM, laser and DED) used in the research.

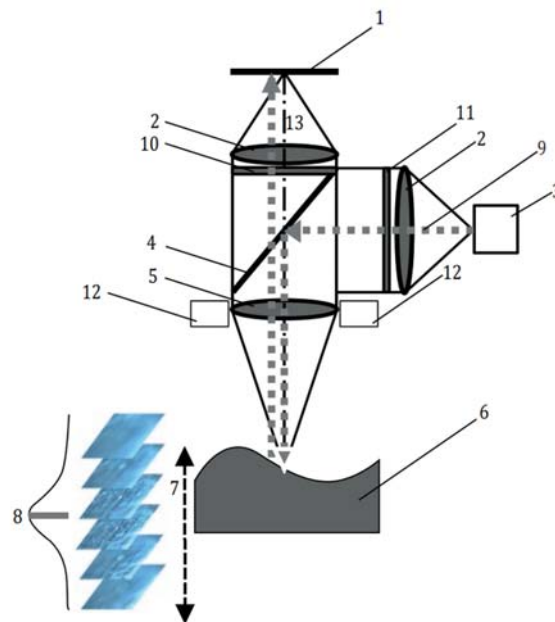
Material	AM process		
	EBM	Laser	DED
Nickel Alloys	0	100%	0
Aluminium alloys	0	100%	0
Stainless steels	0	87%	13%
Other steels	0	83%	17%
Titanium alloys	35%	50%	15%
Others	0	100%	0

2.2.6 Measurement technologies

Historically, surface texture has been measured using contact styli profilometers. Stylus profile texture measurement and characterisation are still ubiquitous in industrial situations, the systems are generally low-cost and there is a comfort-level due to familiarity. In the reviewed literature, 40% of the references used stylus profile measurements. Contact styli may be raster-scanned across the surface and the individual profile measurements may be combined to create an areal height map of the surface, so providing the advantages discussed for areal measurements; however, this raster-scan process tends to be very time consuming. There were no areal raster-scanned stylus measurements in the reviewed literature. Additionally, the typical powder-based AM surface, see Figure 2-4:, presents significant measurement challenges due to re-entrant features, discontinuities, high slope angles and vertical walls. The contact styli may jam and be damaged when traversing the steep slopes, there may be shank contact and also loss of contact. The progressive realisation that areal measurements now provide more information in general [93], but especially for complex AM surfaces, is leading to greater adoption of non-contact (optical) areal measurement systems.

2.2.7 Focus variation

The machine used for reference measurements in this work (an Alicona G4) is an optical areal measurement system using the focus variation measurement method. This method has previously been used for AM areal surface texture measurement [62, 94]. The focus variation process is a combination of narrow depth of field optical elements and vertical scanning of the optics. This process acquires areal surface texture information, with the option, of course, to extract profile data from the areal data sets. A schematic of a typical focus variation system is shown in Figure 2-11: [95]. The Alicona G4 system is shown in Figure 2-12:.



Key

- 1 array detector
- 2 optical components
- 3 white light source
- 4 illumination beam splitter
- 5 objective
- 6 specimen
- 7 vertical scan
- 8 focus information curve with maximum position
- 9 light beam (...)
- 10 analyzer
- 11 polarizer
- 12 ring light
- 13 optical axis (-.-.)

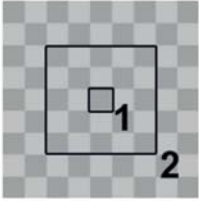
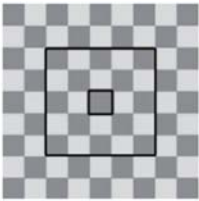
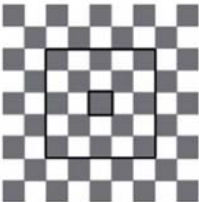
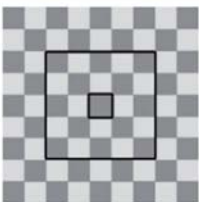
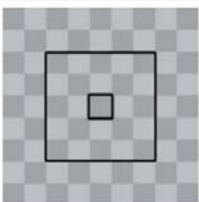
Figure 2-11: Schematic of a typical focus variation system. Reproduced from [95].



Figure 2-12: Alicona G4 focus variation surface measurement system. Reproduced from [96].

The focus variation system includes an integrated turret with selectable objective lenses, with magnifications typically ranging between $\times 2.5$ and $\times 100$ [97], are selected to provide the surface resolution suitable for the sample under test. The following numbered references refer to Figure 2-11: A beam-splitter (4) is used to insert white light (from the white light source (3)) into the optical path [98]. This light is focussed onto the surface (6) by the objective lens (5). Light reflecting from the surface and onto the objective lens is projected onto a planar detector (1). This is similar to the operation of a digital camera. Generally with a digital camera a particular object in the photograph, or perhaps all areas of the image, would ideally be in focus. The lens system in the focus variation system intentionally has a narrow depth of field, so only small areas of the measured object are sharply imaged [98]. The image gathering assembly is mounted on a motorised vertical (z) stage. The plane of focus is positioned just below the lowest point on the sample. An image is acquired, the stage is then lowered a known distance, based on the lens system and resolution, and another image is acquired. This process is repeated until the plane of focus is above the highest point in the sample. This will ensure that every lateral measurement point on the surface (again defined by the selected resolution) will be, or near, full focus at a known height. This technique uses image contrast to verify focus and therefore the height for a particular area: the higher the

image contrast the more focussed the image. To ascertain contrast for a particular location the neighbouring pixels are compared to the pixel at the location of interest [95, 99]. The highest contrast image has the greatest standard deviation for the local pixel grey-scale values, see Figure 2-13:.

Scan position	Surface image	Standard deviation
Out of focus		10
Almost in focus		20
In focus		50
Almost in focus		20
Out of focus		10

1 Point of interest for which the focus information is calculated.
2 5x5 neighbourhood of points used to calculate the focus information (standard deviation).

Figure 2-13: Focus variation information at a position of interest. (1) position of interest, (2) quantification of focus based on the standard deviation of the intensities of neighbouring points. Reproduced from [99].

The acquired height and location data is used to generate height map data for the component under test. Through-the-lens illumination may be supplemented by additional lighting sources, such as a ring light (12) which preferentially illuminates the sides, rather than the top, of the surface being measured. This reduces the contrast between top and sides and permits measurement of surfaces with slopes greater than 80° [100]. The focus variation system includes an (x,y) stage that allows the sample to be moved beneath the optical measurement system. This is used to locate the region of interest, but also allows image stacks to be acquired from adjacent (overlapping) areas. The data from all measurements is then combined to produce height map data for a larger measurement area. This stitching may be required to comply with the measurement resolution and sampling area requirements defined by standards such as ISO 25178. Focus variation is not suitable for very reflective or specular surfaces as there will generally be too much contrast between the specular and non-specular areas. Transparent surfaces will also present a problem as the system is unable to differentiate between outer and inner surfaces. The surfaces of as-built powder bed fusion metal AM components generally are well within the measurement capability of focus variation systems [101].

2.2.8 Surface characterisation

Once the surface has been measured then meaningful, quantitative, data needs to be extracted. As discussed in 2.2.2, selecting the correct scale-of-interest of the surface is critical for obtaining the most useful information from the surface measurement. This selection governs the filtering to be applied to the data, so only the data of relevant scales is evaluated, and is not swamped by (primarily longer wavelength, larger amplitude) non-critical data. The function of the surface will also dictate the type of surface texture parameter extracted from the data: amplitude, spatial, hybrid for example [93, 102]. As has been discussed in section 2.2.4, ISO 25178-2 defines areal parameters. ASME B46=1-2009 [103] and JIS B 0601:2013 [104] also define areal parameter sets, but a review of the standards used for the

characterisation of AM surfaces [15] showed the literature referenced only the ISO standard for area measurement and characterisation.

2.2.9 Parameters sensitive to AM surface and component performance

2.2.9.1 Profile parameters

Within the references reviewed, approximately 20% used areal parameters for surface analysis. The majority (80%) of AM surface measurement references used profile parameters, with, by far, the most commonly used parameter being the ISO 4287 profile parameters R_a , the arithmetic mean deviation of the assessed profile [52, 63, 65, 81, 85, 105, 106]. Another ISO 4287 profile parameter, R_q , is the second most used parameter. R_q is the root mean square of the ordinate values within the sampling length, that is, the sample standard deviation [59, 67, 107]. Other profile parameters have also been used successfully to characterise AM surfaces: R_z , the maximum peak-to-valley height of the measured profile [59, 67] and the material ratio curve [53]. The material ratio curve is also known as the Abbott-Firestone curve. This curve is the material ratio as a function of height down from the highest peak to the deepest valley (at the peak the value is zero; at the deepest valley the value is 100%). The predominant application of profile parameters (and R_a in particular) for AM surface texture metrology is perhaps not surprising. R_a is the standard surface measurement parameter in non-AM engineering manufacturing, where the advantages of areal measurement (see 2.2.4) are still gaining acceptance.

2.2.9.2 Areal parameters

Perhaps, not surprisingly, the most widely adopted ISO 25178-2 areal parameter is S_a , which is the arithmetic mean height of the scale-limited surface. S_a is the areal equivalent of the profile parameter R_a . It should be noted that the majority of definitions of the areal parameters in ISO 25178-2 specify a scale-limited-surface, that is, surface texture data after the application of hi-pass and low-pass filtration to remove non-relevant wavelengths, see

section 2.2.2. Results for these parameters will vary considerably at different scales (i.e. after application of different filter sets), so definition and reporting of these filtration values is imperative. The parameter Sa was used in 90% of the references where areal parameter data was reported.

2.2.9.2.1 Sa

Sa , as defined in ISO 25178-2, is the arithmetic mean of the absolute of the ordinate values within a definition area, (A), see Equation 3.

$$Sa = \frac{1}{A} \iint_A |z(x, y)| dx dy \quad \text{Equation 3}$$

2.2.9.3 Surface and function

The parameters chosen to characterise the AM surface need to be sensitive to changes in the surface texture. These changes can be caused either by modification of the AM build parameters or through post-processing of the as-built AM surface. Figure 2-14: shows false-colour height maps of the surfaces of SLM Ti6Al4V components pre and post vibro-finishing. The areal parameters most sensitive to the changes produced by the vibro-finishing process were peak material volume (Vmp), developed interfacial area ration (Sdr), reduced peak height (Spk) skewness (Ssk), autocorrelation length (Sal), material ratio (dales) $Smr2$. Moylan [108] proposed using a combination of mean roughness (that is Ra or Sa), peak to valley height (Rz or Sz), skewness (Rsk or Ssk) and kurtosis (Rku or Sku) as a parameter set to be used to characterise the surfaces of AM components. Skewness and kurtosis are the third and fourth order moments of the probability distribution for the surface height. Skewness is an indicator of the bias of the surface material in relation to the mean line between the peak and valley. Kurtosis is an indicator of the "peakedness" of the surface. The greater the kurtosis the greater the "peakedness".

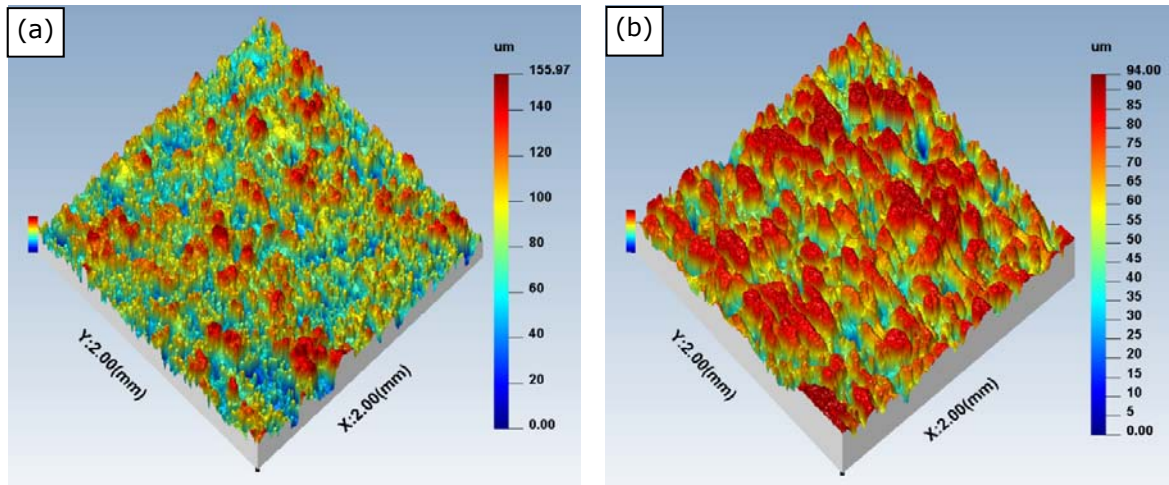


Figure 2-14: Focus variation height maps of a Ti6Al4V SLM part side surface. (a) as-built, S_a 21 μm (b) post vibro-finishing, S_a 12 μm . Modified from [15].

Research has related surface texture to fatigue life [50, 109, 110]. In Ref. [109] Ti6Al4V SLM and EBM components were analysed and fatigue life was correlated to R_a . It was found that as the R_a increased from 3 μm to 1000 μm the fatigue life decreased from 10^5 to 10^4 cycles. This work also reported that surface defects had the most impact on reducing the high-cycle fatigue life. Generally, research into the surface texture of powder bed fusion AM components has been performed to gain an understanding of the physics and to optimise individual process parameters for PBF processes [15]. A bullet-point list of conclusions drawn for specific AM build variation is reported here.

- Beard [111] found that lower scan speed and higher power tend to improve top surface roughness.
- Grimm [112] found a correlation between the surface orientation of SLM parts and S_{dr} (developed interfacial area ratio).
- Mumtaz [63] investigating SLM Inconel 625 parts, found that adjusting parameters to achieve minimum top surface and bottom surface R_a values concurrently was not possible. Parameters that promote a reduction in top surface R_a : increased overlap, reduced scan speed, tend to increase the balling effect (surface tension produces round

beads of melted material) and increase side surface Ra . Increasing peak power (to the point of significant material vaporisation) reduces both top and side Ra .

- Safdar [52] researching EBM Ti6Al4V artefacts noted Ra values increased with increasing beam current and decreased with an increase in offset focus (moving the plane of focus of the electron beam vertically in relation to the powder layer) and scan speed.
- Strano [85] noted SLM upskin (upward facing) surface roughness was influenced by build orientation and layer thickness and downskin surfaces were additionally influenced by laser power.
- Triantaphyllou [62] found that Sa and Sq were suitable measurement parameters for SLM and EBM Ti6Al4V components and that Ssk (skewness) differentiated upskin from downskin surfaces.

Example surface texture parameters used in AM research are shown in Table 3.

Table 3: Examples of surface texture parameters used in AM research, from [15].

Author	Ref.	Surface texture parameter	Area of research
Frazier	[109]	Ra	EBM and SLM Ti6Al4V fatigue life
Grimm	[112]	Sdr	SLM Hastelloy X surface build angle (hemi-sphere)
Jamshidinia	[53]	Rk, Rpk, Sa , Material ratio	EBM Ti6Al4V heat accumulation
Moylan	[108]	$Ra, Sa, Rz, Sz, Rsk, Ssk, Rku, Sku$	AM surface and build angle (platens)
Mumtaz	[63]	Ra	SLM Inconel 625 build parameters to optimise horizontal and vertical surfaces
Pyka	[59]	Ra, Rq, Rz	SLM Ti6Al4V lattice surface treatment
Safdar	[52]	Ra	EBM Ti6Al4V build parameters
Triantaphyllou	[62]	Sa, Sq, Ssk	SLM and EBM Ti6Al4V build angle (platens)
University of Huddersfield	-	$Vmp, Sdr, Spk, Ssk, Sal, Smr2$	SLM T6Al4V vibro-finishing

Unfortunately, it is difficult to generalise AM machine setup parameters as each machine design and each powder configuration are different. However, in general there is an energy density "sweet-spot" below which insufficient melting occurs and above which there is powder vaporisation and spatter [63]. One conclusion from Ref. [62] was that the direction of profile measurement in relation to the laser scan direction had little effect on the calculated surface roughness for the EMB or SLM test samples. Similarly, the ASTM F42/ISO TC 261 Joint Group

for Standard Test Artefacts (STAR) concluded that the stair-step effect (the approximation of an angled surface due to the finite build layer thickness) was not the dominating factor influencing the surface roughness of PBF platens built at different angles to the plane of the build plate [108]. Indeed, Taylor [42] found that, with certain build conditions, the primary surface lay was not parallel to the laser scanning direction.

2.2.9.4 Process modelling

The AM build process is complex with many interactions between build parameters and physical processes, see Table 1. The importance of computer simulation and modelling of the AM process, to help understand this relationship between the build process and the surface topography, has been recognised [42, 84, 113, 114]. There are many factors to be modelled to accurately represent the physical process. King et al. [115] have modelled the PBF process and have reported that a simulation of a 1 mm laser pass may take many days on a multi-processor computer. The validity of these modelling operations can now be verified by comparison to real-time monitoring of the PBF build process using synchrotron X-ray imaging and diffraction [116]. There are now commercial organisations, such as 3D SIM, developing process-solvers that combine simulation with a priori data to analyse build data and component configuration to optimise build parameters on a part-by-part basis [117]. This complexity highlights the importance of having a target, based on function, to assure optimisation of the build for the intended use of the part.

2.2.9.5 Feature extraction

An advantage of areal surface measurement is the ability to image complete surface features (as opposed to cross-section information obtained from profile measurements). There are established pattern recognition and segmentation systems [16, 118-120] for feature extraction. The process described in ISO 25178-2 includes terms relating to topological geographical features to aid understanding: hills (peaks), ridgelines, dales (pits), courses and

saddles. The surface is segmented based on these boundaries and a change tree based on these segmented areas is developed. This initial segmentation typically produces an over-segmented surface, so segmented areas are combined by "pruning". This process involves combining adjacent segments, starting with adjacent segments with the smallest peak-to-saddle or pit-to-saddle distance. This can be visualised by filling all dales with water to the same pit to water surface level. At some height the water will overflow from the dale with the smallest pit-to-saddle distance and the water will flow into the adjacent dale. These adjacent dales will then be combined. The process continues until a specified threshold is reached, such as a defined number of peaks or a defined peak-to-saddle distance. The final segmentation map may then be used as a map applied to the original surface texture data to extract, for instance, only significant hills (peaks). By selecting map configurations the extracted surface features or the underlying surface without features may be independently analysed. This analysis technique has application to PBF AM surfaces, where the surface asperities may be extracted and analysed independently from the base surface. Similarly the asperities may be extracted and removed, allowing analysis of the underlying surface [121]. There may be significant information about the build process contained in the surface texture data of the underlying surface that would otherwise be overwhelmed with data from the asperities. Post-processing applications to remove the asperities may significantly damage the underlying surface, potentially destroying this useful information. The surface of an SLM ALSi10Mg component is shown in Figure 2-15:(a) shows the false colour height map of the surface section after measurement on a focus variation instrument. Figure 2-15:(b) shows the surface after application of a global threshold to the surface: all surface texture information below the threshold height is removed. Figure 2-15:(c) shows watershed segmentation, as described above, followed by Wolf pruning per ISO 25178-2 at a threshold of 1% Sz. Figure 2-15:(d) shows the surface after watershed segmentation followed by 8% Sz Wolf pruning. The surface features remaining may now be extracted and analysis, or the surface features may be removed to allow analysis of the remaining surface.

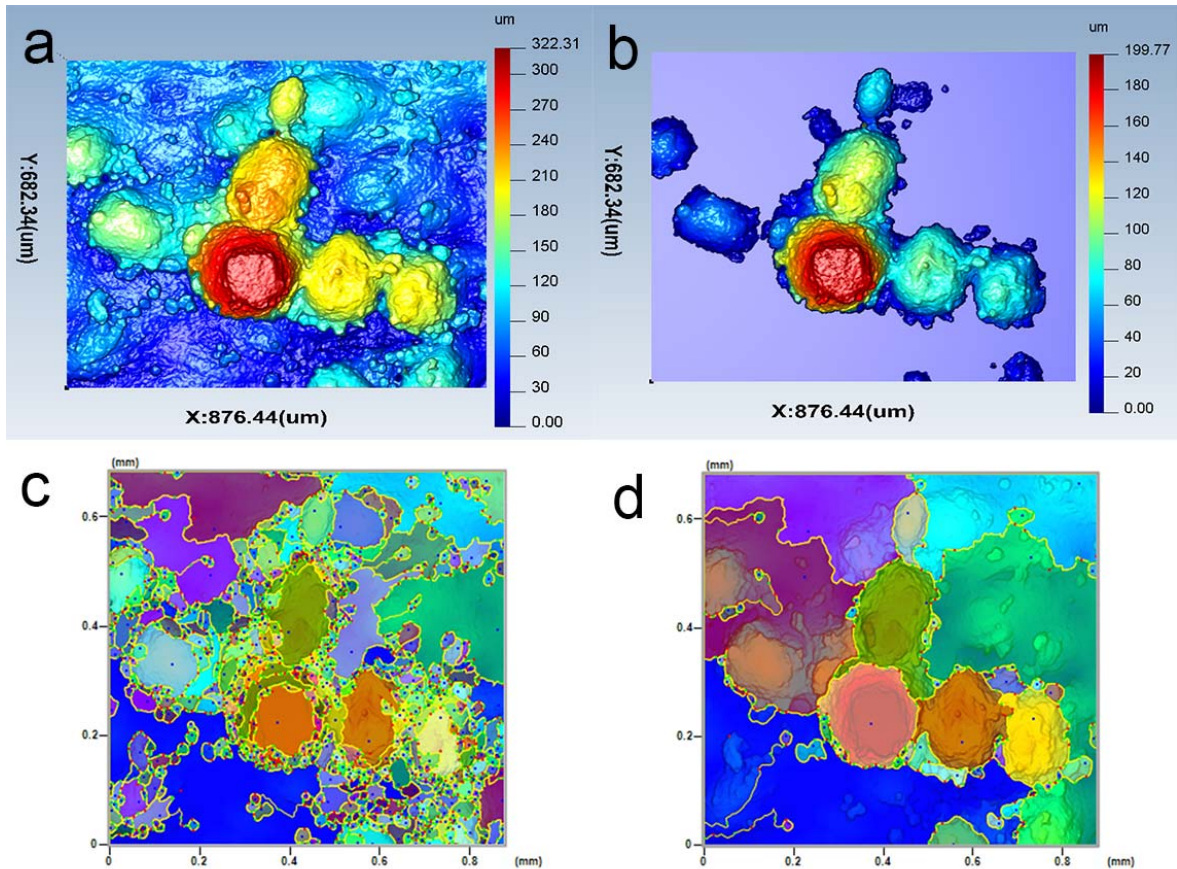


Figure 2-15: Surface feature extraction from and SLM part top surface. (a) False colour height map (original data), (b) After levelling and thresholding, (c) Watershed segmentation followed by 1 % Sz Wolf pruning, (d) After 8 % Sz Wolf pruning. Reproduced from [15].

2.2.10 Areal surface data processing

Surface texture has been defined in ISO 25178-2 as the scale-limited surface that remains after the application of a series of operations applied to the primary extracted surface. Per ISO 25178-2 the F-operation removes the form (as required). This is followed by an L-filter nesting index (high-pass filter) and S-filter nesting index (low-pass filter) that remove the long wavelength and short wavelength features respectively. The S-L (L-filter nesting index and S-filter nesting index) process was used for all surface samples reported here, see Figure 2-16:.

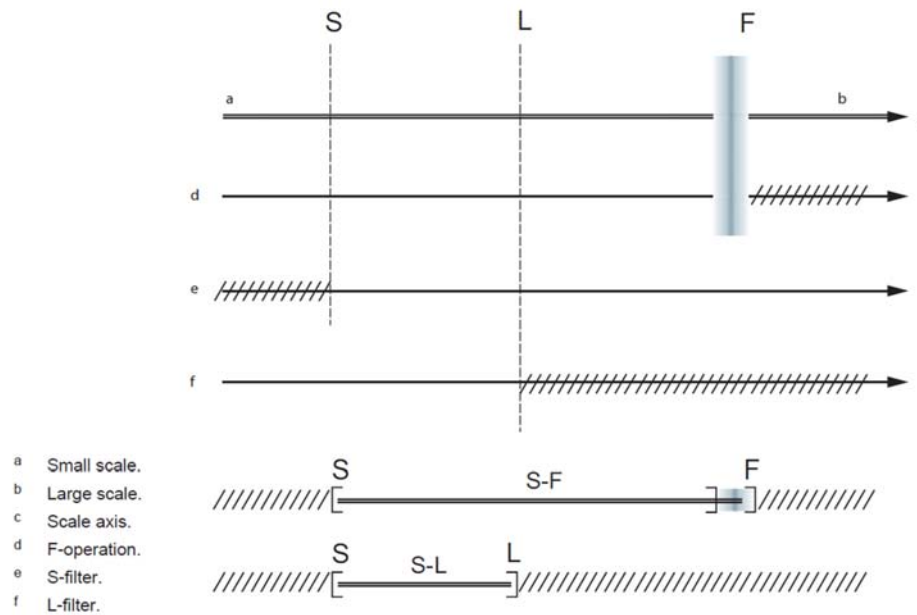


Figure 2-16: ISO 25178-2 Surface filtering. Showing the S-L (L-filter nesting index and S-filter nesting index) filtering system. Reproduced from [16].

The values of the parameters extracted from surface data are dependent upon the measurement and processing techniques. As has been discussed, in general the measurement, scale-of-interest, filtering and parameter selection should be based, if possible, on the surface function [38]. If this is not possible then the filtering recommendations of the ISO standards should be applied. It is important, if possible, to have an understanding of this relationship between function and surface texture, in particular finding scales of interest (hence filtering) and parameters that provide maximum sensitivity to the surface changes that will most influence functional performance. The results will vary significantly depending upon the filtering applied. As an example, Figure 2-17: shows the effect of changing the L-filter nesting index value for an 8 mm x 8 mm measurement of the top (upskin) surface of an SLM AISi10Mg aluminium block. Figure 2-18: shows the effect of changing the L-filter nesting index value for an 8 mm x 8 mm measurement of the side surface of an EBM Ti6Al4V titanium block. The S-filter nesting index was 0.025 mm for both data sets. It can be seen that there is significant reduction in S_a value below an L-filter nesting index value of approximately 2 mm.

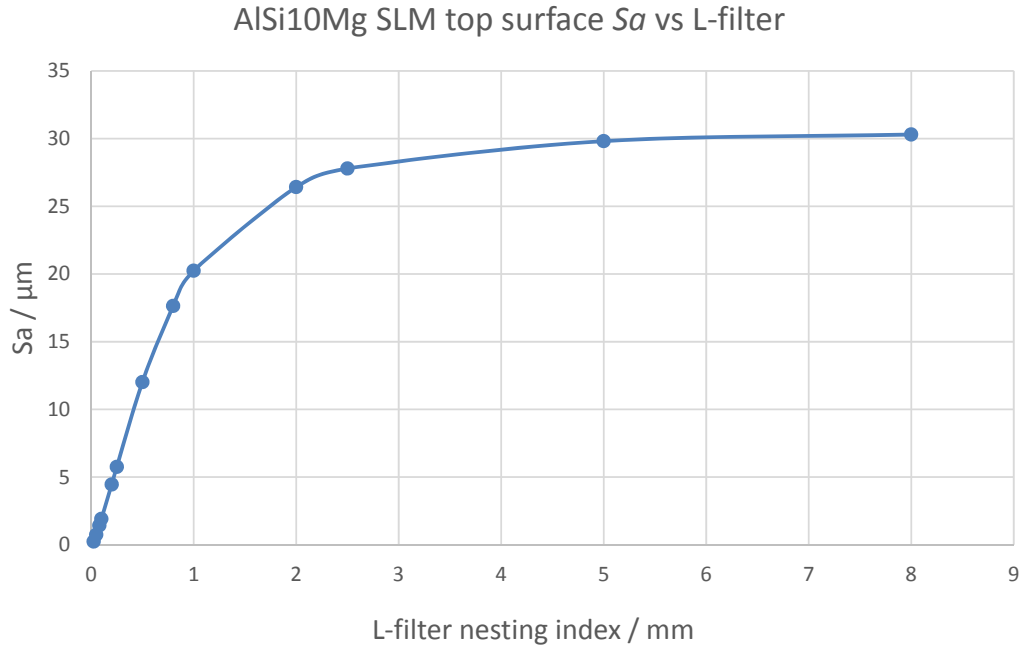


Figure 2-17: Effect of changing L-filter nesting index on S_a value, SLM sample. Surface extracted from the top surface of an AlSi10Mg SLM sample.

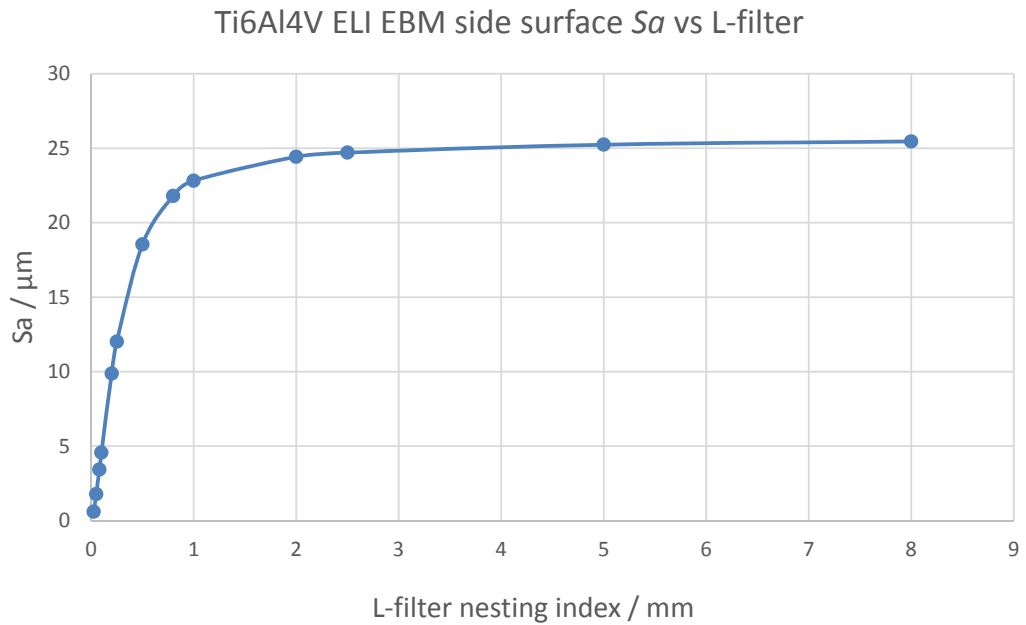


Figure 2-18: Effect of changing L-filter nesting index on S_a value, EBM sample. Surface extracted from the side surface of a Ti6Al4V EBM side sample.

Filtering is normally a combination of a low-pass and high pass filter. The choice of high-pass filter (λ_c per ISO 4288 for profile measurements, L-filter nesting index per ISO 25178-3 for areal measurements) will generally have a greater effect on the extracted parameter data. The low-pass filter is often considered a noise filter. ISO 25178-3 suggests an L-filter nesting index value of 5x the largest scale of interest: "*The value of the L-filter nesting index is typically five times the scale of the coarsest structure of interest*". Often, however, the exact scale of interest is not known and the choice may be arbitrary. The profile standards do define a cutoff (λ_c) value, based on the surface roughness value. This is based on the type of surface. For a stochastic surface, such as a ground or additively manufactured surface, Table 1 of ISO 4288 [122] defines the high-pass filter to be used, see Table 4.

Table 4: ISO 4288, table 1.
Showing sample and evaluation lengths for measured profile Ra values.

Ra	Roughness sampling length l_r	Roughness evaluation length l_n
μm	mm	mm
$(0,006) < Ra \leq 0,02$	0,08	0,4
$(0,02) < Ra \leq 0,1$	0,25	1,25
$0,1 < Ra \leq 2$	0,8	4
$2 < Ra \leq 10$	2,5	12,5
$10 < Ra \leq 80$	8	40

For example, a surface roughness of Ra 5 μm would require a sampling length of 2.5 mm with equivalent cut-off value (λ_c) of 2.5 mm. The evaluation length in the table are five times the sampling length. Five individual measurement results, each with a sampling length as specified in the table are averaged. This cut-off filtering value corresponds to an areal filter (L-filter nesting index) of the same value (so that the same wavelength information is removed). Per ISO 251278-3, the required surface, if possible, should be a square with sides with a length equivalent to the L-filter nesting index value. Per ISO 25178-3, the default L-filter is an areal Gaussian filter. This default filter has been used for all the research reported

here. The low-pass filter (S-filter nesting index) can be selected from ISO25178-3 table 1, see Table 5.

Table 5: ISO 25178-3 table 1.
Showing the relationship between areal L-filter nesting index, S-filter nesting index and bandwidth ratio.

F-operation or L-filter nesting index value mm	S-filter nesting index value mm	Approximate bandwidth ratio between the F-operation or L-filter and S-filter nesting index values
...
0,1	0,001	100:1
	0,000 5	200:1
	0,000 2	500:1
	0,000 1	1 000:1
0,2	0,002	100:1
	0,001	200:1
	0,000 5	400:1
	0,000 2	1 000:1
0,25	0,002 5	100:1
	0,000 8	300:1
	0,000 25	1 000:1
0,5	0,005	100:1
	0,002	250:1
	0,001	500:1
	0,000 5	1 000:1
0,8	0,008	100:1
	0,002 5	300:1
	0,000 8	1 000:1
1	0,01	100:1
	0,005	200:1
	0,002	500:1
	0,001	1 000:1
2	0,02	100:1
	0,01	200:1
	0,005	400:1
	0,002	1 000:1
2,5	0,025	100:1
	0,008	300:1
	0,002 5	1 000:1
5	0,05	100:1
	0,02	250:1
	0,01	500:1
	0,005	1 000:1
8	0,08	100:1
	0,025	300:1
	0,008	1 000:1
...

The S-filter value is based on the L-filter nesting index. ISO 25178-3 table 3, see Table 6, requires that the sampling distance for optical instruments should be a maximum of one third of value the chosen S-filter nesting index. Optical instruments, such as the Alcona G4, require that the lateral resolution is selected prior to a surface measurement (the lateral resolution value is equivalent to the S-filter nesting index value). The sampling distance is then automatically set to one third this value.

Table 6: ISO 25178-3 table 3.
Showing the relationship between S-filter nesting index, sampling distance and lateral period limit for optical surfaces.

S-filter nesting index value ^a mm	Maximum sampling distance mm	Maximum lateral period limit mm
...
0,000 1	0,000 03	0,000 1
0,000 2	0,000 06	0,000 2
0,000 25	0,000 08	0,000 25
0,000 5	0,000 15	0,000 5
0,000 8	0,000 25	0,000 8
0,001	0,000 3	0,001
0,002	0,000 6	0,002
0,002 5	0,000 8	0,002 5
0,005	0,001 5	0,005
0,008	0,002 5	0,008
0,01	0,003	0,01
0,02	0,006	0,02
0,025	0,008	0,025
0,05	0,015	0,05
0,08	0,025	0,08
0,1	0,03	0,1
0,2	0,06	0,2
0,25	0,08	0,25
...

^a Alternatively, the optical method used to probe the surface may provide an inherent filter giving rise to the lateral period limit that approximates a Gaussian filter; in these cases, the lateral period limit may be used to define the short-wavelength nesting index instead of a digital S-filter.

In the researched literature, 70% of the references report values of the nesting indexes. This reporting is very important as it will allow others to duplicate the measurements and characterisation techniques. Work has been performed to evaluate whether cut off values required by ISO 4288 are applicable to additively manufactured surfaces. Triantaphyllou [62] manufactured SLM and EBM Ti6Al4V components, both with surface Ra values that would require a high-pass filter (λ_c) per ISO 4288 of 8 mm. The areal measurement area was a square with sides 8 mm. The value of L-filter nesting index was established by using area-scale analysis techniques developed by Brown [123]. The results obtained showed that, for their samples, the L-filter nesting index, and hence the length of the sides of the measurement square needed to be no more than 2.5 mm to characterise the surface (i.e. the majority of the information about the surface was contained within the wavelengths less than 2.5 mm, there was little significant data with wavelengths between 2.5 mm and 8 mm). This is a promising technique, and would allow a significant reduction in required measurement area and processing time, however the area-scale analysis would need to be applied and results obtained on a case by case basis. If the measurement is taken using a smaller area it may be difficult to re-measure with a larger area if larger scales are found to be of interest. Conversely, measuring and characterising data extracted from the larger area (for example 8 mm x 8 mm), of course means that a selected, smaller area may be analysed later.

2.2.11 Conclusions

There has been some investigation into the effect of surface texture on functional performance, but the majority has been AM build parameter optimisation. Areal surface texture measurements provide significant advantages over profile measurements and areal techniques are becoming adopted by industry and academia. Areal cut-off filtering selection, per ISO 25178-3, can be based on 5x the largest scale of interest. If the scale of interest is not known, as in the work performed here, then the default position is that the L-filter nesting index can be set to the profile cut-off filter value specified in ISO 4288. These values will be

used in the work that follows. Similarly, the default filter type, as specified in ISO 25178-3, is Gaussian and will be used in the work that follows.

2.3 CT for AM metrology

2.3.1 Computed tomography

Computed tomography imaging was invented in 1972 by Godfrey Hounsfield (EMI) and Allan Cormack (Tufts University). The invention won them both the Nobel prize in physiology or medicine, 1979 “for the development of computer assisted tomography” [124]. The word “Tomography” derives from the Greek words “tomos” which means slice and “graphia” meaning describing. CT is the computational combination of individual X-ray images, taken of the subject at different angles, to produce cross-sectional image slices of the subject. The data is then processed to create 3D volume information. Initial applications were medical, with commercial machines available in the 1970s. CT machines for industrial inspection applications began to appear in the early 1990s. The fundamental difference between medical and industrial machines is the imaging technique: through necessity, the X-ray source and detector incorporated in medical CT machines rotate around the patient. The majority of industrial machines operate with the X-ray source and detector at fixed, known, positions and the component being inspected mounted on a stage with known centre of rotation between the two. The stage then rotates around the axis and an X-ray image is taken at known rotational intervals (for this research the number of individual rotational images ranged from 1583 to 3142). The CT machines used in this research have a cone-beam configuration with a planar detector, see Figure 2-19:.

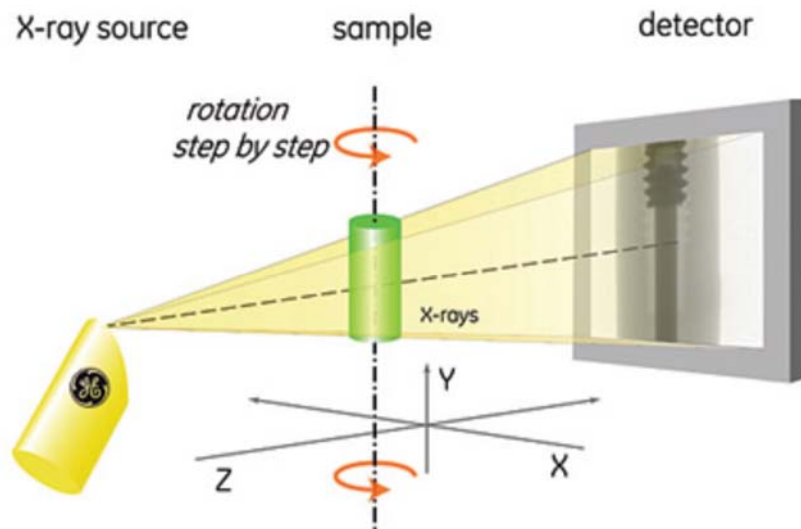


Figure 2-19: Cone beam CT schematic. Showing the X-ray source “gun”, rotating sample under test and the image projected onto the detector. Reproduced from [125].

The detector panel in the CT has pixels, similar to a camera sensor. When the X-ray image data is processed to produce 3D information, voxel information is produced. Voxels (volumetric pixels) are the 3D equivalent of pixels. The source-to-detector distance is fixed in these applications and so the magnification is adjusted by varying the position of the sample between the source and detector. Some of the X-rays from the source are absorbed as they pass through the component, the air, the fixture etc. The absorption equation is (Beer-Lambert law):

$$I = I_0 e^{-\mu t} \quad \text{Equation 4}$$

Where I is the intensity of the X-rays, μ is the attenuation coefficient and t is the thickness of the material. The voxel information is generally calculated from the projection information using the exponential decay of the X-ray beam penetrating the material. This requires that the logarithm of data be taken to linearize the decay characteristic, so the attenuation for each ray is calculated as $\ln(I_0/I)$. After this process the pixel values in the images are the sum of the density values along the beam path from source to detector. The individual X-ray

images (grey-scale images) are then combined to produce a 3D grey-scale volume of the component and background. This is done using filtered back projection. This process can be envisaged as projecting back from the pixel data towards the focal spot location (so in a cone shape, equivalent to the cone-beam). Each projection image has no depth information, just a single grey value for each pixel projected back toward the source. One way to visualise the combination of each of the projection images is to consider the volume stationary and each projection rotating around the stationary volume, the information for each projection adding to all previous projections. Prior to the back projection each of the views is convolved with a filter kernel (convolution matrix) to correct blurring that will occur with simple back projection, see Figure 2-20:.

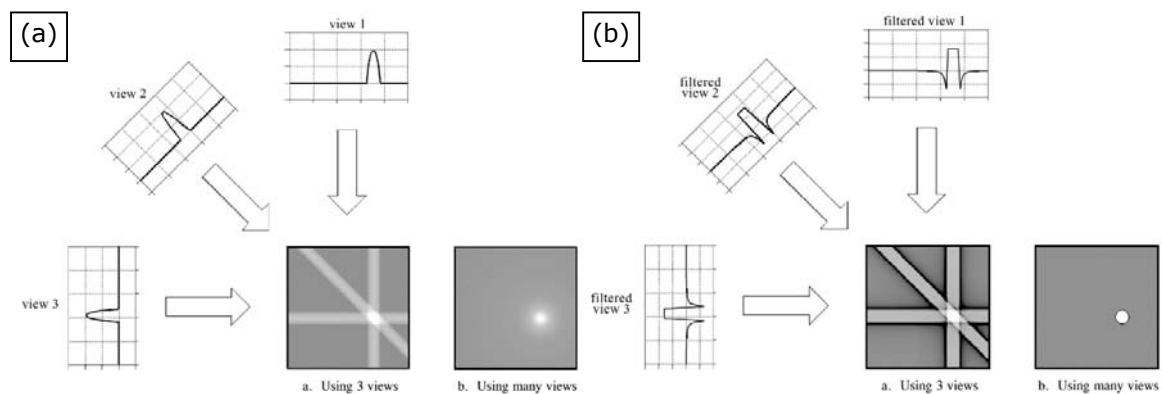


Figure 2-20: CT reconstruction from multiple projections. (a) unfiltered back projection, showing generation of the final image from multiple projections (b) filtered back projection, showing the correction of image blurring. Reproduced from [126].

2.3.1.1 Resolution

In general, the higher the magnification, the greater the resolution. However, the resolution is effected by the X-ray spot size. Above a certain energy per unit area, the electron beam is de-focused to maintain energy density below a maximum value and therefore prevent target damage. The power used in all machines in this research was maintained below 10 W to avoid having to defocus the electron beam. This defocussing of the electron beam produces a

defocussed (blurred) X-ray beam. This is similar to the umbra and penumbra shadow effect produced by the sun, because the sun, just as is the case with the X-ray source is not a single point. The nominal (fully focussed) electron beam spot size for the machines used in this research is 3 μm .

2.3.1.2 Beam hardening

X-ray generation leads to the production of polychromatic beams. This means the absorption becomes non-linear, weak X-rays are readily absorbed, "hardening" the beam. This leads to apparent density differences within the component, particularly on the outside where a ring of apparently denser material may be apparent. One method to compensate for beam hardening is with mechanical filtering, such as using aluminium or copper filters, usually placed just in front of the X-ray gun, see Figure 3-7: and Figure 4-4:.. These filters attenuate the X-ray beam and will preferentially remove low-energy (low kV) X-rays. This increases the mean energy of the beam and tends to make the beam monochromatic. In many applications this mechanical filtering is sufficient to alleviate the effects of beam hardening [127]. Depending upon application, perhaps where mechanical filtering is not possible, complex computational correction may be required. Mechanical filters, importantly, also reduce the contrast in the image. This contrast reduction may be necessary to maintain a suitable intensity range between background and sample intensity levels at the detector, avoiding over-exposing the background image and under-exposing the sample image.

2.3.2 X-ray generation

The CT X-ray source consists of an evacuated tube containing a target (such as tungsten). A filament within the tube, also normally tungsten, is heated electrically. Free electrons are generated through thermionic emission. The electrons are accelerated by an electrical field generated between the filament (cathode [-ve]) and an electrode (anode [+ve]) within the chamber. The generated electron beam is focussed as it passes through the magnetic field

generated by focussing coils. The current flowing through the filament determines the quantity of electrons generated and the acceleration voltage determines the energy the electrons have when they hit the target. Two types of X-ray are produced when the electrons hit the target. Characteristic radiation is target material dependent. This radiation occurs when an electron excites an electron in the inner shell of a target atom. When this electron is ejected and replaced by an electron from a higher energy level (or remains and returns to a lower energy state) a photon of characteristic energy is produced. The majority of the X-ray energy produced is Bremsstrahlung radiation. This radiation is produced when an electron from the beam interacts with a nucleus of a target material atom. The deceleration of the electron produces an X-ray photon. The energy level of Bremsstrahlung X-rays photons produced will range up to the energy level of the impacting electron. The highest level of the X-rays produced determines the penetrating potential of the X-ray. The X-ray energy per unit time (radiant flux), relates to the number of electrons impacting the target, and hence the current flowing through the electron-generation filament. The acceleration voltage needs to be sufficiently high to provide penetration through the object being inspected. There is a balance between filament current and exposure time. A larger current, and hence larger X-ray flux, will require less time to detect sufficient photons on the detector. However, the combination of voltage and current determines the power. As discussed in 2.3.1.1, to avoid having to de-focus the beam (and hence reduce resolution) the power has to be kept below a specific level (10 W for the Nikon XT H 225 used throughout this work). Hence, the current level may be set lower and the exposure time higher for each projection to allow the use of a fully focussed beam and still provide the correct photon accumulation per projection.

2.3.3 Surface determination

Once the grey-scale voxel data have been produced, the actual component surface has to be defined prior to dimensional or surface texture analysis. This process, surface determination, is critical to the accuracy of the generated component. Often dimensional calibration of the

CT machine is performed using centre-to-centre distances of spheres to avoid inaccuracies caused by surface determination selection. There are several methods of surface determination that can broadly be divided into two categories: global and local. Global surface determination locates the surface at a single specific grey value. This is often based on analysis of the grey-scale histogram, or by selecting a volume of background material (such as air) and a volume of component material. The grey-scale value for the surface is then often selected at the grey-level mid-way between these two values, referred to as the ISO 50 value. Local surface determination involves selecting a target grey value, such as the ISO 50 value, and then evaluating the grey-levels within a certain distance (for example, within a band four voxels from the target grey value) of this initial surface. The final surface is then located at the location of maximum grey-scale value gradient. With both methods, interpolation is performed to give sub-voxel surface location. Local surface determination, although more time consuming, mitigates the effect of local absolute grey-scale variation, such as caused by beam hardening.

2.3.4 CT for metrology

2.3.4.1 Dimensional and volumetric analysis

In 2011, Kruth et al. [125] reviewed the use of CT for dimensional metrology. They concluded that CT had the potential for use as a dimensional quality control tool, particularly for the non-destructive measurement of internal dimensions, not measurable using conventional techniques. They noted that the technique acquires a dataset for the entire component and so would allow the extraction and analysis of many features from one measurement set up. They noted measurement accuracy, uncertainty and system traceability were challenges, but that the number of systems and applications was increasing rapidly. In 2014, De Chiffre et al [128] reviewed current industrial applications of CT. It was noted that one of the primary applications for industrial CT was for the detection of component defects (inclusions, porosity and cracks). Region-of-interest scanning was introduced as a method of obtaining higher

resolution information for a localised area. This technique involves scanning the entire object at lower resolution followed by scanning a portion of the object at higher magnification, therefore higher resolution. The region of interest is then reconstructed using information from the entire object scan [129]. This region of interest scanning may have future application for surface texture measurement where high resolution is required for a localised area. It has been noted [125, 128] that CT allows measurement of two characteristics of components at the same time: dimensions and material quality (porosity, inclusions etc). This may now be extended to surface texture information. It was noted [128] that CT measurements can be combined with CAD information to produce deviation analyses and porosity maps. The final machined component CAD model may be superimposed onto the CT scan of a casting for example to ascertain whether any porosity contained within the component will become a surface defect once the component is machined. Surface defects may not be acceptable on critical sealing surfaces for example, or where fatigue has to be considered. Rejecting the component at the casting stage, prior to performing post processing, may save considerable time and money and may provide early indication of process failure [130]. To be comparable to coordinate measuring machine (CMM), optical or tactile systems, the measurement accuracy of CT needs to be improved [131]. Also, region of interest scanning plus selective analysis, involving only the reconstructions at the required resolutions for each section, will reduce reconstruction time.

2.3.4.2 Surface Texture

The importance of CT for the measurement of the surface texture of additively manufactured parts has been recognised [15, 132], but, until the work reported here, the extraction of quantitative surface information from CT scans of AM surfaces has been limited to a series of publications detailing profile surface analysis of individual struts extracted from a lattice structure [59-61, 67], see Figure 2-21:.

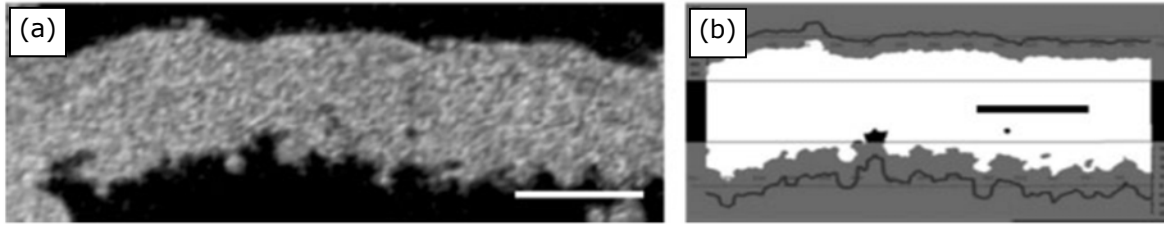


Figure 2-21: CT image of a Ti6Al4V AM lattice strut. (a) CT cross section of single a Ti6Al4V lattice strut, (b) binarized section with lines indicating the extracted profile. Scale bars: 200 μm . Reproduced from [61].

The development of techniques to extract and analyse areal surface texture data from CT and to produce quantitative numbers for all surface texture parameters per ISO 25178-2 has the potential to provide industry and the research community with significant analysis and inspection capability. However, it should be made clear that surfaces that *can* be measured using other techniques (outside surfaces) generally *should* be measured using the standard techniques. The current resolution of CT, and hence the basic quality of the surface extracted, lags significantly behind other techniques. Additionally, the estimation of measurement uncertainty for CT is complex and has not been fully addressed in the research community, leading to potential traceability issues. However, just as the AM process itself presents many challenges, CT surface measurement has challenges that will be faced and hence need to be resolved because of the unique advantages that CT provides, particularly for the AM sector. CT is the prime method used for porosity and internal dimensional measurement of AM components. Review papers [15, 133] discussed the potential of using CT for the extraction and analysis of AM surfaces because of the ability of CT to image internal and re-entrant features, surfaces that cannot be measured using conventional metrology techniques. The reviews indicated that surface data extraction had been performed only by extracting 2D profiles from CT data and recognised that areal measurement and characterisation has significant advantages, particularly with complex surfaces such as those which can be produced using AM. The review performed by this author [15] together with the realisation that CT appeared capable of sufficient resolution to extract data from the surface of AM components (Figure 1-4:) lead directly to the research reported here.

2.4 Literature review conclusions

Commercial AM, although a relatively recent technological development, has potential that has been recognised by the aerospace, medical and automotive industries. These quality-driven industries are aware of the significant advantages AM has over conventional manufacturing techniques, such as milling, turning and grinding. Perhaps the most significant advantage is the ability to manufacture components not constrained by the tool path restrictions of conventional techniques. With this advantage comes the challenges of measuring and characterising many of the features of AM components, such as internal, re-entrant or structured features. These industries need quantitative, accept / reject criteria for all drawing call-outs, irrespective of the manufacturing techniques or measurement challenges. At the present time, PBF techniques are seeing the greatest application in industry, and indeed, in academic research. There are two primary PBF techniques, electron beam and laser beam based. The characteristics of the build process, powder configuration and as-built surface vary but the surface metrology challenges are broadly similar. Computed tomography is being used extensively for analysing porosity and dimensions of PBF AM components as it allows imaging of internal features of AM components. There has been no published extraction of areal surface texture data from CT scans of AM components, with only limited extraction of profile data, for which the accuracy has not been verified. Areal and 3D data extraction has significant advantages over profile surface measurements as surfaces are three dimensional in nature and cannot be fully defined using two dimensional profiles. Extracting quantitative areal and 3D surface data from internal, re-entrant and structured surfaces using CT, and verifying the accuracy of the measurements and characterisation by comparison to conventional surface metrology systems, such as focus variation, will be the first steps on the path towards the standardisation of methods and techniques to be adopted by industry.

Chapter 3 Areal surface texture data from CT

“It is always wise to look ahead, but difficult to look further than you can see.”
Winston Churchill (1874-1965)

This chapter reports on the extraction and characterisation of AM surfaces using CT and the efficacy of using data extracted from CT scans for the generation of surface texture data per an accepted standard, ISO 25178. The research investigates whether CT systems have the capability to become a surface metrology tool, particularly relevant where the surface of internal and recessed surfaces needs to be characterised without destructively testing the component. A journal paper, first author A. Townsend, titled "*Areal surface texture data extraction from X-ray computed tomography reconstructions of metal additively manufactured parts*" [18] is included in Appendix 2. This work was reported at conference, first author A. Townsend, "*Investigating the capability of microfocus X-ray computed tomography for areal surface analysis of additively manufactured parts*" [17], ASPE/euspen 2016 summer topical meeting, Dimensional accuracy and surface finish in additive manufacturing, Raleigh, NC, USA, June 2016. The conference paper is included in Appendix 3.

The literature review (Chapter 2) showed that there had been no published research on the extraction of areal surface texture data from CT reconstructions of AM components prior to this work. The scan of the moth head using the Nikon XT H 225, Figure 1-4:, showed there was suitable resolution to potentially extract data and characterise the as-built AM surface. This chapter describes the methods developed to extract topographical data from CT scans. Many components that exploit the manufacturing advantages of AM include surfaces, such as internal and recessed, that cannot be measured using conventional line-of-sight optical or stylus techniques. As has been reported in Chapter 2, CT has been used for dimensional metrology for AM and is the obvious first choice for measurement of these surfaces. If this process were to be viable it would allow the non-destructive measurement and

characterisation of internal surfaces of AM components, potentially important for component functions including flow, coating adhesion and bio-attachment. Unfortunately the data produced by CT systems has not been in a form that makes it easily useable for quantitative surface assessment. It has been shown that areal measurement and characterisation per standards such as ISO 25178 has advantages over simple profile measurements, and areal measurement is seeing increased adoption as the advantages over profile measurements are becoming more apparent. Surfaces are three dimensional in nature and thus areal measurements are more representative of the functional surface. It should be noted that, using the techniques discussed here, it is a simple task to extract individual profiles from the areal data sets, if desired.

3.1 Methodology

CT measurements were performed on two artefacts scanned simultaneously: an AM surface artefact and a dimensional artefact. The AM sample (AM artefact) was an AlSi10Mg aluminium alloy sample manufactured on an SLM AM machine. The extracted AM surface section was aligned to the same surface as measured on an Alicona G4 focus variation instrument. The literature review highlighted focus variation as one of the most popular methods for the measurement and characterisation of complex metal AM surfaces. The Alicona G4 was chosen for these measurements because its high z-axis range makes it capable of measuring the high aspect ratio features present on as-built AM surfaces and its ability to image surfaces with high slope angles [134]. The data sets were levelled and filtered per ISO 25178-3 [135] and areal parameters per ISO 25178-2 were generated. The AM artefact was mounted in an additively manufactured acrylonitrile butadiene styrene (ABS) fixture. Included in the fixture for each scan was an additional artefact (DIM artefact) made from a similar material to the AM artefact. The DIM artefact was designed for the evaluation of surface determination performance and dimensional scaling. Dimensions extracted from the artefact were compared

to reference measurements taken on a CMM. Measurement instrument and process repeatability were investigated. Details of the method are outlined in the following sections.

3.1.1 Artefacts

3.1.1.1 AM artefact

The AM artefact was a cube, 10 mm per side, manufactured from aluminium alloy AlSi10Mg. The artefact was manufactured using a Renishaw AM250 SLM machine. The nominal powder size was 15–45 μm . The upskin (top) surface was the extracted and evaluated surface. Figure 3-1:(a) shows a scanning electron microscope (SEM) secondary electron (SE) micrograph of a section of the surface. Figure 3-1:(b) shows a false colour height map of a section of the surface, as measured using an Alicona G4.

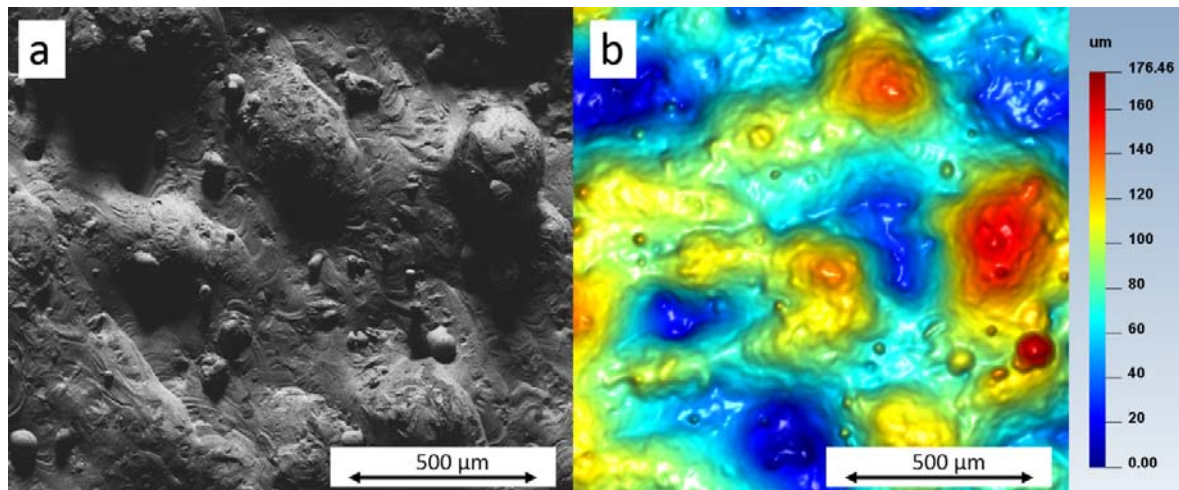


Figure 3-1: Images of an AlSi10Mg SLM upskin surface. (a) SEM micrograph, (b) false-colour height map. Reproduced from [18].

3.1.1.2 Dimensional artefact

A second measurement artefact was included in each scan. The artefact was machined from aluminium alloy 6082-T6 bar stock. The artefact size and material were chosen to provide similar X-ray attenuation characteristics to the AM artefact permitting CT measurement setting optimisation for both artefacts simultaneously. This resulted in similar surface

determination challenges for the AM and DIM artefacts. Three dimensions were measured on the DIM artefact: an outside diameter (OD), an inside diameter (ID) and a step-length between two parallel surfaces, see Figure 3-2:.

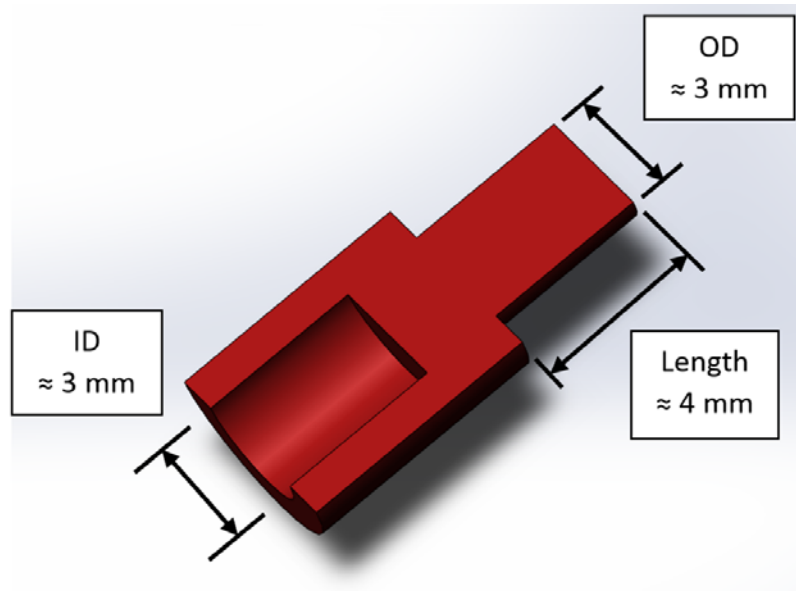


Figure 3-2: Cross section of the dimensional artefact. Showing the evaluated dimensions. Reproduced from [18].

These dimensions were designed to provide an indication of surface determination errors and global scaling errors. The configuration of the design provide the ability to differentiate between these two independent errors. If the CT measured part is smaller than the reference measurement then the OD, ID and length would be undersize. If the surface determination positioned the surface outside the part surface the OD would be generated oversize and the ID undersize. Surface determination would have negligible effect on the length measurement. Figure 3-3: shows the position of the generated surface using two surface determination methods for the same part location (white line). Figure 3-3:(a) shows a global surface determination, where the material surface is defined by one grey value for the entire part. Figure 3-3:(b) shows a local iterative surface determination where the local voxel grey values in proximity to an initial preliminary surface location are examined and the surface is iteratively positioned at the location of highest local voxel grey-level gradient. Performing

local analysis of the voxel grey-scale values largely compensates for any local deviations caused by beam hardening. The combination of correct mechanical X-ray filtering and local iterative surface determination often eliminate all effects of beam hardening.

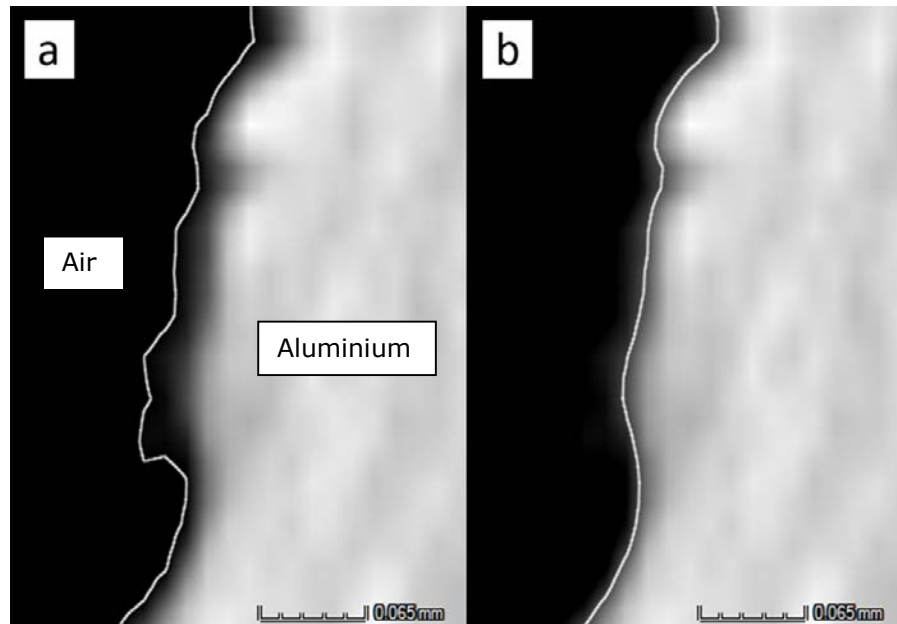


Figure 3-3: Surface determination images of an AlSi10Mg part. Showing the calculated surface (white line) (a) Standard surface determination (ISO 50), (b) local iterative surface determination implemented in VGStudio MAX 2.2. Reproduced from [18].

The difference in surface position is clearly visible. Local surface determination, implemented in VGStudio MAX 2.2 [136], was used for all the measurements performed here. Discussion of surface determination errors is included in Chapter 5.

3.1.2 Measurements

Reference measurements were taken of the AM artefact and the dimensional artefact. The reference surface texture measurements for the AM artefact were taken using an Alicona G4 focus variation instrument. The reference measurements for the dimensional artefact were taken using a Zeiss Prismo (CMM). After the reference measurements had been taken the

artefacts were assembled into an additively manufactured ABS fixture. The artefacts were then scanned together using a Nikon XT H 225 industrial CT.

3.1.2.1 AM artefact focus variation surface measurement

The measurements were taken with a x10 objective lens installed in the Alicona. With this configuration, the system step-height accuracy is $\pm 0.05\%$ using a 1 mm measurement step; the maximum lateral resolution is 1.75 μm and the maximum vertical resolution is 100 nm, with a repeatability of 30 nm. The complete top surface of the AM artefact was measured ten times. The artefact was removed from the fixture and replaced between measurements. This removal and replacement procedure was followed to give an indication of the measurement repeatability possible during an industrial measurement where a number of components from a batch are measured using the same fixture or jig, see Figure 3-4:.

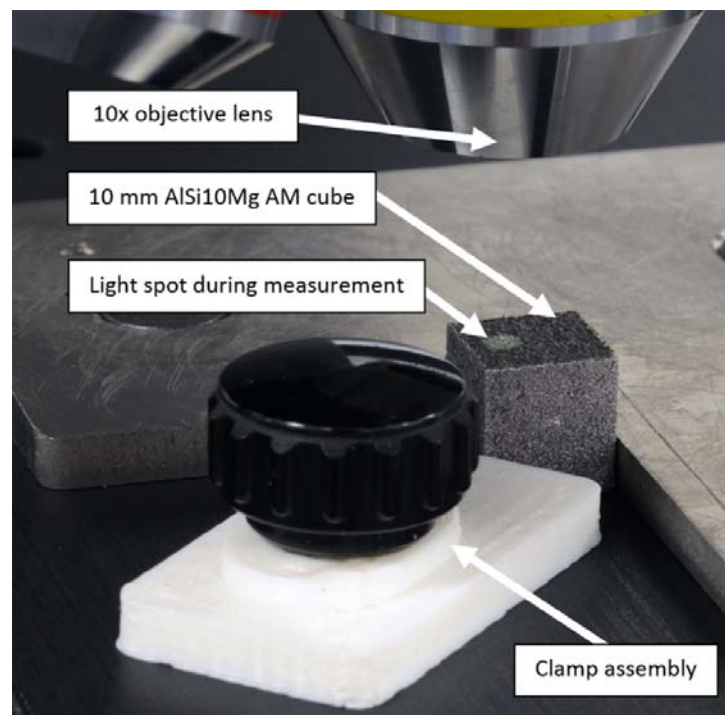


Figure 3-4: Focus variation test fixture used for the AM surface measurements. Showing the 10 mm AlSi10Mg cube. Reproduced from [18].

The measurement consisted of 8 x 10 stitched measurements. The Alicona lateral sampling distance was 2.33 μm . The measured area was cropped to a square 8 mm x 8 mm prior to surface texture parameter generation. The measurement parameters were chosen based on the nominal surface roughness of the sample. A profile roughness value, R_a , of approximately 40 μm was obtained. Per ISO 4288 Table 1 [122], a profile measurement of a surface with this R_a value would require a sampling length and λ_c cut-off wavelength of 8 mm. These profile parameters would correspond to an ISO 25178-3 L-filter nesting index also of 8 mm, with an evaluation area of 8 mm x 8 mm. The L-filter nesting index, similar to the profile λ_c , is a high-pass filter that removes long wavelength components of the measurement. An S-filter nesting index (low-pass filter) of 0.025 mm per ISO 25178-3 table 1 was chosen. For an optical instrument, such as the Alicona G4, the ratio between the sampling distance and the S-filter nesting index value is required to be a minimum of 3:1. This would require a sampling distance of 8.33 μm or less. The ratio of S-filter nesting index (25 μm) to the sampling distance used (2.33 μm) is over 10:1. All Alicona measurement data was saved using an STL file format. This allows simultaneous processing with extracted CT surface data.

3.1.2.2 Dimensional artefact CMM measurement

A Zeiss Prismo CMM was used to measure the dimensional artefact. The maximum permissible error (MPE) of the Zeiss Prismo is $(1.9+L/300)$ μm (L in mm). All measurements were taken with a CMM stylus tip of 1 mm. Scanning mode was used, whereby the tip remains in contact with the surface during the measurement. The artefact was measured at four locations on the OD and four locations on the ID, see Figure 3-5:. Each set of four measurements was taken at 0.5 mm, 1.25 mm, 2 mm and 2.75 mm from the respective datum face. Each measurement consisted of 100 points in each circle. The artefact was not removed from the fixture between measurements.

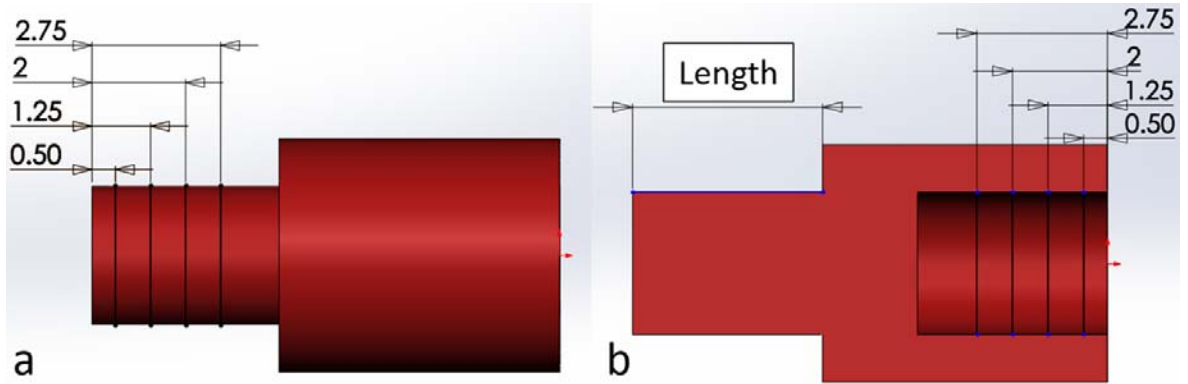


Figure 3-5: Aluminium dimensional artefact CMM measurement locations. (all dimensions in mm). Reproduced from [18].

3.1.2.3 CT measurements

The AM and dimensional artefacts were mounted in the ABS fixture. Both artefacts were positively retained using nylon screws. The fixture and screw materials were chosen to have a significantly lower density than the artefacts to have a low X-ray attenuation. The surface of the AM artefact to be measured (the upskin surface) was situated facing downward, at an angle of 45° to the horizontal to minimise cone-beam artefacts, see 4.7.4 and Figure 3-6:(a).

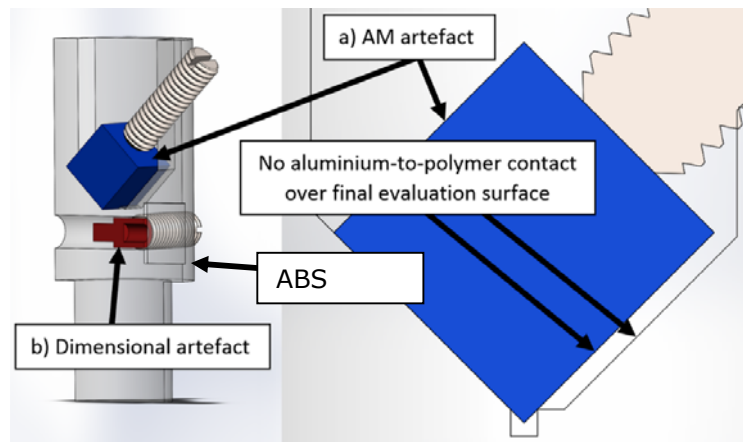


Figure 3-6: CAD rendering of the ABS fixture and artefacts. Reproduced from [18].

The fixture was designed so that none of the surfaces to be evaluated (the AM surface and the OD, ID and length surfaces of the dimensional artefact) were in direct contact with the ABS of the fixture. This would create optimal surface determination conditions where the only

interface is between two materials: aluminium and air. The assembly was mounted to the rotary stage of the Nikon XT H 225, see Figure 3-7:.

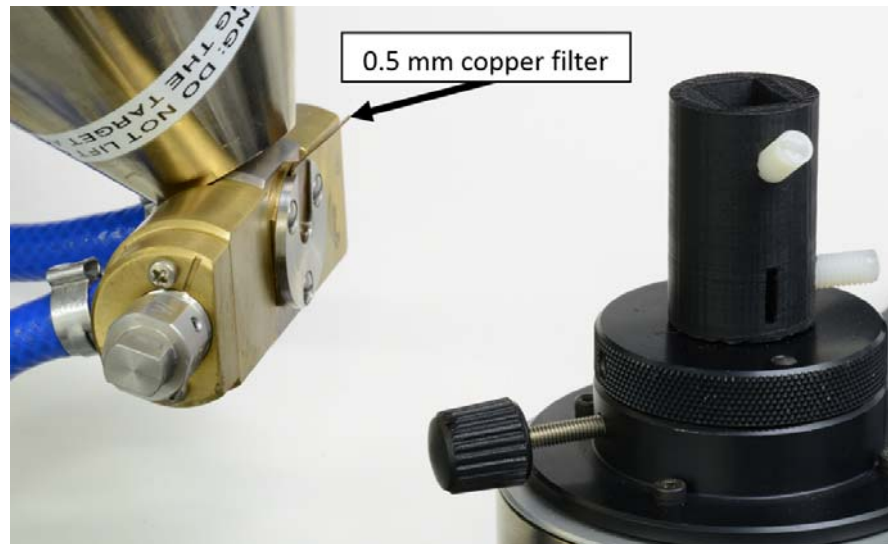


Figure 3-7: Measurement artefact assembly mounted in the Nikon XT H 225. Reproduced from [18].

The CT settings are shown in Table 7. These settings were used for all measurements. The acceleration voltage was chosen so the part would be penetrated at every measurement angle. The CT filament power (filament voltage x filament current) was kept below 10 W. At this power level “normal” focus can be used on the CT. Above this power level “auto defocus” is used, which incrementally defocusses the electron beam as the power increases to avoid damage to the X-ray target. The result of auto-defocusing is a blurring of the projected images. The copper filter was used to reduce the image contrast and beam hardening effects. The component was positioned so both artefacts were just within the image field of view at every rotational position, thus allowinging correct volume reconstruction of the artefacts.

Table 7: Nikon XT H 225 measurement settings

Parameter	Value	Parameter	Value
Source to object	84.2 mm	Filter material	Copper
Source to detector	972 mm	Filter thickness	0.5 mm
Acceleration voltage	150 kV	Number of projections	1583
Filament current	67 μ A	Detector pixels	1008 x 1008
Exposure time	2829 ms	Voxel size	17.3 μ m

Nikon CT Pro 3D software was used to perform reconstruction from the 1583 TIFF images. VGStudio MAX 2.2 was used to perform surface determination. Air was selected as the *background* material. The location of the air selected was consistent for all scans: a volume inside the $\varnothing 3$ mm bore of the dimensional artefact, see Figure 3-2:. Similarly a section of the dimensional artefact was chosen as the *material* for all scans. An initial surface was generated based on these selections. Iterative surface determination was then performed, based on the initial surface location. A search distance from the initial location is defined and the software then locates the final surface at the location of highest grey-scale gradient within the search distance. The software default distance of 4.0 voxels was used as the search distance. Two regions of interest were then extracted from each measurement, the first a section from the AM sample including the surface region of interest ROI (the as-built AM upskin surface). The second ROI was the entire dimensional artefact. Both ROI were saved as STL files. The VGStudio MAX 2.2 "Super Precise" setting was used for both extracted surfaces. This setting provides the highest resolution with no simplification of the mesh. Three measurement sets were taken on the Nikon XT H 225.

3.1.2.3.1 CT Set 1: artefacts not disturbed between measurements

Set 1 consisted of five measurements. The artefacts were not disturbed between each of the measurements.

3.1.2.3.2 CT Set 2: post filament change, artefacts not disturbed

The XT H 225 includes a tungsten electron-generation filament, see Figure 3-8:. The life of the filament used in the Nikon XT H 225 has historically ranged from 20 hours to 130 hours. The situation may arise during an industrial inspection process where the filament fails and has to be replaced mid-batch. Variation in the surface texture data extracted pre and post filament change could potentially influence the measurement accuracy, repeatability and lot acceptance.

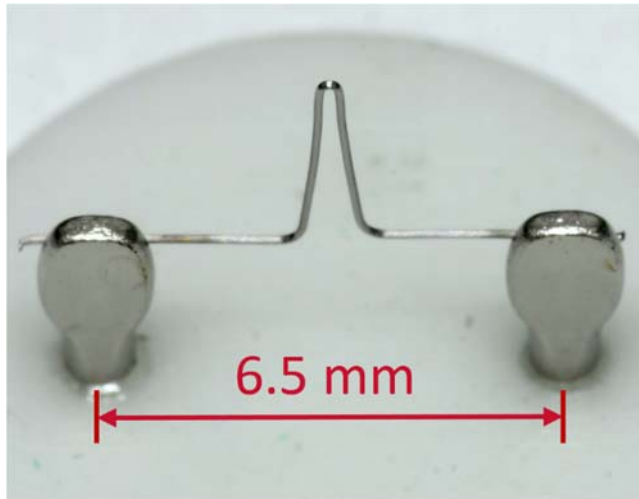


Figure 3-8: Nikon XT H 225 electron-generation filament.

On completion of measurement set 1 the CT tungsten electron-generation filament was replaced, five measurements were then taken. The artefacts were not disturbed between measurements and the measurement parameters were not changed. During the filament change process the measurement stage was moved away from the gun to allow access to the filament assembly, see Figure 3-9:.

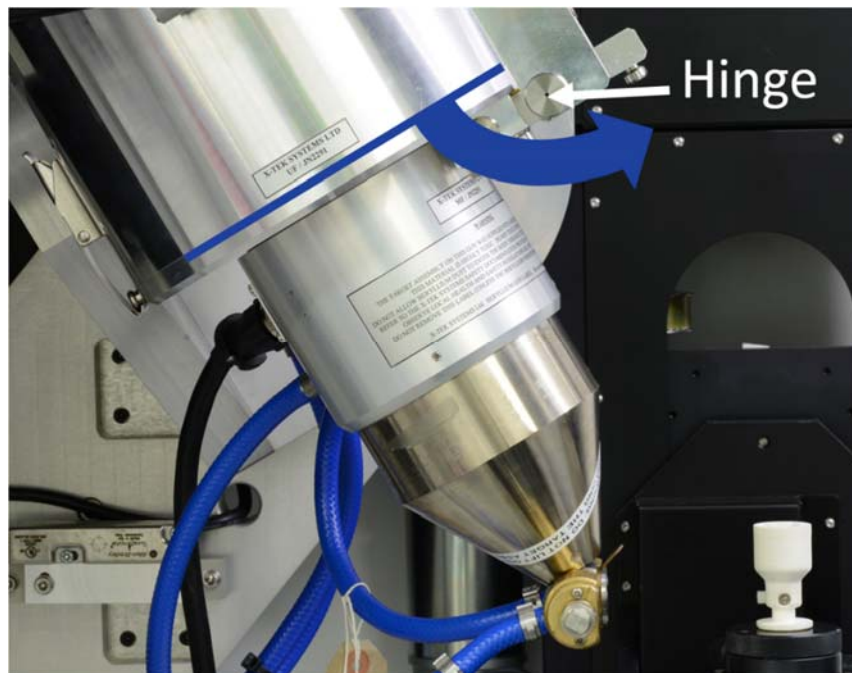


Figure 3-9: XT H 225 X-ray "gun" showing the assembly joint and hinge.

To investigate whether physically moving the stage away from the gun and then back after the filament change had influenced the data, five measurements were taken, moving the stage away and back to the same saved position between measurements, without changing the filament.

3.1.2.3.3 CT Set 3: AM component rotated 90° between measurements

The final set of five measurements was also performed to simulate an industrial application wherein a series of parts will be mounted in a fixture and measured. The fixture was removed from the rotary stage prior to the first measurement of the set and between each subsequent measurement; the AM component was removed from the fixture. The AM artefact was rotated 90° CCW and replaced in the fixture (the measurement surface remained in the same location, but rotated 90°). The fixture was then replaced on the rotary stage. The dimensional artefact was not removed between measurements.

3.1.3 Data processing

3.1.3.1 AM surface data processing sequence

The aim of the processing was to generate height maps of the same area of the AM sample from all measurements (focus variation (FV) and CT) of the correct size (8 mm x 8 mm) with the correct filtering per ISO 25178-3 (L-filter 8 mm, S-filter 0.025 mm) and to generate and compare surface texture parameters per ISO 25178-2. Data processing is a nine stage sequence that incorporates custom-computation with the use of commercially available software. This protocol was used to process all data files from the Alicona G4 reference measurements and the CT measurements.

3.1.3.1.1 (1) Data trimming

The CT measurement ROI includes the AM sample top surface and some side information. The Alicona G4 STL contains the entire top surface of the AM sample. Both measurements were cropped to approximately 9 mm x 9 mm, with the cropping location centred on the middle of the 10 mm x 10 mm face.

3.1.3.1.2 (2) Conversion from STL to PLY format

The data format for the extracted AM surface was changed from STL to PLY format. PLY mesh data format contains vertex and face information, without repetition of shared vertices in STL file information. The PLY file format is approximately one third the size of STL format files, so reducing storage requirements and computation time. The conversion is a lossless process.

3.1.3.1.3 (3) Surface alignment

One of the Alicona G4 measurements was chosen arbitrarily as the master for the alignment and cropping of all other data sets. The master was not trimmed (per 3.1.3.1.1) and so was larger than the other surfaces. This was done to allow the maximum area of the measurement

sets to be used for the alignment process. Least squares alignment was performed between each of the data sets and the master.

3.1.3.1.4 (4) Cropping the surface to 8.4 mm x 8.4 mm

Once the alignment was complete each of the aligned surfaces was cropped to 8.4 mm x 8.4 mm. The location used for all cropping operations was based on the coordinate system for the master file, thus ensuring the same area was cropped for all samples.

3.1.3.1.5 (5) Mesh cleaning

This step was performed on the CT data sets. CT data sets are true 3D (x,y,z) , with information including undercuts and re-entrant features. Converting the CT data to height map format for analysis in standard surface analysis software requires projecting the point cloud data onto a plane and assigning a z value at each plane grid location. Errors will occur if the data to be converted has more than one z value at one location (such as with re-entrant features). To avoid this occurring, the CT mesh data was cleaned to remove non-visible features. This process was performed after alignment to the master Alicona measurement because the CT visible areas should then correspond to the areas "seen" by the line-of-sight Alicona measurement. Chapter 6 contains research on extraction of information from undercuts and re-entrant features.

3.1.3.1.6 (6) Conversion to height map format

All 8.4 mm x 8.4 mm cropped samples were then converted from PLY mesh format to height map format by linear interpolation between vertices and projection onto a plane with a square grid spacing of 2.5 μm .

3.1.3.1.7 (7) Cropping to 8 mm x 8 mm per ISO 25178-3

The height map data was then cropped to 8 mm x 8 mm per the requirements of ISO 25178-3. All height map files were saved as surface data file (SDF) [137] format.

3.1.3.1.8 (8) Filtering per ISO 25178-3

Levelling and filtering were then performed. A Gaussian regression L-filter nesting index of 8 mm and an S-filter nesting index of 0.025 mm per ISO 25178-3 were then applied to all surfaces.

3.1.3.1.9 (9) ISO 25178-2 parameter generation

Parameter data per ISO 25178-2 was then generated from each surface. The extracted parameter data for the same location on the sample as measured on the Alicona G4 and the Nikon XT H 225 could now be compared.

3.1.3.2 AM surface measurement and characterisation summary

The measurement and characterisation sequence is summarised in Figure 3-10:. Two false colour height maps are shown in Figure 3-11:. Figure 3-11:(a) is the extracted surface as measured on the Alicona G4. Figure 3-11:(b) is the extracted surface measured on the Nikon XT H 225. It can be seen that the two maps are visually very similar.

3.1.3.3 Dimensional artefact data processing

The data processing for the dimensional artefact was a less complex process. Least-squares best-fit cylinders were fitted to the CT STL data OD and ID at distances 0.5-2.75 mm from the respective datum faces (see Figure 3-5:). Best-fit planes were fitted to the artefact end face and the step face distance was calculated. The CT data was then compared to the CMM measurement data for the artefact.

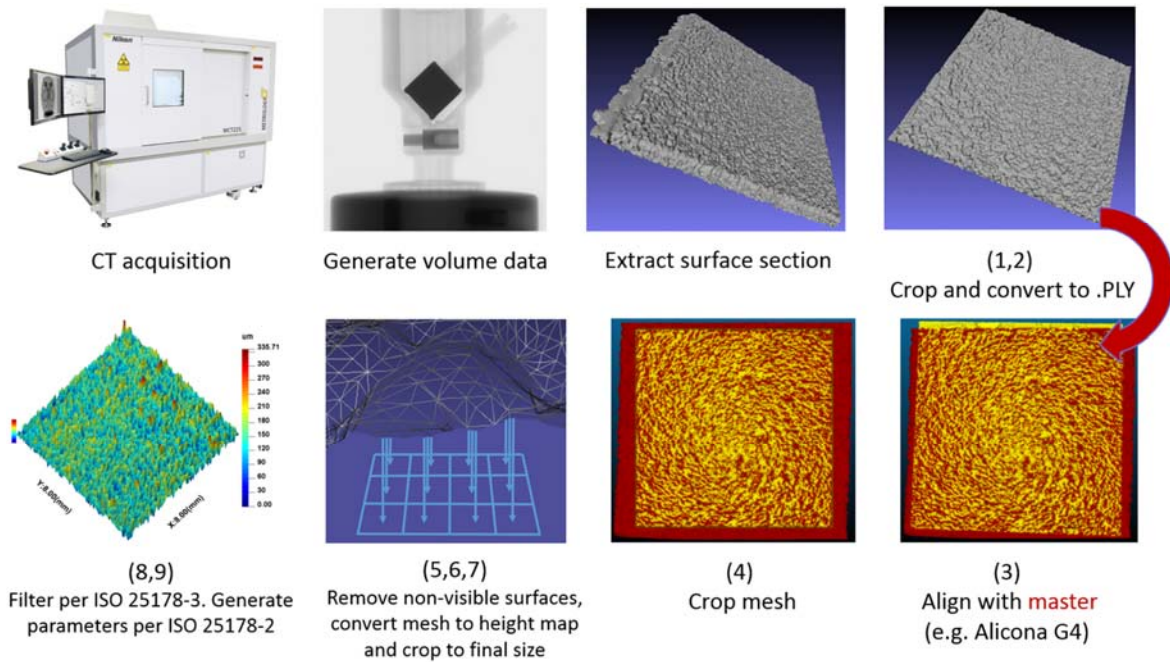


Figure 3-10: CT AM surface measurement and characterisation sequence. Sequence numbers in parentheses are listed in paragraphs 3.1.3.1.1 to 3.1.3.1.9.

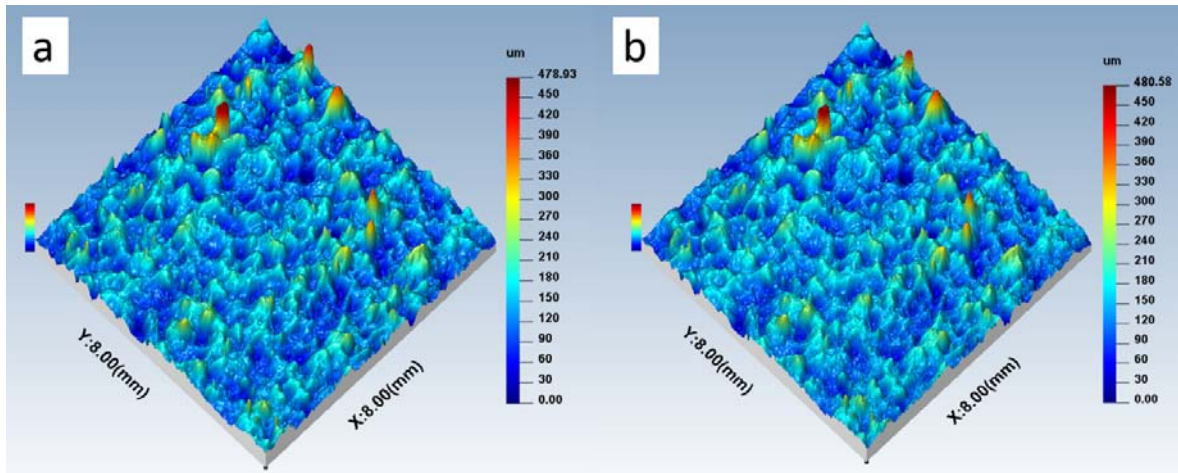


Figure 3-11: False colour height maps of the AISi10Mg AM surface. (a) Alicona G4, (b) Nikon XT H 225.

3.2 Results

3.2.1 AM surface results

3.2.1.1 Process verification

Two verifications were performed prior to analysis of the CT measurement data: verification of the alignment and parameter extraction process itself and verification of the precision of the Alicona G4 measurements combined with the alignment and parameter extraction process.

3.2.1.1.1 Computational alignment and process extraction process verification

This verification consisted of making a copy of the master Alicona STL surface file and then processing this surface through the multi-step process, generating surface texture parameters and comparing to parameter data from the master file. Iterative closest point (ICP) alignment was performed with a threshold maximum root mean square (RMS) difference between consecutive iterations of 5×10^{-5} mm. The aligned surface area was approximately 9 mm x 9 mm. A deviation analysis was performed after alignment. The mean distance after alignment was less than 1 nm with a standard deviation of 88 nm. The purpose of the alignment process is simply to make sure the area used for parameter data generation is the same for each sample. The alignment process performed here is significantly better than that required for this purpose. Both surfaces were then processed per the multi-step process, including cropping, cleaning, conversion to height map (SDR) format, final crop to 8 mm x 8 mm, levelling and filtering per ISO 25178-3 and parameter extraction per ISO 25178-2. The extracted parameter values are given in Table 8. The parameters in bold have been shown elsewhere to be sensitive to AM build parameter variation and post-processing surface changes (see Table 3). The parameters in shaded boxes will be reported for the remainder of the analyses, but it should be noted that a complete set of parameters (and profile parameters if required) are easily generated from the height maps using standard software packages such as SurfStand [138] or MountainsMap [139].

Table 8: Master Alicona and copy ISO 25178-2 parameter values and differences.

Parameter per ISO 25178-2	Master	Copy of Master	Percentage difference (in relation to Master) [(Δ) is absolute difference]
Height parameters			
<i>Sq</i> / μm	41.186	41.186	<0.001
<i>Ssk</i>	1.413	1.413	<0.001
<i>Sku</i>	9.297	9.297	<0.001
<i>Sp</i> / μm	342.593	342.601	0.002
<i>Sv</i> / μm	137.346	137.329	-0.012
<i>Sz</i> / μm	479.939	479.93	-0.002
<i>Sa</i> / μm	30.301	30.301	<0.001
Spatial parameters			
<i>Str</i>	0.77	0.77	<0.001
<i>Sal</i> / mm	0.287	0.287	<0.001
Hybrid parameters			
<i>Sdq</i>	0.626	0.626	<0.001
<i>Sdr</i> / %	15.895	15.894	(Δ) -0.001
Volume parameters			
<i>Vmp</i> / (μm ³ /μm ²)	3.44	3.44	<0.001
<i>Vmc</i> / (μm ³ /μm ²)	31.70	31.70	<0.001
<i>Vvc</i> / (μm ³ /μm ²)	47.60	47.60	<0.001
<i>Vvv</i> / (μm ³ /μm ²)	3.46	3.46	<0.001
Sk family parameters			
<i>Spk</i> / μm	66.229	66.230	0.002
<i>Sk</i> / μm	90.248	90.253	0.006
<i>Svk</i> / μm	28.196	28.195	-0.004
Material ratio parameters			
<i>Smr1</i> / %	12.8	12.8	(Δ) <0.001
<i>Smr2</i> / %	92	92	(Δ) <0.001

The parameter with the largest percentage difference between the master and its copy is *Sv* (the maximum pit height of the scale-limited surface). The difference is 0.012%. The majority of the parameters have a percentage difference of less than 0.001%. The author considers this (Alicona to Alicona) to be verification that the multi-step process has acceptable accuracy for the CT to Alicona extraction analysis.

3.2.1.1.2 Alicona measurement and process verification

This second verification was performed to check the precision of the Alicona G4 measurement and analysis process. The ten Alicona measurements were processed using the multi-stage process per 3.1.3.1. Surface texture parameter mean values and standard deviations were generated (see Table 9). The mean value of Sa was 30.31 μm with a standard deviation of 0.0055 μm . The mean value of Sq was 41.19 μm with a standard deviation of 0.0068 μm . The process standard deviation values were orders of magnitude less than the Alicona to CT result differences, thus the process is considered sufficiently sensitive and repeatable for the comparison of CT and Alicona measurements.

Table 9: ISO 25178-2 parameter values for the Alicona G4 ten measurements.

Parameter	Mean	Sample standard deviation
Height parameters		
$Sq / \mu\text{m}$	41.19	0.0068
Ssk	1.41	0.0012
Sku	9.29	0.009
$Sz / \mu\text{m}$	479.61	0.31
$Sa / \mu\text{m}$	30.31	0.0055
Spatial parameters		
Sal / mm	0.29	0.0005
Hybrid parameters		
$Sdr / \%$	15.92	0.012
Sk family parameters		
$Sk / \mu\text{m}$	90.25	0.025
Material ratio parameters		
$Smr2 / \%$	91.98	0.042

A deviation analysis was performed between the master Alicona sample and another Alicona measurement sample. Figure 3-12: shows the deviation map and the distance histogram.

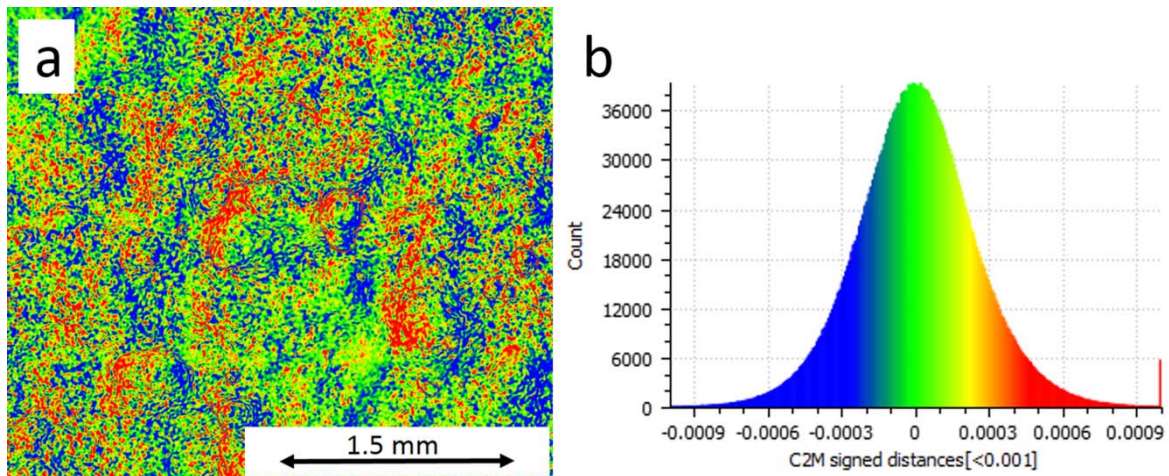


Figure 3-12: Deviation analysis between two aligned Alicona measurements. (a) deviation map (b) distance histogram (all values in mm). Colours in the deviation map correspond to the distances specified in the histogram. Reproduced from [18].

The mean distance between the meshes is 4 nm with a standard deviation of 250 nm. The purpose of the alignment between the samples and the master is to make sure the same area of the part is used for generation of surface texture parameters. This alignment accuracy is significantly better than that required for this purpose.

3.2.1.2 CT measurements

The three sets of CT measurements were processed per section 0. Surface texture parameter data were generated. The results are reported here.

3.2.1.2.1 Set 1: artefacts not disturbed between measurements

Set 1 consisted of five measurements on the CT. The fixture and artefacts were not disturbed during this measurement set. Surface texture parameter mean and standard deviation values are shown in Table 10.

Table 10: CT set 1 AM surface parameter mean and standard deviation values. Five measurements, AM artefact not disturbed between each measurement.

Parameter	Mean	Sample standard deviation
Height parameters		
$Sq / \mu\text{m}$	40.46	0.03
Ssk	1.35	0.0075
Sku	9.04	0.065
$Sz / \mu\text{m}$	479.07	1.76
$Sa / \mu\text{m}$	29.84	0.038
Spatial parameters		
Sal / mm	0.298	0.0009
Hybrid parameters		
$Sdr / \%$	13.30	0.17
Sk family parameters		
$Sk / \mu\text{m}$	89.76	0.27
Material ratio parameters		
$Smr2 / \%$	91.70	0.071

3.2.1.2.2 Set 2: post filament change, artefacts not disturbed

The stage position was saved in the system memory, the stage was moved away from CT gun to allow access to the filament chamber. After changing the filament, the stage was returned to the saved position and automatic fine focus was performed. The CT settings were unchanged from those used for set 1 measurements. Set 2 consisted of five measurements on the CT. Charts for selected parameters are shown in Figure 3-13:. The mean and standard deviation for the generated surface texture parameters are shown in Table 11. The difference between selected mean parameter values of set 2 (post filament change) and the mean values of set 1 (pre filament change), though not large, are statistically significant (the 95% confidence intervals for the two measurement sets do not overlap) and, depending upon application, may have to be taken into consideration. For example, for set 1 the mean value of Sa was 29.84 μm with a standard deviation of 0.038 μm . Post filament change the mean value of Sa was 29.59 μm with a standard deviation of 0.045 μm . The difference of the mean values is approximately 0.84%. The mean value of Sq pre filament change was 40.46 μm with a standard deviation of 0.03 μm . Post filament change the mean value of Sq was 40.07 μm with a standard deviation of 0.06 μm . The difference of the mean values is approximately 1%. The change in values for the remaining selected parameters is not

significant. The XT H 225, the type used for these analyses, is an industrial machine. It should be noted that Nikon produces a metrology CT machine, the MCT225, which does include a protocol and supplied artefact to be used post-filament change for system calibration. Measurements comparing the XT H 225 commercial CT and the MCT225 metrology CT are reported in Chapter 4.

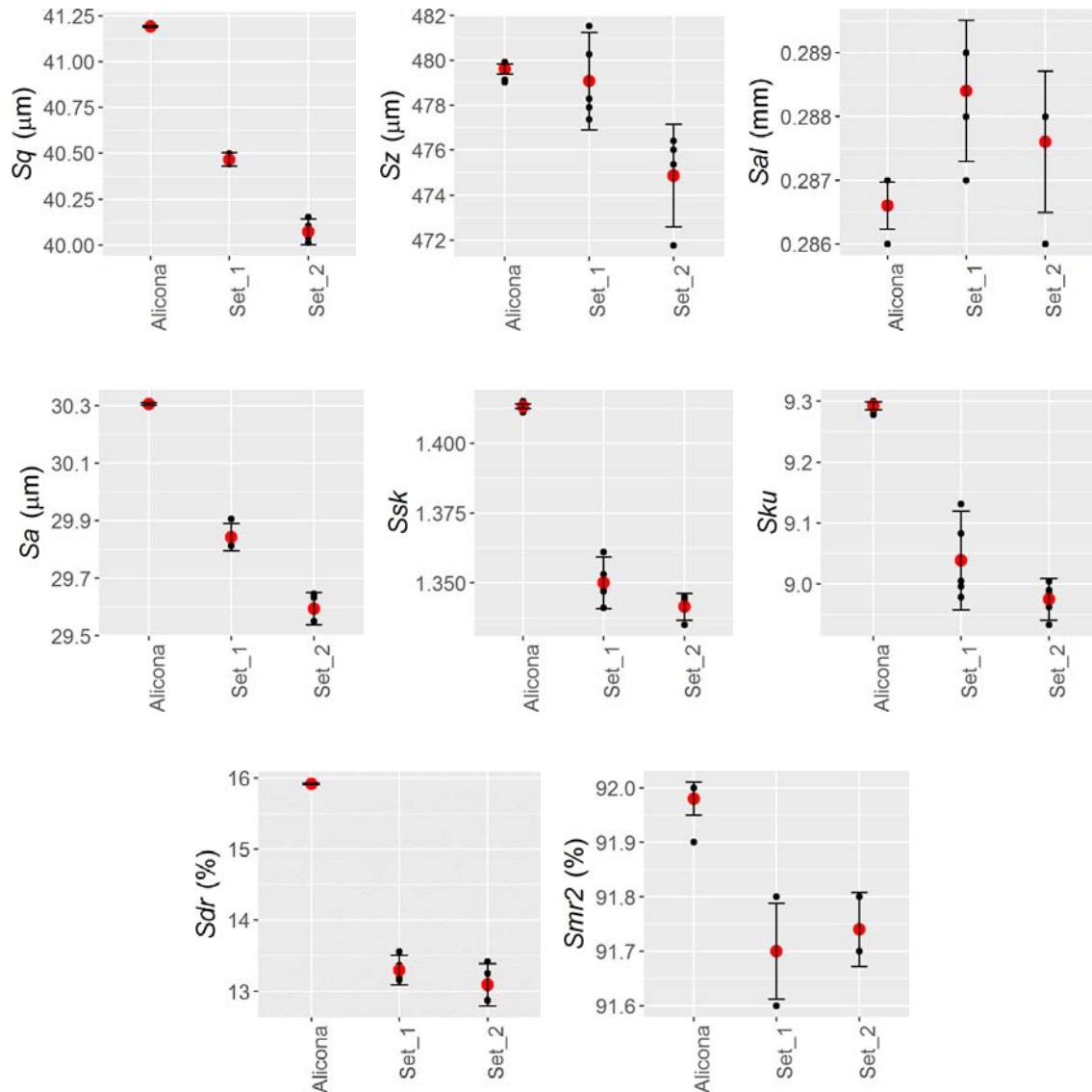


Figure 3-13: Filament change areal parameter data. Results for Alicona and Pre (Set 1) and Post (Set 2) CT filament change, showing 95% confidence intervals [24].

Table 11: CT set 2 AM surface parameter mean and standard deviation values. Five measurements, after performing a filament change. The AM artefact was not disturbed between each of the measurements.

Parameter	Mean	Sample standard deviation
Height parameters		
$Sq / \mu\text{m}$	40.07	0.056
Ssk	1.34	0.0039
Sku	8.98	0.028
$Sz / \mu\text{m}$	474.87	1.84
$Sa / \mu\text{m}$	29.59	0.045
Spatial parameters		
Sal / mm	0.29	0.0009
Hybrid parameters		
$Sdr / \%$	13.09	0.24
Sk family parameters		
$Sk / \mu\text{m}$	89.01	0.18
Material ratio parameters		
$Smr2 / \%$	91.74	0.055

A single test was run, post filament change, but returning the autofocus setting to the pre-filament change value. This was performed to investigate whether the autofocus setting had an influence on the extracted data set results. With the auto focus set to the pre-filament-change value, the mean Sq value was 40.15 μm . This value is within the range of values obtained post-filament change and so the adjustment of fine focus had an insignificant effect on the parameter results.

3.2.1.2.3 Stage positioning

A set of five measurements were taken with the stage moved away from and back to the saved position between each measurement. The stage was positioned at the saved position that was used for sets 1–3 for each measurement. The results of the extracted parameters are shown in Table 12 and Figure 3-14:. The standard deviation values are very similar to those obtained for sets 1-3. There is no evidence that moving the stage from and back to the saved position during the filament change process had an influence on the extracted parameter data. The conclusion is that the filament change process itself will affect measurement results. It should be noted that the measurements for this (stage positioning)

test were performed over one year after the initial testing for sets 1-3 and the mean value obtained here is within the range of the means for sets 1-3. This indicates general machine (and sample) stability over this time period.

Table 12: Surface parameter and standard deviation values for the stage positioning test.
The stage was moved away and returned to the measurement position between each of the five measurement.

Parameter	Mean	Sample standard deviation
Height parameters		
<i>Sq</i> / μm	40.14	0.050
<i>Ssk</i>	1.35	0.0052
<i>Sku</i>	9.01	0.023
<i>Sz</i> / μm	469.25	2.01
<i>Sa</i> / μm	29.61	0.042
Spatial parameters		
<i>Sal</i> / mm	0.29	0.0005
Hybrid parameters		
<i>Sdr</i> / %	12.56	0.10
<i>Sk</i> family parameters		
<i>Sk</i> / μm	89.11	0.13
Material ratio parameters		
<i>Smr2</i> / %	91.8	0.071

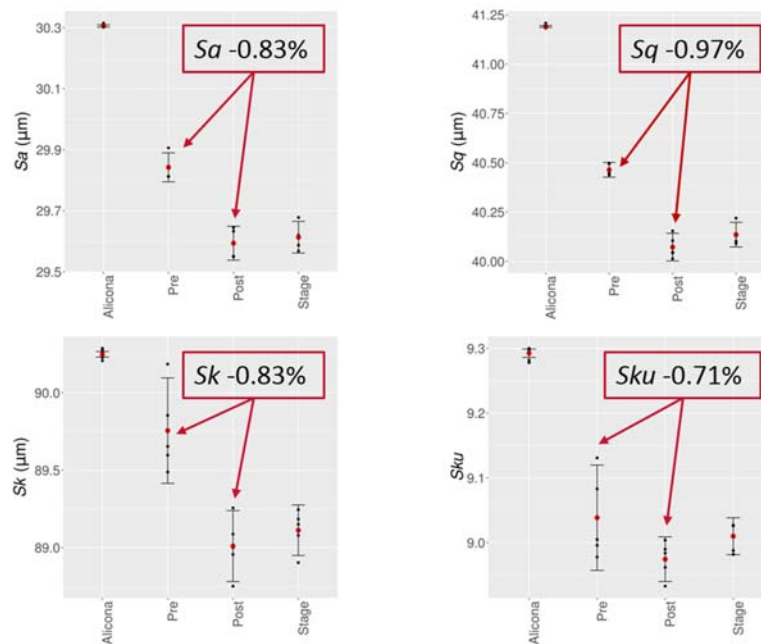


Figure 3-14: AM surface parameter values including stage-move data.

3.2.1.2.4 Set 3: AM component rotated 90° between measurements

Set 3 consisted of five measurements on the CT. Prior to the first measurement and between subsequent measurements, the fixture was removed from the stage (without moving the stage), the AM artefact was removed from the fixture, rotated 90° and replaced. The fixture was then replaced in the stage and the next measurement was taken. The surface texture parameter mean and standard deviation values for set 3 are shown in Table 13. The mean values are very similar to the mean values for set 2; for example the Sq mean for both set 2 and set 3 are 40.07 μm . It should be noted that the standard deviation values for set 3, for which the artefact is removed and replaced in a different orientation, are generally less than the standard deviation values for sets 1 and 2 for which the artefacts were not disturbed between measurements. This shows slight changes in component orientation will have an insignificant effect on the extracted data. This bodes well for consistent part-to-part measurement accuracy when batch testing components.

Table 13: CT set 3 AM surface parameter mean and standard deviation values. The AM artefact was removed and replaced between each of the five measurements.

Parameter	Mean	Sample standard deviation
Height parameters		
$Sq / \mu\text{m}$	40.07	0.012
Ssk	1.35	0.0068
Sku	8.99	0.036
$Sz / \mu\text{m}$	472.53	1.88
$Sa / \mu\text{m}$	29.58	0.013
Spatial parameters		
Sal / mm	0.29	0.0005
Hybrid parameters		
$Sdr / \%$	12.79	0.12
Sk family parameters		
$Sk / \mu\text{m}$	88.74	0.11
Material ratio parameters		
$Smr2 / \%$	91.74	0.055

3.2.1.3 Comparison of CT and Alicona results

The percentage differences between the mean values of the surface texture parameters from sets 1-3 measurements on the CT and the Alicona (as a percentage of the Alicona values) are shown in

Table 14. The percentage difference between the mean value of S_a for sets 1, 2 and 3 and the Alicona mean reading are -1.8%, -2.7% and -2.7%, respectively. Considering the very different measurement technologies involved this is a remarkably low percentage difference. The change from -1.8% difference for the set 1 results to -2.7% for the results for both set 2 and set 3 appears to be solely a result of the filament change. Graphs of selected areal parameters are shown in Figure 3-15:.. These are for Alicona, and set 1-3 CT measurement sets. The error bars are the 95% confidence interval (± 1.96 sample standards deviations).

Table 14: Surface parameter values and percentage differences. Comparing CT sets 1–3 to the Alicona measurements.

Parameter	Alicona mean value	Set 1 mean value	Set 2 mean value	Set 3 mean value	Percentage difference, Set 1 to Alicona	Percentage difference, Set 2 to Alicona	Percentage difference, Set 3 to Alicona
Height parameters							
$S_q / \mu\text{m}$	41.19	40.46	40.07	40.07	-1.8	-2.7	-2.7
S_{sk}	1.41	1.35	1.34	1.35	-4.5	-5.1	-4.8
S_{ku}	9.29	9.04	8.98	8.99	-2.7	-3.4	-3.3
$S_z / \mu\text{m}$	479.61	479.07	474.87	472.53	-0.1	-1.0	-1.5
$S_a / \mu\text{m}$	30.31	29.84	29.59	29.58	-1.5	-2.3	-2.4
Spatial parameters							
S_{al} / mm	0.29	0.29	0.29	0.29	0.6	0.3	0.3
Hybrid parameters							
$S_{dr} / \%$	15.92	13.30	13.09	12.79	(Δ) -2.6	(Δ) -2.8	(Δ) -3.1
S_k family paramters							
$S_k / \mu\text{m}$	90.25	89.76	89.01	88.74	-0.5	-1.4	-1.7
Material ratio parameters							
$S_{mr2} / \%$	91.98	91.70	91.74	91.74	(Δ) -0.3	(Δ) -0.2	(Δ) -0.2

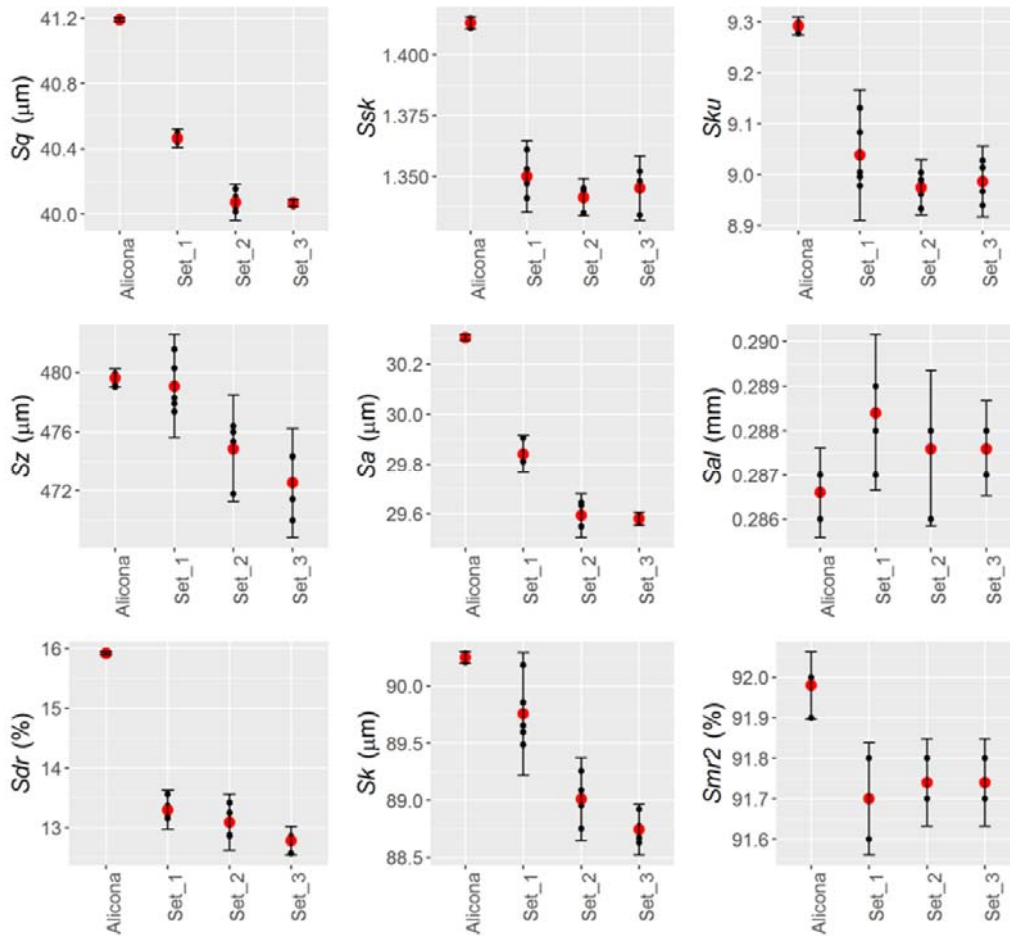


Figure 3-15: ISO 25178-2 parameters, Alicona to CT comparison charts [18].

3.2.2 Dimensional artefact results

Table 15 shows the dimensional artefact results. These include the OD, ID and Length measurements on the CMM and CT for the sets 1, 2 and 3. The table includes the differences between the mean CT measurements and the mean CMM dimensions, together with the sample standard deviation values for the measurement sets. Charts for OD, ID and Length, including the 95% confidence interval, are shown in Figure 3-16:. The change of the mean dimensions for OD, ID and Length between CT set 1 and CT set 2 (the set prior and the set post filament change) were -0.75%, -0.76% and -0.74%, respectively, clearly visible in the charts. All dimensional results obtained for the dimensions extracted from the CT scans were within 1% of the mean values obtained from the CMM measurements of the artefact.

Table 15: CMM and CT artefact dimensional results. OD, ID and Length, including standard deviation values.

Measurement method	Mean OD (mm) [% dif. c.w. CMM]	Sample std. dev. (mm)	Mean ID (mm) [% dif. c.w. CMM]	Sample std. dev. (mm)	Mean Length (mm) [% dif. c.w. CMM]	Sample std. dev. (mm)
CMM (10 meas.)	2.9946	0.00016	3.1926	0.00019	3.9542	0.00013
CT Set 1 (5 meas.)	2.9934 [-0.04%]	0.00050	3.1856 [-0.22%]	0.00040	3.9570 [-0.07%]	0.00070
CT Set 2 (5 meas.)	2.9709 [-0.79%]	0.00060	3.1615 [-0.97%]	0.00030	3.9278 [-0.67%]	0.00040
CT Set 3 (5 meas.)	2.9714 [-0.77%]	0.00060	3.1624 [-0.95%]	0.00030	3.9280 [-0.66%]	0.00070

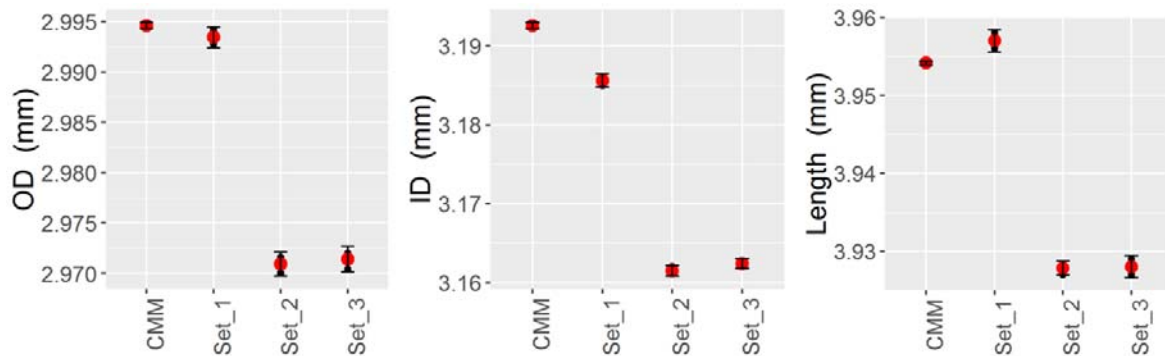


Figure 3-16: OD, ID and Length measurement comparisons. Comparing CMM and CT sets 1-3 [18].

The dimensional results do not indicate a significant error due to incorrect surface determination. The mean of all the CT OD measurements was -0.53% (-15.9 μm) less than the mean CMM OD measurement. The mean of the Length and ID measurements on the CT were -0.47% (-18.6 μm) and -0.71% (-22.3 μm) less than the respective measurement means on the CMM. The difference between set 1 and set 2 do suggest the filament change had a statistically significant effect on the overall scaling (of approximately 0.75%). A summary of the surface texture parameter results is given in Table 16. The CT machine used in this study, the Nikon XT H 225, is an industrial machine. As noted in 3.2.1.2.2, Nikon manufactures a metrology CT, the MCT225, which includes a protocol to perform a dimensional calibration using a ball-plate artefact after each filament change and then scale the reconstruction accordingly.

Table 16: Mean CT parameter value, pre and post filament change.

Parameter	Set 1 mean value	Set 2 mean value	Percentage difference [(Δ) is absolute difference]
Height parameters			
<i>Sq</i> / μm	40.46	40.07	-0.97
<i>Ssk</i>	1.35	1.34	-0.64
<i>Sku</i>	9.04	8.98	-0.71
<i>Sz</i> / μm	479.07	474.87	-0.88
<i>Sa</i> / μm	29.84	29.59	-0.83
Spatial parameters			
<i>Sal</i> / mm	0.29	0.29	-0.28
Hybrid parameters			
<i>Sdr</i> / %	13.30	13.09	(Δ) -0.21
<i>Sk</i> family parameters			
<i>Sk</i> / μm	89.76	89.01	-0.83
Material ratio parameters			
<i>Smr2</i> / %	91.70	91.74	(Δ) 0.04

3.3 Discussion

The process validation for the alignment and extraction of surface texture data from the master surface and a copy, together with the data extraction from ten Alicona measurements, showed good repeatability for both the process and the Alicona measurements, producing a stable and sensitive process for the evaluation of surface extraction from CT.

The dimensional artefact, manufactured from a material similar to the AM surface artefact, allows monitoring of potential surface determination problems and scaling effects from factors such as filament changes. Changing the filament produced a global change in dimension of approximately -0.75%. There was a corresponding change in the surface texture parameters pre to post filament change, indicating the importance of monitoring with a traceable artefact to obtain optimal results, particularly with machines without a post filament change calibration protocol. Further evaluation of the application of the correction of scaling and surface determination errors using a dimensional artefact is included in Chapter 4.

3.4 Conclusion

This chapter reported on the development of a novel technique to extract quantitative areal surface texture information (per ISO 25178-2) from CT scans of AM components. The technique has been shown to be robust and sensitive to surface texture changes such as those may be produced when the CT system filament is changed. The values of extracted parameters are remarkably similar to the surface texture results produced from an established measurement technique: focus variation. Repeatability of the CT measurement has been shown to be good, including the measurements taken when artefact was removed and replaced into the fixture, similar to potential industrial lot testing; for example S_a , with a five-sample mean value $29.6 \mu\text{m}$, had a sample standard deviation of less than $0.013 \mu\text{m}$. These tests were performed on one CT machine with one artefact. For industrial applications it is important to verify other machines will produce acceptable results and the process has to be shown to be applicable to other industrial AM materials and processes. Additionally, the relationship between maximum CT measurement voxel size and surface roughness for successful surface characterisation will be required as part of defining suitable measurement envelopes. Work to address these issues is reported in Chapter 4.

Chapter 4 CT-STARR Stage 1

“Coming together is a beginning; keeping together is progress; working together is success.”

Henry Ford (1863–1947)

This chapter documents the development and implementation of an interlaboratory comparison (round robin (RR)) based on the techniques reported in 0. The development work was presented at the 7th conference on industrial computed tomography, Leuven, Belgium, February 2017. A. Townsend et al. “*Development of an interlaboratory comparison investigating the generation of surface texture data per ISO 25178-2 from XCT*” [22], The paper is included in Appendix 4.

The results were presented at euspen’s 17th international conference and exhibition, Hannover, DE, May 2017. A. Townsend et al. “Results from an interlaboratory comparison of areal surface texture parameter extraction from X-ray computed tomography of additively manufactured parts” [23], The paper is included in Appendix 5.

4.1 Introduction

The work reported in Chapter 3 detailed the development of an artefact system comprised of two artefacts and a bespoke additively manufactured fixture. The artefacts were one AM artefact used for the evaluation of surface extraction and parameterisation and one reference dimensional artefact for scaling and surface determination evaluation. The reported work showed the method was robust and a viable technique for surface texture measurement. For the method to have academic research and industrial applications it would need to function for other CT machines and with a variety of materials. This has prompted the development of the interlaboratory comparison reported here. Initial consideration was given to performing a global comparison involving many types of CT machines and, through necessity, allowing the participants to select their own set up parameters and conditions. However, it was decided

that, initially, a smaller scale, geographically local, RR would be a sensible approach. The intention being to provide valuable information to guide an expanded Stage 2 interlaboratory comparison. Stage 1 RR included four participants using similar CT machines and so similar system parameters could be used. If there were no performance conclusions to be drawn from a tightly controlled RR there would be little point in expanding the RR. The Stage 1 RR was performed in the UK, so making it easier to transport the samples to the test laboratories and supervise/perform the measurements. This face-to-face contact proved invaluable because, even though the participants had similar machines, all had individual input, opinions and expertise on CT use.

4.1.1 Lessons learned

Lessons learned during the research reported in Chapter 3 resulted in changes to the artefact design and minor time-saving processing changes that were incorporated into the RR process. The ABS artefact holder design was modified to include a necked-down section that would allow an unobstructed path between the X-ray emitter and the detector; this would allow use of the “flux normalisation” feature during CT measurement, see Figure 4-1:.

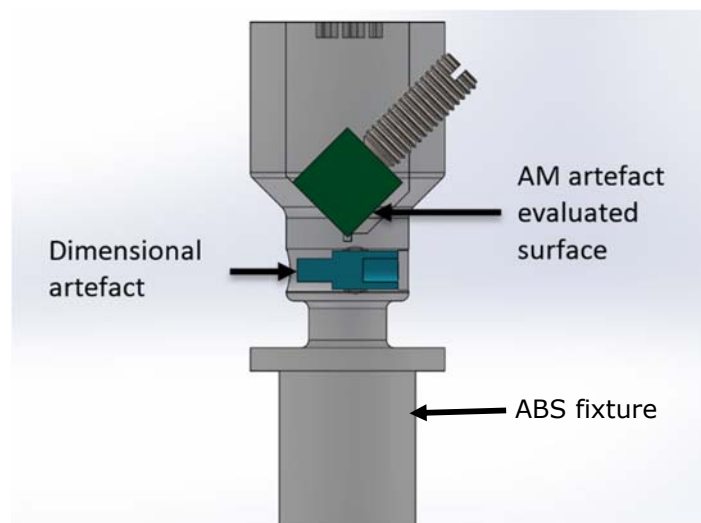


Figure 4-1: CAD section view of the RR CT fixture. Showing the dimensional artefact, AM artefact with the evaluated surface.

Flux normalisation compensates for any change of flux during the complete measurement process. In this process an area on the detector is selected. There must be an unobstructed path between the x-ray source and this selected area of the detector during the entire scan sequence because the grey-scale values for this selected area for each of the CT projections are compared and normalised. The fixture was designed to give an air gap around all the measured surfaces of the AM and dimensional artefact, similar to the fixture utilised in Chapter 3. The dimensional artefact was manufactured with a longer solid centre section to provide greater engagement with the clamping screw, see Figure 4-2:.

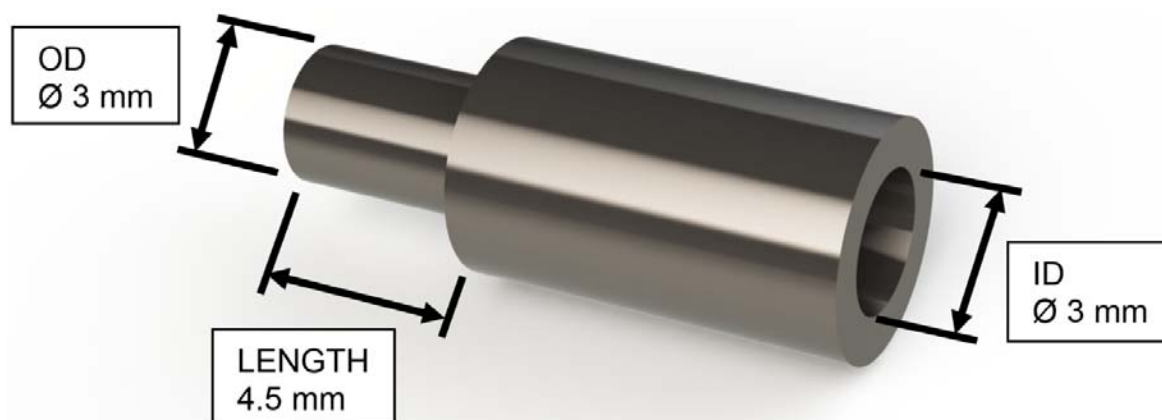


Figure 4-2: CAD rendering of the dimensional artefact. Showing the dimensions for the OD, ID and Length.

Several small changes were made to the data processing sequence to reduce time:

The master AM surface, chosen randomly from the Alicona G4 measurement data sets, was converted from STL to PLY format. The AM surface, extracted in VGStudio MAX 3.0, was saved directly in the PLY format (rather than STL format). The AM surface data processing was then performed using PLY files. This reduced processing and manipulation time. Instead of extracting and performing surface determination on the dimensional artefact and the entire AM artefact, only a section of the AM artefact containing the surface-of-interest was extracted. This reduced surface determination calculation time. VGStudio MAX 3.0 "normal" conversion

was used to generate the dimensional artefact STL file. This reduced the processing time (VGStudio MAX 3.0 “Super Precise” conversion was still used for the AM surface conversion).

4.2 Methodology

CT-STARR Stage 1 was designed to investigate the repeatability and reproducibility of measurement and characterisation of AM surfaces using similar CT machines. There were four RR participants; three of the participants used the Nikon MCT225 metrology CT for the measurements, one participant used the Nikon XT H 225 industrial machine. The participants, together with their machines, are shown in Table 17.

Table 17: Round robin participants and their CT machines.

Laboratory	CT machine
University of Huddersfield, Huddersfield, UK	Nikon XT H 225 Industrial CT
University of Nottingham, Nottingham, UK	Nikon MCT225 Metrology CT
National Physical Laboratory, Teddington, UK	Nikon MCT225 Metrology CT
Nikon Metrology, Tring, UK	Nikon MCT225 Metrology CT

4.3 Measurement artefacts

4.3.1 AM artefact

Initial research (Chapter 30) was performed using aluminium AM and dimensional artefacts. The AM artefact had been manufactured using an SLM machine. The top (upskin) surface of the artefact was used as the surface-of-interest. It is important that the techniques reported be verified for other materials and surface conditions, so the raw material, manufacturing process and surface measurement location were all changed for the RR. The material chosen was Ti6Al4V ELI (extra-low interstitial, Grade 23). This material is widely used in the aerospace and medical industries. Ti6Al4V ELI is a high-purity version of Ti6Al4V (Grade 5) with lower specified limits on iron, nitrogen, carbon and oxygen. Grade 23 has superior fracture toughness, has better cryogenic mechanical properties and has excellent bio-compatibility. Grade 23 is commonly used to manufacture medical and dental implants. The RR AM artefact was produced using the electron beam melting (EBM) process. The artefact was manufactured on an ARCAM Q10 machine; nominal powder size was 45–100 μm .

A vertical (side) surface was chosen as the surface-of-interest for the RR measurements. The artefact was a 10 mm per-side cube, similar to the size of the aluminium artefact used in Chapter 3. The size of this artefact was dictated by the required measurement area (8 mm x 8 mm) with additional margin for cropping of the extracted surface. The required measurement area was derived from the profile roughness (R_a approximately 30 μm) using Table 1 of ISO 4288 [122] (profile) and ISO 25178 (areal) specification standards.

4.3.2 Dimensional artefact

The dimensional artefact included in each scan was also machined from Ti6Al4V ELI bar stock to provide similar X-ray attenuation properties as the AM artefact. This dimensional artefact included three measured dimensions: an OD and an inside diameter ID of approximately 3 mm and a step length between two parallel surfaces of approximately 4 mm. Surface determination is the calculation of the surface position during CT reconstruction; the calculated position of the surface is based on the grey-scale values of the CT images. As reported in Chapter 3, inaccuracies in this surface determination would affect these three dimensions differently: if the surface determination were to calculate the surface inside the actual surface, then the calculated OD would be undersized, the ID would be oversized and the length would be minimally effected by errors, as the surfaces are parallel and facing the same direction. These three different dimensional changes produced by surface determination errors would allow separation of surface determination errors from overall scaling errors (scaling errors would produce similar changes for all three dimensions). For example, the OD would increase, the ID would increase and the length would increase. The AM surface and dimensional artefacts were measured using an Alicona G4 focus variation instrument and a Zeiss Prismo CMM, respectively, prior to the RR. The two artefacts were mounted within an AM fixture designed to maintain an air gap between all measured surfaces and the fixture (see Figure 4-1:). This was done to create a two-material, rather than three-material surface

determination calculation. The artefacts were not removed from the fixture during the complete set of RR measurements.

4.4 CT measurement settings

The artefact assembly, mounted in the Nikon XT H 225, is shown in Figure 4-3:. The settings for the single Nikon XT H 225 are shown in Table 18. The 1 mm copper filter can be seen in front of the X-ray window in Figure 4-3:. The measurement settings were selected to optimise the exposure contrast while maintaining a fully-focussed electron beam (and hence X-ray beam).

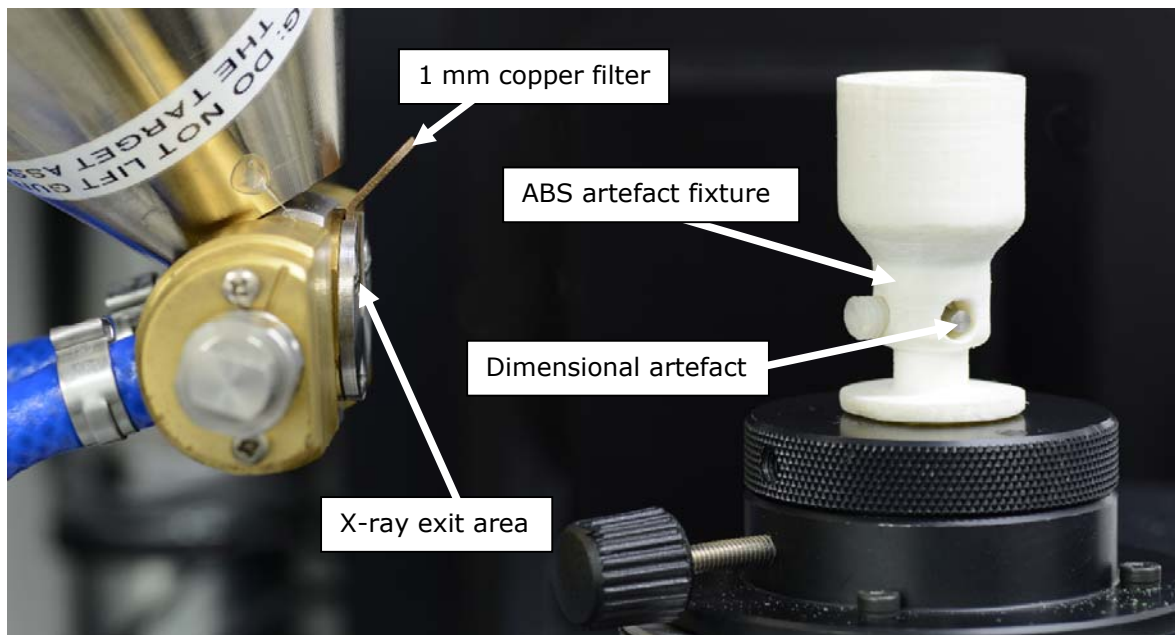


Figure 4-3: Artefact assembly mounted in the Nikon XT H 225. Showing the X-ray gun and 1 mm copper filter.

Table 18: Nikon XT H 225 measurement settings for the RR measurements.

Parameter	Value	Parameter	Value
Filter material	Copper	Exposure time	2829 ms
Filter thickness	1.0 mm	Voxel size	17.3 μm
Acceleration voltage	160 kV	Number of projections	1583
Filament current	62 μA	Detector size (pixels)	1008 x 1008

The artefact assembly mounted in the Nikon MCT225 is shown in Figure 4-4:. The CT settings are shown in Table 19. These settings were used for all three MCT225 machines used in the RR. Where applicable, the majority of the settings were similar to those for the XT H 225.

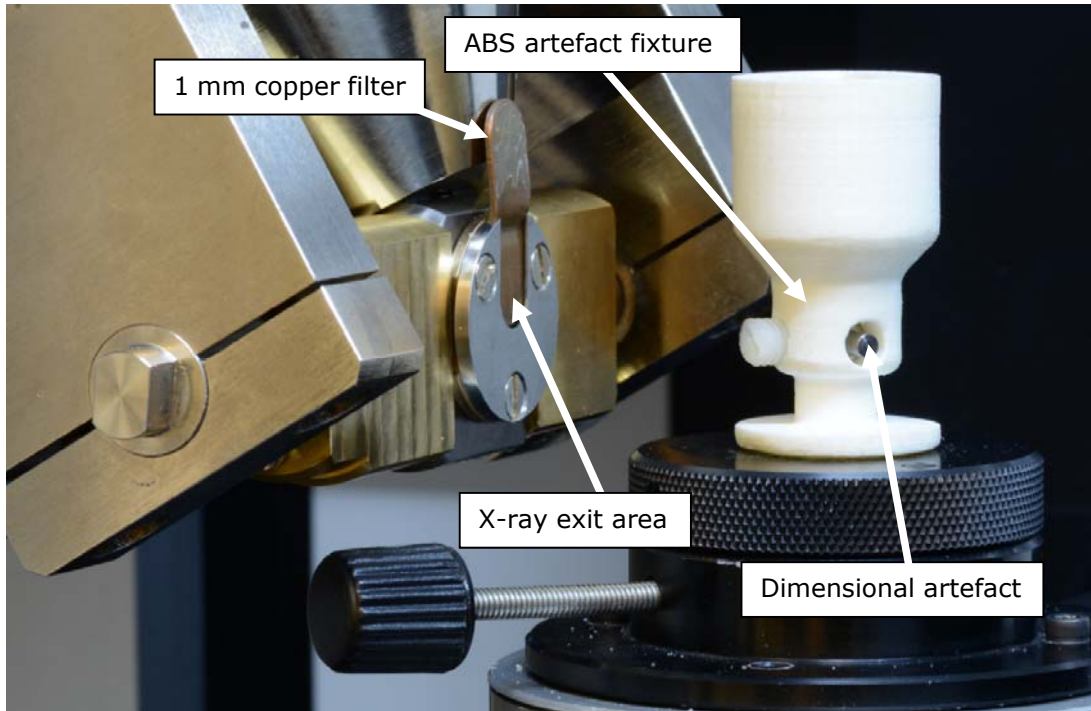


Figure 4-4: Artefact assembly mounted in a Nikon MCT225. Showing the X-ray gun and 1mm copper filter.

Table 19: Nikon MCT225 measurement settings for the RR measurements.

Parameter	Value	Parameter	Value
Filter material	Copper	Exposure time	2829 ms
Filter thickness	1.0 mm	Voxel size	8.7 μm
Acceleration voltage	160 kV	Number of projections	3142
Filament current	62 μA	Detector size (pixels)	2000 x 2000

The most significant difference between the CT machine settings was that the voxel size for the MCT225 measurements was 8.7 μm , compared to 17.3 μm for the XT H 225. This difference in resolution is due, primarily, to the increased number of pixels in the detector of the MCT225. Five measurements were taken on each CT machine. The artefacts were not disturbed between each of the measurements. Removing and replacing the artefacts would increase the probability of component damage during the RR process. The AM artefact had

been removed and replaced during the initial process analysis (Chapter 30) and there had been no observed difference in the extracted surface and dimensional data between measurement sets where the sample was removed and replaced and measurement sets where the sample was not disturbed.

4.5 Reconstruction

All reconstruction, surface analysis steps and parameter extraction was performed by the author to reduce variability. Reconstruction was performed using Nikon CT Pro 3D. Surface determination was performed using VGStudio MAX 3.0. Local iterative surface determination was performed with a search distance of 4.0 voxels. Two regions of interest were extracted: the AM surface-of-interest and the complete dimensional artefact. The dimensional artefact was converted to STL file format using the "normal" setting and the AM surface to PLY format using the "Super Precise" setting.

4.6 Comparative measurements

Reference dimensional artefact measurements were taken using the Zeiss Prismo CMM using the same protocol and measurement locations specified in 3.1.2.2. Similarly, five surface measurements were taken using the Alicona G4 using the same settings specified in 3.1.2.1. One of the Alicona G4 measurements was used as the master for all subsequent alignment and processing steps. Alignment, cropping and conversion to height map format (SDF) were performed per section 0. All extracted surface data was aligned to one of the FV measurements. The surface was and filtered using an L-filter nesting index of 8 mm and an S-filter nesting index of 0.025 mm per ISO 25178-3. Data was extracted and values of parameters per ISO 25178-2 were generated.

4.7 Results

4.7.1 AM surface texture artefact

The surface texture parameter mean values and sample standard deviations for the Alicona G4 FV measurement set and the four CT machine measurement sets are shown in Table 20. The results are from the XT H 225 industrial CT at the University of Huddersfield (XCTHUD), the MCT225 metrology CT at the University of Nottingham (XCTNOT), the MCT225 CT at Nikon (XCTNIK) and the MCT225 CT at the National Physical Laboratory (XCTNPL). The differences between the CT mean value and the FV mean values are shown in Table 21.

Table 20: RR surface texture parameter mean values and sample standard deviation.

Parameter	Mean FV	SD FV	Mean XCTHUD	SD XCTHUD	Mean XCTNOT	SD XCTNOT	Mean XCTNIK	SD XCTNIK	Mean XCTNPL	SD NPL
<i>Sa</i> / μm	25.5	0.001	24.1	0.027	25.5	0.011	25.5	0.019	25.6	0.006
<i>Sq</i> / μm	32.6	0.002	30.9	0.032	32.5	0.009	32.5	0.023	32.6	0.007
<i>Sz</i> / μm	335.3	0.199	324.0	2.941	335.2	1.244	334.2	1.423	335.4	2.332
<i>Ssk</i>	0.26	<0.001	0.08	0.015	0.20	0.001	0.21	0.001	0.21	0.001
<i>Sku</i>	3.7	<0.001	3.7	0.010	3.6	0.004	3.6	0.005	3.6	0.003
<i>Sdr</i> (%)	40.2	0.014	28.3	0.131	41.9	0.117	42.4	0.137	43.8	0.103

Table 21: Differences between CT and Alicona mean measurements.

Parameter	Difference between mean CT and FV values			
	XCTHUD	XCTNOT	XCTNIK	XCTNPL
<i>Sa</i> / μm	-5.2 %	0.2 %	0.3 %	0.5 %
<i>Sq</i> / μm	-5.2 %	-0.1 %	-0.1 %	0.2 %
<i>Sz</i> / μm	-3.4 %	0.0 %	-0.3 %	0.1 %
<i>Ssk</i> (absolute)	-0.2	-0.1	0.0	0.0
<i>Sku</i>	-2.0 %	-2.9 %	-3.1 %	-3.1 %
<i>Sdr</i> (%) (absolute)	-12.0	1.7	2.2	3.5

Comparing the percentage differences between CT measurements and FV measurements, the results for the MCT225 metrology machine measurement sets for *Sa*, *Sq* and *Sz* were an order of magnitude better than those for the XT H 225 industrial machine. For example, the difference between the XCTNPL MCT225 *Sa* value and the FV value was 0.5 %; the difference between the XCTHUD XT H 225 *Sa* value and the FV value was 5.2%. Figure 4-5 shows the false colour height maps for one Alicona G4 measurement and one MCT225 measurement

from the NPL set. The false colour height maps illustrate the accuracy of the alignment process as well as the surface characterisation. It is not easy to visually distinguish the two height maps. Figure 4-6 shows results of S_a , S_q and S_z for all machines.

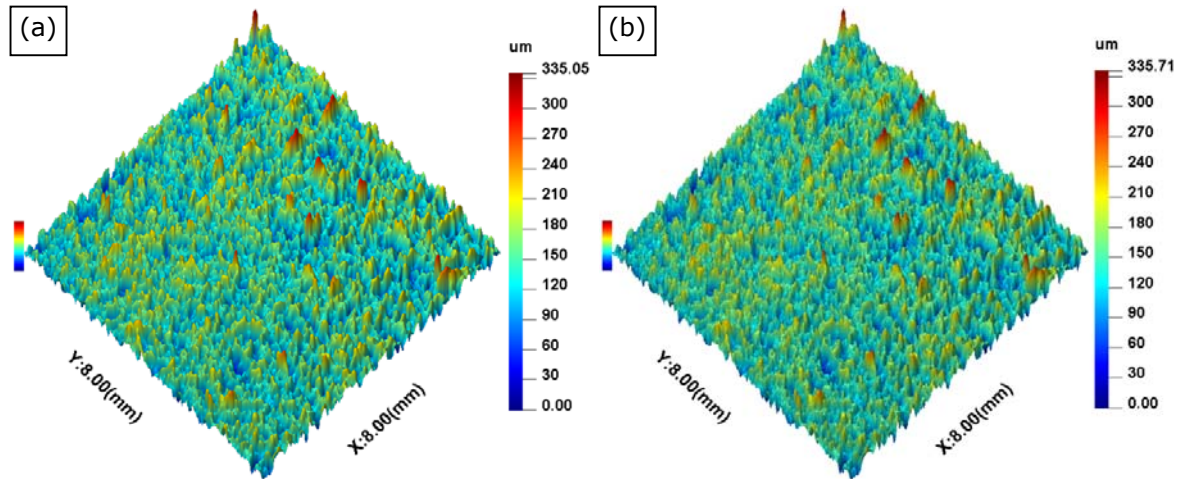


Figure 4-5: False colour height maps of the RR Ti6Al4V EBM surface. (a) Alicona G4, (b) NPL MCT225.

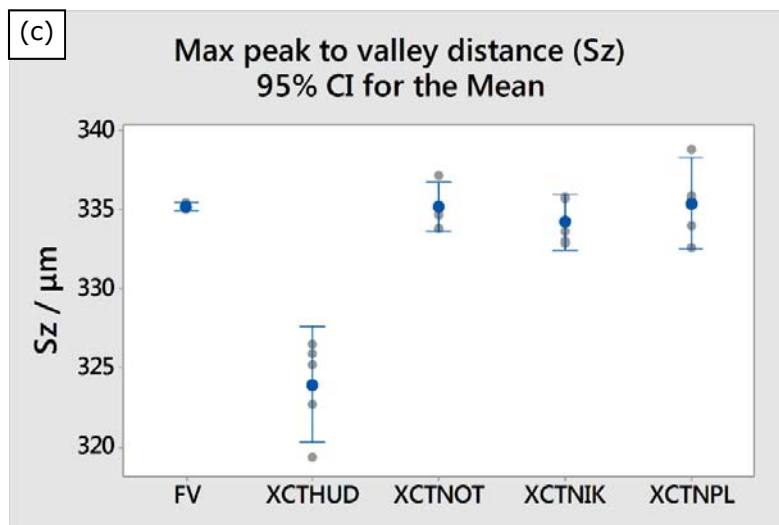
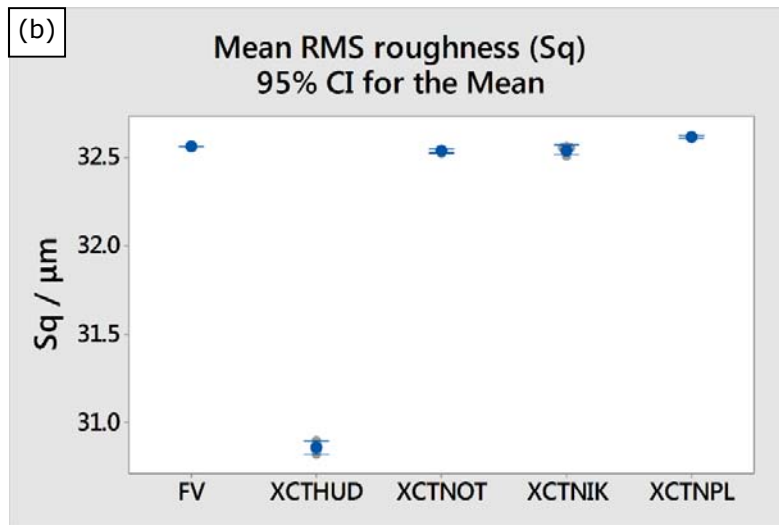
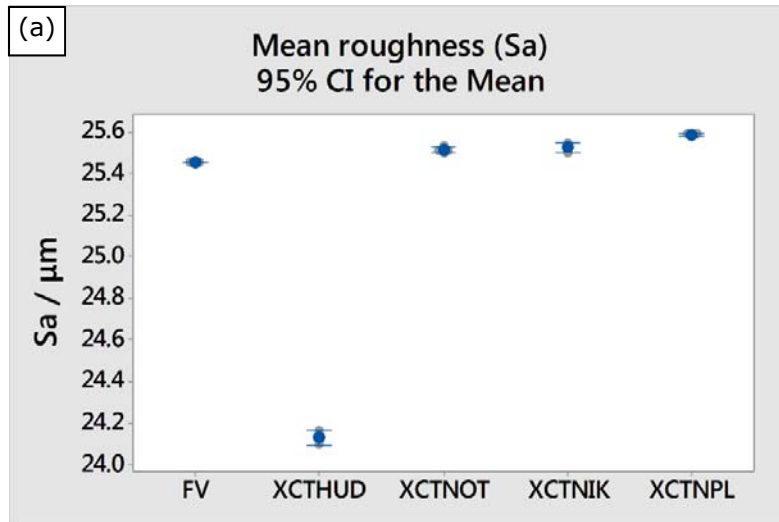


Figure 4-6: RR surface texture results (a) S_a , (b) S_q , (c) S_z .

4.7.2 Dimensional artefact

4.7.2.1 Measurement MPE values

The Nikon MCT225 metrology CT and Zeiss Prismo CMM have maximum permissible error (MPE) values as follows:

Nikon MCT225 MPE: $\pm (9 + L/50) \mu\text{m}$. (L in mm).

Zeiss Prismo CMM MPE: $\pm (1.9 + L/300) \mu\text{m}$. (L in mm).

The *CT reduced MPE limits* displayed on the charts for the dimensional measurements in Chapter 4 are the CT manufacturer's MPE limits reduced by the value of the CMM MPE limit:

MCT225 upper limit is CMM lower MPE value + $(9 + L/50)$.

MCT225 lower limit is CMM upper MPE value - $(9 + L/50)$.

This tightening of the CT MPE limits allows for the fact that the actual component dimensions may be anywhere within the MPE limit range of the reported CMM value. This means that all measurements displayed within the *CT reduced MPE limits* will be within the $(9 + L/50) \mu\text{m}$ of the *actual* dimension. This is similar to the reduction of component measurement tolerance based on the inspection instrument accuracy [140].

The MPE limits are shown on the charts as follows:

—— CMM MPE limits. - - - - CT reduced MPE limits.

4.7.2.2 Dimensional results

The dimensional results for the CMM and the CT measurement sets are shown in Table 22. The sample standard deviations for all CT measurements are all less than or equal to 1.2 μm showing excellent repeatability for all measurements.

Table 22: CMM and CT dimensional artefact mean and standard deviation results.

Measurement method	Mean Length (mm) [% dif. cw CMM]	Sample std. dev. (mm)	Mean OD (mm) [% dif. cw CMM]	Sample std. dev. (mm)	Mean ID (mm) [% dif. cw CMM]	Sample std. dev. (mm)
CMM (10 meas.)	4.6240	<0.00005	2.9735	0.00005	2.9846	0.00005
XCTHUD (5 meas.)	4.5992 [-0.54%]	0.0008	2.9655 [-0.27%]	0.0003	2.9597 [-0.83%]	0.0004
XCTNOT (5 meas.)	4.6238 [0.00%]	0.0008	2.9804 [0.23%]	0.0002	2.9806 [-0.13%]	0.0003
XCTNIK (5 meas.)	4.6216 [-0.05%]	0.0005	2.9778 [0.15%]	0.0002	2.9769 [-0.26%]	0.0003
XCTNPL (5 meas.)	4.6250 [0.02%]	0.0012	2.9803 [0.23%]	0.0002	2.9807 [-0.29%]	0.0002

Charts showing length, OD and ID are shown in Figure 4-7:. It can be seen that the length values for all MCT225 metrology CT measurements are significantly within the CT manufacturer's specified MPE limits as shown in Figure 4-7:(a). The length measurement on the artefact (step-face distanced), just like the centre-centre calibration measurement, is insensitive to surface determination errors. The non-metrology XT H 225 mean length measurement was -0.54 % less than the mean CMM measurement. The artefact OD and ID CT measurements are both sensitive to surface determination errors. The percentage difference between the CT OD values and the CMM OD values are all greater (more positive) than the percentage difference between the CT length values and the length CMM values. Similarly, the percentage difference between the CT ID values and the CMM ID values are all less (more negative) than the percentage difference between the CT length values and the length CMM values. This suggests the surface determination is computing the surface with additional material beyond the actual surface.

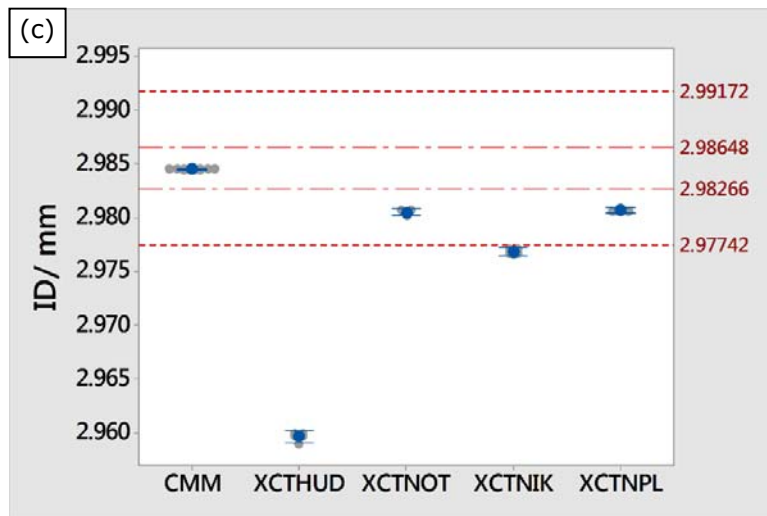
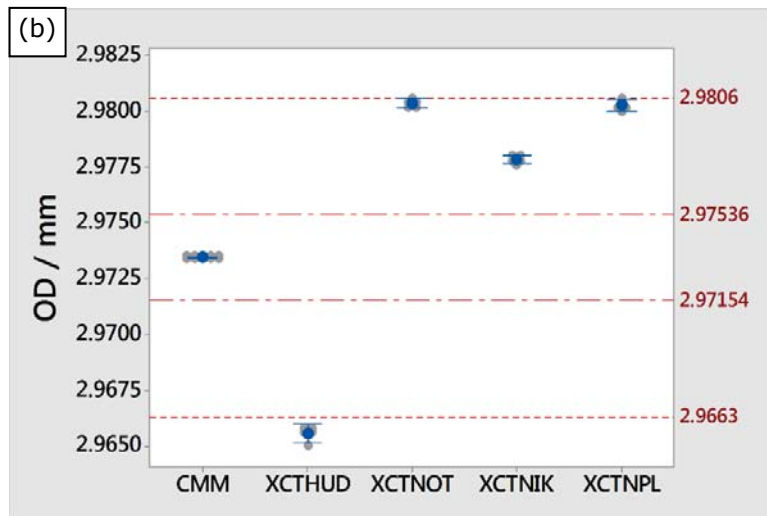
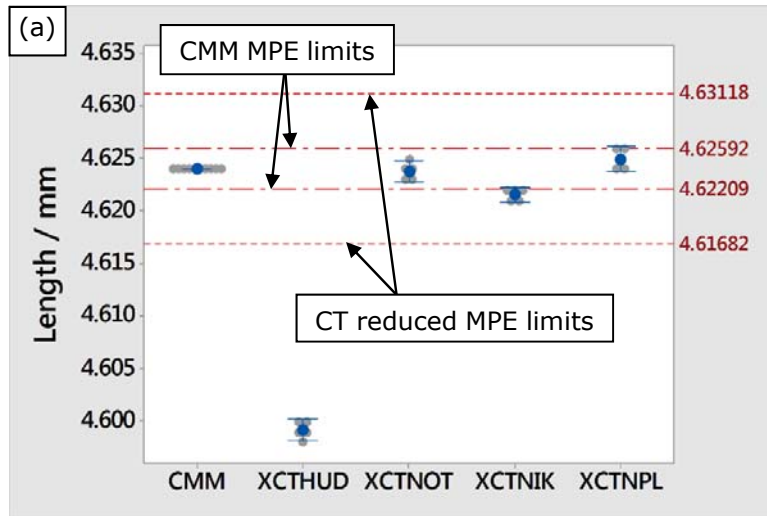


Figure 4-7: CMM and CT dimensional results.
 (a) Length, (b) Outside diameter, (c) Inside diameter.

The difference between the computed surface and the actual surface has been noted for other materials: when using ISO 50 surface determination aluminium components have been computed as undersize (the surface determination computing the surface toward the component material compared to the actual surface location) and steel and ZrO₂ components have been computed as oversize (the surface determination computing the surface toward the background compared to the actual surface) [125].

4.7.2.3 Applying corrections

As discussed in section 4.3.2, the artefact has been designed to differentiate between surface determination errors and global scaling errors. Two corrections were applied to the extracted CT dimensional data: a mathematical correction based on the surface determination error followed by a global scaling correction.

4.7.2.3.1 Surface determination correction

The surface determination applied was found to be computing the surface with additional material beyond the actual surface (the OD was oversize, the ID was undersize). Therefore, the correction should remove material, see Figure 4-8:. The OD becomes smaller, the ID larger and the Length is unchanged. The required surface determination correction was different for all CT machines. The surface determination is per surface, so the OD and ID dimensions will change by twice the surface determination correction value. These mathematical corrections are equivalent to moving the calculated surface toward the component material, thus the OD values reduce and the ID values increase. The surface determination corrections applied are shown in Table 23. The calculated surface determination correction for the MCT225 machines were similar, at between 2.6 µm and 3.0 µm. The calculated surface determination correction for the XT H 225 was higher at 4.2 µm per surface.

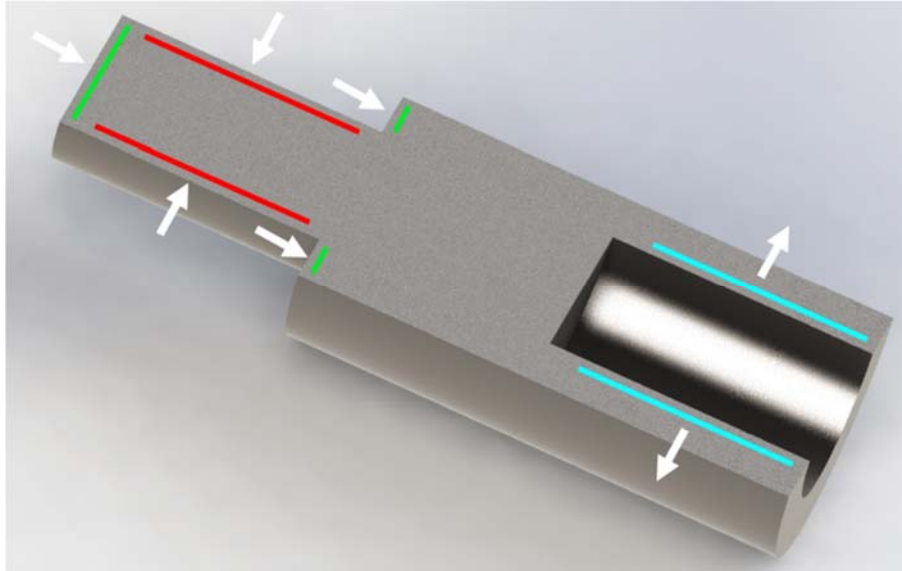


Figure 4-8: Effect of surface determination correction.
The OD decreases, ID increases and the Length is unchanged.

Table 23: Surface determination correction applied to OD and ID.

LAB	Surface determination correction / μm
XCTHUD	4.2
XCTNOT	2.8
XCTNIK	3.0
XCTNPL	2.6

Figure 4-9: shows charts of Length, OD and ID after surface determination correction. Again, it should be noted that one surface determination correction value was applied to all measurements in each set: Length, OD and ID. The values of OD (Figure 4-9:(b)) are reduced and ID (Figure 4-9:(c)) are increased compared with the results prior to surface determination correction (Figure 4-7:(b) and Figure 4-7:(c)). The length results (Figure 4-9:(a)) are the same as the results prior to surface determination correction (Figure 4-7:(a)).

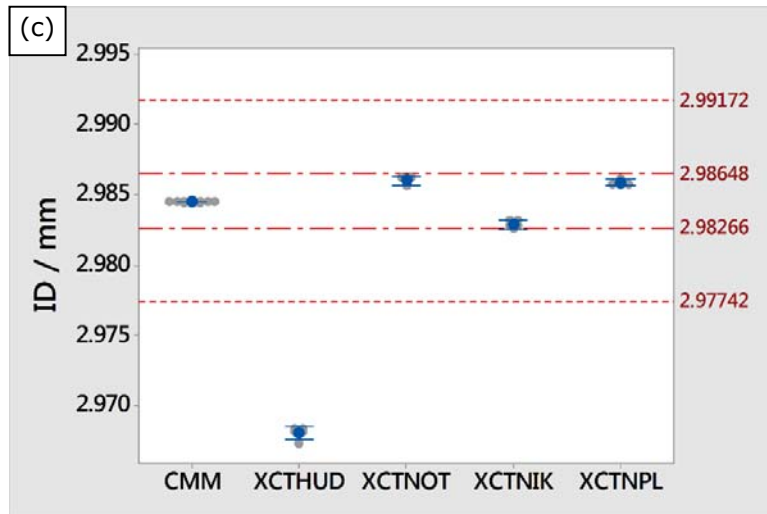
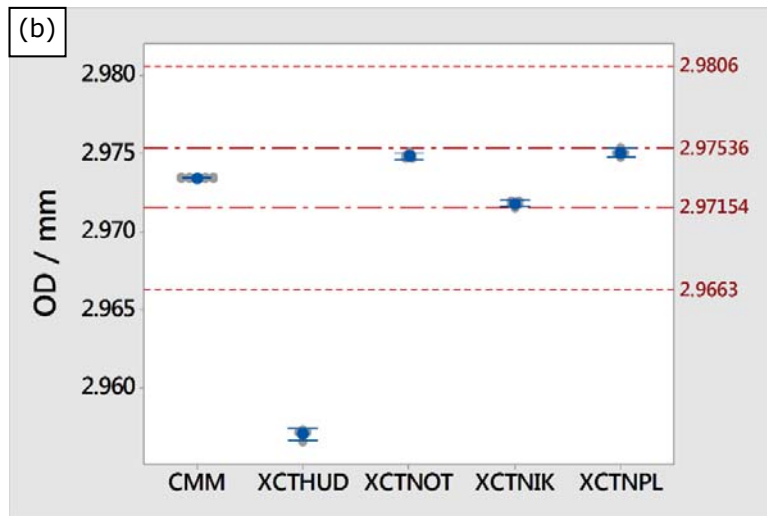
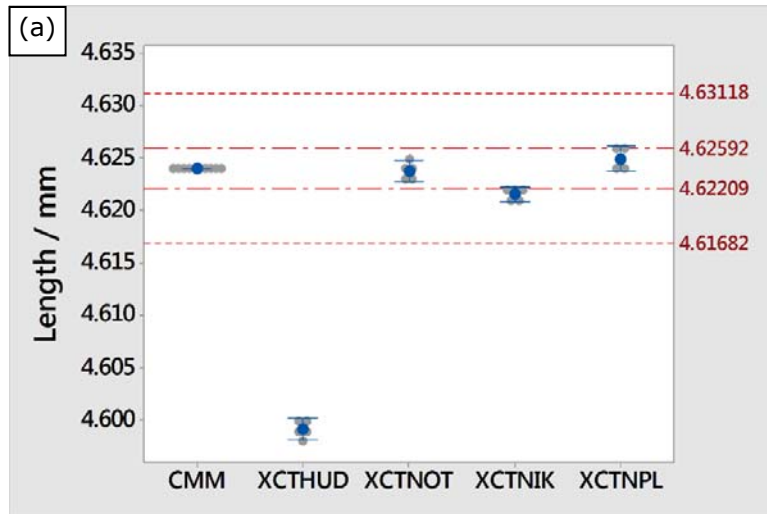


Figure 4-9: Dimensional results after surface determination correction (a) Length, (b) Outside diameter, (c) Inside diameter.

4.7.2.3.2 Surface determination followed by global scaling correction

A second, global, scaling correction can now be applied based on the length measurements. Instead of eroding the surface (making the OD smaller and ID larger) or dilating the surface (OD larger and ID smaller), as the surface determination correction would produce, this global correction increases or decreases the overall size. Figure 4-10: shows an example of globally reducing the size.

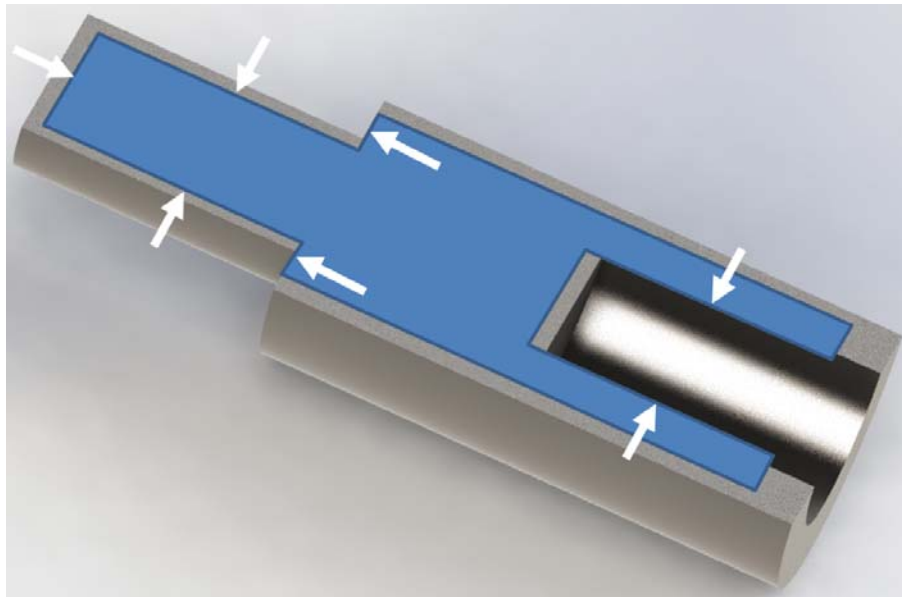


Figure 4-10: Effect of global scaling correction. The OD reduces, the ID reduces and the Length reduces.

Once globally corrected, the mean lengths for all CT measurements are equivalent to the CMM mean length, see Figure 4-11:(a). It can be seen that the OD and ID measurements for all CT machines, including the XT H 225, are well within the MPE limits of the metrology CT and all are also within the MPE of the CMM, see Figure 4-11:(b) and Figure 4-11:(c).

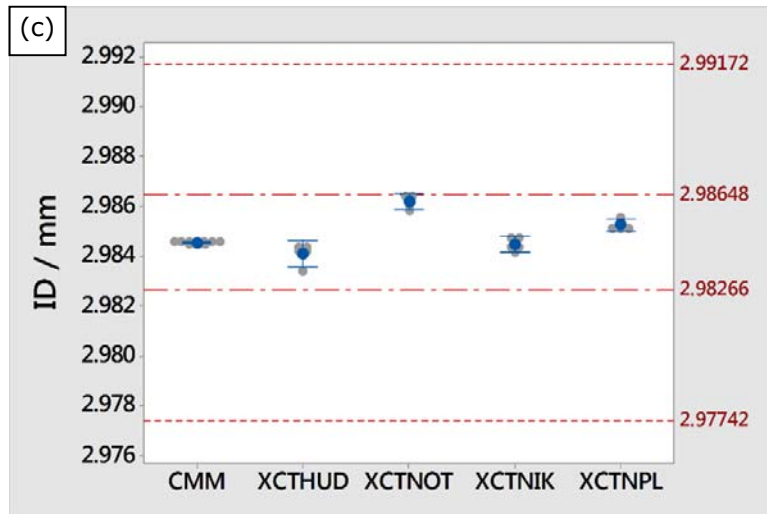
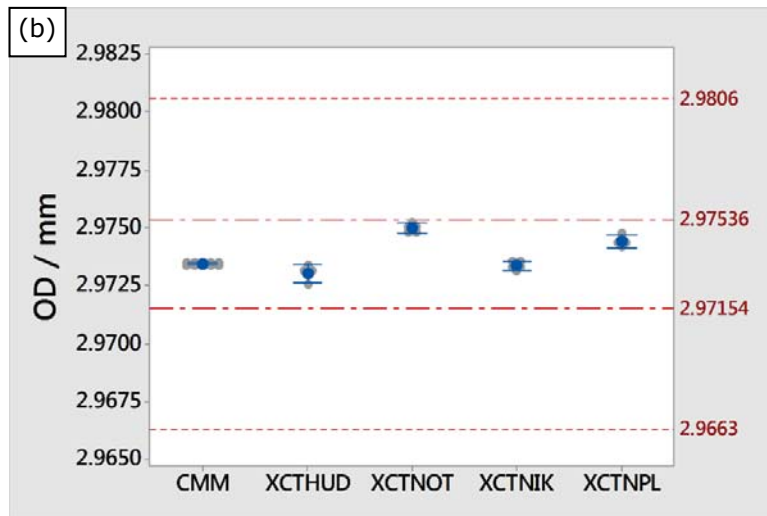
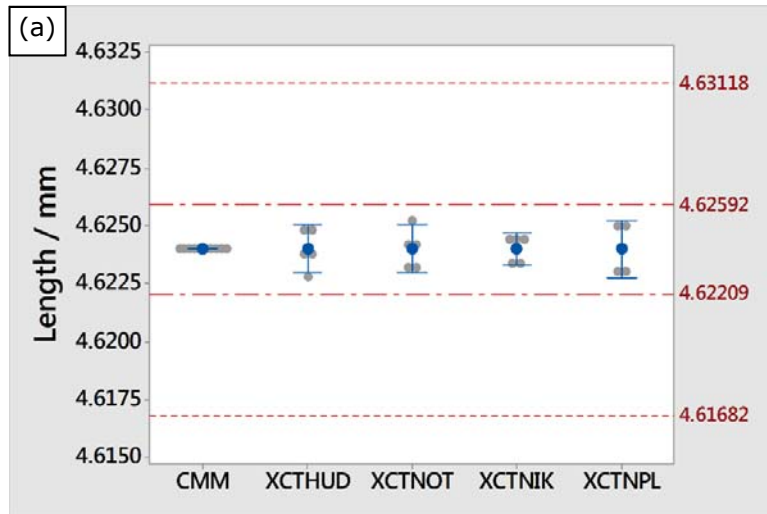


Figure 4-11: Dimensional results after SD and scaling correction. (a) Length, (b) Outside diameter, (c) Inside diameter.

As an illustration of the complete two-stage correction process, using the data reported in Table 22 for the XCTHUD measurement and comparing the dimensions extracted from the CT measurement to the reference CMM measurements, the OD, ID and Length errors were: -0.27%, -0.83% and -0.54%, respectively. If a surface determination correction of 4.2 μm is applied per surface (moving the calculated surface into the part) the errors for OD, ID and Length become -0.55%, -0.55% and -0.54%, respectively. A global (x,y,z) scaling correction of +0.54% (based on the length error) can then be applied, increasing Length, OD and ID. The correction process reduces the Length, OD and ID errors from -0.27%, -0.83% and -0.54%, respectively, to less than 0.02% for all dimensions. After these corrections, the measurements for all CT machines (including the XT H 225 industrial machine) are not just within the MPE of the MCT225 metrology CT, but also within the MPE of the reference CMM.

4.7.2.3.3 Global scaling correction (no surface determination correction)

Results after performing just the global scaling correction are shown in Figure 4-12:. It can be seen that, without performing surface determination correction prior to global scaling correction, the mean length dimensions for the CT measurement are the same as the mean CMM measurement Figure 4-12:(a). However, the OD and ID measurement values for the XT H 225 exceed the metrology CT MPE limits and all values for all measurements exceed the CMM MPE limits. This illustrates the potential impact of surface determination on measurements and the advantages of correcting for surface determination and global scaling.

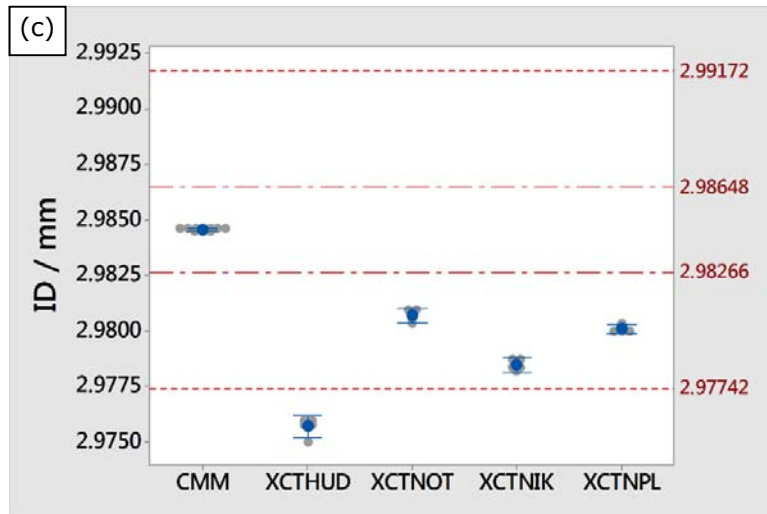
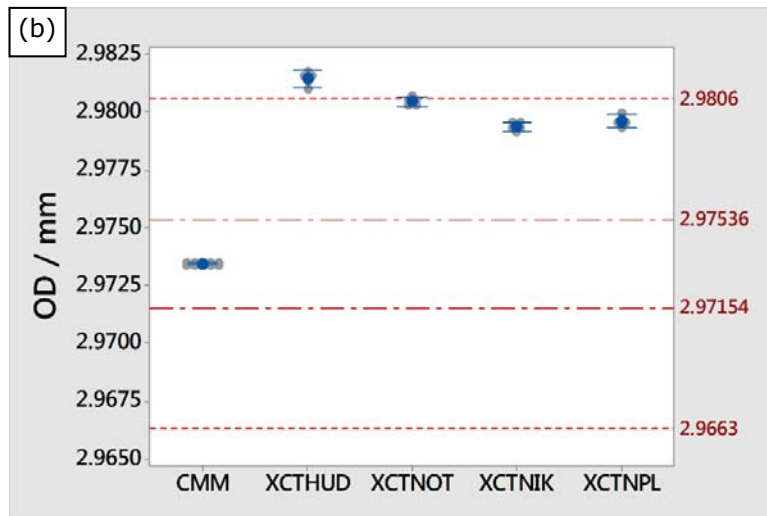
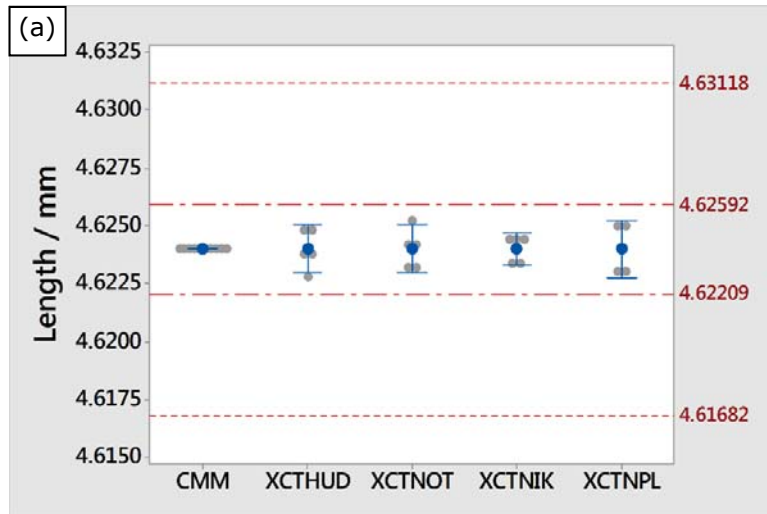


Figure 4-12: Dimensional results after just scaling correction. (a) Length, (b) Outside diameter, (c) Inside diameter.

4.7.3 Measurement voxel size

The voxel size for the MCT225 measurements was 8.7 μm . The voxel size for the Huddersfield XT H 225 measurements was 17.2 μm . A single test (XCTNOT11.5) was performed using the Nottingham MCT225 with the sample moved away from the X-ray source at a magnification and voxel size similar to the Huddersfield measurements (see Table 24). The other CT measurement parameters were unchanged (see Table 19).

Table 24: Voxel size and magnification for each measurement.

Lab	Voxel size / μm	Magnification
XCTHUD	17.2	11.5
XCTNOT	8.7	23
XCTNOT11.5	17.3	11.5

4.7.3.1 Surface texture results

Extracted surface texture results are shown in Table 25. The difference between the CT mean values and the FV mean values are shown in Table 26. Charts for S_a , S_q and S_z are shown in Figure 4-13:.

Table 25: Surface texture results.

Parameter	Mean FV	Mean XCTHUD	Mean XCTNOT	XCTNOT11.5
S_a / μm	25.5	24.1	25.5	24.7
S_q / μm	32.6	30.9	32.5	31.6
S_z / μm	335.3	324.0	335.2	330.5
S_{sk}	0.26	0.08	0.20	0.10
S_{ku}	3.7	3.7	3.6	3.7
S_{dr} (%)	40.2	28.3	41.9	33.0

Table 26: Differences between CT mean values and FV mean values.

Parameter	Difference between mean CT and FV values		
	XCTHUD	XCTNOT	XCTNOT11.5
S_a / μm	-5.2 %	0.2 %	-2.9 %
S_q / μm	-5.2 %	-0.1 %	-3.0 %
S_z / μm	-3.4 %	0.0 %	-1.4 %
S_{sk} (absolute)	-0.2	-0.1	-0.2
S_{ku}	-2.0 %	-2.9 %	-2.5 %
S_{dr} (%) (absolute)	-12.0	1.7	-7.2

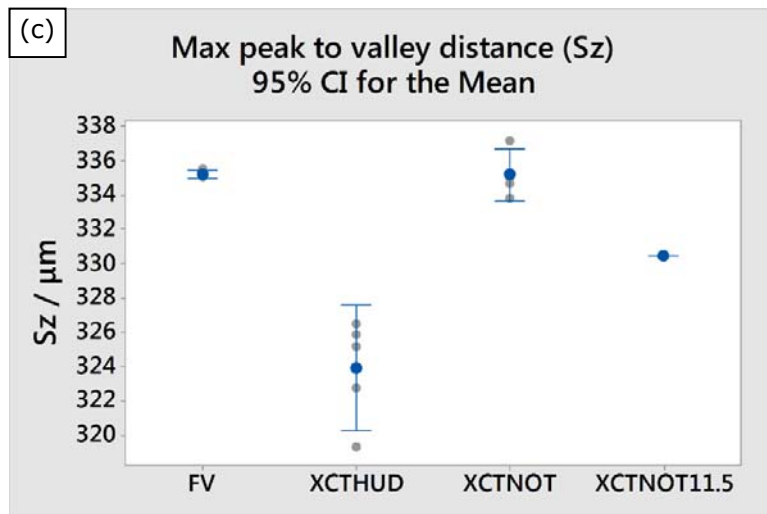
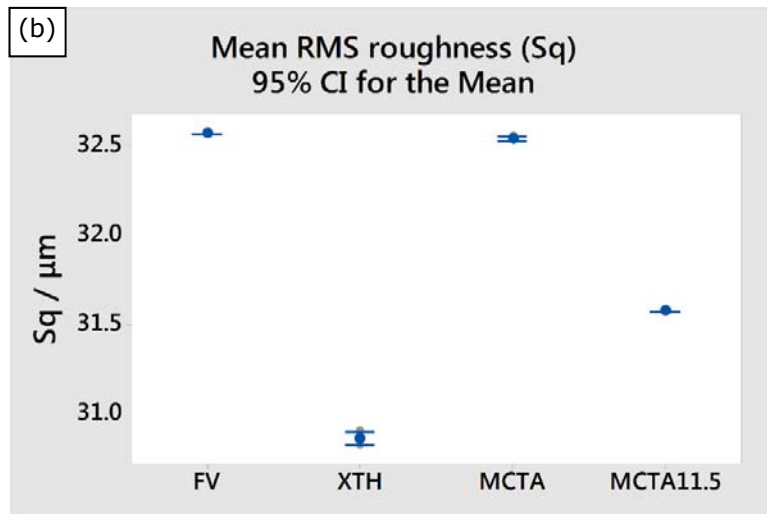
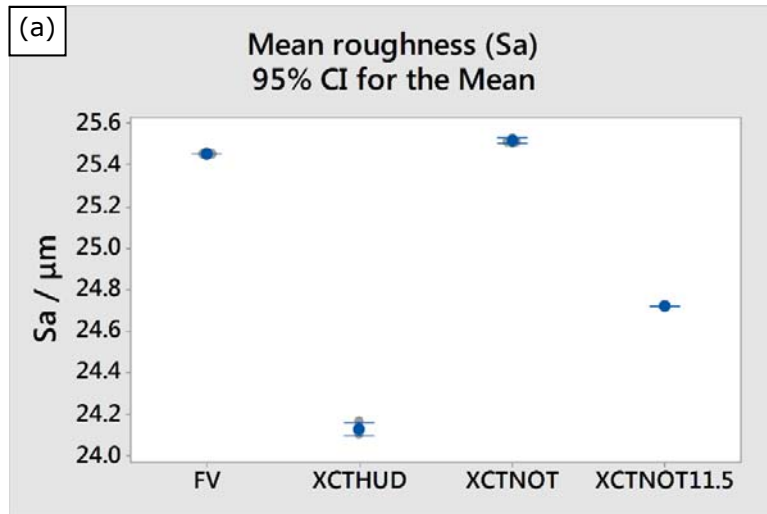
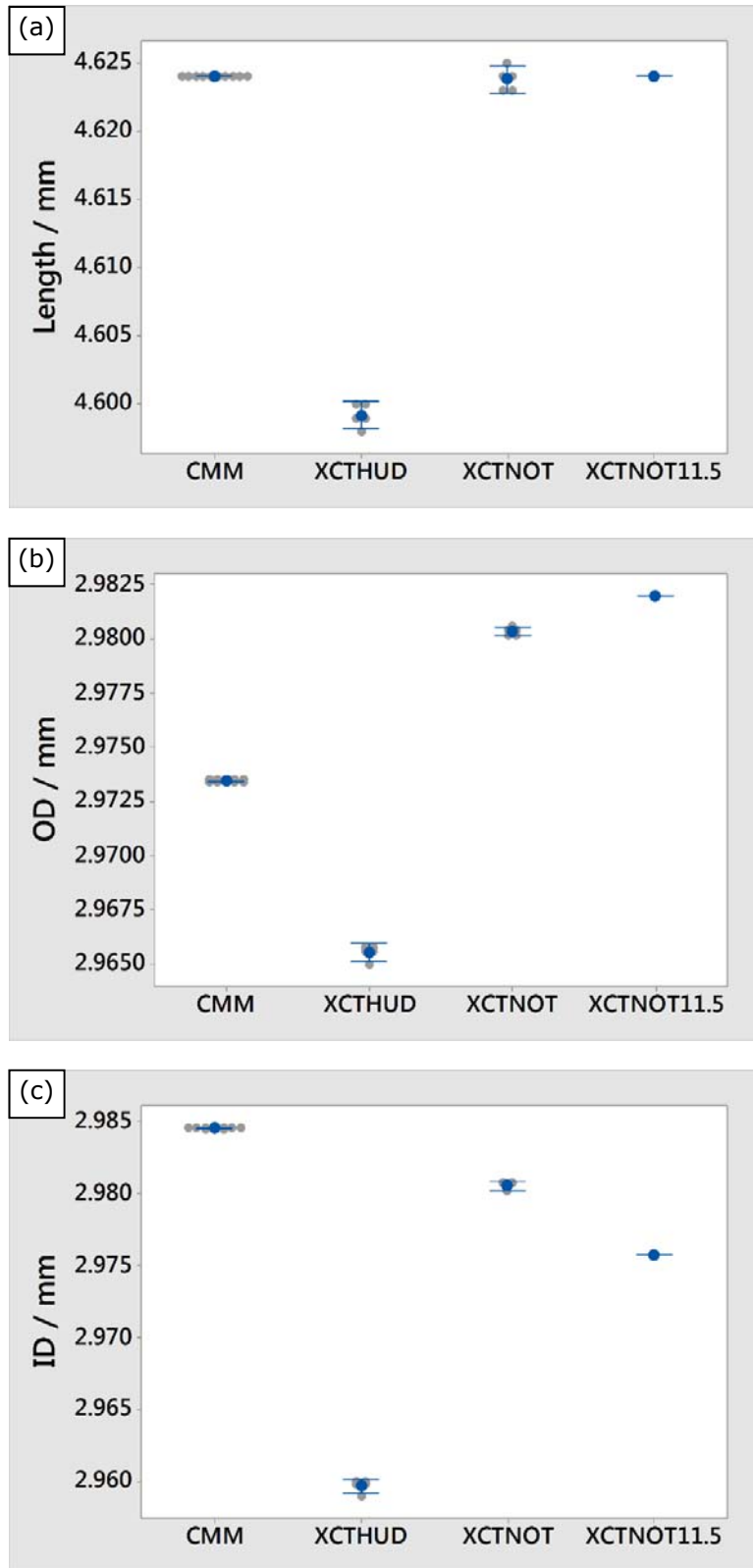


Figure 4-13: Surface texture results for HUD and NOTS.
(a) S_a , (b) S_q , (c) S_z .

The values of S_a , S_q and S_z for the XCTNOT11.5 measurements were significantly lower than those obtained with the smaller voxel size using the initial higher magnification measurement on the same machine. The values were, however, not comparable to the XCTHUD measurements; it can be seen that the difference between the XCTHUD and FV measurement values was approximately twice the difference between the XCTNOT11.5 values and the FV values. The lower XCTHUD results are due to a combination of factors, including the scaling error present in the XT H 225 measurements: the Huddersfield mean length (from the dimensional measurement) is 0.54% undersize (see Table 22). A scaling reduction will result in lower surface texture parameters such as S_a and S_q . The filament change, reported in Chapter 3, resulted in scaling difference of approximately -0.75%. The value of S_a and S_q also reduced, by 0.83% and 0.97%, respectively. As a result of these initial measurement results, the effect of voxel size on the accuracy of the extracted surface texture data is investigated in section 5.2.

4.7.3.2 Dimensional results

The length dimension extracted from the single XCTNOT11.5 measurement matched the CMM mean length measurement (4.624 mm) (see Figure 4-14:). The optimisation of the CT dimensional measurements required a 4.3 μm surface determination correction, similar to the 4.2 μm correction applied to the XCTHUD measurements and more than the 2.7 μm correction applied to the x23 magnification XCTNOT measurements. Once this correction was applied the difference between the XCTNOT11.5 OD and ID measurements and the mean CMM measurements were 0.1 μm (<0.01%). No scaling correction was required as the XCTNOT11.5 length measurement matched the mean CMM length measurement, see Figure 4-15:.



**Figure 4-14: Dimensional results for HUD and NOTS.
 (a) Length, (b) Outside diameter, (c) Inside diameter.**

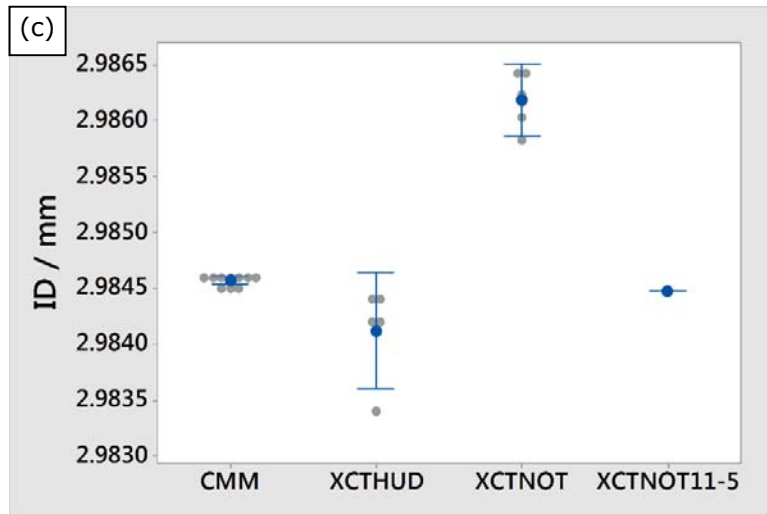
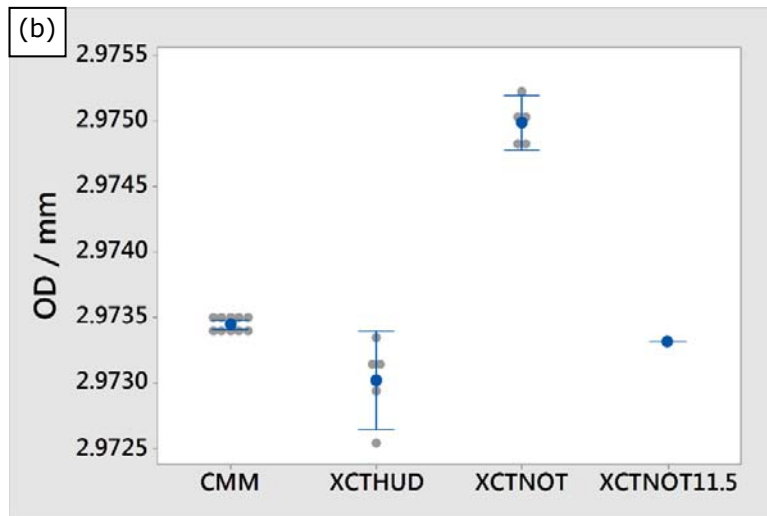
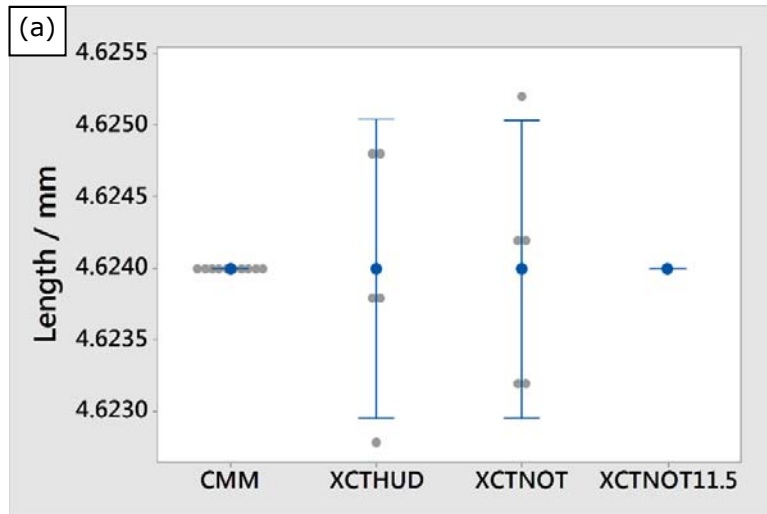


Figure 4-15: Dimensional results including SD and dimensional correction. (a) Length, (b) Outside diameter, (c) Inside diameter.

4.7.4 Cone beam artefacts

During the analysis it was noted that there were local cone beam artefacts on the OD and ID of the CT reconstructions of the dimensional artefact (primarily on the MCT225 measurements). Cone beam artefacts (caused by volume data reconstruction errors) increase as the X-ray cone angle increases from the ideal central plane which is perpendicular to the plane of the detector. Cone beam artefacts may be generated on horizontal surfaces such as the edge of the horizontally aligned dimensional artefact. The cone beam artefacts were more prevalent on the underside of the artefact because, due to the position of the artefact in the scan, the angle of the X-ray beam is greater for the underside surface, see Figure 4-16:(b).

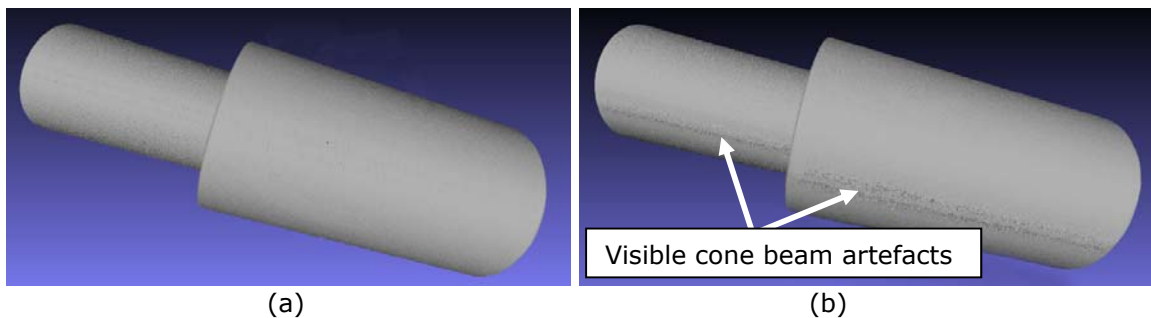
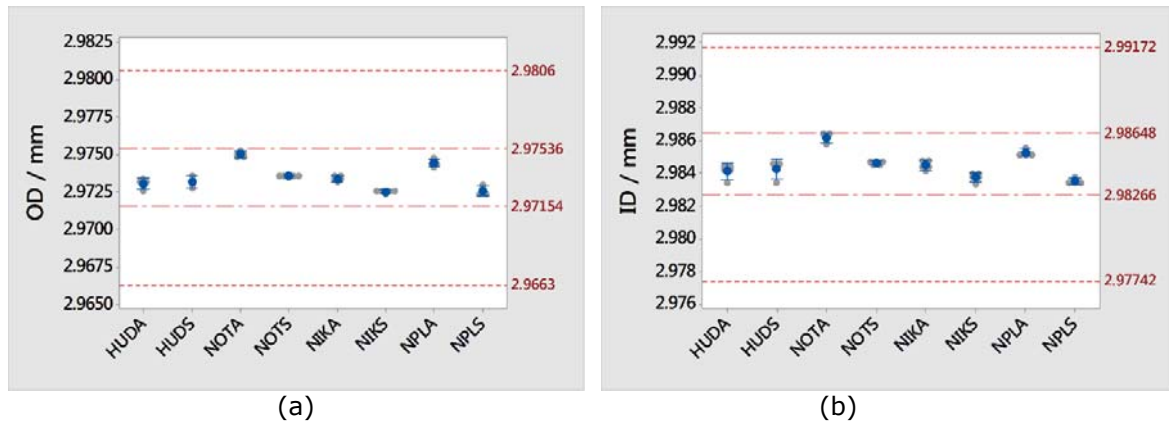


Figure 4-16: MCT225 dimensional artefact reconstruction. (a) topside, (b) underside. Cone beam artefacts are visible on the underside.

The standard dimensional analysis reported here included generating dimensional data from the complete OD and ID cylinders extracted from the STL files. The analysis was repeated using approximately 80% of the cylinder areas—removing the local upper and lower horizontal areas with cone beam artefacts. The process of surface determination and scaling correction was then performed. The results for all area (A) and selected area (S) for the OD and ID are shown in Table 27 and Figure 4-17:. Cone beam artefacts were not present on the planar surfaces used for calculation of the Length dimension. There was a small difference in final values. However, the OD and ID measurements after correction (including the non-metrology XT H 225) were still within the MPE of the MCT225 and, additionally, within the MPE of the Zeiss CMM.

Table 27: Dimensions using all areas and selected areas.

LAB	OD / mm			ID / mm		
	All area (A)	Selected (S)	Delta / mm	All area (A)	Selected (S)	Delta / mm
HUD	2.9729	2.9731	-0.0001	2.9842	2.984286	-0.0001
NOT	2.9750	2.9735	0.0015	2.9862	2.984649	0.0015
NIK	2.9734	2.9725	0.0008	2.9845	2.983689	0.0008
NPL	2.9743	2.9725	0.0019	2.9854	2.983595	0.0018

**Figure 4-17: Charts of cylinder dimensions (a) OD, (b) ID. All cylinder area (A) and selected cylinder area (S) analysed.**

The dimensional artefact was positioned horizontally within the fixture to avoid overlap between the dimensional artefact and the AM artefact surface while allowing maximum magnification of the AM artefact. If the artefact was angled significantly then either the artefacts would overlap during some projections or the magnification would have to be reduced to include all required areas of both artefacts. Redesign of the fixture for CT-STARR Stage 2 will be considered to reduce the cone beam artefact effect.

4.7.5 Conclusions

The results from a four-participant interlaboratory comparison investigating the extraction of ISO 25178-2 areal surface texture data from X-ray CT has been reported. The results show the robustness of the extraction and analysis process reported in Chapter 3. The results confirm the validity of using CT for the extraction of surface texture data from additively manufactured parts, for example the value of mean surface roughness, S_a for all metrology CTs was within 0.5% of the results obtained using the focus variation instrument. There was

good repeatability and reproducibility of all measurement results. The baseline results indicate the process is in control and provide a good knowledge grounding for and expanded Stage 2 CT-STARR interlaboratory comparison. A reference dimensional artefact, manufactured from a similar material to the AM artefact, was included in all scans. Surface determination and scaling correction resulted in dimensional numbers very similar to reference CMM measurements. For example, the artefact errors for the XT H 225 commercial CT for Length, OD and ID reduced from -0.27%, -0.83% and -0.54%, respectively, to all < 0.02%. Using a dimensional artefact during the CT measurement of AM surfaces provides good process validation and should be invaluable during CT-STARR Stage 2. Future work will include generation of algorithms to correct the extracted surface texture data based on the dimensional artefact surface determination and global scaling results. One change to be made as result of the CT-STARR Stage 1 measurements is to redesign the artefact fixture to avoid horizontal edges on the dimensional artefact to minimise cone beam artefacts. During the work performed here, factors effecting the accuracy of the results were discussed such as surface determination and measurement voxel size. Further investigation of the impact of these and other factors on measurement accuracy will be reported in Chapter 5. This is important for creating a recommended measurement and analysis envelope within which to work for optimised results.

Chapter 5 Factors affecting the accuracy of CT surface measurements

“Fast is fine, but accuracy is everything.”

Wyatt Earp (1848-1929)

A published journal paper, first author A. Townsend, underpins the work reported here, “Factors affecting the accuracy of areal surface texture data extraction from X-ray CT” [24]. The journal paper is included in Appendix 6.

This section reports on an investigation into CT measurement and data processing factors that may have an effect on the accuracy of the extracted surface texture results. The factors have been chosen for their widespread applicability to CT systems in general rather than being CT machine-specific. Changes in surface texture and dimensional results pre and post filament change have already been discussed in Chapter 3. Surface determination correction was discussed in Chapter 3 and evaluated in Chapter 4. The potential effect of voxel size on the accuracy of the extracted surface data was introduced in Chapter 4. Partially as a result of the potential effects noted in this preceding work, this chapter reports on an investigation into three factors with potential to affect the accuracy and repeatability of extracted AM surface texture data from CT measurements.

This chapter is divided into three sections:

- CT surface determination
- Component magnification and voxel size
- Internal / external surfaces

5.1 CT surface determination

Surface determination is the process of defining the location of the surface of a component scanned using CT. This process is based on evaluation of the grey-scale (density) values of the reconstructed voxels. The surface defines the boundary between the component material and the background (usually air). The method employed to define this surface boundary has been shown to have a significant effect on dimensional information extracted from CT scans [125, 141]. The CT user has to make a non-intuitive choice of surface determination method during the data extraction process. This section reports on the effects of this method choice on the extracted surface texture data. This section reports on the application of four surface determination methods to generate the surface from metal Rubert surface comparator plates [142]. Rubert roughness comparison specimens are primarily used in industry for workshop use. Rubert plates are used to evaluate the surfaces of workpieces using visual and tactile (fingernail) comparison. The manufacturing technique of the Rubert plate is chosen to match the match the manufacturing technique of the workpiece being checked, for example turned, ground or cast. Rubert plate sections were chosen for the surface determination analysis because they include sections manufactured with the same technique, but with different roughness values, see Figure 5-1.



Figure 5-1: Microsurf Rubert 335 (casting) comparator plate. Showing similar surface configuration on each of the seven segments, but with different mean roughness values.

The CT settings for all measurements were identical. The extracted surfaces were processed per the multi-stage process as presented in Chapter 3.

5.1.1 Surface plates

Two rectangular plates, approximately 10 mm x 20 mm, were cut from a Rubert Microsurf 334 (casting) test panel. The casting panel was used as this surface was considered to most closely represent the surface of a PBF metal AM component. The nominal surface R_a values for the plates used for this work were 50 μm and 25 μm as these approximate the as-built PBF metal AM surface roughness [131]. The individual samples were imaged using the Nikon XT H 225 industrial CT machine. Acceleration voltage was 190 kV, filament current was 53 μA , with an acquisition time of 4000 ms. A 1 mm copper filter was used to reduce contrast and beam hardening. Auto-defocus was deactivated. The voxel size for all measurements was 12.9 μm (x,y,z).

5.1.2 Surface determination methods

CT surface determination was performed using four methods: three global methods and one local method. Global methods compute one single grey-scale value to define the surface across the entire extracted volume. Local surface determination evaluates local grey-scale change gradient and creates the surface at the location of highest local gradient.

The four surface determination methods evaluated were:

Manual surface determination, whereby the global surface determination was set by the user by visually optimizing the surface location; that is, looking at a section of the volume material-to-background interface and adjusting the software "scroll bar" until the generated surface visually appears to be at the location of highest grey-scale gradient. Implemented in VGStudio MAX 2.2.

ISO 50 surface determination. The ISO 50 method defines a global threshold which is computed as the mean of two peaks (background and material) of the grey value histogram. ISO 50 was also implemented in VGStudio MAX 2.2.

Otsu method surface determination. The Otsu method [143], also a global surface determination method, was implemented in Insight Segmentation and Registration Toolkit (ITK) software [144]. Otsu surface determination finds two clusters (material and background) in the grey value histogram such that the sum of the within-class variances of the material and background are minimised. Used extensively in image processing, this method works most effectively when the data is generally bi-modal (containing two distinct classes) such as is the case for two-material CT data sets.

Local iterative surface determination. Implemented in VGStudio Max 2.2, the local surface determination performs surface determination based on the local surface grey values. An initial baseline grey value is selected based on the material and background (in this case Rubert plate and air). The iterative surface determination searches within a specified distance (in this case four voxels) from this initial distance and calculates the final surface based on the location of the greatest grey-scale gradient [145].

A section of the surface boundary, created using ISO 50 and local iterative surface determination, are shown in Figure 5-2:. The location of the generated surface (white line) is clearly different using the two processes.

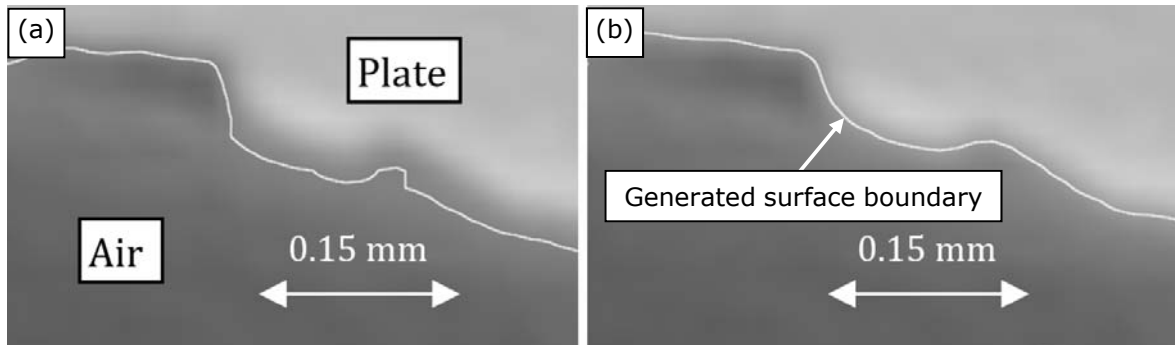


Figure 5-2: Rubert 50 plate surface determination (VGStudio MAX 2.2 [136]). (a) ISO 50 surface determination (b) local iterative surface determination. Modified from [24].

After surface determination was completed using the four surface determination methods the Rubert surfaces were converted to PLY format in VGStudio MAX 2.2 using the “Super Precise” setting.

5.1.3 CT-focus variation comparison

The results from the CT scans were compared to the same section of the plate measured on the Alicona G4. The Alicona measurements were performed using a x5 objective lens. Lateral sampling distance was 5 μm with a lateral resolution of 15 μm . Surface extraction and processing was performed as described in Chapter 3. Four sample areas, each 5 mm x 5 mm, were extracted from each of the 25 μm and 50 μm R_a samples. The measurements were then levelled and filtered with an L-filter nesting index of 5 mm and an S-filter nesting index of 0.020 mm. A surface texture parameter set per ISO 25178-2 was generated using SurfStand software [138].

5.1.4 Analysis of results

Figure 5-3: shows the false colour height maps of one surface area of the nominal 50 μm R_a Rubert sample as measured on the Alicona G4 and on the XT H 225. Table 28 shows the mean value of the parameters generated from the Alicona G4 measurements. A paired t-test was performed for each of the Rubert sections. A paired t-test is used to compare the means of

two populations where there are two samples in which observations in one sample can be paired with observations in the second sample. The null hypothesis was that the difference between the mean parameter as measured on the CT and on the Alicona G4 would be zero. The 95% confidence interval of the mean was generated for each of the samples. The percentage difference between the mean Alicona and CT readings, together with the 95% confidence interval for the nominal 50 μm Rubert sample, were plotted for each of the ISO 25178-2 parameters Sq , Sz , Sal and Sa , see Figure 5-4:. The absolute differences between the CT and FV results for the parameters Ssk , Sku , Sdr and $Smr2$ are shown in Figure 5-5:. These parameters were chosen as they have been shown to be sensitive to AM surface characteristics, see Table 3.

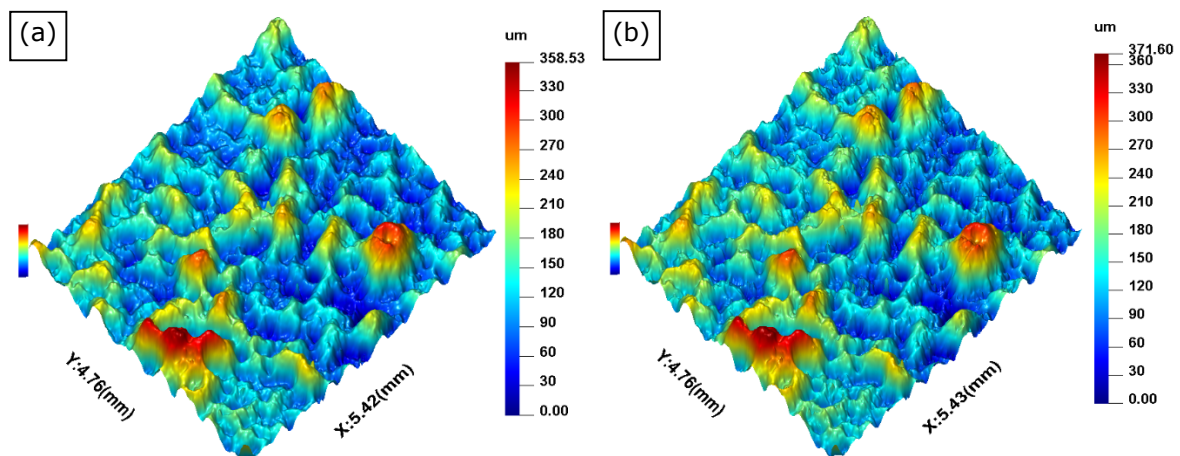


Figure 5-3: False colour height maps of the nominal Ra 50 μm Rubert sample. (a) Alicona G4, (b) Nikon XT H 225 CT. Iterative surface determination used in both cases.

Table 28 Mean values of Alicona measurements of nominal Ra 50 μm Rubert sample

Parameter (ISO 25178-2)	Alicona mean value
Sq	69.1 μm
Sz	507 μm
Sal	0.36 mm
Sa	50.9 μm
Ssk	1.3
Sku	6.0
Sdr	22.6%
$Smr2$	93.2%

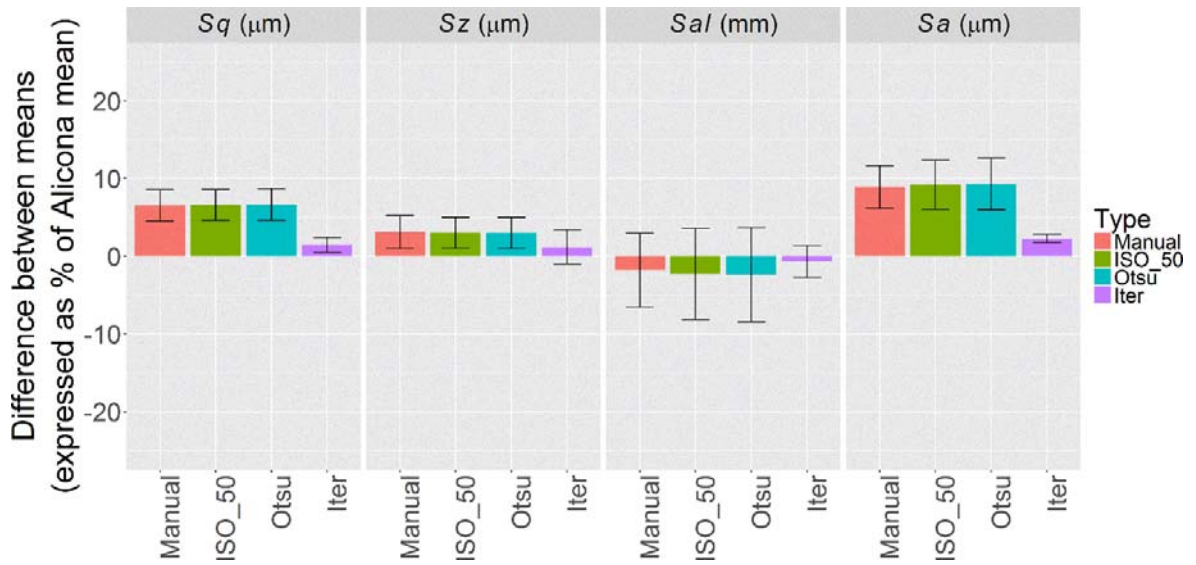


Figure 5-4: Percentage difference, CT to FV of nominal 50 μm Ra Rubert sample.

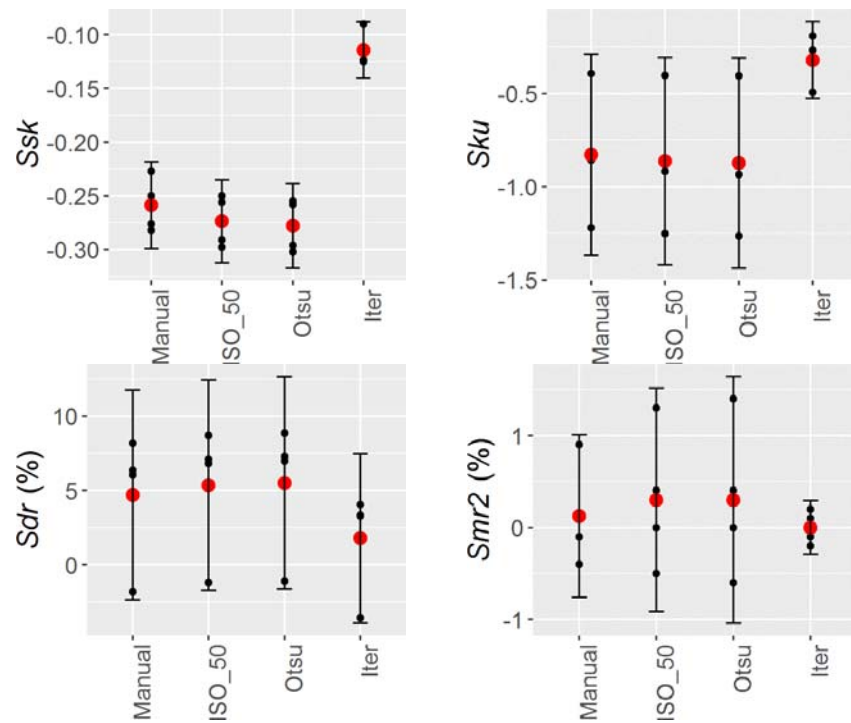


Figure 5-5: Absolute difference, CT to FV of nominal 50 μm Ra Rubert sample.

Figure 5-6: shows the false colour height maps of one surface area of the nominal 25 μm Ra Rubert sample as measured on the Alicona G4 and on the XT H 225. Table 29 shows the mean value of the parameters generated from the Alicona G4 measurements.

The percentage difference between the mean Alicona and CT readings, together with the 95% confidence interval for the nominal 25 μm Rubert sample, were plotted for each of the ISO 25178-2 parameters Sq , Sz , Sal and Sa as shown in Figure 5-7:. The absolute differences between the CT and FV results for the parameters Ssk , Sku , Sdr and $Smr2$ are shown in Figure 5-8:.

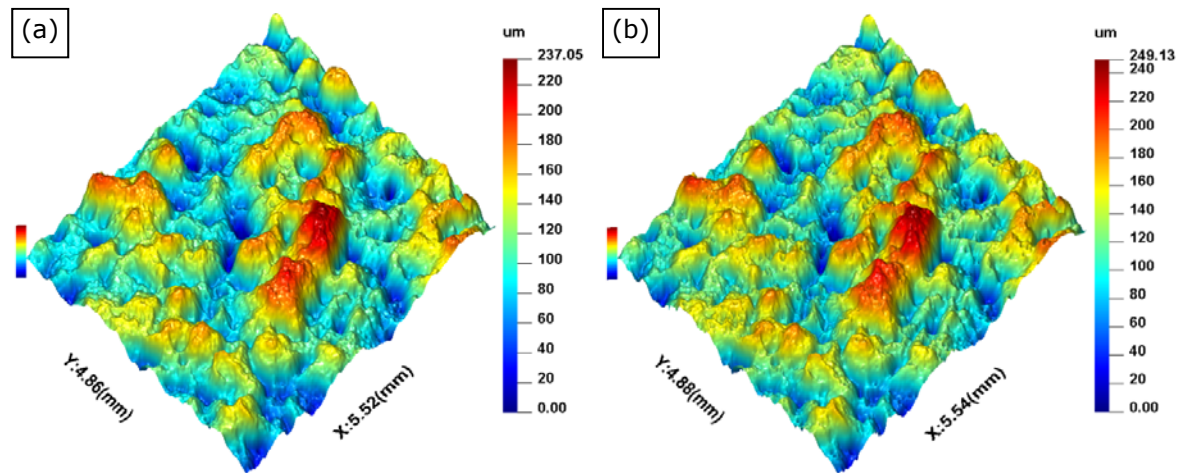


Figure 5-6: False colour height maps of the nominal Ra 25 μm Rubert sample. (a) Alicona G4, (b) Nikon XT H 225 CT. Iterative surface determination used in both cases.

Table 29: Mean values of Alicona measurements of nominal Ra 25 μm Rubert sample.

Parameter (ISO 25178-2)	Alicona mean value
Sq	34.5 μm
Sz	239 μm
Sal	0.37 mm
Sa	27.4 μm
Ssk	0.26
Sku	3.1
Sdr	4.8%
$Smr2$	91.4%

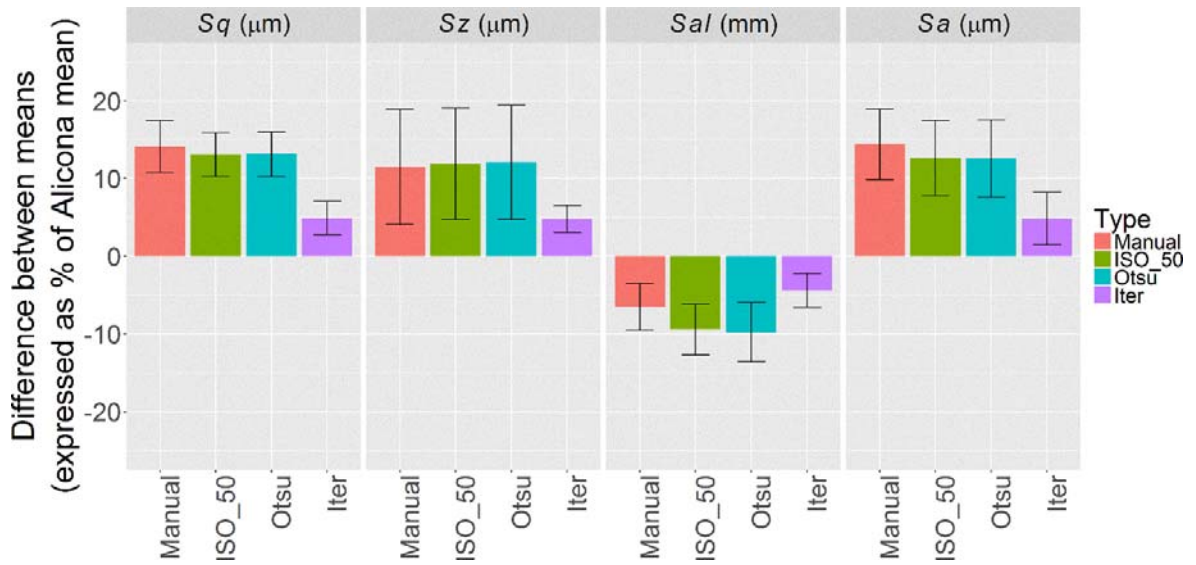


Figure 5-7: Percentage difference, CT to FV of nominal 25 μm Ra Rubert sample.

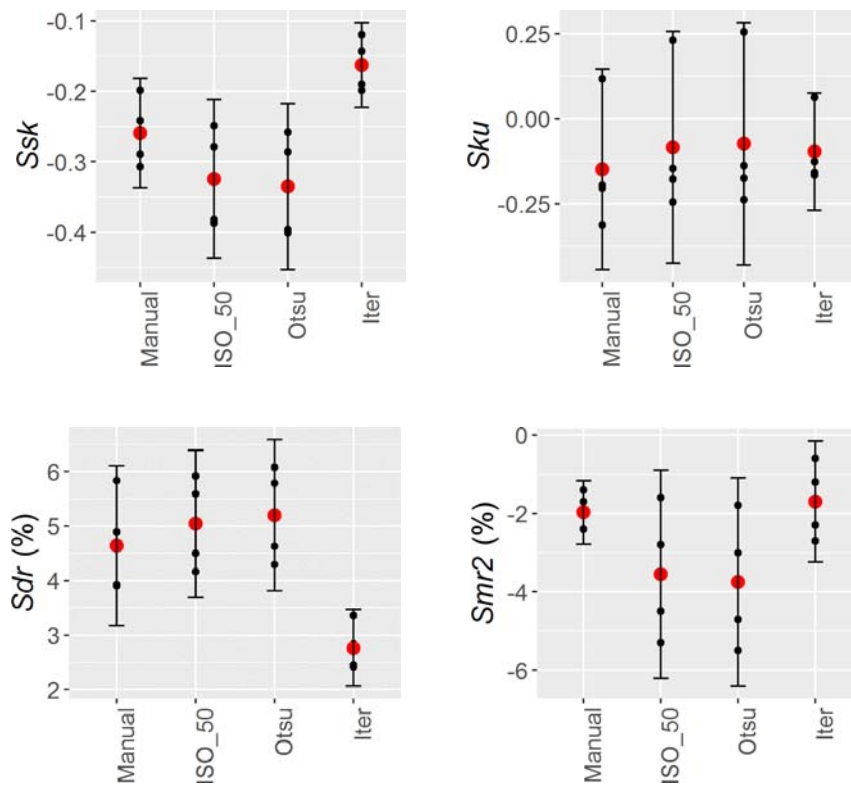


Figure 5-8: Absolute difference, CT to FV of nominal 25 μm Ra Rubert sample.

5.1.5 Surface determination conclusions

The parameter values generated from the three global surface determination methods were generally similar. In some instances it can be seen that the manual surface determination has slightly better parameter estimation than the automatic global methods. Comparing the local with the global surface determination methods for both the 50 μm *Ra* and 25 μm *Ra* plates it can be seen that the local iterative method achieves results significantly closer to those obtained using the Alicona G4 in all cases. Local iterative surface determination has been used for all the analyses performed elsewhere in this report; however, it has been shown in Chapter 4 that, although the results are generally good, correcting for surface determination does improve the dimensional accuracy of the measured component. Future work will include generating correction algorithms for extracted surface texture data.

5.2 Component magnification and voxel size

An investigation into the effect of voxel size on the extracted ISO 25178-2 parameters was performed using two AM surface artefacts. The first sample was the AlSi10Mg SLM AM component and fixture used for the measurement and analysis in Chapter 3. The second sample was the Ti6Al4V ELI EBM AM component and the fixture was the same as used in the interlaboratory comparison in Chapter 4. In both cases the same surface as evaluated previously was measured during this work. Both samples were measured on the Huddersfield XT H 225 CT. The measurement settings for each artefact were the same as the settings reported previously. The measurement settings were also the same for all ten measurements in each set. The initial position (and therefore voxel size) for this evaluation, was similar to that used in the previous chapters (17.3 μm). After the first scan at this voxel size, the component was positioned further away from the X-ray source to increase voxel size and reduce magnification.

Sample measurements were taken at ten positions within the chamber with the voxel size at each position, V_n , in μm , defined by:

$$V_n = 16 + n^{(x+(ny))} \quad \text{Equation 5}$$

Where:

$$1 \leq n \leq 10$$

$$x = 1.4, y = 0.065$$

The values of x and y were chosen to give a non-linear distribution with more information points near the initial "ideal", maximum resolution, position and ten measurement positions within the range of CT travel limits. The initial position was configured in the previous work to be as close as possible to the X-ray "gun" to give the correct surface size per ISO 25178-3 with extra material for cropping. Positioning the sample closer to the X-ray "gun" than this initial position would result in part of the AM component projected outside the range of the detector, resulting in an incomplete image data set. The surface data were extracted and filtered using the same filtering employed for the other measurements: 8 mm L-filter nesting index and 0.025 mm S-filter nesting index. The value of Sa for both samples, together with the respective mean Alicona G4 measurements, are shown in Figure 5-9:. It can be seen that the general trend is that the mean roughness, Sa , decreases as the voxel size increases. This trend is understandable as, at the limit, the square extracted triangular surface will contain only two triangles, and, once levelled, the Sa would be zero. It can be seen that the Sa values for the SLM surface are similar at the first two voxel sizes (17 and 19 μm), see Figure 5-10:.. This is an indication that the voxels size is sufficiently small to allow full characterisation of the surface within the scale-of-interest (defined by the applied filtering). At these measurement resolutions (17 and 19 μm) the value of Sa is approximately 2% less than the Alicona reference value. The SLM surface roughness is significantly greater than that of the titanium EBM surface: the Alicona mean Sa values are 30 μm and 25 μm , respectively. The

S_a value for the extracted EBM surface is not similar at the two initial measurement voxel sizes (17 and 19 μm): as the voxel size reduces the S_a value continues to increase. This indicates that at the minimum voxel size, the resolution may not be sufficient to fully characterise the surface at the required scale-of-interest. At the 17 μm voxel size measurement the value of S_a extracted from the titanium EBM sample was approximately 5.5% less than the Alcona reference measurement—a larger difference than that for the aluminium SLM component.

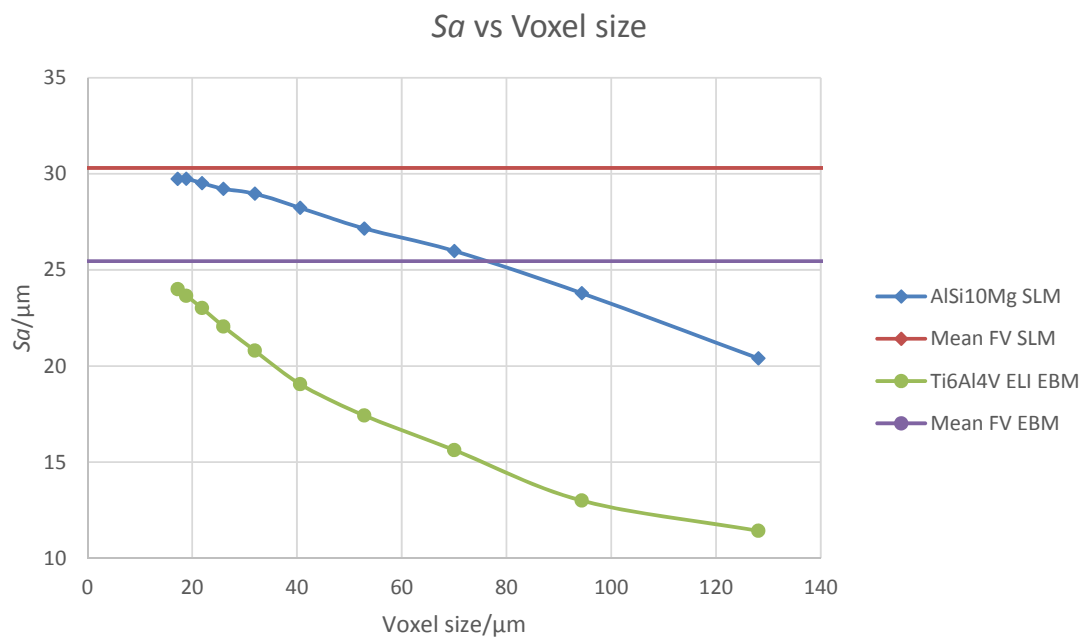


Figure 5-9: S_a values for the CT SLM and EBM sample measurements. Showing the focus variation values obtained for the same samples.

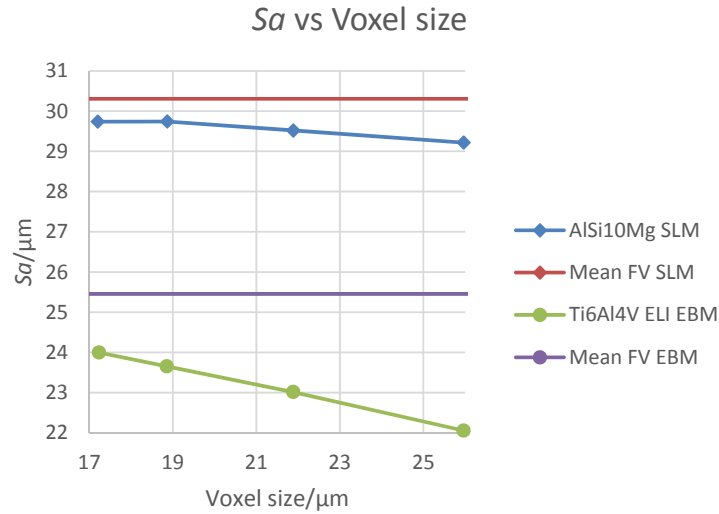


Figure 5-10: Detail of S_a vs voxel size, XT H 225 CT. From Figure 5-9.

5.2.1 Voxel size and magnification conclusions

At a voxel size of 17 μm , the rougher SLM surface appears to be fully characterised at the selected scale-of-interest, whereas the smoother EBM surface does not appear to be fully characterised. These results will provide a basis for further investigating of the maximum voxel size required for full characterisation for a range of AM surfaces together with investigations into other areas, such as the effect of scale-of-interest (and therefore filtering) changes. The EBM sample was used in Stage 1 of the interlaboratory comparison (Chapter 4). The results obtained here will provide vital information for possible changes for the Stage 2 comparison such as fixture modifications and AM sample selection.

5.3 Comparison of external and internal measurement results

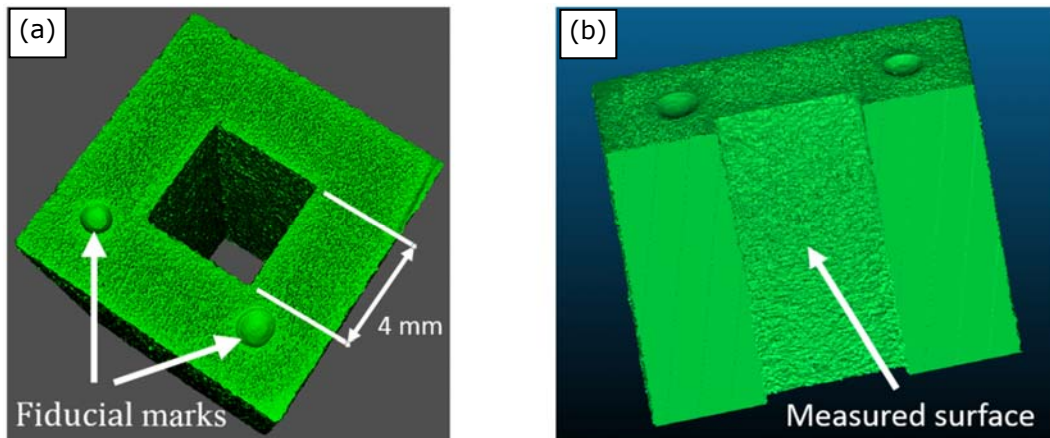


Figure 5-11: Ti6Al4V bar (a) scan of original part, (b) after physical sectioning. The part was milled to create an external surface from an internal surface. Modified from [24].

AM techniques now enable the manufacture of components with complex and critical internal features. For the advantages of both CT and AM to be realised, it is important to verify that the surface data from CT extracted from internal surfaces is no different to that extracted from identical external surfaces. This internal/external equivalency is important if, for example, a reference measurement is taken on an outside surface using a stylus or optical instrument and then compared to both external and internal surface data extracted from CT scans of the same component. The research in this section was performed to investigate whether a surface inside a component reconstructs and analyses differently from the same surface on the outside of the part. Reference measurements of the surface, such as focus variation that has been reported previously, are not reported here as the aim of this section is to evaluate the reconstructed surface of the internal features compared to external features when measured on a CT system and not to quantify the CT measurement deviations.

5.3.1 CT measurement

The measured component was an as-built 10 mm square section SLM titanium Ti6Al4V bar, 50 mm long with a 4 mm square internal bore. The bar was imaged using the Nikon XT H 225. The component was then physically sectioned such that the measured

“internal” surface now becoming “external”. The part was then scanned again on the CT, see Figure 5-11: . CT measurement settings were identical for both scans. The acceleration voltage was 210 kV, filament current was 48 μ A and the acquisition time was 4000 ms. A 1.0 mm copper filter was used. Auto-defocus was de-activated. The voxel size of both reconstructed volumes was 15.9 μ m (x,y,z). The surfaces were extracted using local iterative surface determination implemented in VGStudio MAX 2.2. Initial manual alignment of the surfaces from pre and post-sectioned scans was performed utilising the fiducial marks. Iterative closest point alignment was used for final alignment. After the alignment, each mesh was cut into four sub-samples each with a dimension of approximately 3 mm x 3 mm. A uniform re-sampling with a nominal resolution of 1.5 μ m was performed. This re-sampling resolution was set to be significantly less than the S-filter nesting index value to avoid any impact of the sampling on the filtered data. The samples were levelled and filtered using an L-filter nesting index of 2 mm and an S-filter nesting index of 0.005 mm. With a confidence level of 95%, the null hypothesis of equality of the means cannot be rejected for all the roughness parameters analysed. The charts of the percentage differences between the internal and external surface CT measurements for parameters Sq , Sz , Sal and Sa including the 95% confidence interval are shown in Figure 5-12:(a). The absolute values and 95% confidence interval of Ssk , Sku , Sdr and $Smr2$ are shown in Figure 5-12:(b-e). These results show there was insignificant difference between the same surface as an internal and as an external surface.

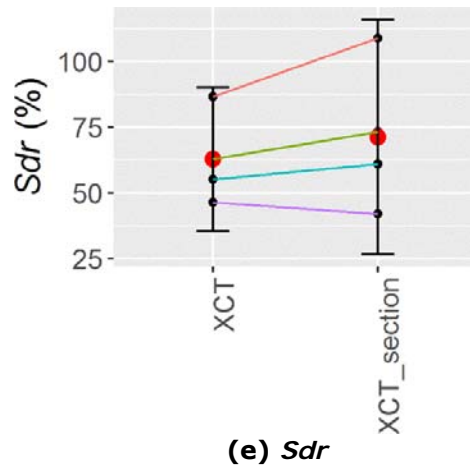
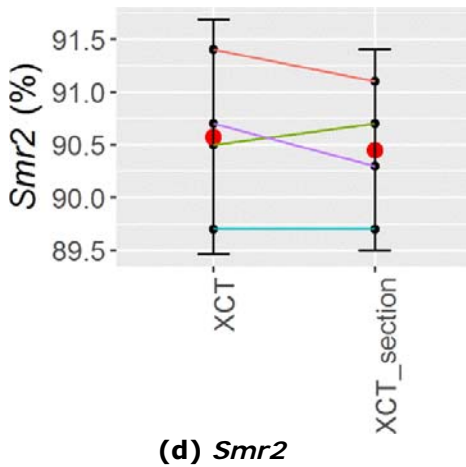
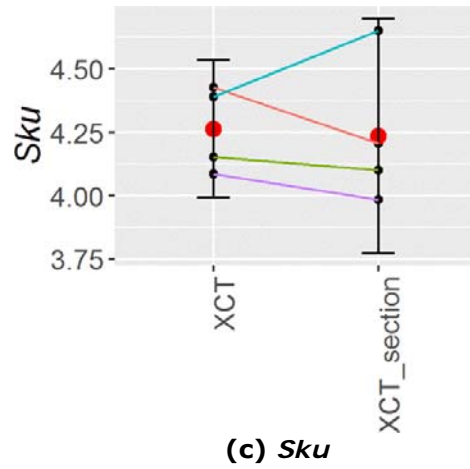
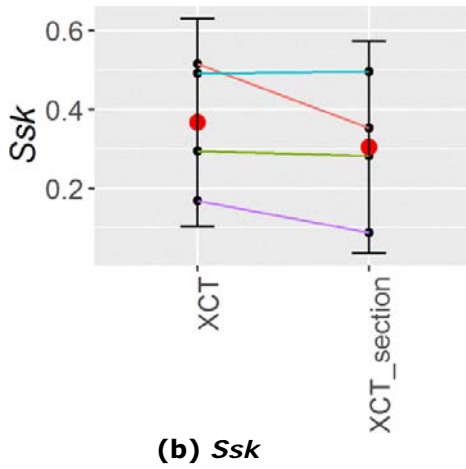
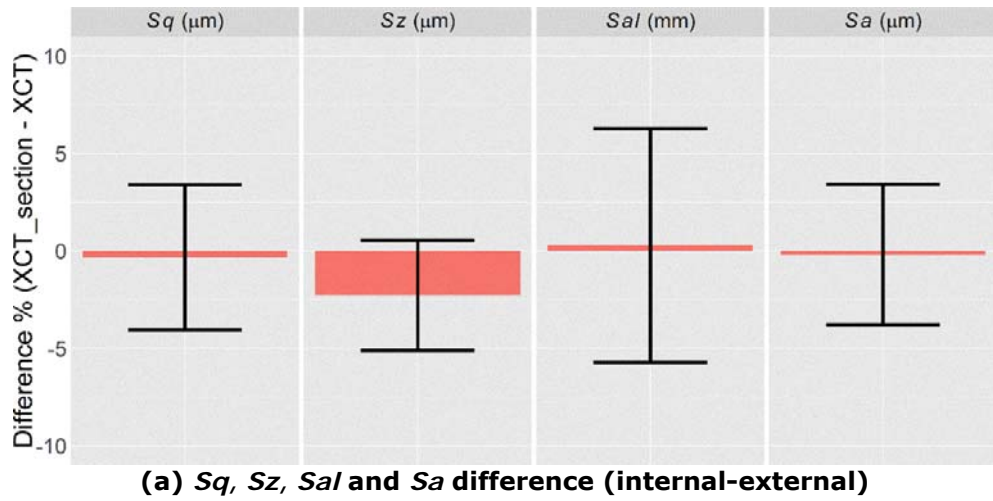


Figure 5-12: Internal and external measurements results. Showing differences between the same surface as an internal surface and external surface.

5.3.2 External/internal surface conclusions

The side surface of an as-built SLM Ti6Al4V component has been imaged using CT: first as an external surface and then, after physical sectioning, as an external surface. There was no significant difference in the extracted ISO 25178-2 parameters between the two measurements. This is important because reference measurements may be taken on the outside of a component to verify CT data. However, without part sectioning there is no way to verify internal measurements. If the CT internal measurements are equivalent to the CT external measurements then there is no need for additional comparison to reference internal measurements.

5.4 Section conclusions

The effect of changing the electron generation filament on the extracted surface texture parameter data was reported in Chapter 4. This chapter reported on three additional measurement and processing factors that may potentially affect the accuracy of extracted surface data. These parameters were chosen to be, as far as possible, applicable to most CT systems and AM surfaces and not machine-specific. The conclusions (including results from the filament change reported in Chapter 4) are as follows:

Changing the filament has been shown to change the surface roughness value (S_a) by approximately 0.8%. Depending upon application this may be significant. Performing a calibration or system verification may be necessary after filament changes.

The analysis of scanned Rubert comparator plates has shown that using local iterative surface determination during CT reconstruction will provide the most accurate results for surface texture parameter generation.

The voxel size affects the extracted parameter data. At larger voxel sizes the resolution may not be sufficient to allow full characterisation of the surface at the required scale of interest.

If the voxel size is too large to characterise the surface, further increases in voxel size will reduce the surface roughness value. The closest position the component can be located to the X-ray source is that which allows complete imaging of the required measurement area at all rotational angles. This position will not generally be at the highest possible magnification (and hence smallest voxel size). However, provided the voxel size produced is sufficiently small then the surface characterisation will not be limited by the measurement resolution. Initial results suggest that, for an AM surface, a voxel size of one half or less than the surface S_a value may be sufficient for full characterisation.

A comparison of areal parameters computed on the same surface section of a Ti6Al4V SLM part as an internal and external feature has been performed. The initial results indicate there is not a significant difference between the mean values of the generated parameters for the internal and external measurements.

These results provide valuable information to aid in the optimisation of the CT surface texture measurement and extraction process for research and industrial applications.

Chapter 6 CT measurement of re-entrant surfaces

“Each success only buys an admission ticket to a more difficult problem.”

Henry Kissinger (1923-)

The work reported here has been presented at conference: “*Measurement and characterisation of additively manufactured re-entrant features*” [146], joint special interest group meeting between euspen and ASPE, Dimensional accuracy and surface finish in additive manufacturing, KU Leuven, Belgium, October 2017. The conference paper is included in Appendix 7. The work reported here has been also accepted for conference: “*CT measurement of re-entrant additively manufactured surfaces*” [147], 8th conference on industrial computed tomography, Wels, Austria, February 2018. The conference paper is included in Appendix 8.

6.1 Introduction

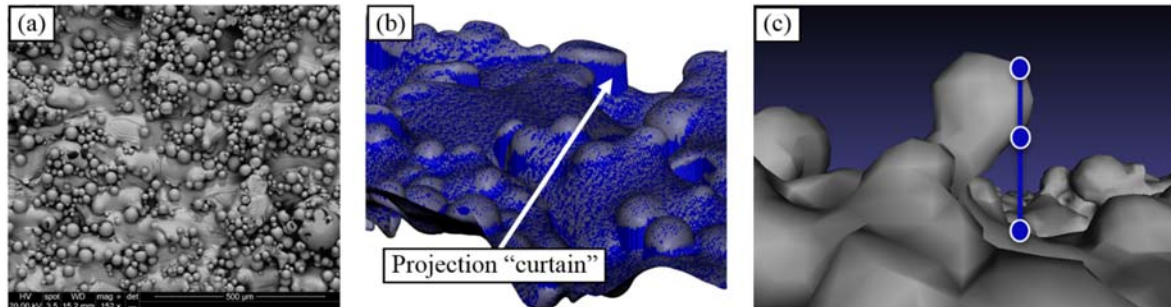


Figure 6-1: SLM re-entrant surface.

(a) Typical SLM side surface, (b) surface showing projection "curtains", (c) re-entrant surface showing three z positions at one (x,y) location.

SLM and EBM powder processes often produce surfaces with re-entrant (overhanging) surfaces, see Figure 6-1:(a). Re-entrant planar surface features are characterised by two or greater z height values for one (x,y) position, see Figure 6-1:(c). These non-intentional re-entrant features may, however, improve functional performance. The AM process itself presents opportunities to create re-entrant surfaces intentionally. The re-entrant features may be designed to improve the functionality of the component. Manufacturing components

including these re-entrant features will provide advantages based on two functional properties of such features. Firstly, re-entrant surfaces increase the specific area: that is, an increase in total surface area for a given planar area or part volume. Increasing the total surface area for a given planar area may have application in paint and coating adhesion, in battery or electrical capacitor design where surface contact between the gel or liquid electrolyte and the plates may be increased [148]. There may be applications in fluid flow and heat transfer where an increase in the surface contact area provides an increased volumetric efficiency [149]. Osseointegration bio-attachment, vital for the success of medical orthopaedic and dental implants, may also be enhanced by an increased surface area [150]. Medical applications may be functionally enhanced by the second functional property of re-entrant features: these features, by their nature, provide a mechanical locking function. Examples of this locking function include masonry keystones, dovetail joints used in woodworking and cabinetry and tooth preparation prior to the application of an amalgam filling. During preparation the dentist drills a pocket with a shelf or internally widening taper to prevent the filling from loosening or falling out. Additive processes allow the generation of similar undercut features at a scale matched to the component function.

These re-entrant surface features are difficult or impossible to measure using conventional line-of-sight methods, but measurement and characterisation of these surfaces may be vital for functional optimisation. This section reports on the measurement of re-entrant features using CT and the extraction of actual surface area information (including re-entrant features), from two as-built AM surfaces: a planar side surface from a medical implant and a section of a lattice structure with nominally cylindrical lattice bars. The medical implant was manufactured from Ti6Al4V ELI using an SLM process. The lattice structure was manufactured from Ti6Al4V ELI using an EBM process. Methodology for the extraction and analysis of the surface information is reported for both surfaces. The results of surface texture data including re-entrant features (mesh) is compared to generated projected grid data to illustrate errors

produced when re-entrant features are not included in the measurement and processing of the surface data. The applicability of parameters per ISO 25178-2 is discussed. A new surface texture parameter Sdr_{prime} is introduced. This parameter is intended to relate directly to the specific surface area and surface function. Sdr_{prime} is the percentage of additional surface contributed by the texture (including re-entrant features) compared to a plane the size of the measurement area. Parameter extraction will be demonstrated for the two AM surfaces and parameter data for a sample surface with designed re-entrant features will be discussed.

6.2 Methodology

The CT parameter settings for the two AM samples and the surface extraction process are discussed in section 6.2.1. The data processing and parameter extraction methods are reported in section 6.2.2.

6.2.1 CT measurements and surface extraction

The SLM medical implant and the EBM lattice were both scanned on the Nikon XT H 225 CT. Reconstruction was performed using Nikon CT Pro 3D. Surface determination was performed using VGStudio MAX 3.0. Local iterative surface determination was performed with a search distance of 4.0 voxels. Both surfaces were extracted using the VGStudio MAX 3.0 "Super Precise" setting. The XT H 225 settings for the SLM medical implant are shown in Table 30. The extracted surface is shown in Figure 6-2:.

Table 30: XT H 225 settings for the SLM medical implant scan.

Parameter	Value	Parameter	Value
Filter	1 mm Cu	Voxel size	7.1 μm
Acceleration voltage	160 kV	Detector size (pixels)	1008 x 1008
Filament current	62 μA	Number of projections	1583
Exposure time	2829 ms		

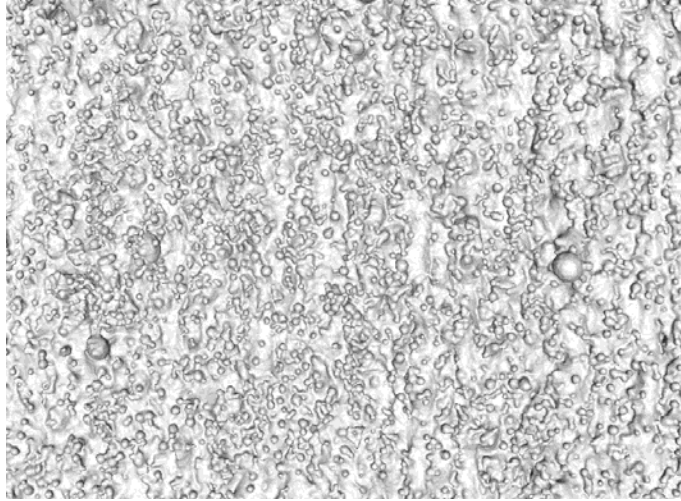


Figure 6-2: Extracted surface of the CT SLM planar surface measurement.

The CT settings for the lattice structure are shown in Table 31. The extracted lattice surface is shown in Figure 6-3:. The selected ROI is highlighted. The dimensions on all figures are in mm.

Table 31: XT H 225 settings for the EBM lattice structure scan.

Parameter	Value	Parameter	Value
Filter material	None	Voxel size	3.6 μm
Acceleration voltage	60 kV	Detector size (pixels)	1008 x 1008
Filament current	100 μA	No. of projections	1583
Exposure time	1000 ms		

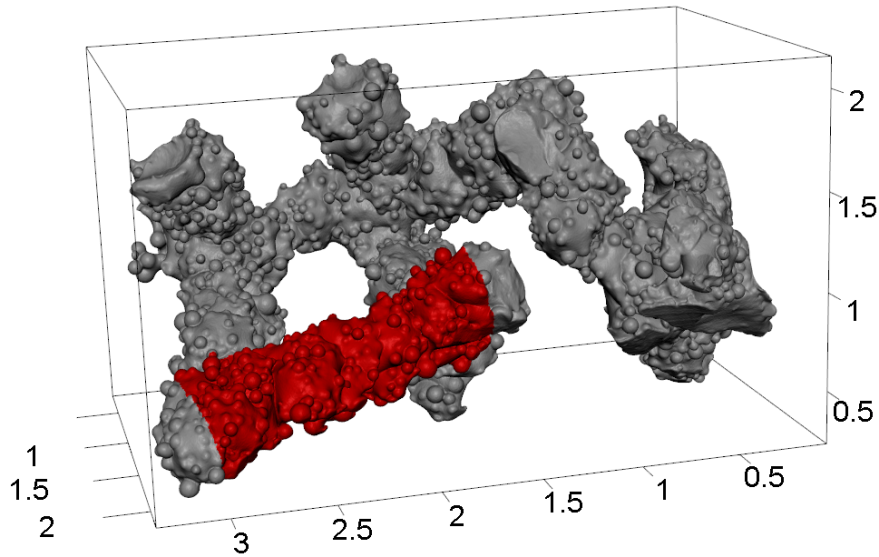


Figure 6-3: Extracted surface of CT scan of the EBM lattice showing ROI (mm).

6.2.2 Data processing and parameter generation

The complete extracted surface from the Ti6Al4V SLM ROI is shown in Figure 6-4:. A detail section of the extracted surface is shown in Figure 6-5:. The (blue) least-squares reference plane can be seen in both figures.

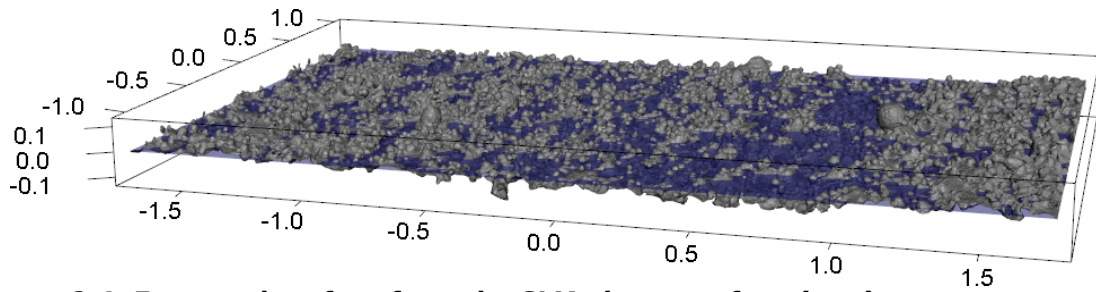


Figure 6-4: Extracted surface from the SLM planar surface (mm). Showing the blue least-squares reference plane.

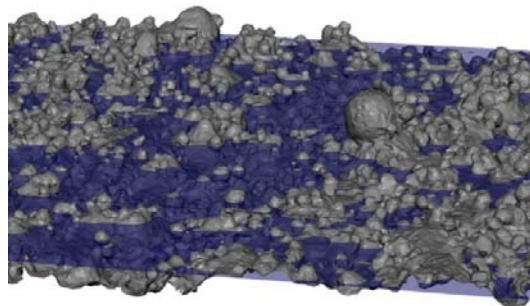


Figure 6-5: Detail of the SLM planar surface.

The extracted surface of the bar of the lattice structure is shown in Figure 6-6:. The cylinder was unwrapped prior to analysis.

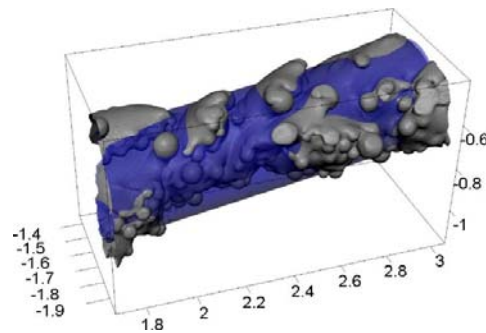


Figure 6-6: Extracted bar ROI from the CT lattice structure. Showing the blue reference plane (mm).

6.2.2.1 Projected (grid) data

The extracted surface data was projected onto a grid (therefore producing a height map of the surfaces). This height map data is then similar to the format and height values that would be produced by line-of-sight measurement instruments. The height map grid in this case may have only one value per matrix location. A section of the unwrapped lattice structure is shown in Figure 6-7:. The projection onto a grid produces an interpolated surface curtain where features are re-entrant (see Figure 6-1:(b) and Figure 6-7:). Surface area and volume data can be calculated from this projected data. However, the true surface area and volume data (i.e. including information from re-entrant features) cannot be generated from projected data, leading to errors. This projected data is similar to that generated from line-of-sight instruments, such as focus variation and stylus, and so is areal, not true 3D data.

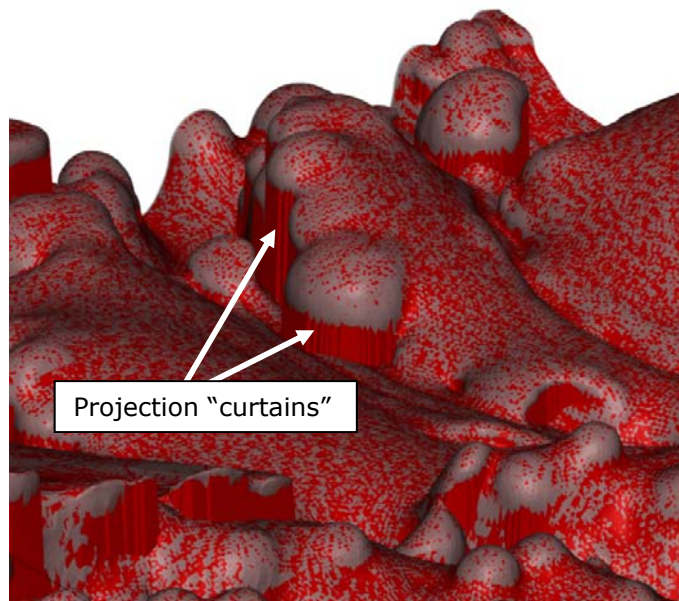


Figure 6-7: Section of unwrapped CT-measured lattice surface. Showing the projection curtains.

6.2.2.2 Comparison of projected and mesh data

The generated height map (grid) data for both samples (which includes no information about re-entrant surfaces) was compared to data generated from the mesh, which does include information about re-entrant surfaces. In both cases the primary (unfiltered) data was used.

6.2.2.2.1 Sdr_{prime}

The surface area of a solid object is a measure of the total area that the surface of that object occupies. Surface area may be considered proportional to the amount of paint needed to cover the surface. The actual surface may contain re-entrant features (undercut or recessed features). The ISO 25178-2 parameter Sdr , the developed interfacial area ratio of the scale-limited surface is the ratio of the increment of the interfacial area of the scale-limited surface within the definition area (A) over the definition area [16].

$$S_{dr} = \frac{1}{A} \left[\iint_A \left(\sqrt{1 + \left(\frac{\partial z(x,y)}{\partial x} \right)^2 + \left(\frac{\partial z(x,y)}{\partial y} \right)^2} - 1 \right) dx dy \right] \quad \text{Equation 6}$$

This is the percentage of additional surface area contributed by the texture as compared to an ideal plane the size of the measurement region [151]. The integration is performed over the area A , which is the (x,y) measurement plane, see Equation 6. This parameter is applicable to height map data and cannot be used to evaluate surfaces that contain re-entrant features. For generation of Sdr , mesh data has to be cleaned of re-entrant feature data, see section 3.1.3.1.5. This parameter may be considered a special case as it is only accurate for non re-entrant surfaces.

The surface characterisation parameter, Sdr_{prime} , proposed here has the ability to extract surface information from true 3D data (x,y,z) , including re-entrant features, such as that produced by CT scans. Sdr_{prime} is the percentage of additional surface (including re-entrant

features) contributed by the texture compared to the area of a plane the size of the measurement area. Sdr_{prime} is the difference between the total surface area (including re-entrant features) and an ideal plane the size of the measurement area A_{prime} , divided by the measurement area A_{prime} , see Equation 7.

Sdr_{prime} is calculated as:

$$Sdr_{\text{prime}} = \frac{1}{A_{\text{prime}}} \left(\iint_{D_S} \|\mathbf{r}_u(u,v) \times \mathbf{r}_v(u,v)\| \, dudv - A_{\text{prime}} \right) \quad \text{Equation 7}$$

A_{prime} is the projected area (equivalent to A in the equation for Sdr per ISO 25178-2).

$\iint_{D_S} \|\mathbf{r}_u(u,v) \times \mathbf{r}_v(u,v)\| \, dudv$, from [152], is the actual measured surface area, including re-entrant features, where $\mathbf{r}(u,v)$ is the measured surface, $\mathbf{r}_n(u,v)$ is the partial derivative in the n direction, D_S is the domain of the measured surface, $\|\bullet\|$ is the vector norm and \times is the cross-product of the two partial derivatives $\mathbf{r}_u(u,v)$ and $\mathbf{r}_v(u,v)$. Calculation of the total mesh surface is generally included in mesh analysis software, such as Meshlab [153]. The calculation is a sum of the individual mesh triangle surface areas.

Sdr_{prime} is sensitive to changes in re-entrant features and allows quantitative evaluation of these features, which relate directly to the two functional advantages of re-entrant features discussed in section 6.1. The ISO 25178-2 parameter does not have this ability as it is only applicable to height map data.

6.3 Results

6.3.1 Structured surface simulation

Two designed (but not manufactured) structured surfaces are presented to illustrate the differences in results obtained for the same surface using projected evaluation (grid) and true 3D evaluation (mesh). Figure 6-8: shows a CAD rendering of a square section “mushroom” designed to include re-entrant features. In this example each mushroom consists of a cap with dimensions 2 mm x 2 mm x 2 mm. The cap is attached to a square section stem with sides 1 mm and height 2 mm, giving a total height of 4 mm.

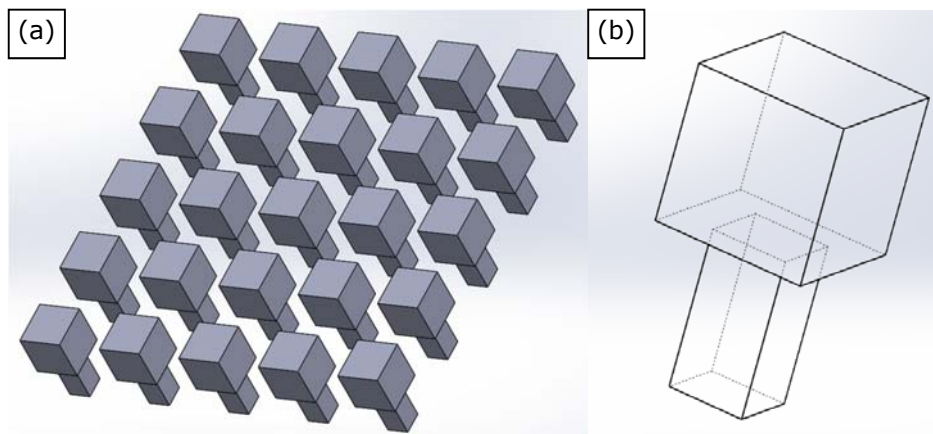


Figure 6-8: (a) Structured “mushroom” surface example, (b) “mushroom” detail”.

The plane area equivalent to the measurement area is 4 mm². This area is used to calculate Sdr_{prime} . The total feature surface area, including the base area directly below the mushroom, is 34 mm². The Sdr_{prime} mesh value would be $(34 - 4) / 4 \times 100 = 750\%$. If a grid projection were used for surface reconstruction the mushroom would be evaluated to be a block 2 x 2 x 4 mm³ (this includes interpolated side curtains). The feature surface area would be calculated as 36 mm², producing an Sdr_{prime} grid value of 800%. This result illustrates that the calculated surface when re-entrant features are included (34 mm²) may be less than the calculated surface when they are not included (36 mm²). Note: the Sdr_{prime} calculation applied to grid data (height values projected onto a plane) produces the same result as the

ISO 25178-2 parameter Sdr for the same grid data. The values for Sdr_{prime} for the mesh and grid are shown in Table 32.

Table 32 Single planar mushroom extracted parameters

Method	Sdr_{prime}
Mesh	750%
Grid	800%

The height vs volume curve is shown in Figure 6-9: and the material ratio curve is shown in Figure 6-10:.

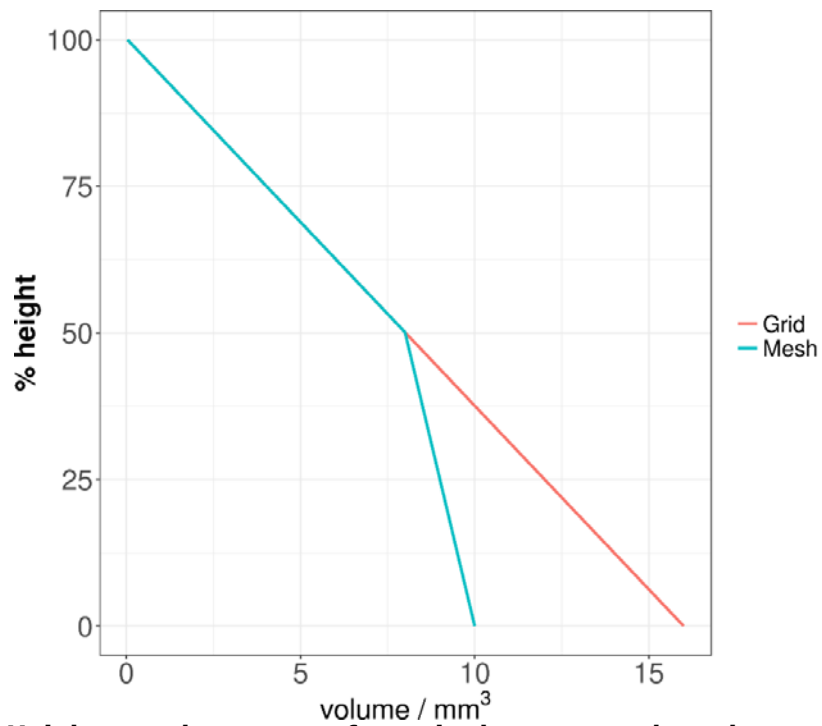


Figure 6-9: Height vs volume curve for a single structured mushroom.

The knee in the curve for the mesh is located at the 50% height, where the shape transitions from cap to stem. The grid projection produces a straight line as the transition is not measured. The calculated volumes for the entire feature (100% volume on the material ratio curve) are 10 mm³ for the mesh and 16 mm³ for the grid projection.

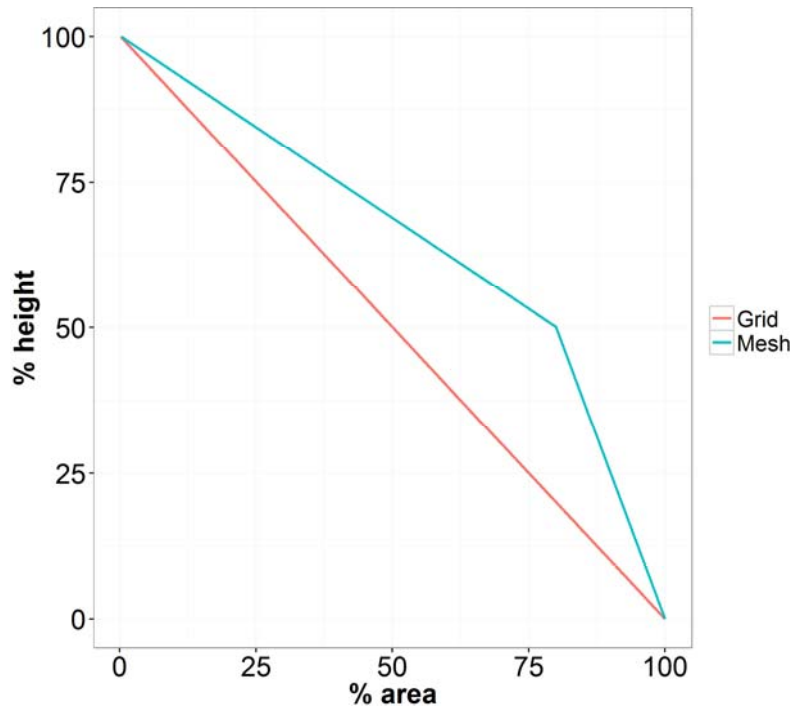


Figure 6-10: Material ratio curve for a single structured mushroom.

A second structured surface example is shown in Figure 6-11:(a). Each structure has a 4 mm diameter cap, 1 mm cap height, 1 mm diameter stem with a 4 mm stem height. The calculated values of Sdr_{prime} for a grid projection is 600%. The value of Sdr_{prime} for the mesh is 487.5%. The total surface areas are 75.4 mm² and 61.3 mm² respectively. The error, when re-entrant information is not considered, is 23%, see Figure 6-11:(b).

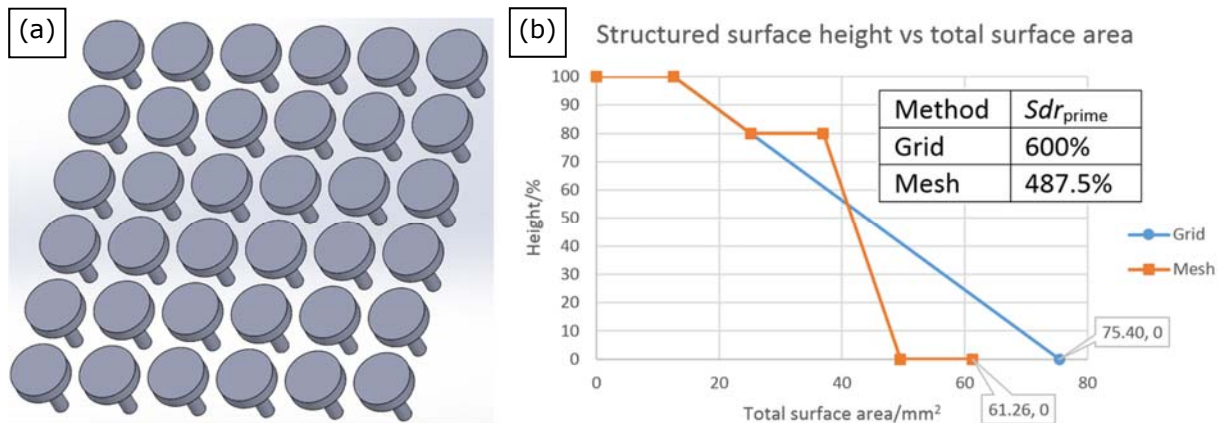


Figure 6-11: Round structured surface. (a) CAD rendering, (b) graph of percentage height down vs surface area.

6.3.2 AM surfaces

6.3.2.1 SLM planar surface

Table 33 shows the values of Sdr_{prime} for mesh and grid for the SLM planar surface.

Table 33: SLM planar surface texture Sdr_{prime} mesh and grid parameters.

Method	Sdr_{prime}
Mesh	79%
Grid	68%

The material ratio curve for the planar surface is shown in Figure 6-12:. The difference between the Sdr_{prime} grid and Sdr_{prime} mesh is -11%.

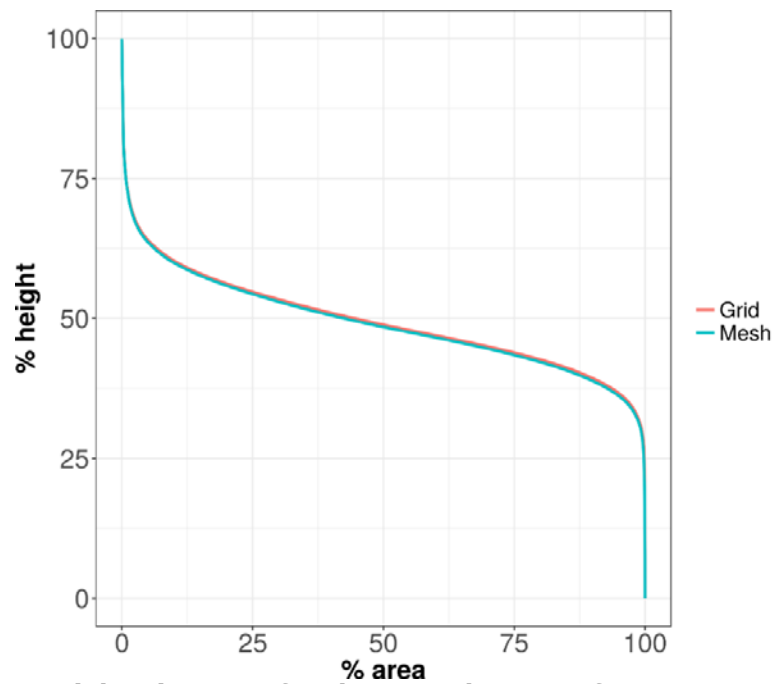


Figure 6-12: Material ratio curve for the SLM planar surface.

6.3.2.2 EBM lattice structure

Table 34 shows the values of Sdr_{prime} mesh and grid for the EBM lattice surface.

Table 34: EBM lattice surface texture Sdr_{prime} mesh and grid parameters.

Method	Sdr_{prime}
Mesh	55%
Grid	49%

The material ratio curve for the lattice structure is shown in Figure 6-13:. The difference between the Sdr_{prime} grid and Sdr_{prime} mesh is -6%.

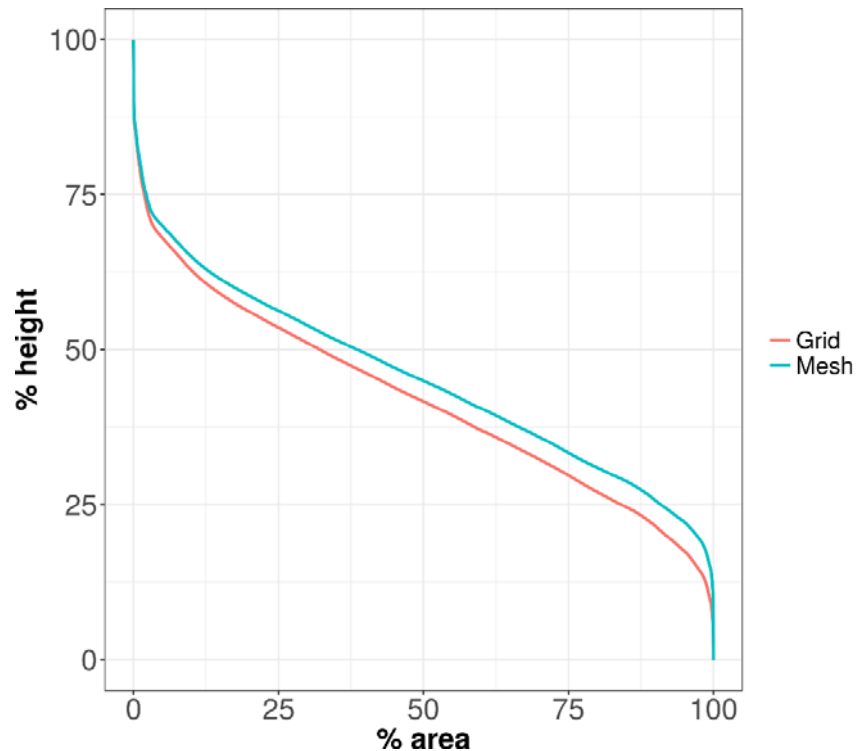


Figure 6-13: Material ratio curve for the EBM lattice.

6.4 Conclusions

AM processes provide the ability to produce complex freeform surfaces and re-entrant features that can enhance component functionality, for bio-attachments, battery design, heating and cooling systems, paint and coating adhesion. The ability to measure and characterise these surfaces accurately will be the key to performance optimisation. These surfaces present measurement and data analysis challenges that require the ability to image and extract meaningful data from complex point clouds or meshes rather than a uniform grid typically generated by line-of-sight instrumentation processes. A method for extraction of surface texture parameters from re-entrant AM surfaces has been demonstrated. CT measurements scans of two AM surfaces have been made which captured data for surfaces that would prove difficult or impossible to obtain using line-of-sight measurements. Actual

surface area and volume data has been extracted and compared to projected (grid) areas for these data. Two example generated structured surfaces have been discussed. A new parameter, Sdr_{prime} has been suggested. This parameter is the percentage of additional surface (including re-entrant surfaces) contributed by the texture as compared to a plane the size of the measurement area. This new parameter was developed to provide a direct relation to functional performance in applications where the actual surface area is important. There are significant errors in calculated area (up to 11% for Sdr_{prime}) when re-entrant features of as-built SLM and EBM AM components are not measured and included in analyses. Including re-entrant features, using the techniques presented here, will provide more accurate data required for analysis and optimisation of the functional performance of AM components.

Chapter 7 Surface-specific artefact design and build chamber characterisation

“Everything should be made as simple as possible, but not simpler.”

Albert Einstein (1879-1955)

“Better to be slapped with the truth than kissed with a lie.”

Russian proverb (n.d.)

The work reported here was presented at the 16th international conference on metrology and properties of engineering surfaces, Gothenburg, Sweden, June 2017.: “*Surface-specific additive manufacturing test artefacts*” [26]. The abstract is included in Appendix 9.

“We still don’t understand why a part comes out slightly differently on one machine than it does on another, or even on the same machine on a different day.”

Prabhjot Singh, Manager, GE Additive Manufacturing Lab (2011) [154].

7.1 Introduction

AM components are now being manufactured with the as-built surface as a functional part of the design, such as the medical implant design measured in Chapter 6—a design which is now in medical service. For these applications, it is vital that the component manufacturer understands the repeatability of their build chamber, together with any variation in component throughout the build chamber volume. AM surfaces are sensitive to process variation [15] and surface changes are being investigated as possible indicators of internal problems, such as porosity within the component. This section details the design, manufacture, measurement and characterisation of a set of surface specific test artefacts and bars produced to characterise a build chamber and highlight any inconsistencies across the chamber and between builds.

7.2 Methodology

A set of artefacts were built using an Arcam Q10 EBM system. The ARCAM Q10 was configured with the default settings (electron beam size, scan rate etc.) optimized by the manufacturer for the build material. The artefacts were manufactured from Ti6AL4V ELI. The nominal powder size was 45–100 μm . The build layer thickness was 50 μm . Four builds were performed. The powder in build 1 had been recycled from previous builds. Build 1 was the 15th build using the powder. Build 2 was the 16th build using the same powder. Builds 3 and 4, through manufacturing constraints, were not built using the same batch of material. Build 3 was the 1st build and build 4 was the 2nd build using the same batch of powder (but a different batch to builds 1 and 2). The measurement artefacts consisted of nine bars, see section 7.3; a series of surface-specific artefacts, designed by this author, see section 7.4; and hemi-sphere artefacts for evaluation of roughness variation at a variety of build angles, see section 7.5. Detailed methodology is included in each of these sections. The build layout is shown in Figure 7-1:.

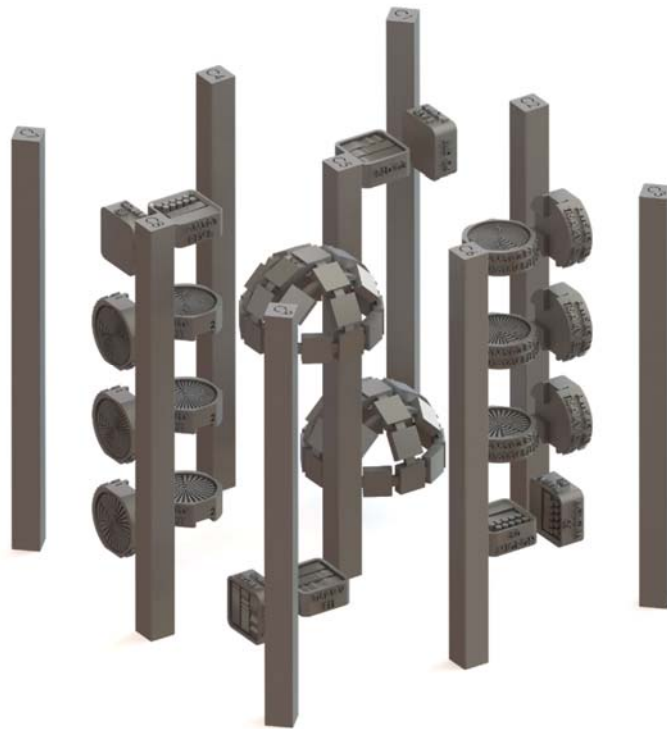


Figure 7-1: CAD rendering of the complete measurement artefact set.

7.3 Measurement bars

A series of nine square cross-section bars were built vertically in the build chamber, see Figure 7-2. The bars were 175 mm high with each side 11 mm. The corners of each bar was radiused to 0.5 mm. These bar dimensions were chosen to allow full-depth characterisation of the build chamber and permit the correct measurement area (8 mm x 8 mm) required per ISO 25178-3 based on the surface roughness. Each bar was marked on the top face with a letter corresponding to the batch and a number (1-9) corresponding to the location within the chamber.

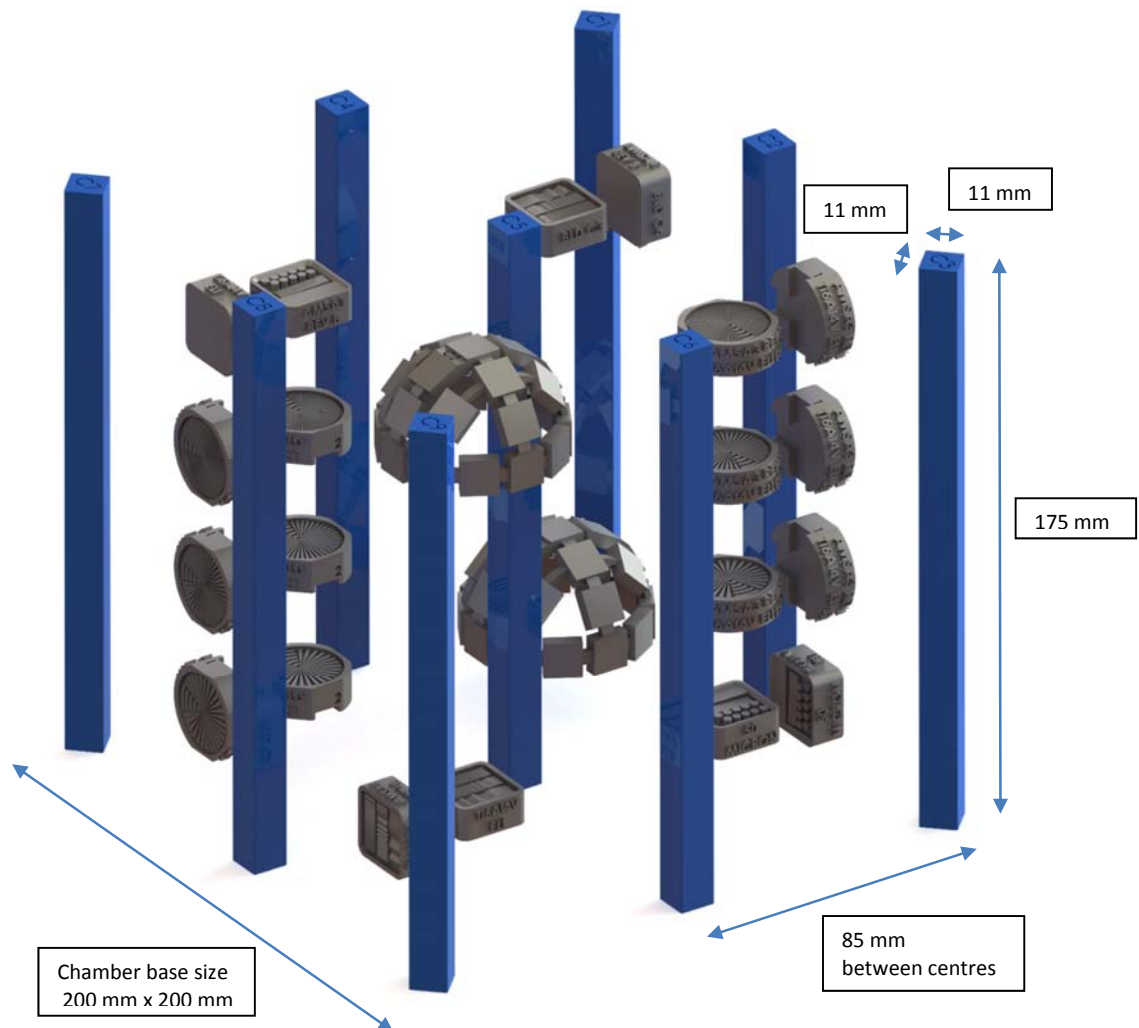


Figure 7-2: Artefact set showing build dimensions, with the nine bars highlighted.

7.3.1 Bar locations

The nine artefacts were positioned in a 3 x 3 grid pattern. The chamber internal plan dimensions were 200 mm x 200 mm. The bars were built 85 mm between centres (x,y). The pattern was centred in the middle of the chamber. The four outside corner bars were oriented with two sides perpendicular to a line drawn between the bar centre and the chamber centre. This configuration was chosen to be most sensitive to e-beam asymmetry as the beam shape on the build surface becomes more elliptical as the beam cone angle increases. The orientations of the numbered bars within the AM build chamber are shown in Figure 7-3:.

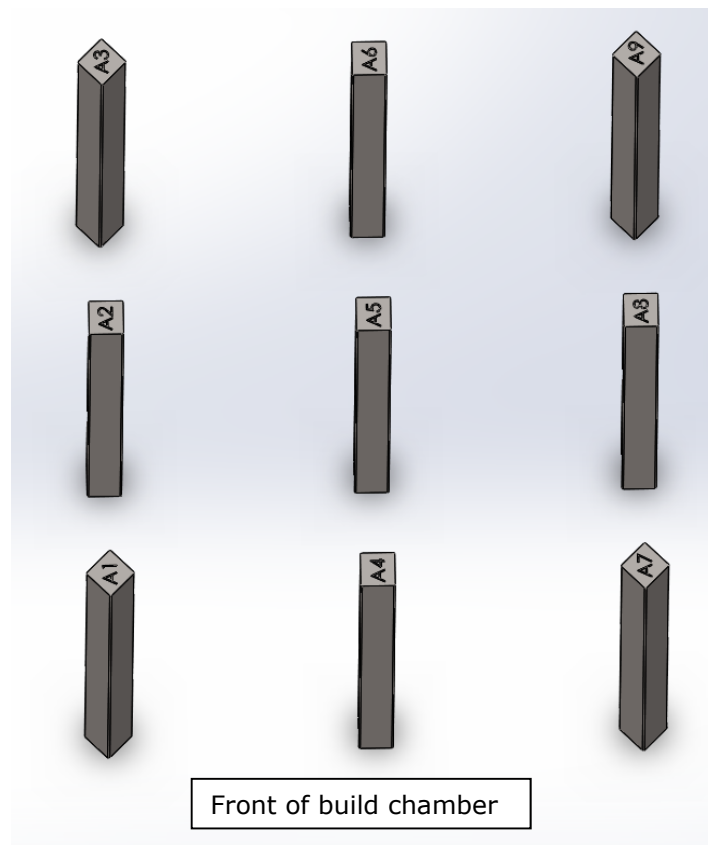


Figure 7-3: Orientation of the bars within the chamber. Showing the location reference numbers printed on the top of the bars.

7.3.2 Bar measurement

The bars were removed from the build plate and the surfaces of the bars were measured using an Alicona G4 focus variation instrument. The nine bars were arranged in a fixture bolted to the Alicona G4 stage. This fixturing provided precise and repeatable location of the bars, see Figure 7-4:. The first measurement area was centred 10 mm from the top face of each bar. Spacing between the four measurement areas along the bars was 51.7 mm on centre. Each bar was measured in four locations along each of the four faces for a total of 16 measurements per bar producing 144 measurements per batch of nine bars. A x5 objective lens was used on the Alicona G4. Each of the 144 measurement areas for each set of bars was 10.3 mm x 9.4 mm, created by automatically stitching 20 individual measurements consisting of five rows x four columns. This area was cropped to 8 mm x 8 mm during data processing, see 7.3.3. Each measurement was taken at a lateral sampling distance of 2.667 μm , lateral resolution of 8 μm and a vertical resolution of 3.5 μm . This measurement and subsequent characterisation was performed to obtain quantitative areal surface texture data per ISO 25178-2. Qualitative information from visual inspection of the bars was recorded.

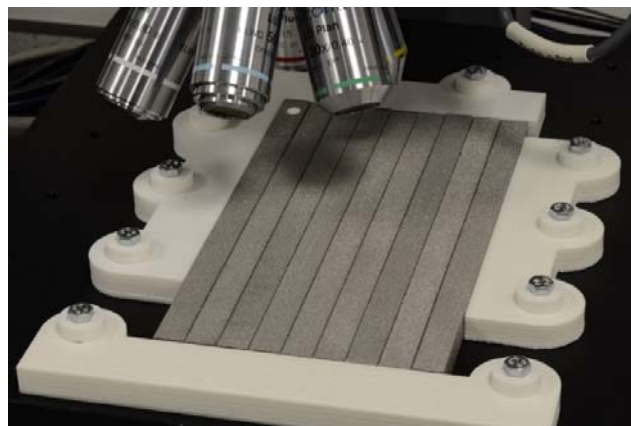


Figure 7-4: Nine bars from batch 1 mounted in the Alicona G4 measurement fixture.

The bars were arranged in numerical sequence in the fixture, as shown in Figure 7-5:. A script was written to take 18 measurements automatically, with the stage moving to the appropriate

position between measurements. The limitations of the Alicona stage movement (100 mm x 100 mm) required that the bars (as a batch, not individually) be repositioned by rotating 180° around the Alicona z axis and replaced in the fixture, so allowing measurement of the same face but at the opposite end of the bars.



Figure 7-5: Batch 1 bars arranged for the first surface measurements of side 1.

On completion of all measurements of one side of the bars, all bars (again, as a batch) were rotated 180° around the z axis and then each bar was individually rotated 90 degrees CCW, to allow measurement of the second side for all bars, see Figure 7-6: . The process was repeated until all 144 measurements had been taken. The measurement location on all four sides is shown in Figure 7-7: .



Figure 7-6: Batch 1 bars arranged for first surface measurements of side 2.

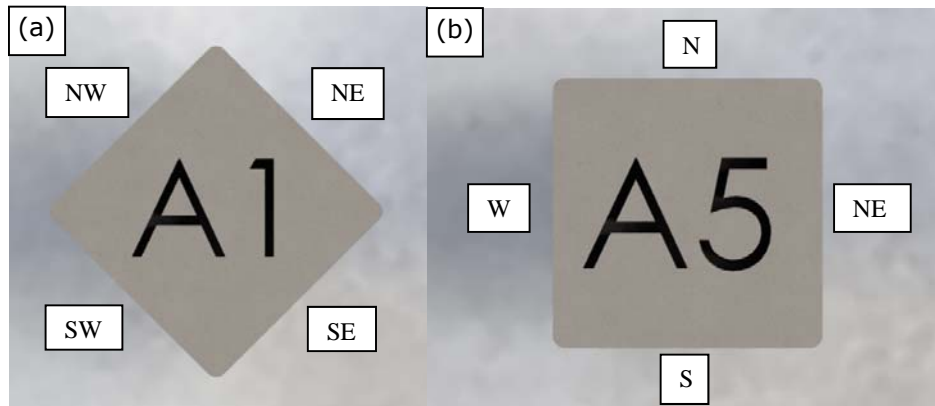


Figure 7-7: Locations of the four sides for (a) corner bars, (b) cross bars. Standard compass cardinal (N, E, S and W) and ordinal (NE, SE, SW and NW) are used for simplicity.

Figure 7-8: shows the bar locations and measurement sequence. The four height measurements along the bar originated at lower end, that is, closest to the build plate so measurement 1 was bar 1, on side NE.

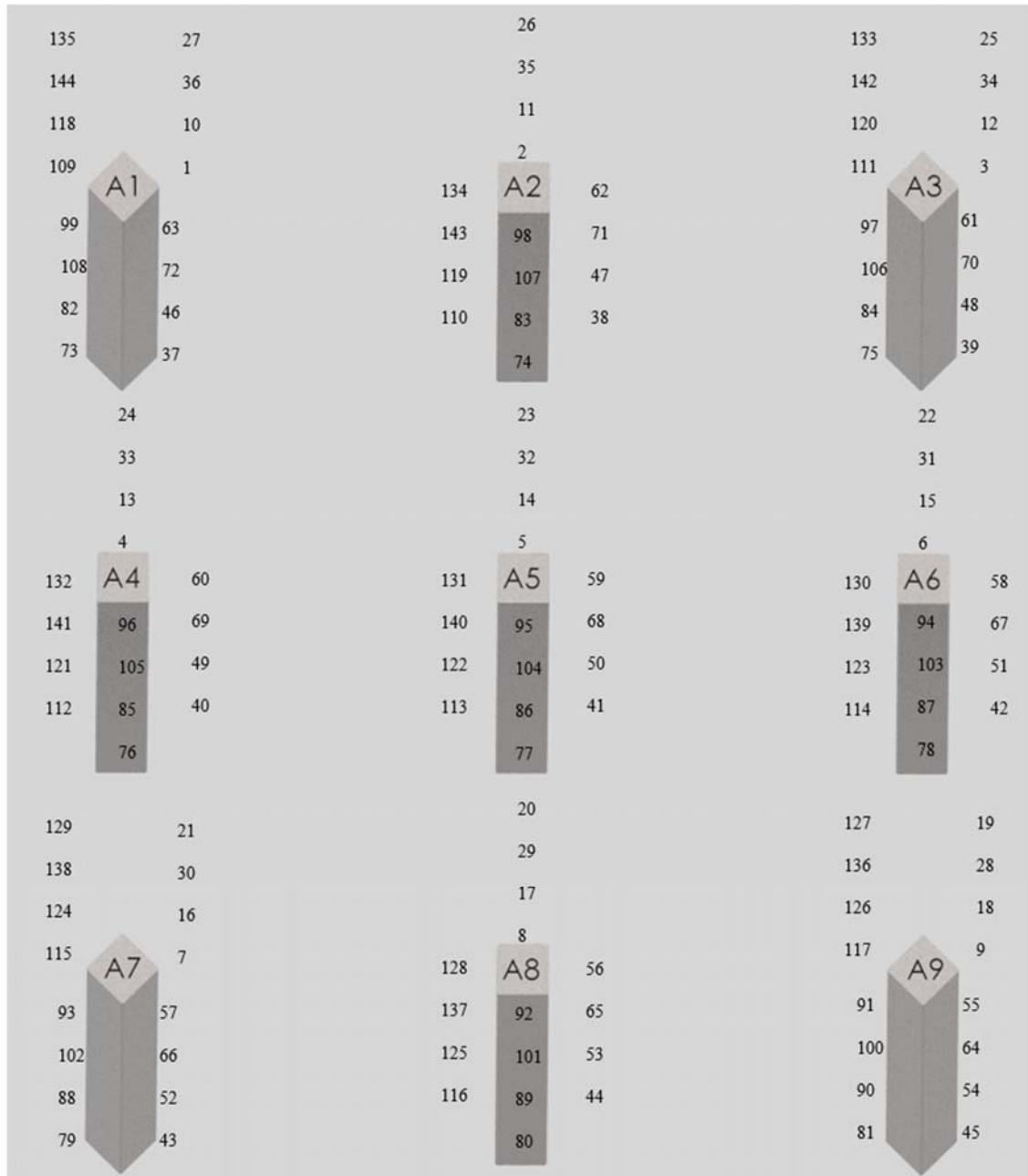


Figure 7-8: Measurement sequence of the nine bars.
The location of the numbers indicate the position and order of the measurements on the nine bar set. The location of the measurements for the non-visible surfaces are shown above the respective surfaces.

7.3.3 Data processing and analysis

The measurement areas required for analysis per ISO 25178-2 were 8 mm x 8 mm. Each of the 144 measurements was cropped to 8 mm x 8 mm, numbered per the measurement sequence and saved as a height map. Each measurement was levelled and Gaussian regression filtering was applied per ISO 25178-3. The high pass L-filter nesting index was set to 8 mm for all measurements. The low pass S-filter nesting index was set to 8 µm. The processing parameters are summarized in Table 35. All bar measurements were processed using these values.

**Table 35: Processing parameters per ISO 25178-3.
These are measurement area, L-filter nesting index and S-filter nesting index.**

Measurement area	L-filter nesting index	S-filter nesting index
8 mm x 8 mm	8 mm	0.008 mm

Parameter data per ISO 25178-2 were generated from the filtered data, numbered in accordance with the measurement sequence and saved as an Excel file. The ISO 25178-2 parameter S_a was chosen for detailed analysis and investigation of build relationships and patterns. In addition to the areal surface texture analysis, a visual inspection of the bars was performed and visual anomalies and surface inconsistencies were recorded.

7.3.4 Areal measurement results

The total number of measurements taken was 576. This was for four builds, nine bars per build, four sides per bar and four measurements per side. An analysis of variance (ANOVA) was performed using the data. The factors used were:

- Build number (1–4)
- Side (N, NE, E, SE, S, SW, W, NW)
- Height (1–4)
- Bar number (1–9)

Residual plots for S_a are shown in Figure 7-9: . The residual plot for S_a shows that the analysed data have good distribution with no significant influence of observation order and so is of acceptable quality for analysis. The main effects plot is shown in Figure 7-10: .

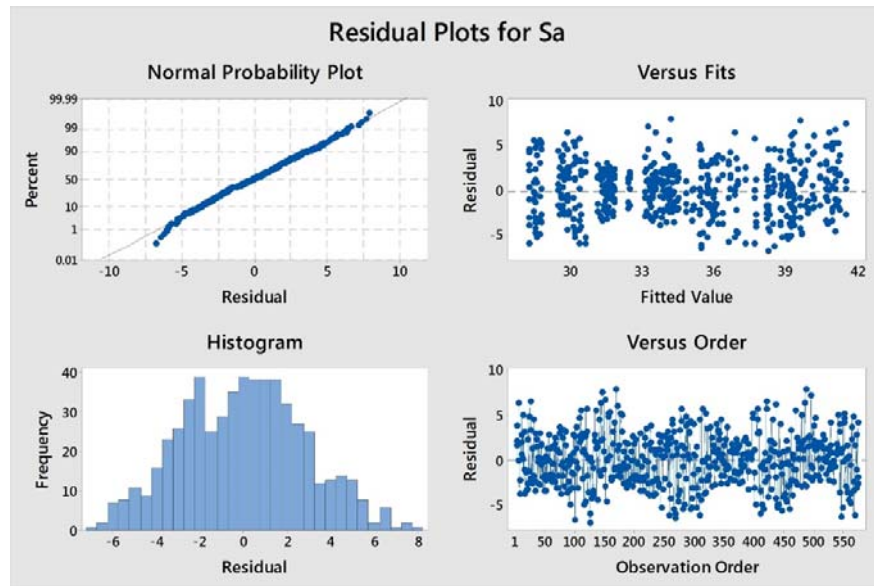


Figure 7-9: Residual plots for the 576 measurements. This includes four measurements on each side of nine square bars for each of four builds.

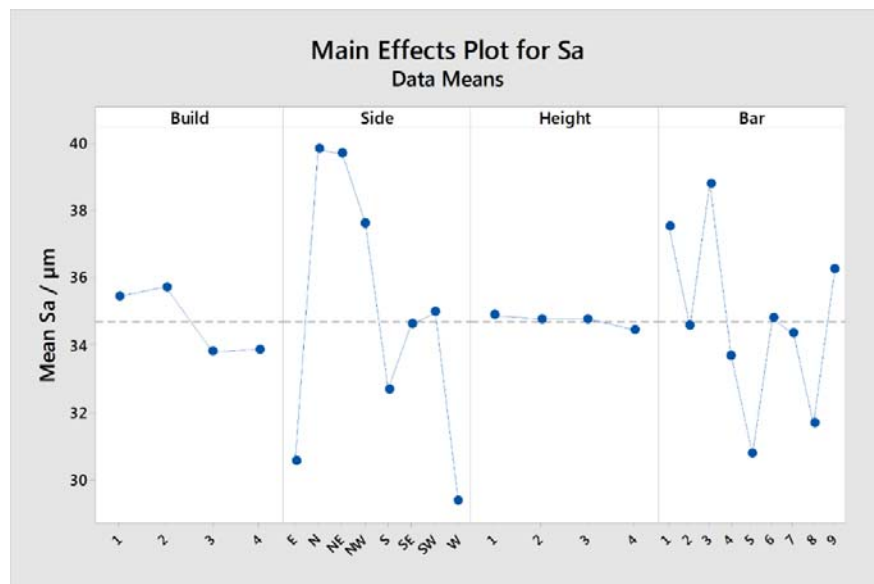


Figure 7-10: Main effects plot. For build number, side orientation, the four measurement heights and for the bar number.

7.3.4.1 Builds

From the main effects plot, Figure 7-10: ("Build" section), it can be seen that the mean S_a values for builds 1 and 2 are similar to each other, as are the mean S_a values for builds 3 and 4. Builds 1 and 2 were from one batch of raw material with re-use count 15 and 16. Builds 3 and 4 were a different batch of raw material and were for builds 1 and 2 using this powder. Figure 7-11: shows the Tukey pairwise comparison for all four builds. The Tukey pairwise comparison creates confidence intervals for all pairwise differences between factor means. If the interval does not contain zero then the corresponding means are significantly different. It can be seen that builds 1-2 and 3-4 are not significantly different. However, every other combination shows significant difference, indicating a significant difference between the S_a values between builds (1+2) and (3+4). A further study is needed to ascertain the individual influences of powder re-use and powder batch change.

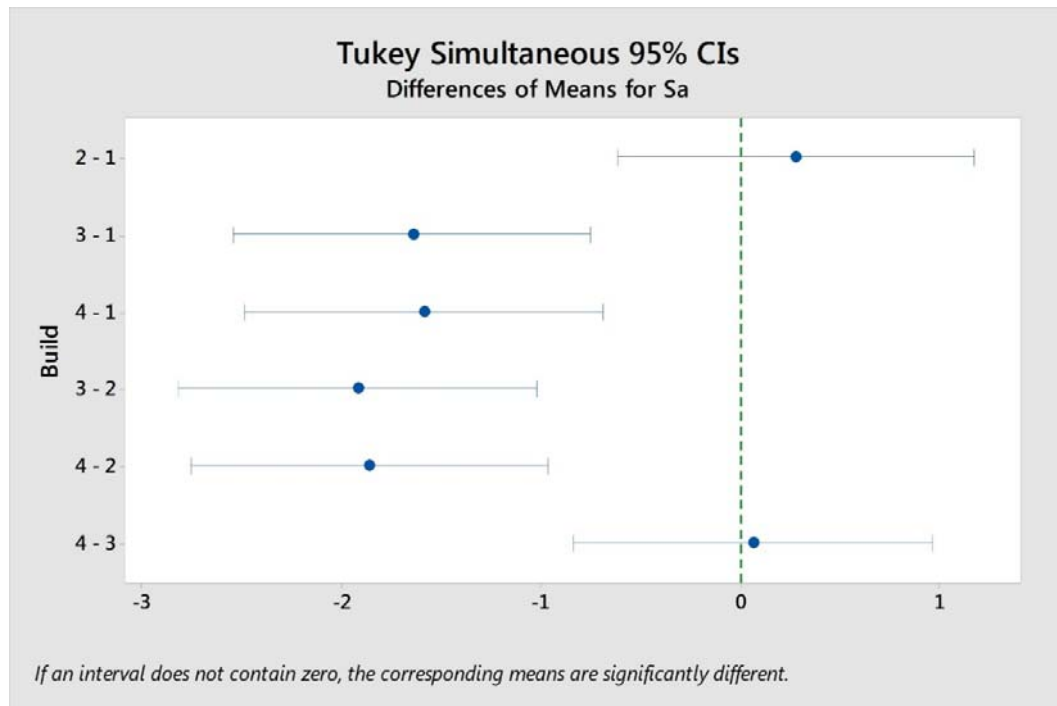


Figure 7-11: Tukey pairwise comparison for builds 1-4. Showing insignificant difference for S_a between builds 2-1 and between builds 4-3. All other combinations have significant differences for S_a .

7.3.4.2 Bar sides

There is a significant difference in S_a depending upon the orientation of the side of the bar. North facing bars have the roughest surface with the west-facing surfaces have the least mean roughness, see the main effects plot in Figure 7-10: ("Side" section). The Tukey pairwise comparison, Figure 7-12:, shows the most significant difference between N-E and between W-N. The only non-significant differences are between W-E, NE-N and SW-SE.

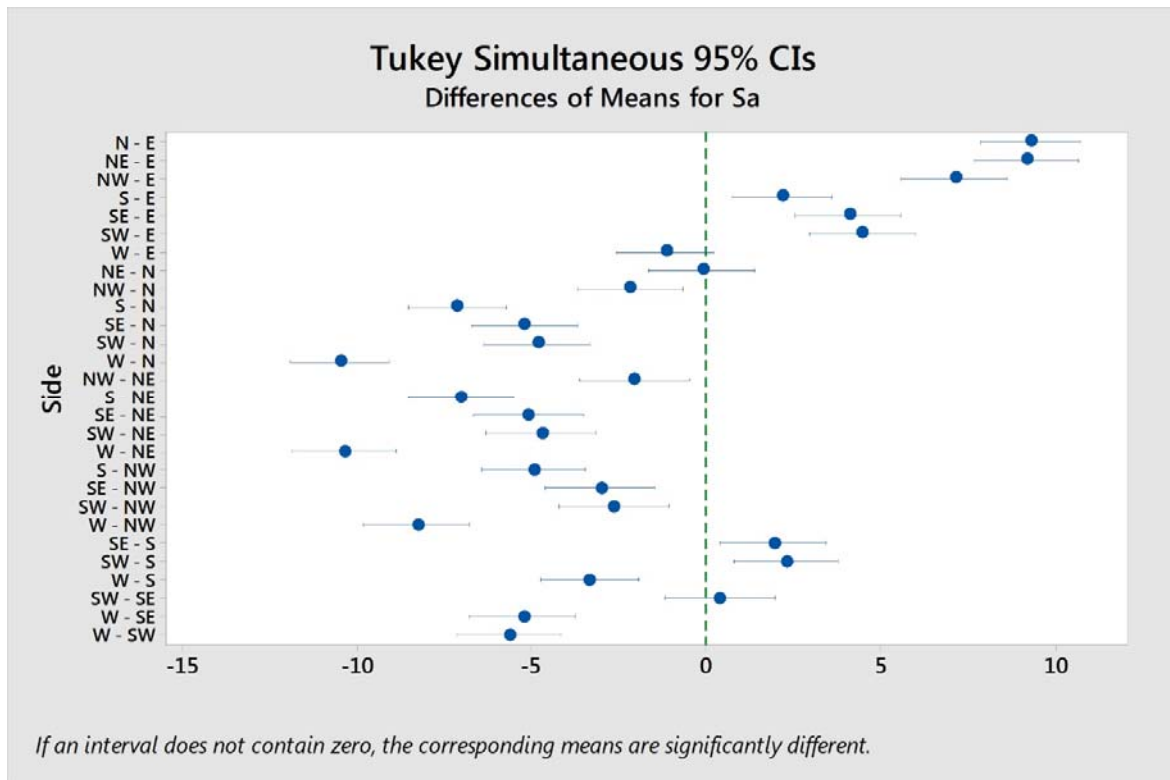


Figure 7-12: Tukey pairwise comparison for bar side orientation. Showing insignificant difference for S_a between W-E facing sides, NE-N facing sides and SW-SE facing sides. All other combinations have significant differences for S_a , with the most significant differences being between N-E and W-N facing sides, with the values S_a for N being approximately 10 μm greater than E and W.

The surfaces facing the North (left hand side of the build chamber when the chamber is viewed from the front) are significantly rougher, on average (approximately 40 μm S_a), than those facing in the other directions. West (29 μm S_a) and East (31 μm S_a) facing surfaces have the

lowest mean roughness so it appears the direction of increased roughness is aligned with the axes of the build chamber. These variations could relate to the powder spreader movement: the rake moves from North to South and back. Additionally, it can be seen that there is a significant difference between South and North facing sides and so there may be asymmetry in the rake or other unidirectional effects.

7.3.4.3 Heights

Figure 7-13: shows the Tukey pairwise comparison for the heights. It can be seen there is no significant difference in roughness in relation to bar height. This is perhaps to be expected as the actual material melting location remains unchanged during the build (the build plate drops between successive layer melting operations).

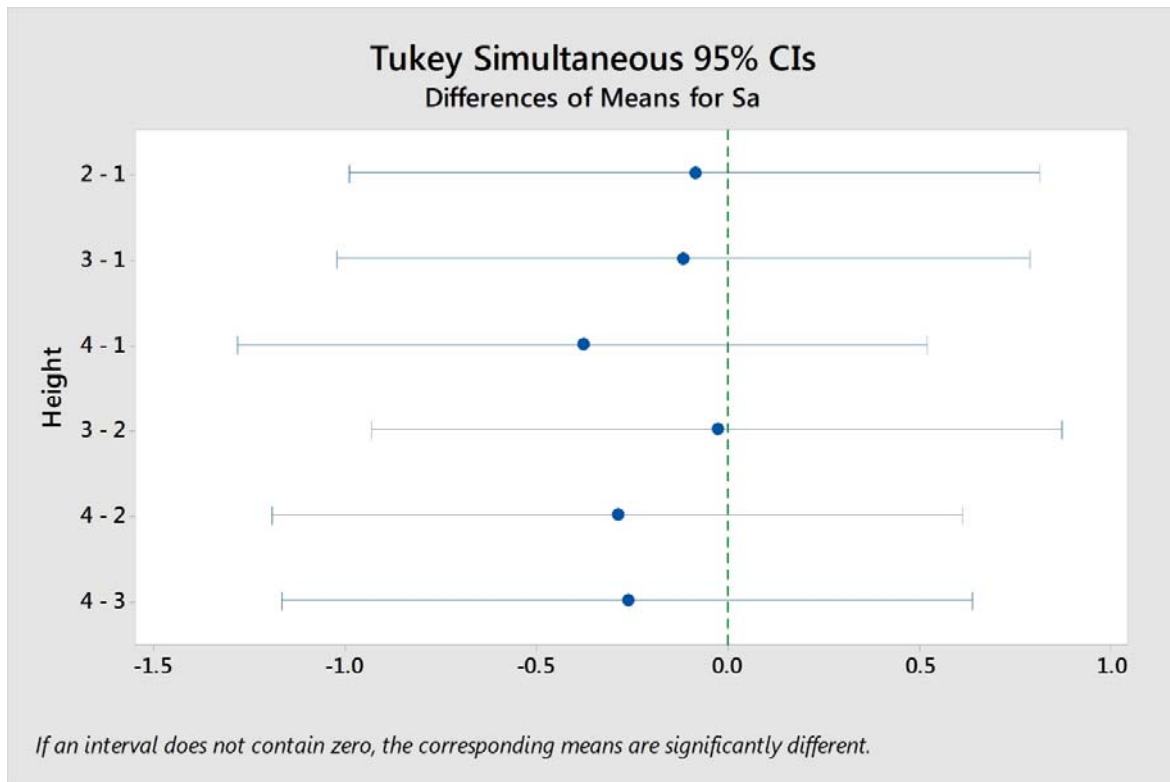


Figure 7-13: Tukey pairwise comparison for bar measurement height. Showing insignificant difference for S_a between any of the four measured height locations.

7.3.4.4 Back-front and side-facing bar sides

This analysis was performed to investigate the effect of beam asymmetry. The beam shape on the build surface becomes more elliptical as the beam cone angle increases. Back-front measurements were taken from faces aligned tangentially to the electron beam axis. Side facing measurements were taken from faces aligned radially to the electron beam axis. The mean S_a value for the side-facing surfaces was less than that for the back-front facing surfaces, but the difference was not significant, see Figure 7-14:.

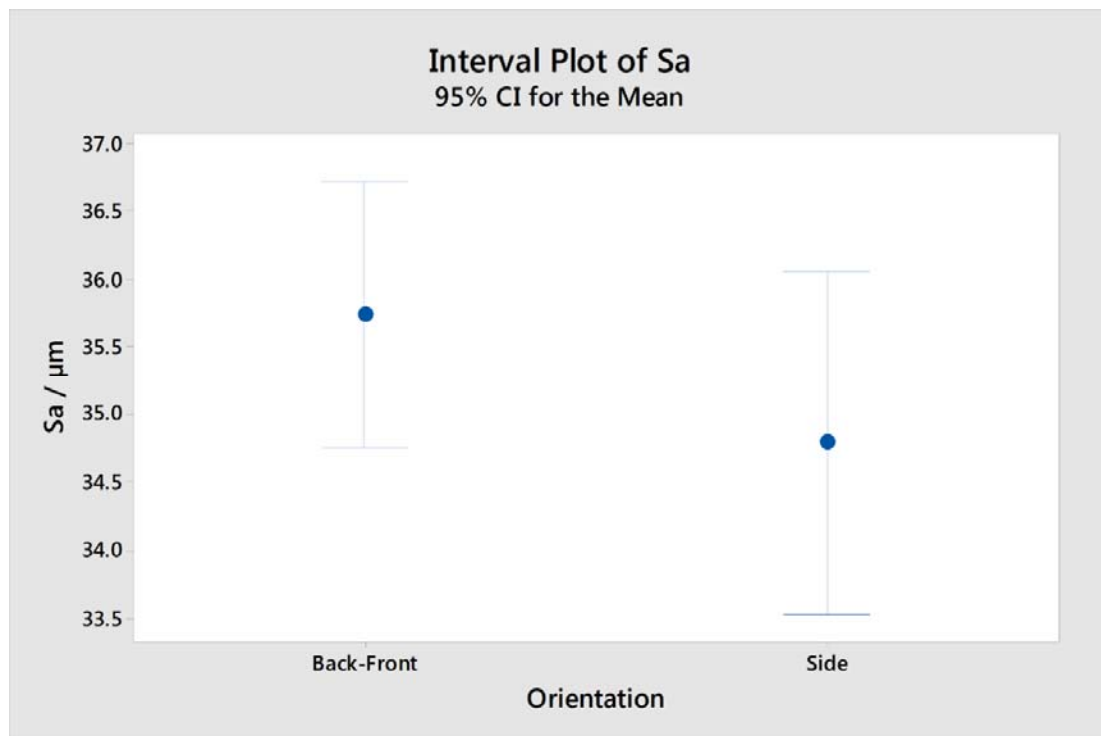


Figure 7-14: Back-front and side facing bar sides. Showing insignificant difference between back-front and side facing measurement locations.

7.3.5 Visual inspection of the bars

Visual inspection of the bars showed there were significant surface anomalies of similar configurations, at the same specific location on bars at the same chamber location in all four builds. The areas with these surface anomalies are shown in Table 36 and the locations of the bars, highlighting the sides of the bars with the irregularities, are shown in Figure 7-15:. It can be seen that the irregularities are clustered around the location of bar 7, which was at the front right of the build chamber.

Table 36: Location of significant surface (visual) irregularities.

Bar	Side (Build 1)	Side (Build 2)	Side (Build 3)	Side (Build 4)
1	NW	NW	SW,NW	SW,NW
4	N,E,W	N,E,W	N,E,W	N,E,W
5	-	-	W	W
6	-	-	S,W	S,W
7	NE,SW,NW	NE,SW,NW	NE,SW,NW	NE,SW,NW
8	N,S,W	N,S,W	N,W	N,W
9	SW,NW	SW,NW	SE,NW	SE,NW

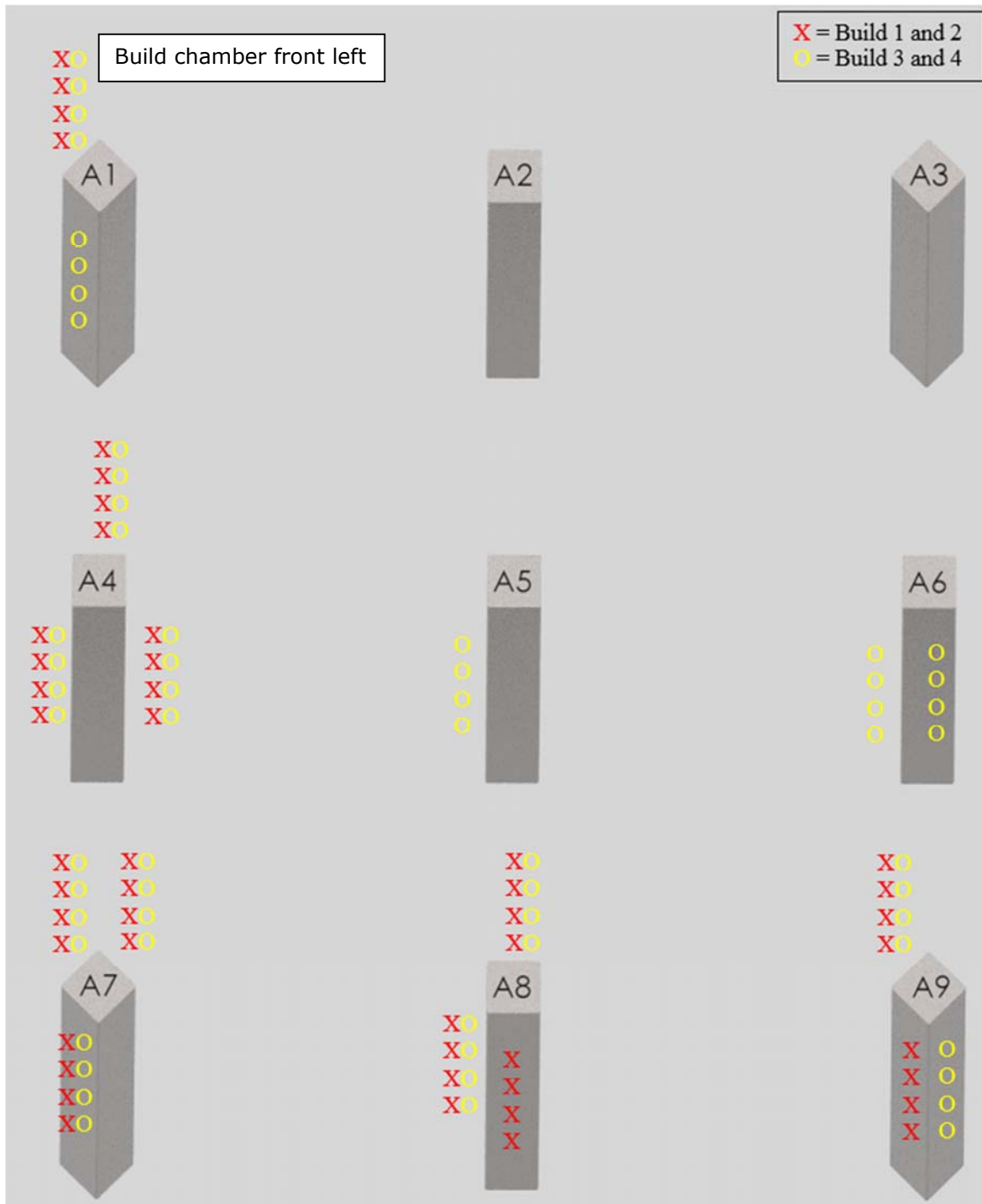
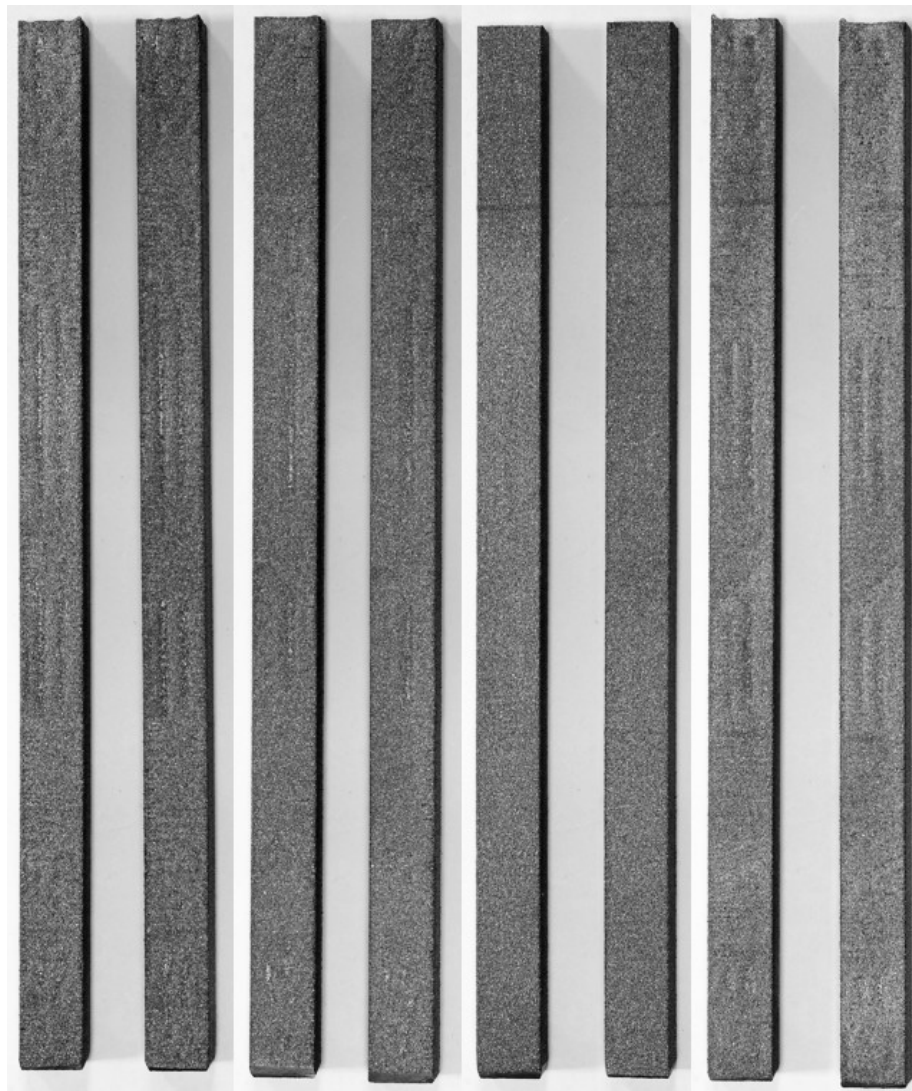


Figure 7-15: Location of visual inconsistencies. Red indicates visual inconsistencies on bars from builds 1 and 2. Yellow indicates visual inconsistencies on bars from builds 3 and 4. The location of the inconsistencies for the non-visible surfaces are shown above the respective surfaces.

Figure 7-16: shows a composite photograph of bar 4 showing each side from build 1 and build 2. Figure 7-17: shows a composite photograph of bar 4 showing each side from build 3 and build 4. These images illustrate how remarkably similar the irregularities are at the same locations. For example, side 4 of build 1 and build 2, shown in the two images to the right of the figure have similar vertical patterns, horizontal lines, diagonal lines and even the top edges of the bars look similar.



Build 1	Build 2	Build 1	Build 2	Build 1	Build 2	Build 1	Build 2
North		East		South		West	

Figure 7-16: Photographs of the four sides of bar 4 from build 1 and build 2. Showing very similar visual inconsistencies at the same locations for both builds.

The visual anomalies do not appear to be due to heat effects caused by the proximity of other components within the build chamber. These local defects may potentially have a significant impact on component performance if the item is used with as-built surfaces; as reported in Chapter 2 it has been shown that the surface defects of metal AM components may have a significant impact on fatigue life.

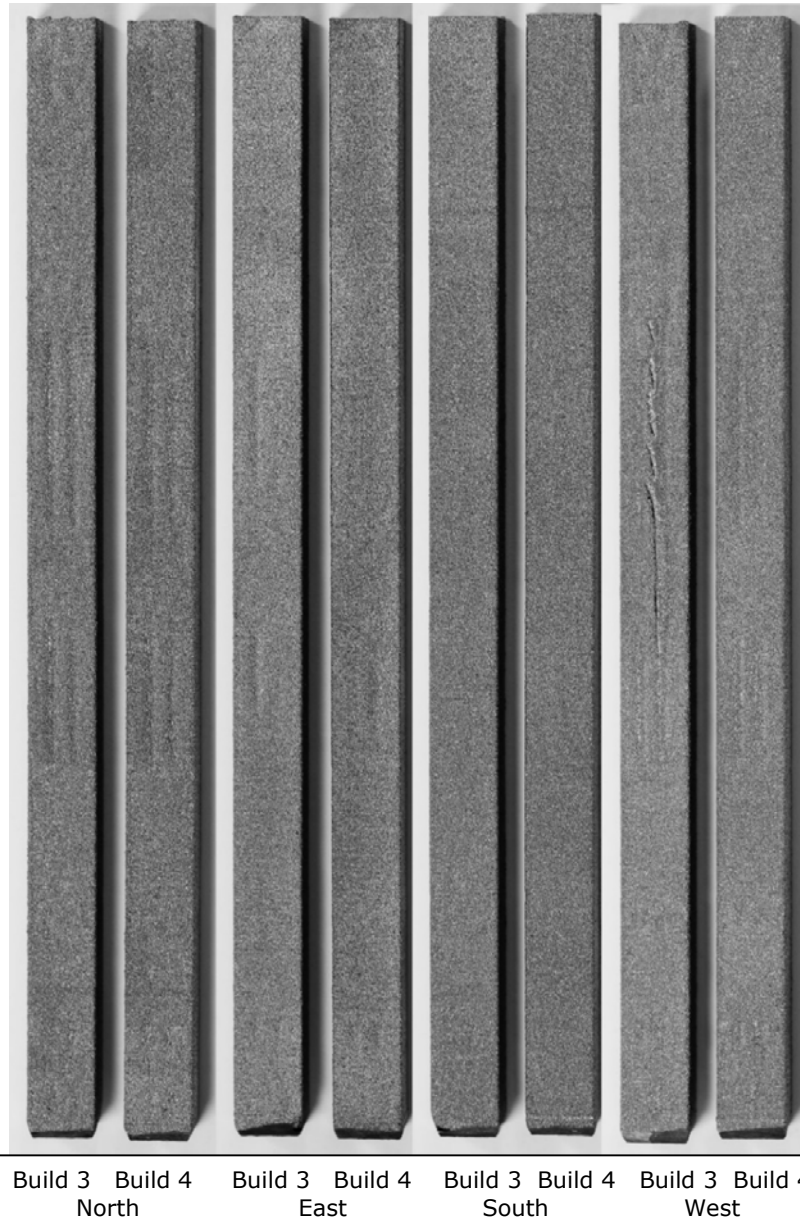


Figure 7-17: Photographs of four sides of bar 4 for build 3 and build 4. Showing very similar visual inconsistencies at the same locations for both builds.

Two height maps for bar four, side one, 10 mm from the top of bar (measurement 24) are shown in Figure 7-18: (build 1) and Figure 7-19: (build 2). The local step visible in both height maps is approximately 200 μm . Again, the similarities between build 1 and build 2 are clear.

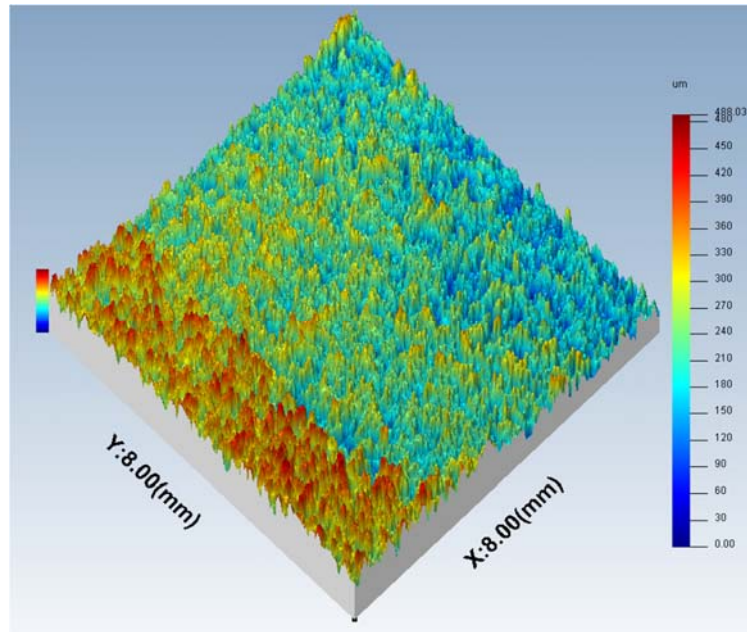


Figure 7-18: False-colour height map of Build 1, measurement 24.

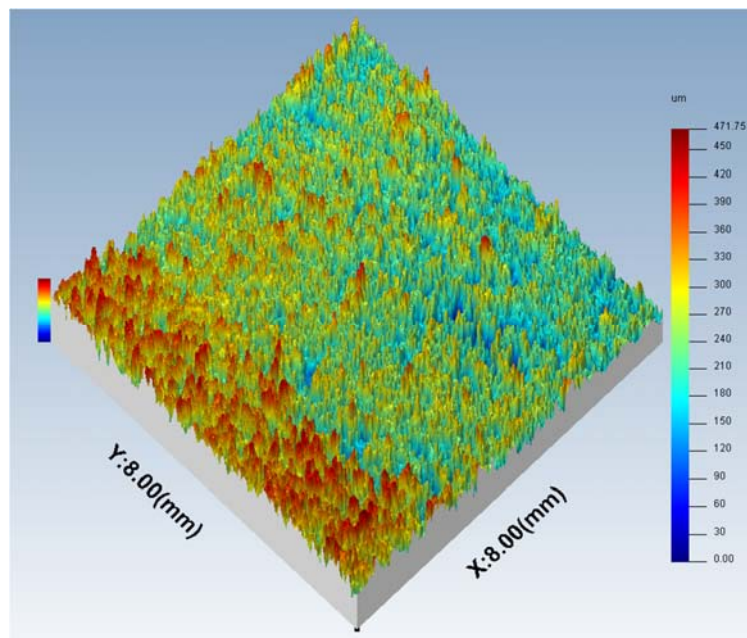
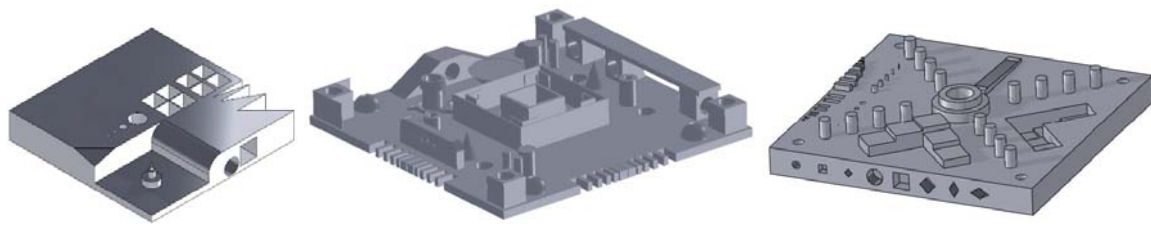


Figure 7-19: False-colour height map of Build 2, measurement 24.

7.4 AMSA artefact analysis

7.4.1 Dimensional artefacts



Kruth et al.

50 mm x 50 mm x 9 mm [155]

Mahesh et al.

170 mm x 170 mm x 5 mm (base) [156]

Moylan et al.

100 mm x 100 mm x 10 mm (base) [157]

Figure 7-20: AM measurement artefacts for form and dimensional measurements.

There have been many manufactured and proposed artefacts for use in AM build systems. The artefacts have primarily been for dimensional or form analysis [155, 156, 158-160]. Some designs include sections designed for surface measurement, such as the 2012 NIST artefact (Moylan et al.) [157], see Figure 7-20. ADDIN EN.CITE [152-154]Figure 7-20:

7.4.2 The AMSA artefacts

A novel set of three types of Additive Manufacturing Surface Artefacts (AMSA) surface-specific artefacts were included in the build, see Figure 7-21:.



AMSA1

AMSA3

AMSA4

Figure 7-21: CAD rendering of the AMSA series artefacts.

Each artefact fits within a cylinder with a diameter of 30 mm and a height of 10 mm.

These artefacts were designed by the author as a comparative tool for machine capability analysis and process variation analysis. These surface-specific artefacts can be made more compact than dimensional or form artefacts as they do not require the large dimensions and spacing between features required for accurate dimensional and form measurements. The artefacts were designed to provide comprehensive information about the component surface and to provide unobstructed access for standard surface measurement and visualisation methods, such as focus variation, stylus profilometry and scanning electron microscopy. The three artefacts, as required, are designed to be included in each build, similar to the inclusion of a test coupon in a heat treatment lot; they include manufactured-in traceability information thus providing a convenient build record.

The artefacts have features designed for:

- Surface texture parameter generation (AMSA1, section 7.4.5)
- Sub-surface analysis (AMSA1, section 7.4.5)
Deviation analysis (AMSA1, AMSA3 and AMSA4)
- Layer edge analysis (AMSA1, section 7.4.5 and AMSA4, section 7.4.7)
- Build resolution comparison (AMSA3, section 7.4.6 and AMSA4, section 7.4.7)
Investigation of the influence of build orientation (AMSA1, AMSA3 and AMSA4)

General features of all AMSA artefacts:

- Built-in traceability (part number, serial number, material, layer thickness)
- Exterior wall 0.5 mm min above critical surfaces: helps to avoid accidental damage, but permit measurement access
- Artefacts will fit in a 30 mm diameter cylinder with height 10 mm
- Low material cost, reduced build time and chamber utilisation

7.4.3 Methodology

Twenty artefacts were included in each EBM build. Ten of the artefacts (two sets of five artefacts) were oriented with the measurement surface positioned horizontally; ten of the artefacts (two sets of five artefacts) were oriented with the measurement surface positioned vertically, see Figure 7-22:. Each set of five artefacts included one AMSA1, see section 7.4.5, three AMSA3, see section 7.4.6 and one AMSA4, see section 7.4.7. The three AMSA3 artefacts were of similar basic design, but each with a slightly different configuration, see section 7.4.6. Additional AMSA artefacts were manufactured on a Renishaw AM250 SLM machine using Ti6AL4V ELI material with a nominal powder size of 15–45 μm . Visual and surface texture comparisons was performed between the SLM and EBM components.

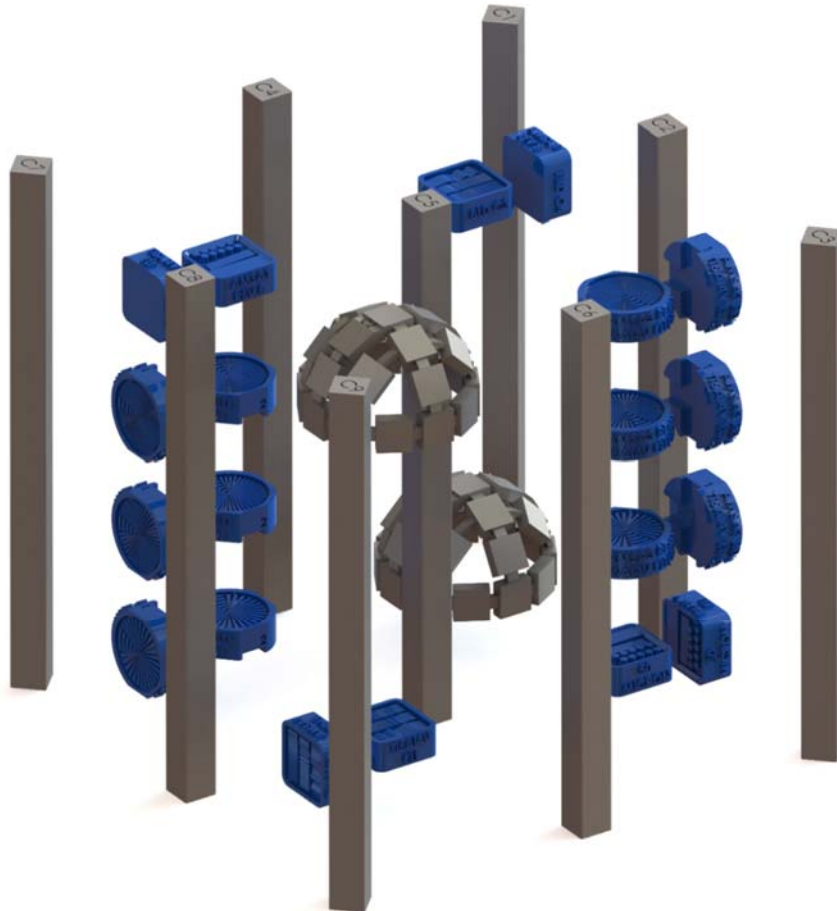


Figure 7-22: CAD rendering of the surface-specific artefacts in blue. Shown as part of the complete artefact set.

7.4.4 Artefact measurement

Measurement results included here are for samples from build 1. The measurements were performed as follows:

7.4.4.1 Deviation analysis

The artefacts were scanned using the Nikon XT H 225 CT system. The system parameters used are shown in Table 37.

Table 37: CT scanning parameters for the AMSA series artefacts.

Voxel size (µm)	Voltage (kV)	Current (µA)	Magnification	Physical filtration (mm)	Exposure time (ms)	Number of projections
40	210	230	5	4	2000	1583

The deviation analysis was performed using the Catia V5 (Dassault Systems, France) software package. The CT mesh data was aligned to the CAD model coordinate system. This involved generating a series of three planes based on a least square fit of user selected surfaces from the mesh. These surfaces were used to create a three plane coordinate system. The three datum planes were defined as follows:

- Primary datum – top plane of the artefact
- Secondary datum – the side face marked “50 Micron” for artefact ASMA1 and AMSA4
– the side face marked “1” for artefact ASMA3
- Tertiary datum – the side face marked “BLD A” for artefacts ASMA1 and AMSA4
– the side face marked “2” for artefacts ASMA3

A deviation analysis was then performed between the actual scanned artefacts and the CAD files. The deviation map generated includes all surfaces of the artefacts. Excess material on the part (shown in green to blue shades) is represented as negative deviation whilst missing material (shown in green to red shades) is represented as positive deviation.

7.4.4.2 Scanning electron microscope imaging

Scanning electron micrographs were taken using a Quanta FEG 250 scanning electron microscope (SEM).

7.4.4.3 Surface texture measurements

Surface texture measurements were performed using the Alicona G4 focus variation instrument.

7.4.5 AMSA1

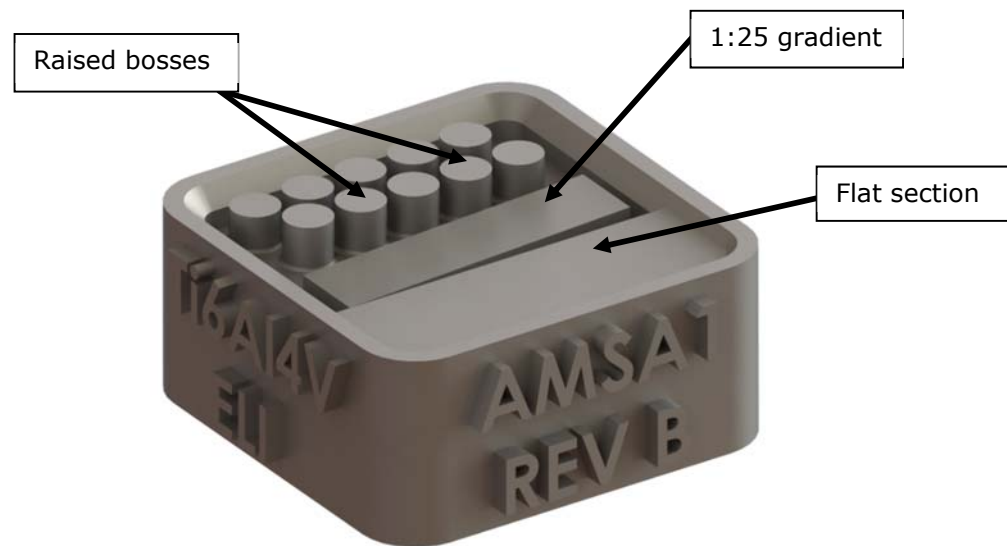


Figure 7-23: CAD rendering of artefact AMSA1. Showing the three evaluation sections: raised bosses, 1:25 gradient and the flat measurement section.

Artefact AMSA1 includes three separate surface evaluation areas on its top face, see Figure 7-23::

- A flat measurement area parallel to the artefact base plane to allow profile or areal surface measurement and parameter extraction; for example per ISO 4288 or ISO 25178-2.
- A sloped section with a 1:25 gradient to allow easy visualization and measurement of the layer transition edge.

- Ten individual $\varnothing 2.5$ mm raised bosses with a height difference between each boss equivalent to the build layer thickness. This will produce the minimum possible distance between the boss heights. If the bosses are milled to the height of the artefact edge wall surfaces then between one and seven layers below the as-built surface will be exposed. Two of the bosses have surfaces below the edge wall height. The height of these bosses will allow calculation of the actual material machined from the higher bosses, which may be especially useful if the edge wall is accidentally machined. The surfaces can be examined for porosity or, after suitable etching and polishing, metallographic inspection of each surface may be performed. Seven layers below the final surface was selected because studies have shown that there may be a seven layer heat effected zone for metal PBF components [113]. To avoid possible operator errors, once the layer height is specified in the design, the layer height is printed on the outside of the artefact and the boss heights are generated automatically.

7.4.5.1 Results

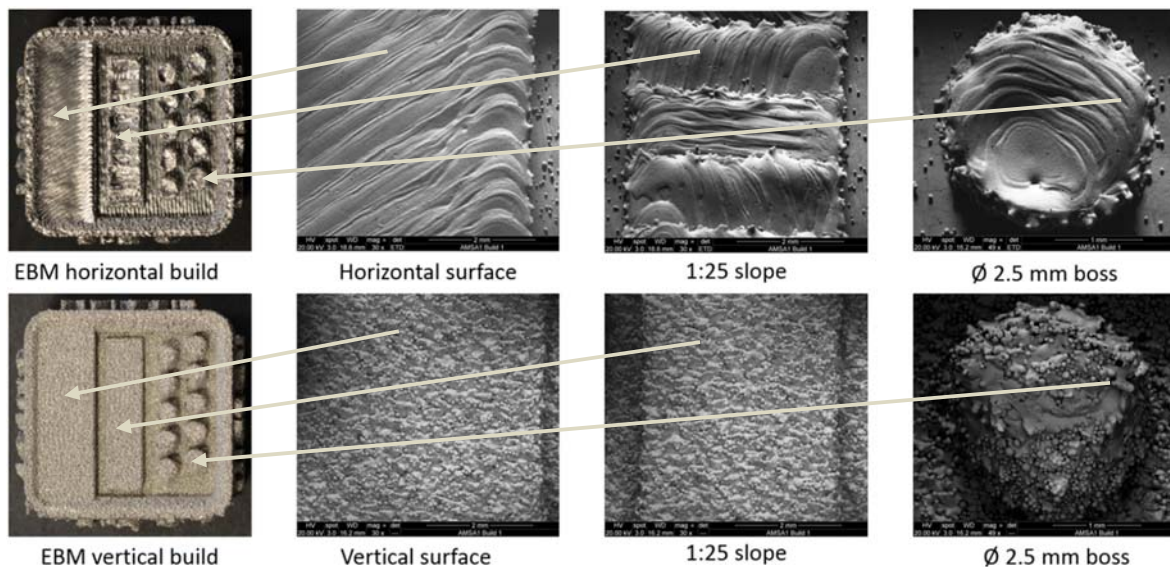


Figure 7-24: EBM AMSA1 horizontal and vertical build surfaces. Showing photographs of the horizontal and vertical faces, together with SEM micrograph details of the three evaluation sections.

Photographs of artefact AMSA1 built horizontally and vertically are shown in Figure 7-24: together with SEM micrographs of the three measurement features. The EBM scan patterns can clearly be seen in the horizontal build micrographs. There is considerable difference in the appearance of the horizontally and vertically built surfaces. The diagonal build strategy can clearly be seen in the horizontal flat surface. The importance of correct part orientation during the build, based on part design function, can clearly be appreciated. Figure 7-25: shows a deviation analysis performed between the CAD model and the horizontally and vertically built EBM AMSA1 artefacts. The horizontally built artefact shows a raised edge around each of the boss features. This is consistent for all cylindrical features across the artefact. The 1:25 gradient slope on the horizontally built artefact also exhibits a raised section around the edge and at the layer transition steps, with some missing material adjacent to the next higher build layer. These errors are due to a combination of model slicing and layer thickness. The bottom sides of the ten boss features on the vertically built artefact are deformed with locally missing material in excess of 0.5 mm. These down-facing areas here were unsupported during the build.

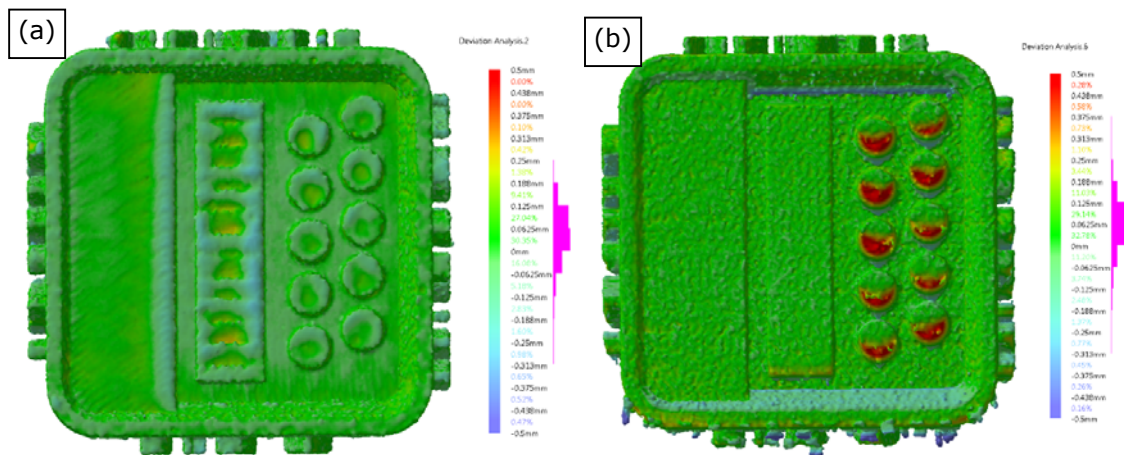


Figure 7-25: EBM AMSA1 artefact deviation analysis (a) horizontal build, (b) vertical build. Deviation reported between the CAD model and the reconstruction from the CT scans.

Figure 7-26: shows the SLM and EBM built AMSA1 artefact. It can be seen that, overall, the SLM build surface finish is superior to the EBM build. Build scan direction is less distinct and there is less deformation on the SLM sample. The flat surface section of each artefact was measured using an Alicona G4 focus variation instrument. The value of S_a , the mean surface roughness for each measurement, together with the filtering used are given in Table 38. It should be noted that the area of the EBM sample suitable for measurement was reduced because of the presence of the raised edge of the flat section, see Figure 7-26:(b) and the false-colour height map, Figure 7-27:.

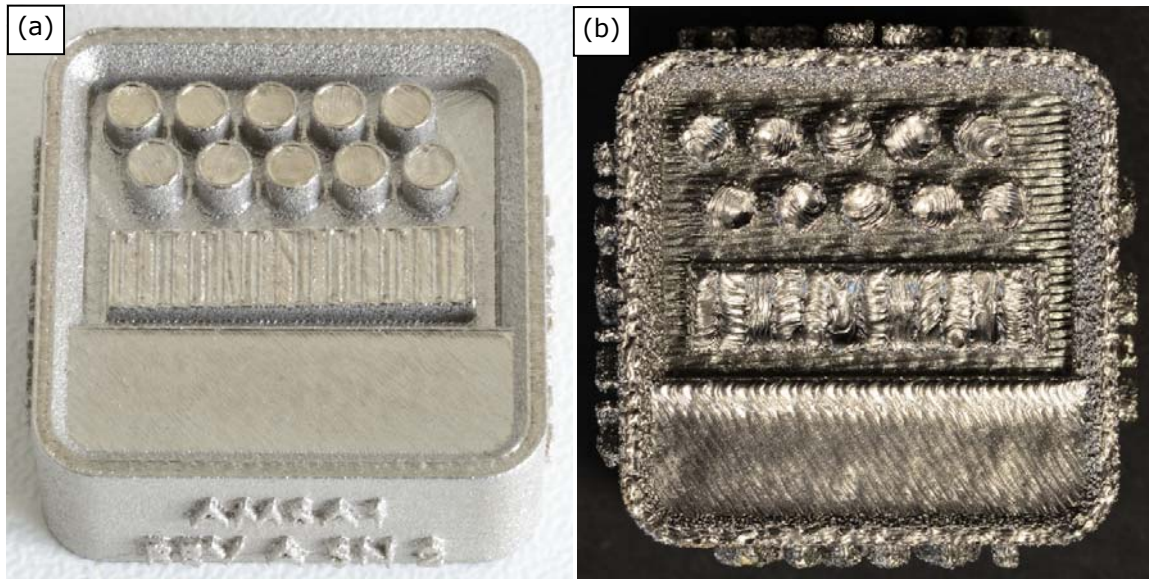


Figure 7-26: Photographs of the AMSA1 horizontal artefacts (a) SLM, (b) EBM.

Table 38: AMSA1 surface S_a values.

Sample	L-filter per ISO 25178-3	S-filter per ISO 25178-3	S_a
SLM horizontal	5 mm	0.020 mm	7 μm
EBM horizontal	3.5 mm	0.020 mm	9 μm
EBM vertical	5 mm	0.020 mm	32 μm

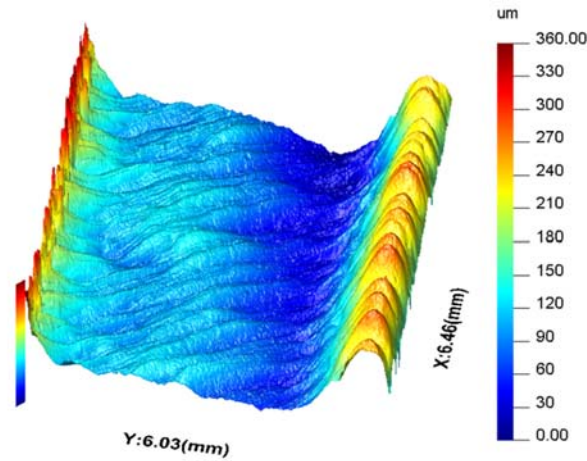


Figure 7-27: False-colour height map of the horizontal EBM flat section.

7.4.6 AMSA3

The AMSA3 artefact series include a Siemens star on the top face. Siemens stars are commonly used to determine the resolution of optical metrology instruments, displays and printers and are included in measurement Standards such as ISO 15775 [161] and have been included in AM research [162]. The spokes of the Siemens star become indistinguishable at some radial distance from the centre when the lateral resolution limit is reached. AMSA3 includes a wedge section with concentric rings to aid in visual location of the resolution-limit. A series of three artefacts were included in the build, each with a different spoke width and spacing (for identification purposes: coarse, medium and fine), see Figure 7-28:. This was done to assess the correct spacing for the build configuration. A single, optimised, AMSA3 artefact will be included in subsequent builds.

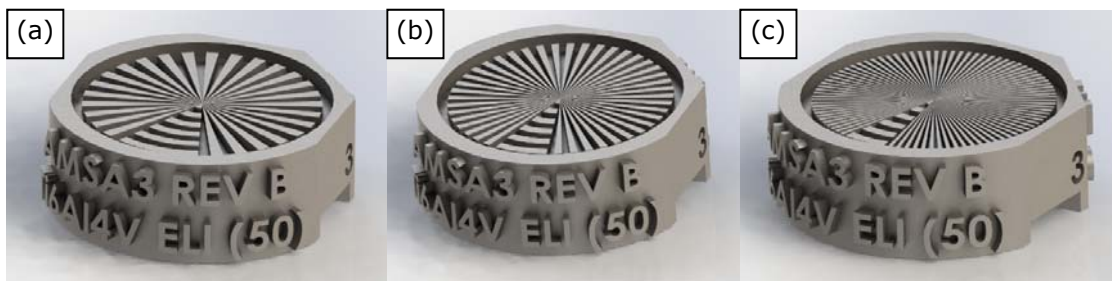


Figure 7-28: CAD rendering of the AMSA3 artefact set. (a) course, (b) medium, (c) fine.

7.4.6.1 Results

AMSA3 horizontally built EBM artefact photographs and deviation analyses are shown in Figure 7-29:.

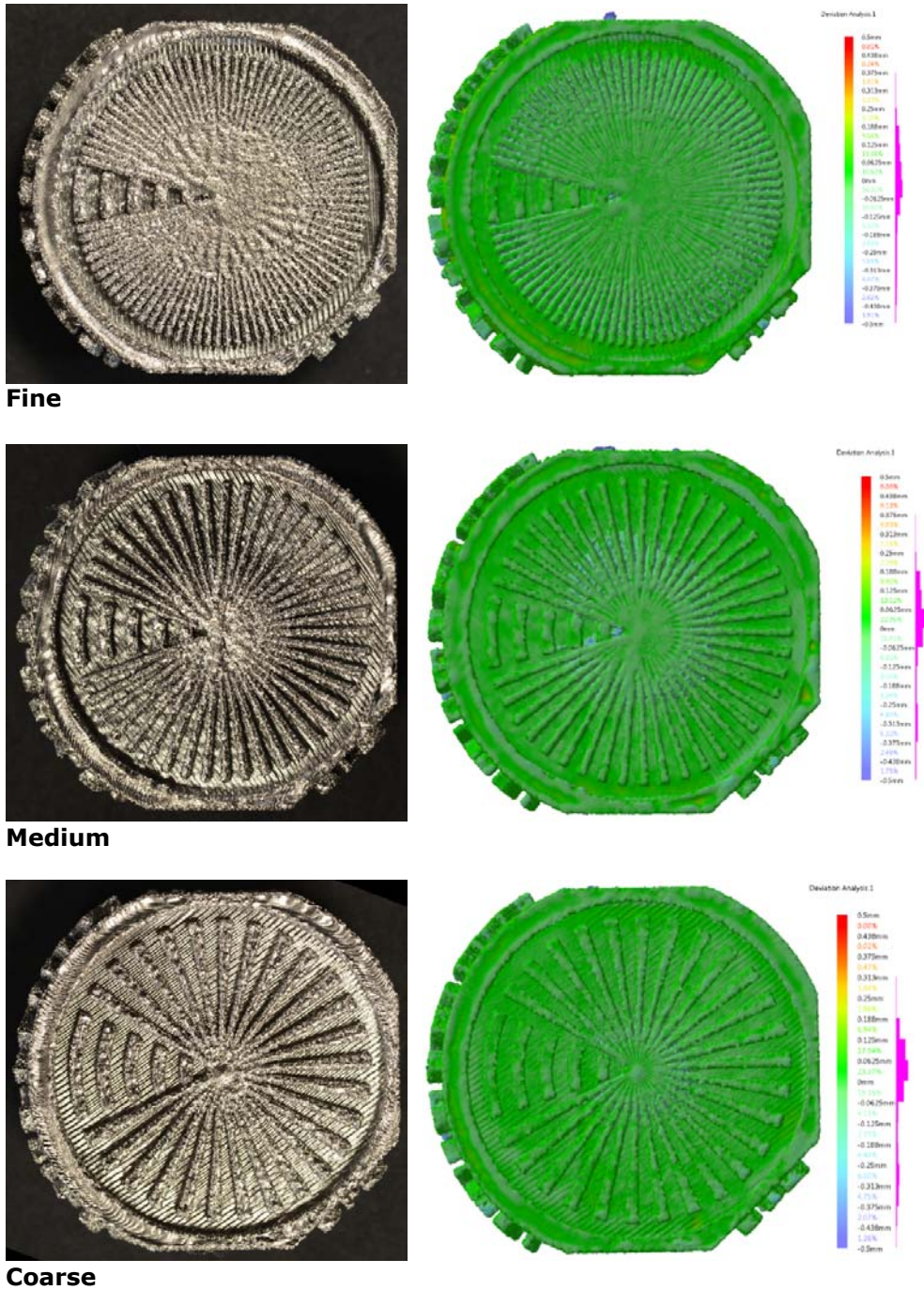
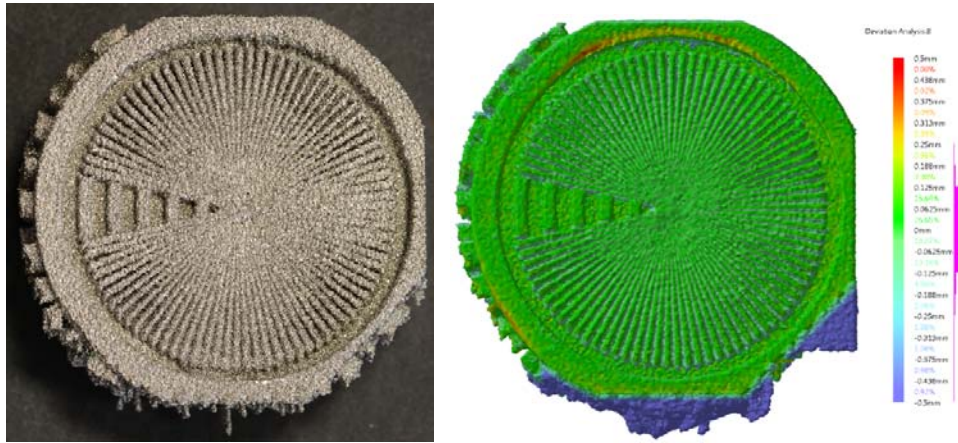
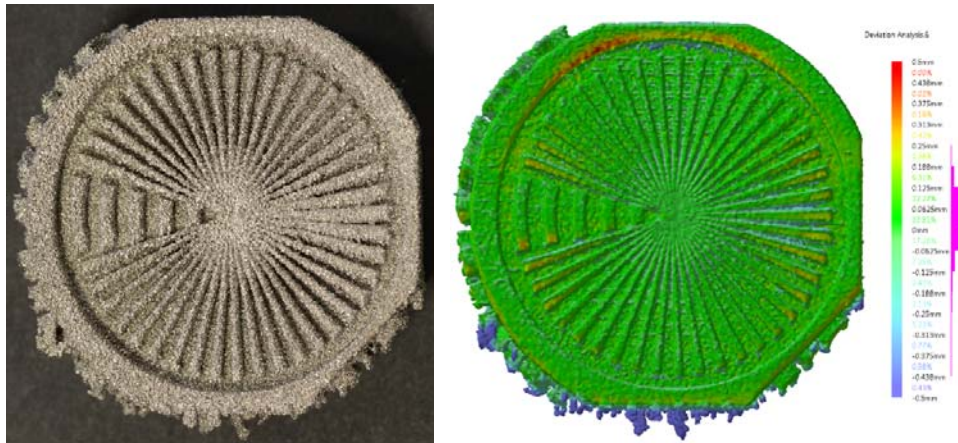


Figure 7-29: EBM horizontal AMSA3 photographs and deviation analyses. Showing the fine, medium and coarse artefact builds.

AMSA3 vertically built EBM artefact photographs and deviation analyses are shown in Figure 7-30:.



Fine



Medium



Coarse

Figure 7-30: EBM vertical AMSA3 photographs and deviation analyses. Showing the fine, medium and coarse artefact builds.

The differentiation between the Siemens star spokes toward the middle of the artefact is clearly better with the vertically built artefact surface, see Figure 7-31:. Down-facing surfaces of the vertically built exhibit local form deviation (missing material—indicated in red, Figure 7-30:). The outer spoke section of the medium AMSA3 (Figure 7-32:) shows the width of the vertically built spoke is approximately 1.5 times the width of the horizontally built spoke at the same location. This deviation is visible in the deviation analysis, Figure 7-30:.

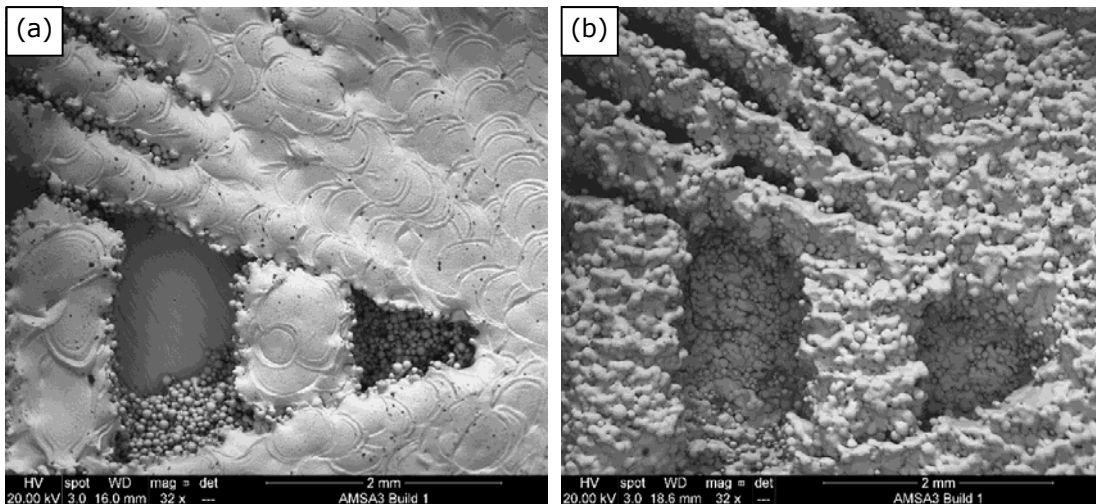


Figure 7-31: SEM micrographs of the AMSA3 medium Siemens Star. (a) horizontal build, (b) vertical build.

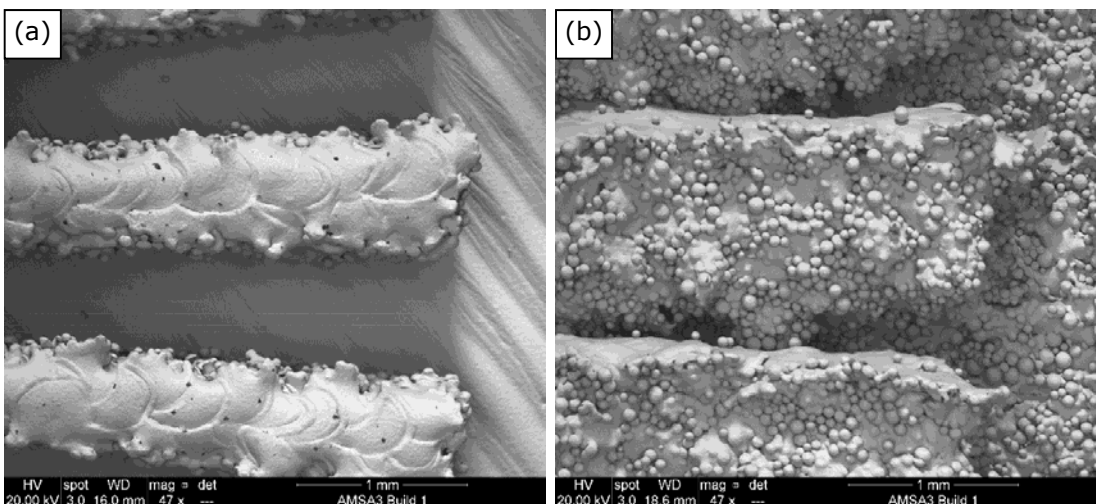


Figure 7-32: SEM micrographs of the AMSA3 medium Siemens Star outer section. (a) horizontal build (b) vertical build.

Figure 7-33: shows the surface of the SLM and EBM fine AMSA3 artefact. Although the resolution of the SLM artefact is superior (the radial location at which the spokes become indistinguishable is closer to the centre of the artefact) there are two concentric rings within the Siemens star where the spokes are enlarged both laterally and vertically, see Figure 7-34:.

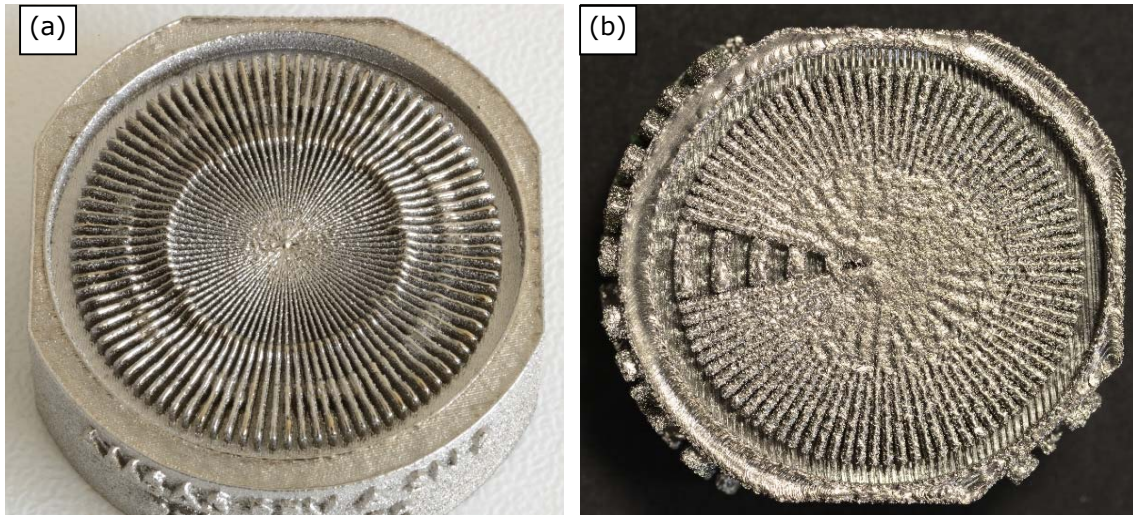


Figure 7-33: Photographs of the AMSA3 artefact horizontal build. (a) SLM, (b) fine EBM (similar spoke width and spacing).

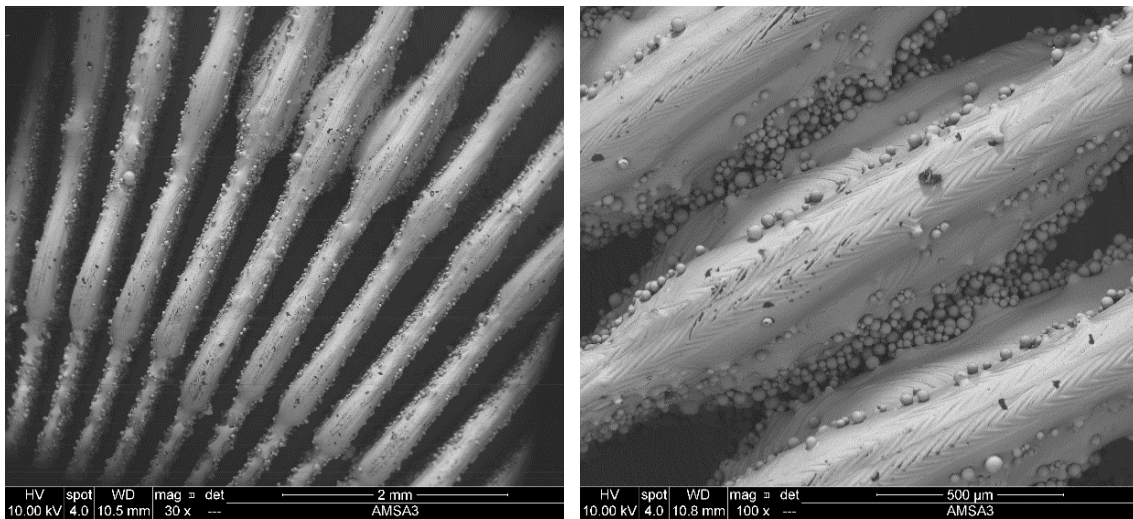


Figure 7-34: SLM AMSA3 artefact SEM micrographs.

7.4.7 AMSA4

Artefact AMSA4 includes three sections that each have constant-amplitude decreasing wavelength structured sine wave surfaces, see Figure 7-35:.



Figure 7-35: CAD rendering of the AMSA4 artefact.

These surfaces may be used for simple visual comparison between builds or a deviation analysis may be performed. The equations for the three sections are Equation 8 (amplitude 800 μm pk-pk), Equation 9 (amplitude 400 μm pk-pk) and Equation 10 (amplitude 200 μm pk-pk). This artefact is designed to give a visual indication of resolution limit and the build-layer edge effect using optical, SEM and deviation analysis when compared to the CAD model.

$$Y = \frac{\sin\left(\left(\frac{X}{4}\right)^2\right)}{2.5} \text{mm} \quad \text{Equation 8}$$

$$Y = \frac{\sin\left(\left(\frac{X}{2}\right)^2\right)}{5} \text{mm} \quad \text{Equation 9}$$

$$Y = \frac{\sin(X^2)}{10} \text{mm} \quad \text{Equation 10}$$

7.4.7.1 Results

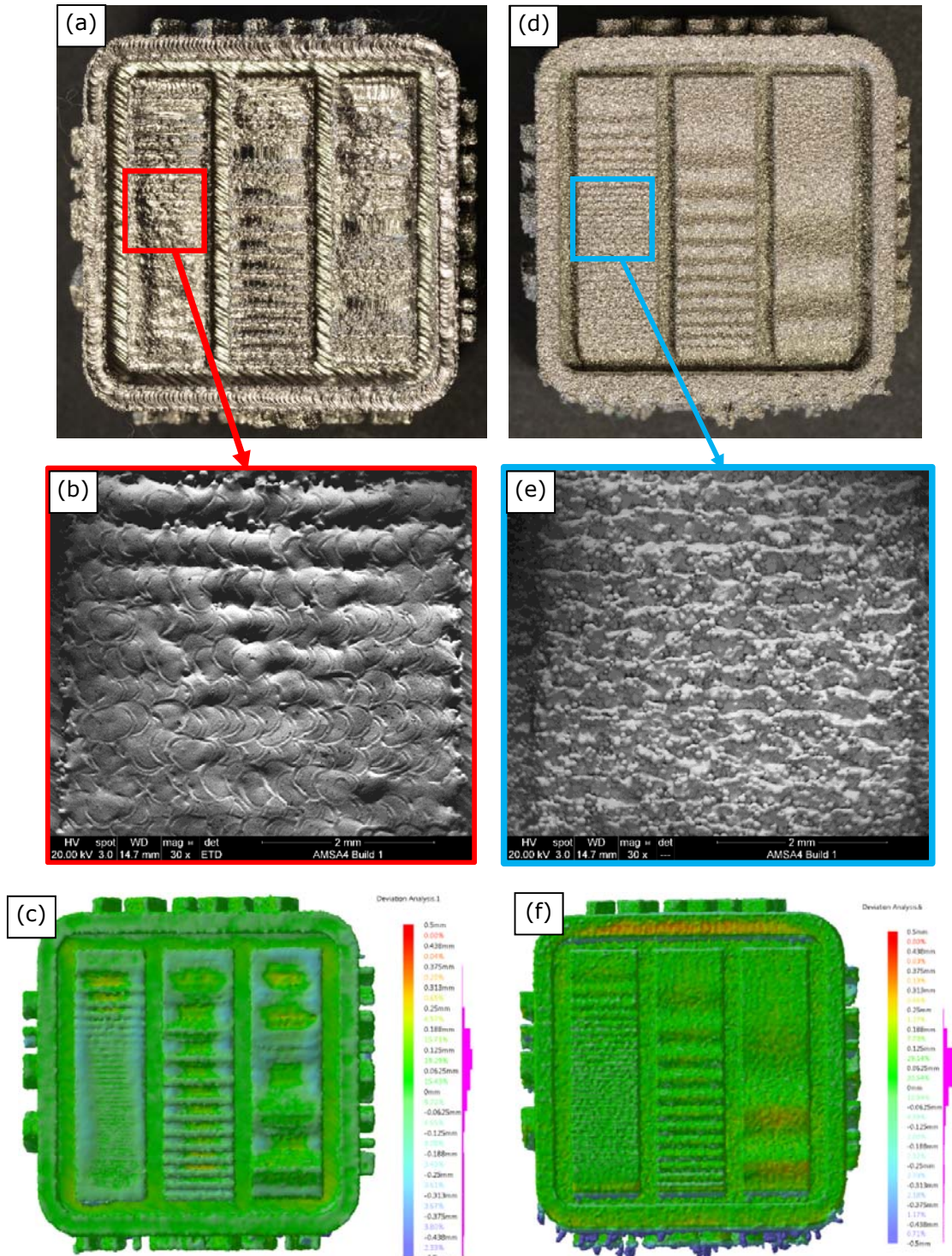


Figure 7-36: Horizontally and vertically built EBM AMSA4 artefacts. Horizontal build (a) photograph, (b) local SEM image, (c) deviation analysis. Vertical build (d) photograph, (e) local SEM image, (f) deviation analysis.

Figure 7-36: shows the horizontally built and vertically built EBM AMSA4 artefact together with the deviation analysis for this artefact. The deviation analysis of the horizontally built artefact shows raised edges and depressed centre sections of all three sine wave features, similar to the ASMA1 features. SEM micrographs of the areas of both builds where the decreasing wavelength sine wave becomes un-resolvable are shown. This demarcation is clearer in the horizontally built surface because of the generally smoother surface present in the horizontal surface.

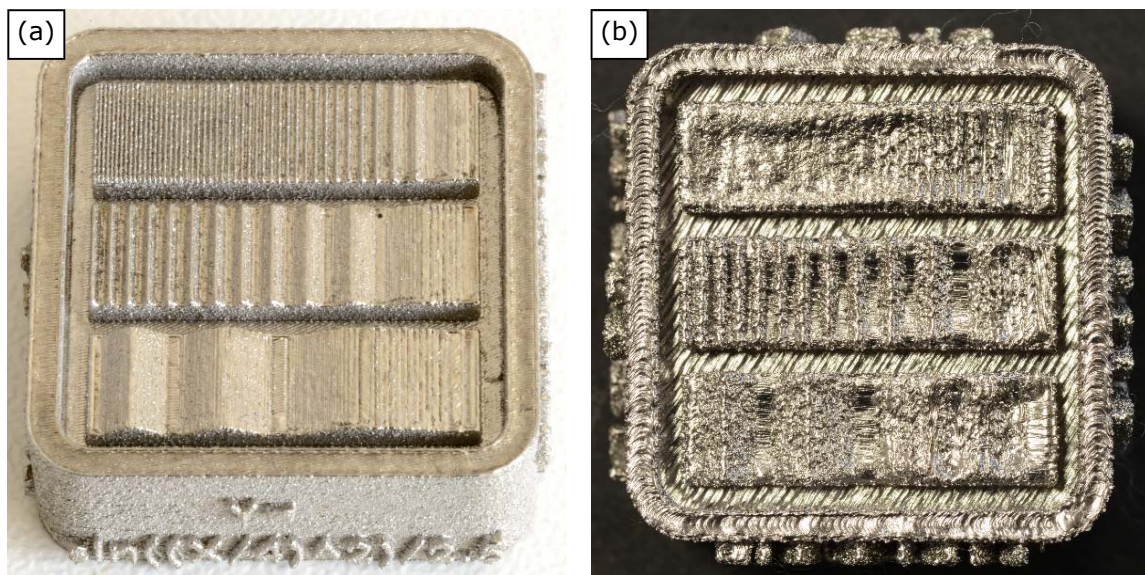


Figure 7-37: Photographs of the horizontally built AMSA4 artefact. (a) SLM, (b) EBM.

Figure 7-37: shows the SLM and EBM AMSA4 surface artefacts. The resolution of the SLM artefact is clearly superior to the EBM artefact. The finest sine-section of the artefact was resolved on the SLM artefact.

7.4.8 Artefact base deviation

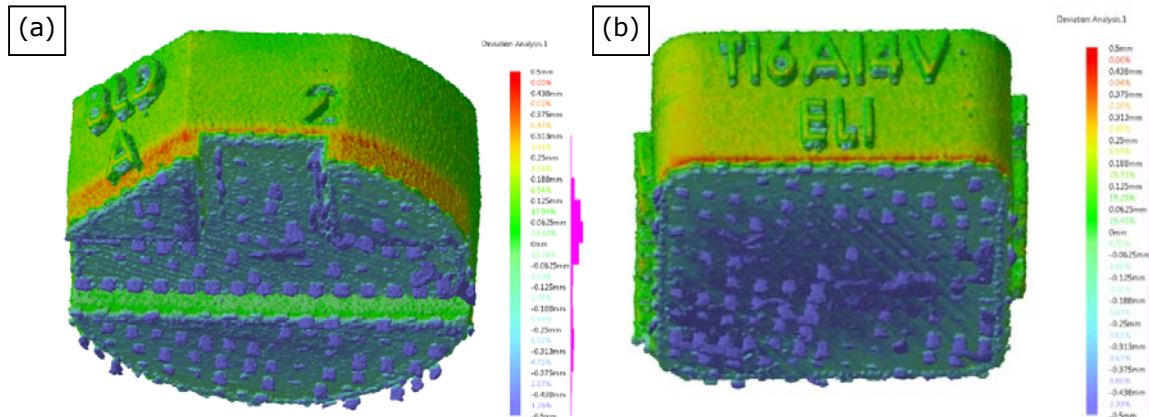


Figure 7-38: Deviation analyses showing the underside of the EBM artefacts. (a) AMSA3 coarse artefact, horizontal build (b) ASMA4 artefact, horizontal build.

The bottom surface of the horizontally positioned artefacts show significant deviation due to the support structure that constitutes extra material (blue) on the part surface, see Figure 7-38:. Some of the artefacts also display an area of deviation where there is missing material on the sides of the artefacts (red). These areas are located at the intersection between the bottom surface and the lateral sides of the artefacts.

7.4.9 AMSA series artefact discussion and conclusions

There is a clear difference between the vertically built and the horizontally built EBM surfaces. The absolute resolution is higher for the vertical surface as observed on the Siemens star. As expected, the characteristic surface is different, with the vertical surface similar to weld tracks with embedded partially-melted raw material particles. The vertically built surface has a higher proportion of partially-melted particles and smaller-scale surface ridges. Unsupported vertical surfaces, such as the side of the bosses of the vertically-built surface have greater than 0.5 mm missing material when compared to the model. This information will influence the amount and location of additional material required to be added prior to the build to assure complete clean-up of any post-processed surface, such as sealing and bearing

surfaces. The surface texture information may be used to configure the build orientation of the production components within the chamber. The SLM component had clearly superior resolution and surface texture but there were local build anomalies highlighted by the Siemens star surface. The configuration of the artefacts is flexible and may be modified based on the initial results obtained. For example, the SLM surface resolution was sufficiently fine that the smallest decreasing sine wave section of AMSA4 was resolved. The intention of these sections was to give a visual indication of the resolution limit. The artefact may simply be re-designed to reduce the wavelength of the section. The anomalies with the SLM Siemens star may be used to guide the modification of AM machine build parameters with further samples made to evaluate the corrective action. The EBM build process produced a raised edge around the flat surface section of the AMSA1 artefact. This raised edge reduced the area suitable for surface texture measurement. The reasons for the raised edge may be investigated and, additionally, if required, the artefact design may be modified to include a wider measurement section. Many machines, such as the laser-based Renishaw AM250, allow the selection of build parameters for each part made within one build. This allows experimentation to optimise build parameters quickly once a problem is discovered.

7.5 Build angle hemi-sphere artefact

Currently, there is an AM measurement artefact suite being proposed by the ASTM F42/ISO TC 261 Joint Group (JG) for Standard Test Artefacts (STAR), see Figure 7-39:. This measurement artefact suite includes angled surface measurement plates. Hemi-spherical artefacts, including angled planar surfaces, were included in the EBM build in the current research. These are similar to a faceted sphere used by Grimm [112]. The angled surfaces are designed to aid analysis of the effect of build angle on surface texture. The size of each panel in the hemi-sphere was chosen to allow the measurement of an area of 8 mm x 8 mm on each plate, as per the requirements of ISO 25178-3.

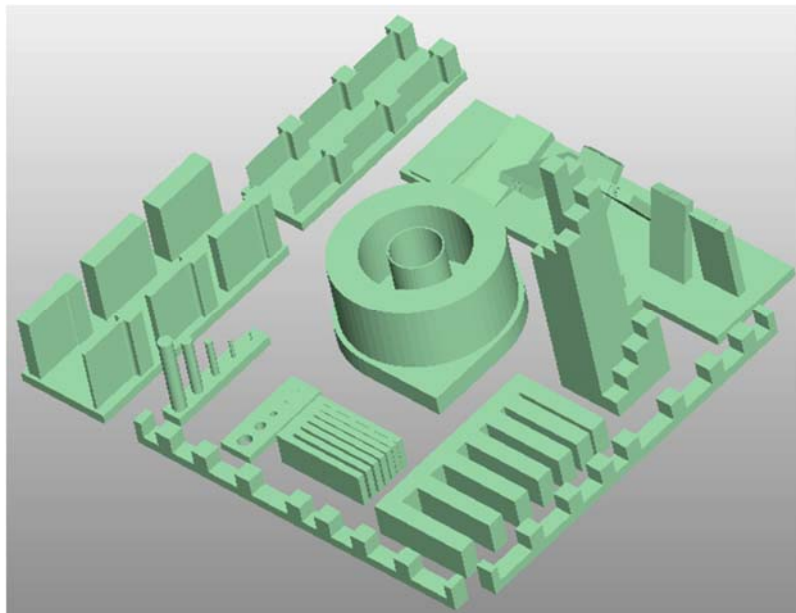


Figure 7-39: Proposed ASTM F42 AM measurement artefact suite, including NPL modified z-axis artefact.

Two multi-faceted hemi-spheres were printed in each of the four builds, see Figure 7-40: and Figure 7-41:. Table 39 shows the build angle and number of sample sections for each build angle. The sections were measured on the Alicona G4, cropped, levelled and filtered per ISO 25178-3 using an L-filter nesting index of 8 mm and an S-filter nesting index of 0.008 mm.

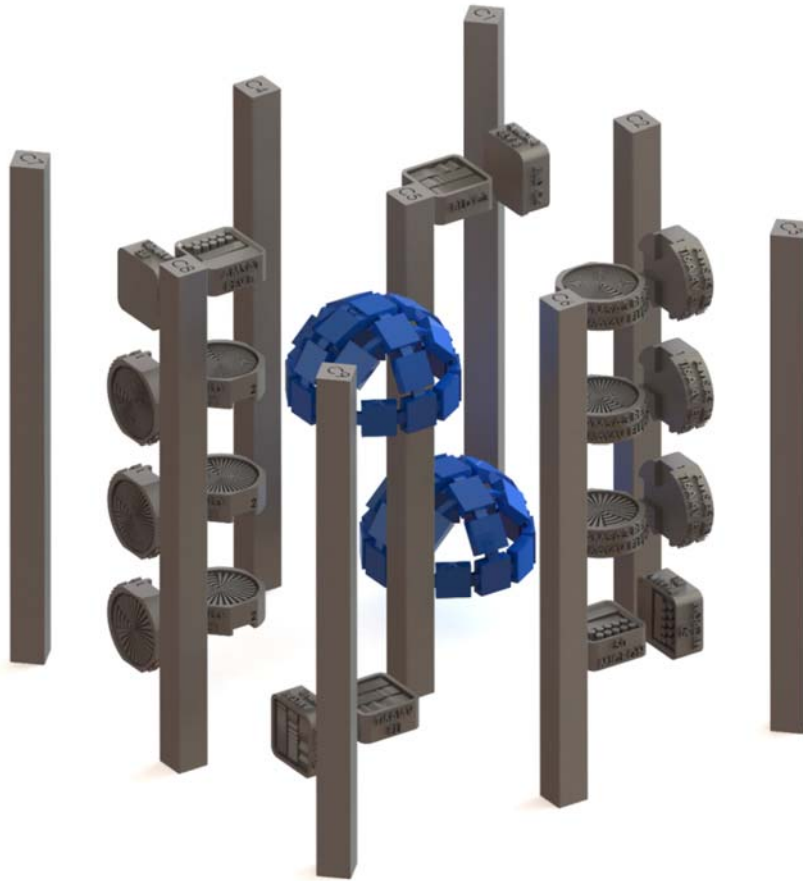


Figure 7-40: CAD rendering of the two hemi-spheres, in blue. Shown as part of the complete artefact set.

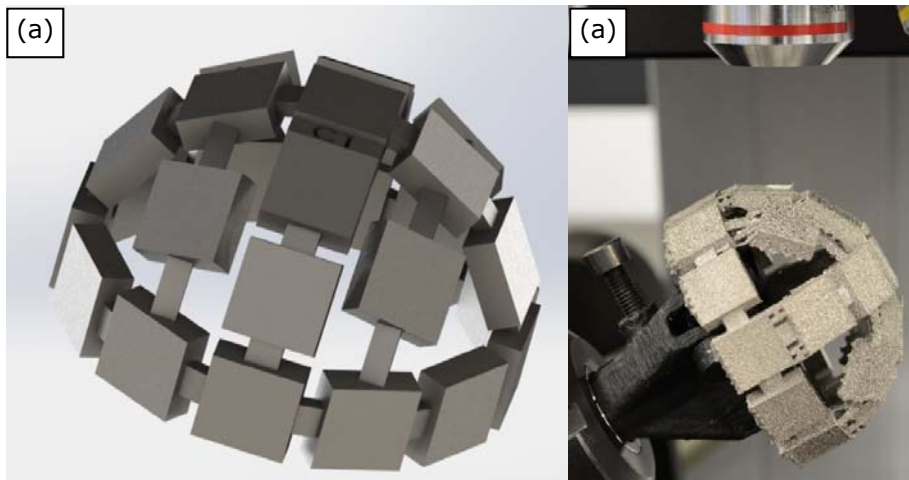


Figure 7-41: Hemi-sphere artefact. (a) CAD rendering, (b) a hemi-sphere mounted on a fixture for Alicona G4 measurement.

Table 39: Hemi-sphere surface angles to the horizontal and number of samples.

Angle to the horizontal (degrees)	Number of samples
90	12
60	4
52.24	4
30	4
0	1

Charts of surface roughness, S_a , at each of the measured build angles for builds one to four are shown in Figure 7-42: to Figure 7-45:.. Each chart includes the 95% confidence intervals for the mean error bars. The mean surface roughness for all four builds vs build angle is shown in Figure 7-46:.. The mean surface roughness for all builds is greatest for the surfaces built at 60° to the horizontal. The mean roughness decreases consistently as the gradient reduces for all four builds. These results are consistent with results obtained for profile roughness measurement, R_a , by Triantaphyllou et al [62].

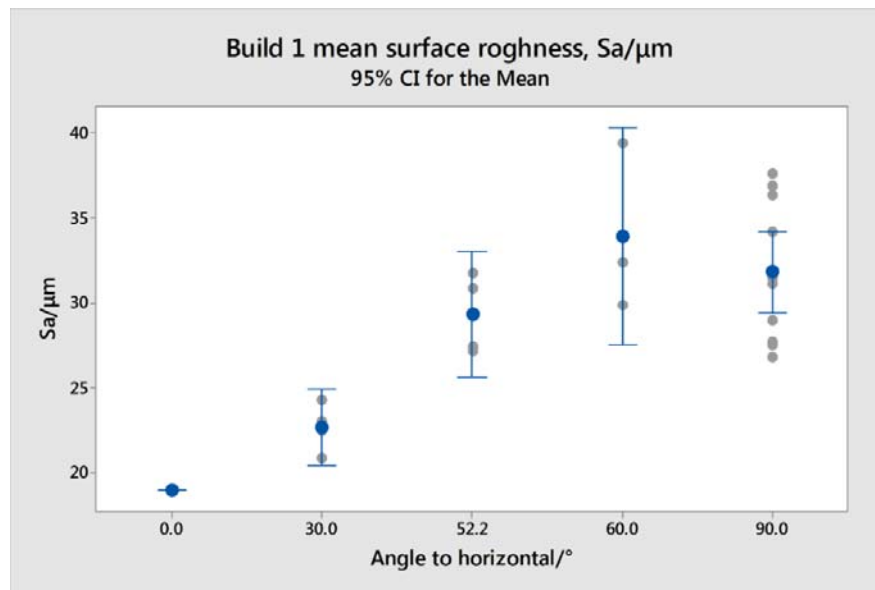


Figure 7-42: Build 1 surface roughness (S_a) at each build angle.

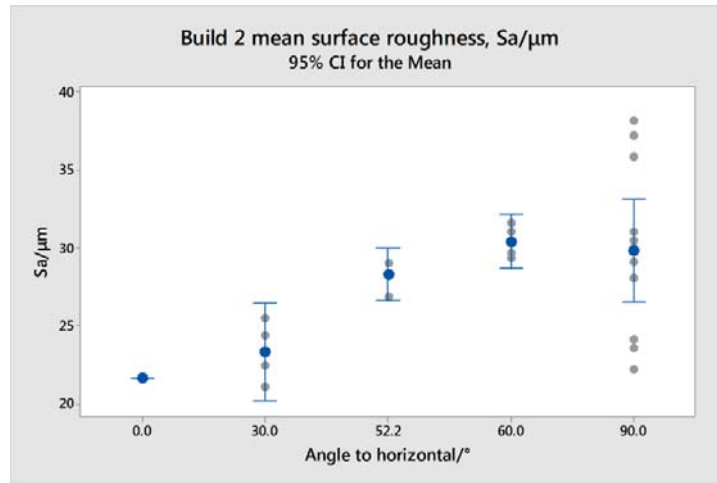


Figure 7-43: Build 2 surface roughness (S_a) at each build angle.

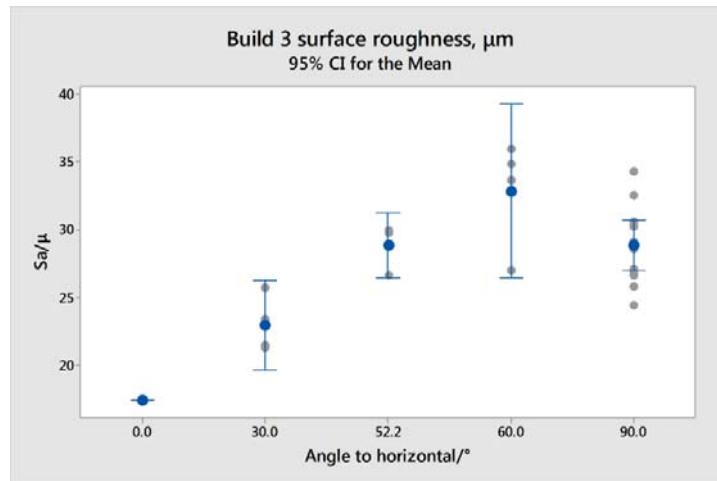


Figure 7-44: Build 3 surface roughness (S_a) at each build angle.

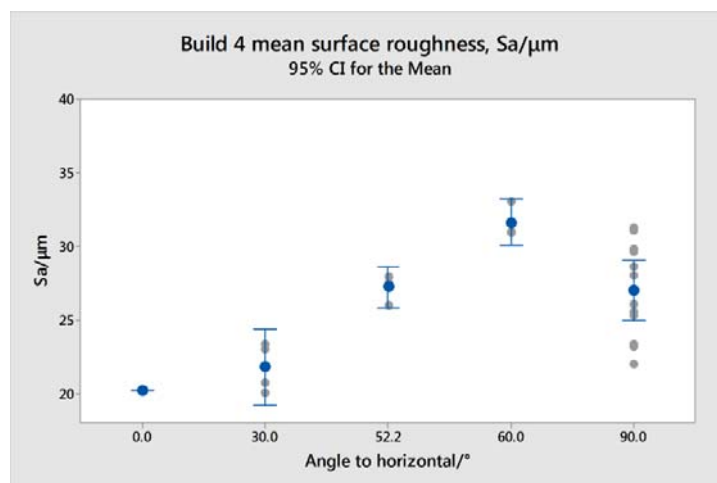


Figure 7-45: Build 4 surface roughness (S_a) at each build angle.

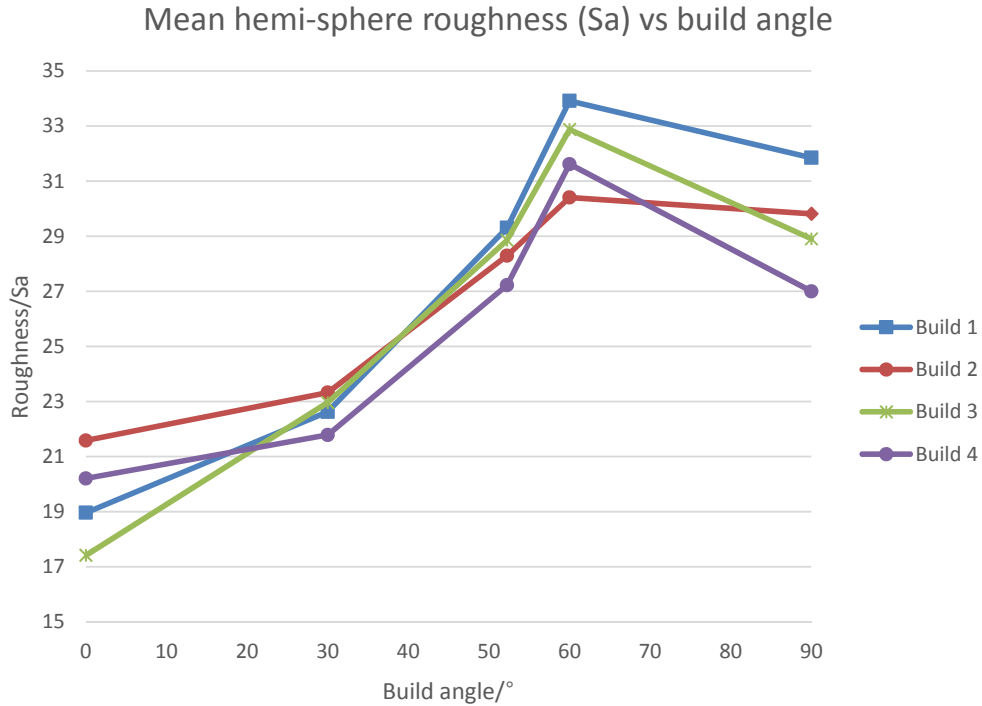


Figure 7-46: Mean roughness (Sa) of the hemi-sphere vs build angle for four builds.

7.6 Surface measurement artefacts conclusions

A suite of surface-specific AM measurement artefacts has been proposed. These artefacts are small, economical to build and suitable for inclusion in every AM build. They include built-in traceability, including part number, serial number, build layer thickness and raw material type and have been designed for easy measurement on standard metrology equipment. The artefact design may be tailored to the specific application to produce the greatest sensitivity to process changes. The artefacts may be used for process verification and to investigate optimum production component build orientation. Deviation analysis between the artefacts and the CAD model have highlighted significant differences in dimensional build errors for artefacts built vertically and horizontally. The data may be used to modify build models to ensure complete clean-up of critical surfaces during post-processing on as-built surfaces.

A bullet-point summary of the measurement suite results for the exemplar builds is given here:

- No significant difference in mean S_a at different build heights.
- No significant difference in mean S_a between surfaces aligned radial or tangentially to the electron beam axis.
- Significant difference in surface texture between builds with different powder re-use cycles and material batch change (further work required to differentiate between the individual effects).
- Significant variation in vertical surface texture, which was dependent upon the surface direction.
- Remarkably similar local defects at the same location on all builds at specific positions within the build chamber. These asymmetrical surface texture anomalies indicate there are systematic problems with the build system itself, and, because there are surfaces that do not have these issues, there is significant potential to correct the underlying cause and hence produce surfaces that are more consistent across the entire build volume.
- Significant difference in surface texture depending upon the surface build angle to the horizontal. There is an approximately linear increase in mean roughness, S_a , from approximately 20 μm to 32 μm as the build angle from horizontal increases from 0° to 60°, respectively, and then a reduction to approximately 29 μm S_a at 90° to the horizontal.

Chapter 8 Discussion and conclusions

“This is not the end. It is not even the beginning of the end. But it is, perhaps, the end of the beginning. ”

Winston Churchill (1874-1965)

Computer defined AM and computed tomography are both historically recent inventions; Chuck Hull’s AM patents in 1986 and Hounsfield and Cormack’s CT Nobel prize in 1979 signalling the start of revolutions in manufacturing and imaging, respectively. CT has seen widespread adoption, initially in the medical field, but now the potential is being realised for industrial applications. CT system accuracy is improving greatly and the CT industry has great interest in partnering with AM research institutions, system manufacturers and end users. The interlaboratory comparison reported here included the participation of one of the field leaders, Nikon Metrology. Interest in Stage 2 of the interlaboratory comparison from others in the CT industry has been strong. The CT manufacturers are aware of the potential of AM for high-value fields such as aerospace, medical and automotive. Witness the attendance of CT manufacturers at AM-specific conferences worldwide. These manufacturers are aware of the excellent match between AM and CT.

AM allows the manufacture of complex components with geometries and internal features that cannot be manufactured with subtractive processes, such as milling, turning and grinding. This ability of AM is, of course, the prime advantage of AM processes. Conventional metrology techniques, including stylus and optical surface texture measurement methods with their line-of-sight restrictions cannot be used to measure these features. CT is the prime method for non-destructive testing of these components. CT development is on-going with resolution and accuracy improving constantly, partly driven by the requirements of the AM industry.

The work reported here takes the first steps in using industrial CT for the measurement and areal characterisation of as-built AM surfaces. This is important as the as-built surface is being

used in functional applications such as the medical applications reported here. Measurement of the AM surface is important for determining how much material stock should be added to permit complete clean-up of surfaces that require post-processing such as O-ring grooves or cylinder bores. As awareness of the potential of AM increases, applications of the technology will also grow and the measurement technologies and methods need to be in place to allow accept/reject evaluations to be made successfully using recognised standards.

Chapter 3 reported on the development of a novel technique to extract quantitative areal surface texture information (per ISO 25178-2) from CT scans of AM components. The technique included comparison to measurements of the same surface area using a focus variation instrument. The extraction and characterisation technique itself was shown to be robust and sensitive to measurement changes such as those produced when the system filament is changed. The values of measurements for the Nikon XT H 225 were remarkably similar to those for the focus variation instrument; for example, the values of S_a obtained from the CT data were within 2.5% of the focus variation measurements. Repeatability of the CT measurement was shown to be good, including the measurements taken when the artefact was removed and replaced back into the fixture (similar to potential industrial lot testing) for which the standard deviation was 0.013 μm for a mean S_a value of 29.6 μm . These tests were performed on one CT machine with one artefact. For industrial applications it was considered important to verify other machines would produce acceptable results and that the process itself should be shown to be applicable to other industrial materials and AM processes.

Chapter 4 reported on the CT-STARR Stage 1 interlaboratory comparison. An EBM artefact was measured using four CT machines, three Nikon MCT225 metrology CTs and the XT H 225 industrial CT used in the development of the extraction method. The results confirmed the robustness of using CT for the extraction of surface texture data from AM parts. As an example, the value of mean surface roughness, S_a , for all the metrology CTs was within a remarkable 0.5% of the results obtained using the focus variation instrument, with good

repeatability and reproducibility of all measurement results. These baseline results would indicate the artefact measurement and analysis process is robust and will guide the development of the Stage 2 CT-STARR interlaboratory comparison, which will include a greater variety of CT machine configurations. Mathematical surface determination and scaling correction (as required) of the dimensional artefact included in every scan resulted in dimensional numbers very similar to reference CMM measurements. Using a dimensional artefact during the CT measurement of AM surfaces provides good process validation and should be invaluable during CT-STARR Stage 2. The three metrology CTs had a different voxel size (8 μm) to the industrial CT (17 μm). The influence of voxel size and surface determination on measurement accuracy were discussed. These influences, together with the measured influence of changing the filament reported in Chapter 3 (approximately -0.75% change in dimensions and -0.8% change in S_a value pre-to-post filament change) highlighted the importance of generating an understanding of individual factors that may affect the accuracy of measured results. This understanding is important as it allows the creation of a recommended measurement and analysis envelope within which to work.

The influence of three measurement and processing factors that were considered to have the potential to affect the accuracy of results were investigated in Chapter 5. These parameters were chosen to be, as far as possible, applicable to most CT systems and AM surfaces. The intention was to choose factors that were important but not machine-specific. The analysis of scanned Rubert comparator plates showed that using local iterative surface determination during CT reconstruction will provide the most accurate results for surface texture parameter generation. This is important as the selection of surface determination method is not intuitive. The inclusion of a known artefact within the user's scans will aid in verification of surface determination verification.

The voxel size effects the extracted parameter data. At larger voxel sizes the resolution may not be sufficient to allow full characterisation of the surface at the required scale of interest. If the voxel size is too large to characterise the surface, further increases in voxel size will

reduce the surface roughness value. Initial results suggest that, for an AM surface, a voxel size of one half or less than the surface S_a may be sufficient for full characterisation. This basic result is easily implemented as the resultant voxel size of a reconstruction is displayed for the CT operator prior to beginning a scan.

A comparison of areal parameters computed on the same surface section of a Ti6Al4V SLM part as an internal and external feature has been performed. The initial results indicated that there was no significant difference between the mean values of the generated surface texture parameters for the internal and external measurements. This is important as there needs to be confidence that the internal (hence less verifiable) surfaces are equivalent to the external (and more easily verifiable) surfaces. These results should provide valuable information to aid in the optimisation of the CT surface texture measurement and extraction process for research and industrial applications.

AM processes have the capability to produce surfaces and re-entrant features that enhance component functionality in applications such as bio-attachment, battery design, heat-transfer systems, paint and coating adhesion. There are existing applications using as-built AM surfaces that include re-entrant features. The ability to measure and characterise designed and as-built re-entrant surfaces accurately will be the key to performance optimisation for some applications. These surfaces present measurement and data analysis challenges that require the ability to image and extract meaningful data from complex point clouds or meshes rather than a uniform grid typically generated by line-of-sight instrumentation processes. A method for extraction of surface texture parameters from re-entrant AM surfaces was demonstrated in Chapter 6. Actual surface area and volume data were extracted and compared to projected (grid) areas and volumes for these data. Two example generated structured surfaces were also discussed and given as an illustration of the process. A new parameter, Sdr_{prime} , has been suggested. This parameter is the percentage of additional surface (including re-entrant surfaces) contributed by the texture as compared to a plane the size of the measurement area. This new parameter was developed to provide a direct relation

to functional performance in applications where the actual surface area is important. There are significant errors in area (up to 11% for Sdr_{prime}) when re-entrant features of as-built SLM and EBM AM components are not measured and included in analyses. Including re-entrant features, using the techniques presented here, will provide more-accurate data required for analysis and optimisation of the functional performance of AM components. Collaborations have shown that AM components, for example percutaneous medical implants, with functional as-built surfaces are now being produced. In addition to the requirement to measure any re-entrant surfaces correctly, as discussed in Chapter 6, these critical applications require consistent production quality across the build chamber and between successive builds. Chapter 7 reported on the measurement and characterisation of an EBM build chamber used for manufacturing medical implants. A Ti6Al4V ELI measurement artefact set was included in four builds. Included in the artefact sets were a novel set of surface-specific measurement artefacts. These small artefacts highlighted the importance of build orientation within the chamber as the artefact features were significantly different depending upon their orientation. Deviation analysis showed there were areas built with missing material, vital for understanding the material allowance to be added prior to the build to ensure complete clean-up of post-AM machined surfaces. The surface-specific artefacts will provide cost-effective process monitoring and machine capability analysis. Only those required for the application need be used. Designs may be tailored to the particular build application. All the artefacts are small, with low material usage and short build times and will fit standard inspection machines, including SEM. Nine square bars were included in each of the four builds. A total of 16 measurements were taken on each bar each of the four builds for a total of 576 measurements. An ANOVA was performed on the data. The surface measurements were sensitive to the differences in build orientation, to both the angle to the horizontal and to the facing-direction of vertical surfaces. The difference between raw material batches and material re-use was also detected. There were significant local defects on several bars with these defects appearing at the same locations on bars in all four builds. There were many

bars with no visible surface defects. These repeating asymmetric and non-uniform results for the bar measurements suggest that there are system anomalies that may be addressed and corrected to create a more-uniform build chamber. This correction may benefit not just the surface texture but perhaps also the internal structure of components.

The novel aspects of the present work are outlined in the following section. The work performed in this research includes novel extraction of areal surface texture from CT. A multi-step process was developed and the accuracy of the measurement and characterisation technique were reported. An interlaboratory comparison was performed using machines at four laboratories. The repeatability and reproduceability of the results using the developed measurement and extraction technique were excellent, with all five measurements performed on all of the three metrology CTs producing surface roughness (S_a) values within 0.5% of the mean reference focus variation measurements. Information and lessons learned will be incorporated into an expanded stage 2 interlaboratory comparison. Factors affecting the accuracy of the extraction process have been investigated, including the effect of changing the CT filament, the effects of CT surface determination methods and the measurement and characterisation of internal, compared to external, AM surfaces. Re-entrant as-built surfaces are now being used in engineering applications and structured AM surfaces are being designed for industrial applications. A new surface texture parameter, Sdr_{prime} , has been proposed. This novel parameter will include information from re-entrant surfaces and is designed to be functionally relevant and applicable to as-built re-entrant surfaces and structured AM surfaces. Surface consistency throughout the AM build platform and between builds is critical for these applications and for components that may require post-processing. A newly designed set of small surface-specific artefacts were included that can be used for design and build orientation optimisation and can be included in successive builds for process verification. An investigation of AM build chamber consistency was performed using an exemplar EBM AM

build. The results highlighted significant variation in surface texture within each build and between builds.

This initial work will provide a foundation for further research into the use of CT for the measurement and characterisation of AM surfaces. AM machines and CT machines are constantly improving and the techniques introduced here will still be applicable as these processes improve. There is potential for a range of future work to expand the AM surface texture, and particularly surface-from-CT, knowledge base.

Chapter 9 Future work

“The man who has no more problems to solve is out of the game.”

Elbert Hubbard (1856-1915)

9.1 Automated surface-from-CT

At this stage, if the AM surface can be measured using conventional metrology techniques, such as focus variation used here, then generally the surface should be measured using these techniques because of their greater resolution and accuracy. However, there are distinct advantages of CT measurements, other than just the ability to image internal features. CT imaging creates a 3D point cloud of the entire component and this data can be used for comparison to the CAD design. The deviation analysis work reported here was performed using this technique. This alignment, using component features, can be used to locate surfaces-of-interest within (or on the outside) of the component. The extraction techniques reported here involved manually selecting the area of interest from the scanned component. This was then followed by a multi-stage process of alignment and conversion to allow comparison to a master surface and the generation of areal parameters per ISO 25178-2. The technology is in place to be able to create a software system to automate the surface measurement, analysis and verification process:

Once the CAD model is entered into the proposed software system, including location and required surface texture parameter and value, for example S_a 25 μm for a 20 mm x 20 mm section of an internal surface, then it is envisaged that the following may be automated (“one click”), after performing the CT scan:

- Adjust the surface determination and scaling based on an artefact included in the scan
- Select the ROI in the scan
- Convert the ROI to a mesh
- Align the mesh to the component model using defined datums

- Locate the exact section (or any number of sections) with the surface requirement
- Extract the surface region of interest
- Convert to a height map
 - (or analyse mesh directly, which allows inclusion of re-entrant features)
- Crop to the correct size, either pre-determined or calculated based on ISO Standards
- Level and filter per ISO 25178-3
- Generate the required parameter set
- Compare the parameter data value to the required value
- Generate report / SPC etc.

This whole process may be automated for all the surfaces with required specific and general (default drawing) texture values. This process, as with the manual process, requires that the measurement resolution and surface texture requirement are compatible. If the resolution is not sufficient to resolve the surface at the scale-of-interest required then the data will not be valid.

9.2 Scaling and surface determination correction

Corrections to the extracted surface texture data, based on the surface determination and global scaling errors extracted from the dimensional artefacts will be investigated. The dimensional artefacts included in the scans reported here were able to differentiate between these two types of errors and mathematical compensation based on these errors produced significant increases in dimensional accuracy. Adjustment of the extracted surface based on the dimensional compensation values has potential to reduce measurement errors. On completion of the development of manual compensation techniques, further work will be performed on automating the compensation process.

9.3 Further CT chamber analysis

Further characterisation of the Nikon XT H 225 CT chamber will be performed. This will include the use of different AM surfaces to refine the ratio between the maximum acceptable voxel size and component surface roughness. A similar evaluation will be performed using additional types of CT system, including CT microscopes, such as the Zeiss Xradia series. ROI scanning will be investigated, whereby a local section of a large component may be scanned at high resolution. Guidelines for component suitability for each machine type will be generated.

9.4 CT-STARR Stage 2

The results from Stage 1 RR reported here will guide modification of the methodology for the expanded Stage 2 RR. Changes to the methodology will include a fixture modification to rotate the dimensional artefact to avoid horizontal edges and reduce cone-beam artefacts. A change to the surface texture artefact will be investigated, based on the minimum S_a to voxel size ratio required to fully characterise the AM surface. Work will be performed with potential Stage 2 participants to verify the resolution requirements for a variety of CT systems prior to the start of Stage 2.

9.5 Re-entrant features and functional analysis

Functional validation of re-entrant surface measurements will be performed to verify the practicality of the parameter Sdr_{prime} . Functional applications will include bio-attachment, chemical bonding, fluid flow, heat transfer and electrical conduction. Additional parameters will be created as necessary, based on their sensitivity to the variation in specific functional performance and a parameter toolbox applicable to CT surface analysis will be generated.

9.6 Surface-specific measurement artefacts

The design of the surface-specific artefacts will be revised, based on the initial batches and the results of long-term build programs. Modifications will be performed to optimise the

sensitivity of specific artefact features to build variation. The artefact set provided significant information about the build process, however refining the artefacts to tailor the design to functional performance, together with build platform and powder configuration will eliminate the manufacture of unnecessary artefacts or those insensitive to functionally relevant build performance.

Chapter 10 References

- [1] P. Markillie, "A third industrial revolution," *The Economist*, vol. Special Report 2012, 2012.
- [2] (2017). *Jomon Culture (ca 10,500-ca. 300 B.C.)*.
- [3] N. W. Encyclopedia. (2017, September 2, 2017). *Igloo*. Available: <http://www.newworldencyclopedia.org/entry/Igloo>
- [4] C. Hull, "Apparatus for production of three-dimensional objects by stereolithography," 1986.
- [5] The Royal Academy of Engineering, "Additive manufacturing: opportunities and constraints," 2013.
- [6] J. Hagel, J. Brown, D. Kulasoorya, C. Giffi, and M. Chen. (2015, October 12, 2017). *The future of manufacturing*. Available: <https://dupress.deloitte.com/dup-us-en/industry/manufacturing/future-of-manufacturing-industry.html>
- [7] E. Sachs, E. Wylonis, S. Allen, M. Cima, and H. Guo, "Production of injection molding tooling with conformal cooling channels using the three dimensional printing process," *Polymer Engineering & Science*, vol. 40, pp. 1232-1247, 2000.
- [8] I. Gibson, D. W. Rosen, and B. Stucker, *Additive manufacturing technologies*: Springer, 2010.
- [9] UK Government Office for Science and Department for Business Innovation and Skills, "The future of manufacturing: A new era of opportunity and challenge for the UK," 2013.
- [10] EOS. (2017, 2017). *Aerospace: EADS and EOS - study demonstrates savings potential for DMLS in the aerospace industry*. Available: https://www.eos.info/press/customer_case_studies/eads
- [11] A. Winston. (2014). *Arup unveils its first 3D-printed structural steel building components*. Available: <https://www.dezeen.com/2014/06/11/arup-3d-printed-structural-steel-building-components/>
- [12] T. Rockstroh, D. Abbott, K. Hix, and J. Mook. (2013). *Additive manufacturing at GE Aviation*. Available: <https://www.industrial-lasers.com/articles/print/volume-28/issue-6/features/additive-manufacturing-at-ge-aviation.html>
- [13] S. K. Everton, M. Hirsch, P. Stravroulakis, R. K. Leach, and A. T. Clare, "Review of in-situ process monitoring and in-situ metrology for metal additive manufacturing," *Materials & Design*, vol. 95, pp. 431-445, 4/5/ 2016.
- [14] P. Stavroulakis and R. Leach, "Review of post-process optical form metrology for industrial-grade metal additive manufactured parts," *Review of Scientific Instruments*, vol. 87, p. 041101, 2016.
- [15] A. Townsend, N. Senin, L. Blunt, R. K. Leach, and J. S. Taylor, "Surface texture metrology for metal additive manufacturing: a review," *Precision Engineering*, vol. 46, pp. 34-47, 2016.
- [16] ISO 25178-2, "Geometrical product specifications (GPS) Surface texture: Areal - Part 2: Terms, definitions and surface texture parameters," ed: ISO, 2012.
- [17] A. Townsend, L. Blunt, and P. Bills, "Investigating the capability of microfocus x-ray computed tomography for areal surface analysis of additively manufactured parts.," in *Dimensional accuracy and surface finish in additive manufacturing, ASPE 2016 Summer Topical Meeting*, Raleigh, NC., 2016.
- [18] A. Townsend, L. Pagani, P. Scott, and L. Blunt, "Areal surface texture data extraction from x-ray computed tomography reconstructions of metal additively manufactured parts," *Precision Engineering*, vol. 48, pp. 254-264, 2016.
- [19] J. Angel and L. De Chiffre, "CIA-CT comparison Inter laboratory comparison on industrial computed tomography Final report," Technical university of Denmark 2013.
- [20] A. Stolfi and L. De Chiffre, "InteraqCT comparison on assemblies technical protocol," TEchnical university of Denmark 2015.

- [21] S. Carmignato, A. Pierobon, and E. Savio, "CT Audit Interlaboratory comparison of computed tomography systems for dimensional metrology final report (overview)," University of Padova 2012.
- [22] A. Townsend, R. Racasan, P. Bills, and L. Blunt, "Development of an interlaboratory comparison investigating the generation of areal surface texture data per ISO 25178 from XCT," presented at the 7th conference on industrial computed tomography, Leuven, Belgium, 2017.
- [23] A. Townsend, R. Racasan, P. Bills, A. Thompson, N. Senin, R. K. Leach, *et al.*, "Results from an interlaboratory comparison of areal surface texture parameter extraction from X-ray computed tomography of additively manufactured parts," presented at the 17th int. euspen Conference, Hannover, Germany, 2017.
- [24] A. Townsend, L. Pagani, L. Blunt, P. J. Scott, and X. Jiang, "Factors affecting the accuracy of areal surface texture data extraction from X-ray CT," *CIRP Annals - Manufacturing Technology*, 2017.
- [25] A. Townsend, L. Pagani, P. J. Scott, and L. Blunt, "Measurement and characterisation of additively manufactured re-entrant features," presented at the Joint Special Interest Group, euspen and ASPE, Dimensional accuracy and surface finish in additive manufacturing, KU Leuven, Belgium, 2017.
- [26] A. Townsend and L. Blunt, "Surface-specific additive manufacturing test artefacts," presented at the The 16th international conference on metrology and properties of engineering surfaces, Gothenburg, Sweden, 2017.
- [27] C. Brown. (n.d., 3-8-17). *Mechanical Engineering*. Available: <http://www.wpi.edu/academics/facultydir/cab.html>
- [28] "ASTM F2792-12a, standard terminology for additive manufacturing technologies (Withdrawn 2015)," ed. West Conshohocken, PA: ASTM International, 2012.
- [29] R. Harris. (n.d., June 2015). *About Additive Manufacturing*. Available: <http://www.lboro.ac.uk/research/amrg/about/the7categoriesofadditivemanufacturing/powderbedfusion/>
- [30] G. Aviation. (2017, September 5, 2017). *GE Aviation*. Available: <https://www.geaviation.com/>
- [31] G. Healthcare. (2017, September 5, 2017). *GE Healthcare*. Available: <http://www3.gehealthcare.com/en>
- [32] B. McKenna. (2017). *General Electric-controlled Arcam kicks off 3D printing's Q4 earnings season*. Available: <https://www.fool.com/investing/2017/02/14/general-electric-controlled-arcam-3d-printing-earn.aspx>
- [33] Renishaw. (2017, September 5, 2017). *Metal powders for AM*. Available: <http://www.renishaw.com/en/metal-powders-for-am--31457>
- [34] Arcam. (2017, September 5, 2017). *Ti6Al4V ELI Titanium alloy*. Available: <http://www.arcam.com/wp-content/uploads/Arcam-Ti6Al4V-ELI-Titanium-Alloy.pdf>
- [35] Arcam. (2017, 31 August 2017). *EBM electron beam melting*. Available: <http://www.arcam.com/technology/electron-beam-melting/>
- [36] Arcam. (2017, 2017). *EBM hardware*. Available: <http://www.arcam.com/technology/electron-beam-melting/hardware/>
- [37] I. Gibson and D. Shi, "Material properties and fabrication parameters in selective laser sintering process," *Rapid Prototyping Journal*, vol. 3, pp. 129-136, 1997.
- [38] D. J. Whitehouse, *Surfaces and their measurement*. London: Hermes Penton Science, 2002.
- [39] G. Schuetz. (2017). *Metrology, Start to finish*. Available: <https://www.mahr.com/en-in/Services/Production-metrology/Know-how/Gaging-Tips/Surface-Measurement-Gaging-Tips/?ContentID=19019&Overview=0>
- [40] AZO materials. (2016). *The relationship between surface topographies and their processing and performance*. Available: <https://www.azom.com/article.aspx?ArticleID=12978>

- [41] NASA. (2015). *New horizons returns first of the best images of Pluto*. Available: <https://www.nasa.gov/feature/new-horizons-returns-first-of-the-best-images-of-pluto>
- [42] J. S. Taylor, "Surface Characteristics of Additive-Manufactured Components," presented at the 15th International conference on metrology and properties of engineering surfaces, University of North Carolina at Charlotte, 2015.
- [43] C. Y. Lin, T. Wirtz, F. LaMarca, and S. J. Hollister, "Structural and mechanical evaluations of a topology optimized titanium interbody fusion cage fabricated by selective laser melting process," *Journal of Biomedical Materials Research Part A*, vol. 83, pp. 272-279, 2007.
- [44] ISO 4287, "Geometrical product specification (GPS) Surface texture: Profile method. Terms, definitions and surface texture parameters," ed: British Standards Institute, 2000.
- [45] R. K. Leach, L. Brown, X. Jiang, R. Blunt, M. Conroy, and D. Mauger, "Guide to the measurement of smooth surface topography using coherence scanning interferometry. NPL Measurement good practice guide No. 108," 2008.
- [46] P. Boyd, "These industries are the future of additive manufacturing," *Industry Week*, 2016.
- [47] B. Vandenbroucke and J.-P. Kruth, "Selective laser melting of biocompatible metals for rapid manufacturing of medical parts," *Rapid Prototyping Journal*, vol. 13, pp. 196-203, 2007.
- [48] N. M. Huang, "Analyzing the Surface Finish of Knee Implants to Determine Criteria for Applications in Direct Metal Laser Sintering," *2012 NCUR*, 2012.
- [49] C. R. Garcia, R. C. Rumpf, H. H. Tsang, and J. H. Barton, "Effects of extreme surface roughness on 3D printed horn antenna," *Electronics Letters*, vol. 49, pp. 734-736, 2013.
- [50] A. Spierings, T. Starr, and K. Wegener, "Fatigue performance of additive manufactured metallic parts," *Rapid Prototyping Journal*, vol. 19, pp. 88-94, 2013.
- [51] D. Gu and Y. Shen, "Balling phenomena in direct laser sintering of stainless steel powder: Metallurgical mechanisms and control methods," *Materials & Design*, vol. 30, pp. 2903-2910, 2009.
- [52] A. Safdar, H. Z. He, L. Y. Wei, A. Snis, and L. E. Chavez de Paz, "Effect of process parameters settings and thickness on surface roughness of EBM produced Ti-6Al-4V," *Rapid Prototyping Journal*, vol. 18, pp. 401-408, 2012.
- [53] M. Jamshidinia and R. Kovacevic, "The influence of heat accumulation on the surface roughness in powder-bed additive manufacturing," *Surface Topography: Metrology and Properties*, vol. 3, p. 014003, 2015.
- [54] H. Tang, M. Qian, N. Liu, X. Zhang, G. Yang, and J. Wang, "Effect of Powder Reuse Times on Additive Manufacturing of Ti-6Al-4V by Selective Electron Beam Melting," *JOM*, vol. 67, pp. 555-563, 2015.
- [55] A. T. Beaucamp, Y. Namba, P. Charlton, and A. A. Graziano, "Finishing of additively manufactured titanium alloy by shape adaptive grinding (SAG)," *Surface Topography: Metrology and Properties*, vol. 3, p. 024001, 2015.
- [56] J. Karlsson, A. Snis, H. Engqvist, and J. Lausmaa, "Characterization and comparison of materials produced by Electron Beam Melting (EBM) of two different Ti-6Al-4V powder fractions," *Journal of Materials Processing Technology*, vol. 213, pp. 2109-2118, 2013.
- [57] M. Svensson and U. Ackelid, "Titanium alloys manufactured with electron beam melting-mechanical and chemical properties," in *Proceedings of the Materials and Processes for Medical Devices Conference*, 2010, pp. 189-194.
- [58] M. C. Badrossamay, THC, "Layer formation studies in selective laser melting of steel powders," in *Proc. SFF Symp., Austin, Texas, USA*, 2006, pp. 268-279.

- [59] G. Pyka, G. Kerckhofs, I. Papantoniou, M. Speirs, J. Schrooten, and M. Wevers, "Surface Roughness and Morphology Customization of Additive Manufactured Open Porous Ti6Al4V Structures," *Materials*, vol. 6, pp. 4737-4757, 2013.
- [60] S. Van Bael, G. Kerckhofs, M. Moesen, G. Pyka, J. Schrooten, and J.-P. Kruth, "Micro-CT-based improvement of geometrical and mechanical controllability of selective laser melted Ti6Al4V porous structures," *Materials Science and Engineering: A*, vol. 528, pp. 7423-7431, 2011.
- [61] G. Kerckhofs, G. Pyka, M. Moesen, S. Van Bael, J. Schrooten, and M. Wevers, "High-Resolution Microfocus X-Ray Computed Tomography for 3D Surface Roughness Measurements of Additive Manufactured Porous Materials," *Advanced Engineering Materials*, vol. 15, pp. 153-158, 2013.
- [62] A. Triantaphyllou, C. L. Giusca, G. D. Macaulay, F. Roerig, M. Hoebel, R. K. Leach, et al., "Surface texture measurement for additive manufacturing," *Surface Topography: Metrology and Properties*, vol. 3, p. 024002, 2015.
- [63] K. Mumtaz and N. Hopkinson, "Top surface and side roughness of Inconel 625 parts processed using selective laser melting," *Rapid Prototyping Journal*, vol. 15, pp. 96-103, 2009.
- [64] A. Diatlov, D. Buchbinder, W. Meiners, K. Wissenbach, and J. Bültmann, "Towards surface topography: Quantification of Selective Laser Melting (SLM) built parts," *Innovative Developments in Virtual and Physical Prototyping - Bartolo et al. (eds)*, 2012.
- [65] M. Król, L. Dobrzański, and I. C. Reimann, "Surface quality in selective laser melting of metal powders," *Archives of Materials Science*, vol. 88, p. 88, 2013.
- [66] J. Slotwinski, E. Garboczi, P. Stutzman, C. Ferraris, S. Watson, and M. Peltz, "Characterization of metal powders used for additive manufacturing," *J. Res. Natl. Inst. Stand. Technol.*, vol. 19, 2014.
- [67] G. Pyka, A. Burakowski, G. Kerckhofs, M. Moesen, S. Van Bael, J. Schrooten, et al., "Surface modification of Ti6Al4V open porous structures produced by additive manufacturing," *Advanced Engineering Materials*, vol. 14, pp. 363-370, 2012.
- [68] E. Yasa and J. P. Kruth, "Application of Laser Re-Melting on Selective Laser Melting Parts," *Advances in Production Engineering & Management*, vol. 6, pp. 259-270, 2011.
- [69] E. Yasa, J. Deckers, and J.-P. Kruth, "The investigation of the influence of laser re-melting on density, surface quality and microstructure of selective laser melting parts," *Rapid Prototyping Journal*, vol. 17, pp. 312-327, 2011.
- [70] J. Yang, H. Ouyang, C. Xu, and Y. Wang, "Top surface quality research for direct metal laser fabrication," *Rapid Prototyping Journal*, vol. 18, pp. 4-15, 2012.
- [71] I. Yadroitsev and I. Smurov, "Surface morphology in selective laser melting of metal powders," *Physics Procedia*, vol. 12, pp. 264-270, 2011.
- [72] A. Spierings, N. Herres, and G. Levy, "Influence of the particle size distribution on surface quality and mechanical properties in AM steel parts," *Rapid Prototyping Journal*, vol. 17, pp. 195-202, 2011.
- [73] M. Simonelli, Y. Y. Tse, and C. Tuck, "On the Texture Formation of Selective Laser Melted Ti-6Al-4V," *Metallurgical and Materials Transactions A*, vol. 45, pp. 2863-2872, 2014.
- [74] J. P. Kruth, E. Yasa, and J. Deckers, "Roughness improvement in selective laser melting," in *Proceedings of the 3rd International Conference on Polymers and Moulds Innovations*, 2008, pp. 170-183.
- [75] D. Buchbinder, H. Schleifenbaum, S. Heidrich, W. Meiners, and J. Bültmann, "High power selective laser melting (HP SLM) of aluminum parts," *Physics Procedia*, vol. 12, pp. 271-278, 2011.
- [76] E. Brinksmeier, G. Levy, D. Meyer, and A. Spierings, "Surface integrity of selective-laser-melted components," *CIRP Annals-Manufacturing Technology*, vol. 59, pp. 601-606, 2010.

- [77] M. Badrossamay and T. Childs, "Further studies in selective laser melting of stainless and tool steel powders," *International Journal of Machine Tools and Manufacture*, vol. 47, pp. 779-784, 2007.
- [78] N. Ahmed, K. Voisey, and D. McCartney, "Investigation into the effect of beam shape on melt pool characteristics using analytical modelling," *Optics and Lasers in Engineering*, vol. 48, pp. 548-554, 2010.
- [79] F. Abe, K. Osakada, M. Shiomi, K. Uematsu, and M. Matsumoto, "The manufacturing of hard tools from metallic powders by selective laser melting," *Journal of materials processing technology*, vol. 111, pp. 210-213, 2001.
- [80] E. Yasa, J. P. Kruth, and J. Deckers, "Manufacturing by combining selective laser melting and selective laser erosion/laser re-melting," *CIRP Annals-Manufacturing Technology*, vol. 60, pp. 263-266, 2011.
- [81] F. Calignano, D. Manfredi, E. P. Ambrosio, L. Iuliano, and P. Fino, "Influence of process parameters on surface roughness of aluminum parts produced by DMLS," *The International Journal of Advanced Manufacturing Technology*, vol. 67, pp. 2743-2751, 2013/08/01 2013.
- [82] J. Ramos, J. Murphy, K. Wood, D. Bourell, and J. Beaman, "Surface roughness enhancement of indirect-SLS metal parts by laser surface polishing," in *Proceedings of the 12th Solid Freeform Fabrication Symposium.*, The University of Texas at Austin, Austin, TX., 2001, pp. 28-38.
- [83] S. Abe, Y. Higashi, I. Fuwa, N. Yoshida, and T. Yoneyama, "Milling-combined laser metal sintering system and production of injection molds with sophisticated functions," in *Towards Synthesis of Micro-/Nano-systems*, ed: Springer, 2007, pp. 285-290.
- [84] N. Patil, D. Pal, M. Anam, H. Gong, H. Gu, S. Dilip, et al., "Predictive modeling capabilities for dimensional accuracy and surface finish in Metal Laser Melting based Additive Manufacturing," in *Dimensional accuracy and surface finish in additive manufacturing, ASPE 2014 Spring Topical Meeting*, University of Berkeley, Berkeley, CA, 2014.
- [85] G. Strano, L. Hao, R. M. Everson, and K. E. Evans, "Surface roughness analysis, modelling and prediction in selective laser melting," *Journal of Materials Processing Technology*, vol. 213, pp. 589-597, 2013.
- [86] O. Oreshkin, M. Küpper, A. Temmler, and E. Willenborg, "Active reduction of waviness through processing with modulated laser power," *Journal of Laser Applications*, vol. 27, p. 022004, 2015.
- [87] E. Brandl, U. Heckenberger, V. Holzinger, and D. Buchbinder, "Additive manufactured AISi10Mg samples using Selective Laser Melting (SLM): Microstructure, high cycle fatigue, and fracture behavior," *Materials & Design*, vol. 34, pp. 159-169, 2012.
- [88] R. Morgan, C. Sutcliffe, and W. O'Neill, "Experimental investigation of nanosecond pulsed Nd: YAG laser re-melted pre-placed powder beds," *Rapid Prototyping Journal*, vol. 7, pp. 159-172, 2001.
- [89] V. K. Meena and Nagahanumaiah, "Optimization of EDM machining parameters using DMLS electrode," *Rapid Prototyping Journal*, vol. 12, pp. 222-228, 2006.
- [90] Y. Liu, Y. Yang, S. Mai, D. Wang, and C. Song, "Investigation into spatter behavior during selective laser melting of AISI 316L stainless steel powder," *Materials & Design*, vol. 87, pp. 797-806, 12/15/ 2015.
- [91] K. Abd-Elghany and D. Bourell, "Property evaluation of 304L stainless steel fabricated by selective laser melting," *Rapid Prototyping Journal*, vol. 18, pp. 420-428, 2012.
- [92] !!! INVALID CITATION !!! [89-95].
- [93] L. Blunt, "Why use areal surface texture measurement?," presented at the DMAC meeting, University of Huddersfield, 2006.
- [94] G. Krolczyk, P. Raos, and S. Legutko, "Experimental analysis of surface roughness and surface texture of machined and fused deposition modelled parts," *Tehnički Vjesnik-Technical Gazette*, vol. 21, pp. 217-221, 2014.

- [95] ISO FDIS 25178-606, "(GPS) Surface texture: areal -- part 606: Nominal characteristics of non-contact (focus variation) instruments," ed, 2015.
- [96] Machinery. (2017, 2017). *MM live 2011 preview - Birmingham NEC from 27-29 September*. Available: <http://www.machinery.co.uk/machinery-features/micro-machining-mm-live-event/36679/>
- [97] Alicona. (2017, 2017). *InfiniteFocus*. Available: <http://www.alicon.com/products/infinitefocus/>
- [98] ISO, "ISO/CD 25178-600," in *Geometrical product specifications (GPS) -- Surface texture: Areal -- Part 600: Metrological characteristics for areal-topography measuring methods*, ed: ISO, 2015.
- [99] T. V. Vorburger, J. Song, and N. Petraco, "Topography measurements and applications in ballistics and tool mark identifications()," *Surface topography : metrology and properties*, vol. 4, p. 013002, 12/17 2016.
- [100] R. Danzl, F. Helml, and S. Scherer, "Focus variation—a robust technology for high resolution optical 3D surface metrology," *Strojniški vestnik-Journal of mechanical engineering*, vol. 57, pp. 245-256, 2011.
- [101] L. Griffiths, "How does design for additive manufacturing measure up?," *TCT 205 2015*.
- [102] Rolls Royce, "AM Components Surface Roughness Assessment," 2014.
- [103] ASME, "ASME B46.1 (2009) Surface texture (surface roughness, waviness and lay)," ed. New York, 2009.
- [104] JIS Standards, "JIS B 0601:2013 Geometrical Product Specifications (GPS) - Surface texture: Profile method - Terms, definitions and surface texture parameters," ed, 2013.
- [105] D. Ahn, J. H. Kweon, S. Kwon, J. Song, and S. Lee, "Representation of surface roughness in fused deposition modeling," *Journal of Materials Processing Technology*, vol. 209, pp. 5593-5600, 8/1/ 2009.
- [106] R. I. Campbell, M. Martorelli, and H. S. Lee, "Surface roughness visualisation for rapid prototyping models," *Computer-Aided Design*, vol. 34, pp. 717-725, 2002.
- [107] B. N. Turner and S. A. Gold, "A review of melt extrusion additive manufacturing processes: II. Materials, dimensional accuracy, and surface roughness," *Rapid Prototyping Journal*, vol. 21, pp. 250-261, 2015.
- [108] S. Moylan, "Progress toward standardized additive manufacturing test artifacts," in *ASPE 2015 Spring Topical Meeting*, Raleigh, NC, 2015.
- [109] W. E. Frazier, "Metal additive manufacturing: A review," *Journal of Materials Engineering and Performance*, vol. 23, pp. 1917-1928, 2014.
- [110] K. S. Chan, M. Koike, R. L. Mason, and T. Okabe, "Fatigue life of titanium alloys fabricated by additive layer manufacturing techniques for dental implants," *Metallurgical and Materials Transactions A*, vol. 44, pp. 1010-1022, 2013.
- [111] M. Beard, O. Ghita, and K. E. Evans, "Using Raman spectroscopy to monitor surface finish and roughness of components manufactured by selective laser sintering," *Journal of Raman Spectroscopy*, vol. 42, pp. 744-748, 2011.
- [112] T. Grimm, G. Wior, and G. Witt, "Characterization of typical surface effects in additive manufacturing with confocal microscopy," *Surface Topography: Metrology and Properties*, vol. 3, p. 014001, 2015.
- [113] J. S. Taylor, "Physical processes linking input parameters and surface morphology in additive manufacturing," in *Achieving precision tolerances in additive manufacturing, ASPE 2015 Spring Topical Meeting*, North Carolina State University, Raleigh, NC., 2015.
- [114] A. Barari and S. Jamiolahmadi, "Estimation of surface roughness of additive manufacturing parts using finite difference method," in *Dimensional accuracy and surface finish in additive manufacturing, ASPE 2014 Spring Topical Meeting*, University of Berkeley, Berkeley, CA., 2014.
- [115] W. King, A. Anderson, D. Brown, R. Ferencz, N. Hodge, C. Kamath, *et al.*, "Modelling the Metal Additive Manufacturing Process at the Scales of the Part and the Powder," in

- 2015 *International Conference on Additive Manufacturing and 3D Printing*, Nottingham, UK, 2015.
- [116] C. Zhao, K. Fezzaa, R. W. Cunningham, H. Wen, F. De Carlo, L. Chen, et al., "Real-time monitoring of laser powder bed fusion process using high-speed X-ray imaging and diffraction," *Scientific Reports*, vol. 7, p. 3602, 2017/06/15 2017.
 - [117] B. Stucker, "Overcoming the Computational Complexity Problem for Additive Manufacturing," in *Additive Manufacturing and 3D Printing*, Nottingham, UK, 2015.
 - [118] N. Senin, R. K. Leach, S. Pini, and L. A. Blunt, "Texture-based segmentation with Gabor filters, wavelet and pyramid decompositions for extracting individual surface features from areal surface topography maps," *Measurement Science and Technology*, vol. 26, p. 095405, 2015.
 - [119] S. Lou, X. Jiang, and P. J. Scott, "Correlating motif analysis and morphological filters for surface texture analysis," *Measurement*, vol. 46, pp. 993-1001, 2013.
 - [120] P. J. Scott, "Pattern analysis and metrology: the extraction of stable features from observable measurements," in *Proceedings of the Royal Society of London A: Mathematical, Physical and Engineering Sciences*, 2004, pp. 2845-2864.
 - [121] S. Lou, A. Townsend, X. Jiang, L. Blunt, W. Zeng, and P. J. Scott, "On characterising surface topography of metal powder bed fusion additive manufactured parts," presented at the euspen's 16th international conference & exhibition, Nottingham, UK, 2016.
 - [122] ISO 4288, "Geometric product specification (GPS) Surface texture. Profile method: Rules and procedures for the assessment of surface texture," ed: ISO, 1998.
 - [123] C. A. Brown, "Areal fractal methods," in *Characterisation of areal surface texture*, R. K. Leach, Ed., ed Berlin: Springer, 2013, pp. 129-153.
 - [124] Nobelprize.org. (2017, 22 Aug 2017). *The Nobel prize in physiology or medicine 1979*. Available: https://www.nobelprize.org/nobel_prizes/medicine/laureates/1979/
 - [125] J. P. Kruth, M. Bartscher, S. Carmignato, R. Schmitt, L. De Chiffre, and A. Weckenmann, "Computed tomography for dimensional metrology," *CIRP Annals-Manufacturing Technology*, vol. 60, pp. 821-842, 2011.
 - [126] S. W. Smith, "The scientist and engineer's guide to digital signal processing," 1997.
 - [127] D. J. Bate, "Practical methods of correcting X-ray CT scans," in *Dimensionla accuracy and surface finish in additive manufacturing*, Raleigh, NC, USA, 2016.
 - [128] L. De Chiffre, S. Carmignato, J.-P. Kruth, R. Schmitt, and A. Weckenmann, "Industrial applications of computed tomography," *CIRP Annals-Manufacturing Technology*, vol. 63, pp. 655-677, 2014.
 - [129] R. Christoph and H. J. Neumann, "X-ray Tomography in Industrial Metrology," ed: Süddeutscher Verlag onpact GmbH, 2011.
 - [130] E. Ambos, O. Brunke, D. Neuber, and G. Sensing, "High-speed computer tomography employed in pressure die casting," *CASTING Plant and Technology*, vol. 3, 2012.
 - [131] S. Carmignato, "Accuracy of industrial computed tomography measurements: experimental results from an international comparison," *CIRP Annals-Manufacturing Technology*, vol. 61, pp. 491-494, 2012.
 - [132] A. Thompson, N. Senin, and R. K. Leach, "Towards an additive surface atlas," in *Proceedings of dimensional accuracy and surface finish in additive manufacturing, ASPE 2016 Summer Topical Meeting*, Raleigh, NC, 2016, pp. 156-161.
 - [133] A. Thompson, I. Maskery, and R. K. Leach, "X-ray computed tomography for additive manufacturing: a review," *Measurement Science and Technology*, 2016.
 - [134] F. Hiersemenzel, J. N. Petzing, R. K. Leach, F. Helml, and J. Singh, "Areal texture and angle measurements of tilted surfaces using focus variation methods," 2012.
 - [135] ISO 25178-3, "Geometrical product specifications (GPS) Surface texture: Areal Part 3: Specification operators," ed: ISO, 2012.
 - [136] Volume Graphics GmbH, "VGStudio MAX."
 - [137] NPL. (2005). *Softgages for the evaluation of profile surface texture parameters*. Available: <http://resource.npl.co.uk/softgauges/Help.htm#sdf>

- [138] U. o. H. The Centre for Precision Technologies, "SurfStand."
- [139] Digital Surf., "MountainsMap."
- [140] Keyence. (2017). *Tolerance and measurement accuracy*. Available: https://www.keyence.com/ss/products/measure/measurement_library/basic/tolerance/
- [141] F. Borges de Oliveira, A. Stolfi, M. Bartscher, L. De Chiffre, and U. Neuschaefer-Rube, "Experimental investigation of surface determination process on multi-material components for dimensional computed tomography," *Case Studies in Nondestructive Testing and Evaluation*, 2016.
- [142] Rubert. (2017, September 12, 2017). *Roughness comparator specimens*. Available: <http://www.rubert.co.uk/comparison-specimens/>
- [143] N. Otsu, "A threshold selection method from gray-level histograms," *Automatica*, vol. 11, pp. 23-27, 1975.
- [144] T. S. Yoo, M. J. Ackerman, W. E. Lorensen, W. Schroeder, V. Chalana, S. Aylward, et al., "Engineering and algorithm design for an image processing API: a technical report on ITK-the insight toolkit," *Studies in health technology and informatics*, pp. 586-592, 2002.
- [145] Volume Graphics GmbH, "VGStudio MAX 2.2 reference manual Ch. 5.," 2013.
- [146] A. Townsend, L. Pagani, P. J. Scott, and L. Blunt, "Measurement and characterisation of additively manufactured re-entrant surfaces," presented at the Joint special interest group meeting between euspen and ASPE, Dimensional accuracy and surface finish in additive manufacturing, KU Leuven, Belgium, 2017.
- [147] A. Townsend, L. Pagani, P. J. Scott, and L. Blunt, "CT measurement of re-entrant additively manufactured surfaces," presented at the 8th conference on industrial computed tomography (iCT 2018), Wels, Austria, 2018.
- [148] E. Gyenge, S. Splinter, J. Jung, and A. Snaper, "High-specific surface area, three-dimensional reticulated electrodes for deep cycle lead-acid batteries," in *Seventeenth Annual Battery Conference on Applications and Advances. Proceedings of Conference (Cat. No.02TH8576)*, 2002, pp. 19-24.
- [149] E. A. Silk, J. Kim, and K. Kiger, "Spray cooling of enhanced surfaces: impact of structured surface geometry and spray axis inclination," *International Journal of Heat and Mass Transfer*, vol. 49, pp. 4910-4920, 2006.
- [150] C. Rungsiyakull, Q. Li, G. Sun, W. Li, and M. V. Swain, "Surface morphology optimization for osseointegration of coated implants," *Biomaterials*, vol. 31, pp. 7196-7204, 2010.
- [151] Michigan Metrology. (2017). *3D S parameters - hybrid parameters*. Available: https://www.michmet.com/3d_s_hybrid_parameters_sdr.htm
- [152] M. P. do Carmo, *Differential geometry of curves and surfaces*: Prentice Hall, 1976.
- [153] Visual Computing Lab - ISTI - CNR. *Meshlab*. Available: <http://meshlab.sourceforge.net/>
- [154] D. H. Freedman, "'Layer by Layer", MIT Technology Review," 2011 2011.
- [155] J.-P. Kruth, B. Vandenbroucke, v. J. Vaerenbergh, and P. Mercelis, "Benchmarking of different SLS/SLM processes as rapid manufacturing techniques," 2005.
- [156] M. Mahesh, Y. Wong, J. Fuh, and H. Loh, "Benchmarking for comparative evaluation of RP systems and processes," *Rapid Prototyping Journal*, vol. 10, pp. 123-135, 2004.
- [157] S. Moylan, J. Slotwinski, A. Cooke, K. Jurens, and M. A. Donmez, "Proposal for a standardized test artifact for additive manufacturing machines and processes," in *Proceedings of the 2012 Annual International Solid Freeform Fabrication Symposium*, The University of Texas at Austin, Austin, TX., 2012, pp. 6-8.
- [158] W. Johnson, M. Rowell, B. Deason, and M. Eubanks, "Benchmarking evaluation of an open source fused deposition modeling additive manufacturing system," in *Proceeding of the 22nd Annual International Solid Freeform Fabrication Symposium*, 2011, pp. 197-211.

- [159] S. Moylan, A. Cooke, K. Jurrens, J. Slotwinski, and M. A. Donmez, "A review of test artifacts for additive manufacturing," *National Institute of Standards and Technology (NIST), Gaithersburg, MD, Report No. NISTIR*, vol. 7858, 2012.
- [160] E. C. Santos, M. Shiomi, K. Osakada, and T. Laoui, "Rapid manufacturing of metal components by laser forming," *International Journal of Machine Tools and Manufacture*, vol. 46, pp. 1459-1468, 2006.
- [161] ISO/IEC 15775, "Information technology - office machines - method of specifying image reproduction of colour copying machines by analog test charts - realisation and application," ed, 1999.
- [162] B. Galovskyi, M. Flessner, A. Loderer, and T. Hausotte, "Systematic form deviations of additive manufactured parts—methods of their identification and correction," in *11 th International Symposium on Measurement and Quality Control*, 2013, pp. 11-13.09.

Chapter 11 Appendices



Contents lists available at ScienceDirect

Precision Engineering

journal homepage: www.elsevier.com/locate/precision



Surface texture metrology for metal additive manufacturing: a review



A. Townsend^{a,*}, N. Senin^{b,c}, L. Blunt^a, R.K. Leach^b, J.S. Taylor^d

^a EPSRC Centre for Innovative Manufacturing in Advanced Metrology, University of Huddersfield, UK

^b Manufacturing Metrology Team, Faculty of Engineering, University of Nottingham, UK

^c The Department of Engineering, University of Perugia, Italy

^d Center for Precision Metrology, University of North Carolina at Charlotte and Lawrence Livermore National Laboratory, USA

ARTICLE INFO

Article history:

Received 22 March 2016

Received in revised form 29 May 2016

Accepted 1 June 2016

Available online 7 June 2016

Keywords:

Metal additive manufacturing

Surface texture

Metrology

ABSTRACT

A comprehensive analysis of literature pertaining to surface texture metrology for metal additive manufacturing has been performed. This review paper structures the results of this analysis into sections that address specific areas of interest: industrial domain; additive manufacturing processes and materials; types of surface investigated; surface measurement technology and surface texture characterisation. Each section reports on how frequently specific techniques, processes or materials have been utilised and discusses how and why they are employed. Based on these results, possible optimisation of methods and reporting is suggested and the areas that may have significant potential for future research are highlighted.

© 2016 The Authors. Published by Elsevier Inc. This is an open access article under the CC BY license (<http://creativecommons.org/licenses/by/4.0/>).

Contents

1. Introduction.....	34
1.1. Surface texture metrology for additive manufacturing of metal parts.....	35
1.2. Contents of the review.....	35
1.3. Reviewing method.....	35
2. Industrial domains, AM processes and materials.....	35
3. Types of surfaces investigated.....	38
4. Surface measurement technologies and strategies.....	39
5. Surface texture characterisation.....	41
5.1. Texture parameters.....	41
5.2. Measurement set-up and processing of acquired data for characterisation.....	43
5.3. Texture characterisation in relation to part function.....	44
6. Conclusions.....	44
Acknowledgements.....	45
References.....	45

1. Introduction

Additive manufacturing (AM) techniques compliment current conventional, subtractive methods by providing additional options to industry: another tool in the manufacturing toolbox. One clear advantage of AM is that it allows the creation of complex geometries and internal features that cannot be produced using

subtractive methods. This advantage is primarily due to the tooling path restrictions inherent in conventional manufacturing [1]. By contrast, a current limitation of AM is the degraded dimensional control and surface integrity of specific surfaces. Hence there is often a requirement for complex support structures to be included in the build.

Another significant advantage to AM is the potential for appreciable reduction in time-to-market, gained through factors such as reduced machine set-up and tooling, potential part count reduction and associated assembly time reduction. AM is now being used to make production parts in high-value applications where complex-

* Corresponding author at: CE3/04 Canalside East, University of Huddersfield, Queensgate, Huddersfield HD1 3DH, UK.
E-mail address: a.townsend@hud.ac.uk (A. Townsend).

<http://dx.doi.org/10.1016/j.precisioneng.2016.06.001>

0141-6359/© 2016 The Authors. Published by Elsevier Inc. This is an open access article under the CC BY license (<http://creativecommons.org/licenses/by/4.0/>).

ity and customisation are key advantages, such as hearing aid shells [1]. The 2013 UK Foresight Report [2] highlighted the role of AM in the mass personalisation of low-cost products as a likely fundamental change in manufacturing in the near future. It is perhaps too early to state whether AM is a *third industrial revolution* [3] but AM certainly has significant industry-specific advantages in relation to conventional manufacturing processes.

Part of the reason for adoption by the aerospace and medical industries since 2011 is that standard high-performance engineering materials currently used in these industries, such as titanium 6Al4V, 17-4 PH stainless steel, cobalt chrome and Inconel 625, are all suitable materials for AM production. Of possible metal AM build processes, powder bed fusion (PBF) has been the process with the greatest economic impact [4]. Consequently there has been more research in to PBF than other metal AM processes, such as layer object manufacture, material extrusion, material jetting and directed energy deposition (DED).

1.1. Surface texture metrology for additive manufacturing of metal parts

This review paper focuses on reporting current research on the use of surface texture metrology solutions for metal AM technologies. Surface metrology is defined as the measurement and characterisation of surface topography [5]. Topography is the term typically used to describe the entire geometric information associated with a surface shape and its features, where shape is typically referred to as form [5]. This review focuses on texture and not form (see Ref. [6] for a review of form metrology for AM).

Per ISO 25178-2 [7], surface texture is the scale-limited surface remaining after a series of operations applied to the primary extracted surface. The F-operation removes form (if required) from the primary surface. This is followed by application of an S-filter to remove small scale lateral components and L-filter to remove large scale lateral components.

Further definitions of surface texture have been proposed, for example by Leach [8]:

Surface texture is the geometrical irregularities present at a surface. Surface texture does not include those geometrical irregularities contributing to the form or shape of the surface.

Surface texture metrology can play an enabling role in AM-related manufacture and research, beyond its use as a tool for verifying compliance to specific surface texture requirements. Surface texture metrology can be used as a means of gaining insight into the physical phenomena taking place during the AM manufacturing process, through examination of the surface features generated by the process and walking backwards through the complex and intertwined network of cause-effect relationships between the involved physical phenomena (for example, conduction heat transfer, balling effects (spheroidisation of the melt pool) [9,10], hydrodynamics and Marangoni circulation (mass transfer due to the surface tension gradient on the melt surface) [11] and process control variables (for example, powder configuration, laser or e-beam spot size, power level and scan speed) [4]. Surface texture metrology becomes a powerful exploration tool, increasing knowledge of the process and ultimately allowing the creation of improved AM processes capable of producing specification-compliant parts.

1.2. Contents of the review

Whilst this review focuses on the broad topic of surface texture metrology as applied to AM research, it is important to clearly state the boundaries of which specific subjects are covered and which are not:

- As stated in Section 1.1, surface texture metrology involves the measurement and characterisation of surface texture; therefore, this paper does not deal with the subject of form/shape inspection and verification, which is typically covered by form metrology [6].
- Given their recently acquired industrial importance, this work focuses on AM technologies for metals. Many of the reported findings and conclusions may also be applicable to other materials (such as polymers and some types of composites), but metals and metal-related issues are the primary area of investigation. Additional references discussing surface metrology issues for non-metal AM processes will be discussed when they have relevance to metal parts.
- Surface texture metrology deals with both measurement (i.e. the process of acquiring topography data from a surface) and characterisation (i.e. the process of extracting useful quantitative information from topography data). Both aspects are covered by the review.

This review deals with inspection, not monitoring. In other words, it reports the current literature on the challenges of how to measure a surface and extract useful information in a one-off, self-contained scenario, generally performed on the completed component after removal from the build chamber. In-situ process monitoring is beyond the scope of this review. Refer to Ref. [12] for an overview of the current literature on monitoring and real-time control for AM processes.

1.3. Reviewing method

To prepare this review, relevant references were retrieved from the main scientific online databases, with publication dates ranging from 1997 [13] to the date of submission of this manuscript. To reorganise the contents retrieved from the literature into a manageable taxonomy, a series of relevant themes was prepared, and initially posed in the form of questions (see Table 1).

In the remainder of this review, each section is dedicated to answering one or multiple questions from the list in Table 1. A general justification/explanation of each subject is reported first, followed by an analysis of the literature contents for the specific subject, and finally, a brief summary of the main findings for the section. Achievements and open issues are discussed, and future opportunities and challenges are reported in the conclusions.

2. Industrial domains, AM processes and materials

Understanding which industrial domains are addressed most often in the literature on surface texture metrology for AM may give an indication as to where industrial and academic research is currently heading, and research results may indicate the key challenges to be faced. Typically, along with the industrial application comes the need for using specific materials. Being able to use an AM technology with a material defined by design specifications is one of the major challenges for the emerging AM technologies, since many technologies have been conceived and developed around very specific materials. Application, material and AM technology often form a strong bond, which must also be considered in AM surface texture measurement planning, execution, data analysis and data processing.

An investigation of the current literature on surface texture metrology for AM indicates that research is still at an early stage and currently lacks strong connections to real applications or application requirements. Most research is still at the stage where surface texture metrology is used to understand manufacturing process capability in a general sense, and application-specific requirements have not yet been introduced in a systematic way. Many references

Table 1
Questions outlining the main themes covered by the review.

Review section	Question and examples
Section 2: Industrial domains, AM processes and materials	What is the industrial domain or application covered, if any? Which AM processes have been researched? For example a specific product or a generic industrial domain, such as aerospace. What are the metrological requirements and challenges specific to that domain (if any)?
Section 3: Types of surfaces investigated	What types of surfaces are investigated? For example, horizontal, tilted or vertical plane, freeform, external, internal, complex 3D (such as trabecular structures), random and structured. Are the surfaces from actual products or artefacts specifically designed for surface investigation? What are the metrological challenges specific to each geometric configuration? Does the surface configuration help verify process capability and provide insight into the manufacturing process?
Section 4: Surface measurement technologies and strategies	What measurement technology is used? What strategy has been used to retrieve reliable data? For example, contact stylus, confocal, focus-variation, interferometric. Areal or profile? What are the challenges and capabilities of each in relation to the specific application scenario and AM process-material combination? What are the metrological challenges connected to the specific process and material (for example, high roughness, undercuts, reflectivity, potential damage from contact probes)?
Section 5: Surface texture characterisation	How is the measurement data processed and analysed? For example, computation of texture parameters, and the application of filtering techniques. What are the specific considerations and challenges for surface metrology? Which surface texture parameters are most sensitive to surface changes during post-processing operations?

discuss the importance of AM processes in specific industrial contexts, but few actually translate this into context-specific research. We note here a few exceptions. There has been examination of bio-compatible materials and their suitability for manufacturing medical and dental parts (including surface texture discussions) [14,15]. The fatigue performance for as-built, machined and polished samples [16] has been investigated, as has the effect of surface roughness on the efficiency of electromagnetic horn antennae [17].

Materials and processes in AM have typically evolved in combination. Specifically concerning metals, the types of AM processes that have been studied in the literature on surface texture metrology for AM is reported as follows:

Powder bed fusion (PBF): [10,14–16,18–56].

Directed energy deposition (DED): [57–63].

It can be seen that the majority of metal-based AM processes investigated are PBF systems. Figs. 1 and 2 show typical as-built surfaces of metal parts generated by the two most common PBF processes: selective laser melting (SLM, see Fig. 1) and electron beam melting (EBM, see Fig. 2). It is evident that a high degree of irregularity is present at different scales of observation. Powder particle sizes and geometries influence the texture of the fabricated layers and partially melted particles can be clearly seen in the scanning electron microscope (SEM) micrographs. Many instruments can be configured to measure surfaces at a wide range of scales-of-interest, for example a focus variation instrument may have selectable objective lenses with magnifications ranging from $\times 2.5$ to $\times 100$. These SEM micrographs illustrate the challenges of selecting the appropriate scale-of-interest, measurement instrument and configuration (see Section 4) together with appropriate surface texture parameters and filtering (see Section 5).

The role of specific materials in terms of the challenges they generate for surface texture metrology has been little investigated in the literature. Most considerations on measurement challenges are not specifically related to material properties, but to the topographies of the generated surfaces. Although generally not as rough as other AM processes such as DED and fused deposition modelling (FDM), PBF processes tend to generate rougher surfaces than turned or ground surfaces. PBF surfaces present significant measurement

challenges due to the frequent discontinuities, vertical walls and re-entrant features. The nature of such topographies is equally challenging for contact and non-contact measurement methods. Stylus may jam against the steep sides of surface asperities causing jump/slip temporary loss of contact and even tip damage; optical measurement may be affected by high slope angles, multiple or diffuse reflections and high image contrast. Softer materials pose the additional challenge of being at risk of damage under the stylus passage, which in turn leads to the need for carefully selecting stylus tip radii and contact forces [64]. It is also known that surface properties may change significantly as a result of post-processing, for example a PBF surface/material combination, which may be dull with little specular reflection presenting minimal challenges for some optical instruments, may become highly specularly reflective after post-processing by grinding or machining, or may change colour and require a more challenging optical measurement setup. Each reference reviewed generally discusses research focussed on a single material type as processing conditions and parameter settings are highly material dependent.

The following is an analysis of metal types used in the references:

In the analysed pool of approximately 60 references where material type and AM build process are specified, nickel alloys cover 5%, Inconel 625 being the subject in 75% of this research. Inconel 625 is a high-strength corrosion-resistant nickel chromium super-alloy with a useable temperature range from cryogenic to 982 °C, making it a good choice for liquid-fuelled rocket engines, gas turbine engines and cryogenic tanks [65].

Aluminium alloys, such as AlSi10Mg, cover 5% of the examined literature on surface texture metrology for AM [28]. Calignano et al. [45] investigated the influence of process parameters scan speed, laser power and hatching distance (the perpendicular distance between successive laser scan lines) on the surface finish of direct metal laser sintered (DMLS) AlSi10Mg surfaces, see Fig. 3. AlSi10Mg has good strength, corrosion resistance, low density and high thermal conductivity compared with other alloys and is often found in aerospace and automotive interior AM components, and in functional prototypes [66,67]. In addition to the aforementioned

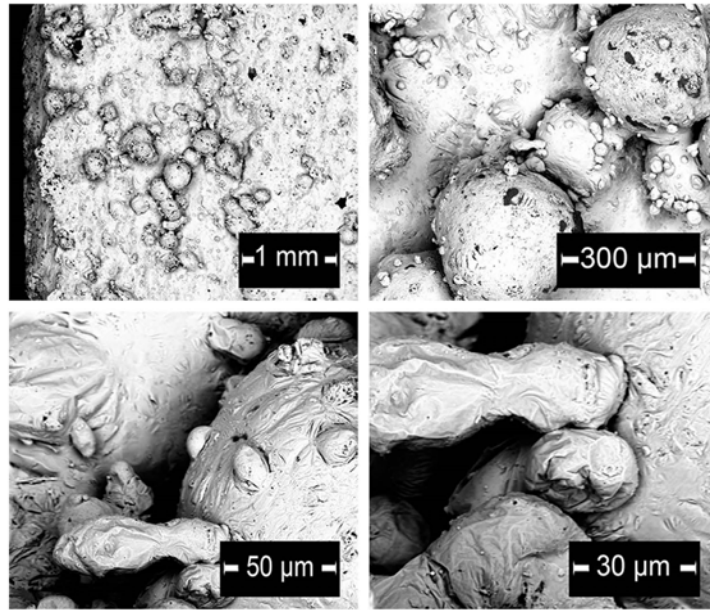


Fig. 1. Multi-scale SEM micrograph of SLM A1Si10Mg part (as built).

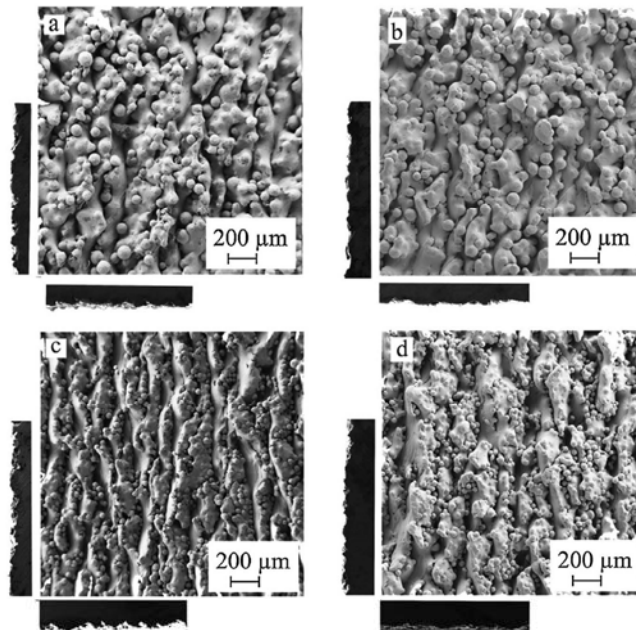


Fig. 2. SEM micrographs of EBM Ti6Al4V part (as built). (a) Built with 45–100 μm powder and 70 μm layer thickness, (b) Built with 45–100 μm powder and 50 μm layer thickness, (c) Built with 25–45 μm powder and 70 μm layer thickness, (d) Built with 25–45 μm powder and 50 μm layer thickness. From Ref. [22].

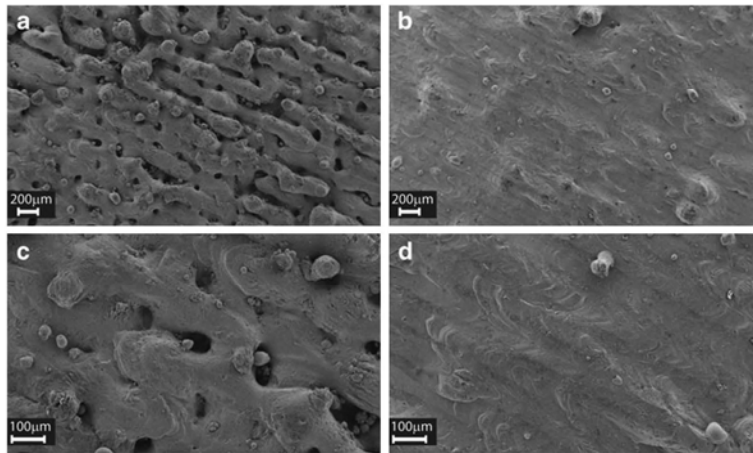


Fig. 3. Field emission SEM images of AlSi10Mg DMLS surfaces. (a and c) Scan speed 1000 mm/s, laser power 190 W, hatching distance 0.2 mm, Ra 24 μm , (b and d) Scan speed 800 mm/s, laser power 190 W, hatching distance 0.1 mm, Ra 14 μm [45].

challenges of measuring very irregular surfaces fabricated via PBF processes, aluminium alloy AM surfaces typically raise additional concerns when measured with contact techniques, due to low hardness, possibly resulting in damage from the stylus. Again, consideration should be given to appropriate selection of stylus radii and contact forces [64].

Stainless steel alloys comprise 39% of the examined literature on surface texture metrology for AM. 316L has been used in 70% of this research. 316L is an austenitic chromium-nickel stainless steel with high strength, high corrosion resistance and is particularly resistant to common acids, such as sulphuric, hydrochloric and acetic. Typical applications include exhaust manifolds, heat exchangers, storage tanks, jet engine parts and many parts for marine applications [68]. Other classes of steel, such as alloy and maraging steel, are used in a combined 10% of the total research pool. PBF steel surfaces typically raise the same concerns as nickel and aluminium alloys. Hardness-related concerns about possible damage from stylus instruments are less relevant for steels than for aluminium parts [64].

Titanium alloys comprise 34% of the analysed references. Ti6Al4V is the alloy used in 95% of these references and is the most studied AM metal. Alloys such as Ti6Al4V exhibit good strength-to-weight ratios, high fatigue and corrosion resistance and high temperature performance, leading to many aerospace applications, such as airframe structural components, aircraft skin, rocket, missile and spacecraft parts [69]. Ti6Al4V is also biocompatible, making it an ideal candidate for biomedical applications [14]. Note that concerns about toxicity of vanadium are motivating development of alloys with different elements, such as substituting niobium for vanadium [70].

Refractory materials, such as cobalt chrome and alumina, have been studied along with tool steels and copper alloys [71,72]. There has been limited research published using AM components manufactured from these materials, amounting to a total of 7% of the pool of analysed references. Table 2 shows the types of AM processes used for each material group.

3. Types of surfaces investigated

Investigating the surfaces of industry-specific parts initially appears to have the advantage that there is a high probability

Table 2
AM processes used for each material group.

Material	EBM	Laser	DED
Nickel alloys	0	100%	0
Aluminium alloys	0	100%	0
Stainless steels	0	87%	13%
Other steels	0	83%	17%
Titanium alloys	35%	50%	15%
Others	0	100%	0

that the research will address the real conditions and challenges expected in production. However, AM fabrication of metal parts is still in its infancy, thus little research literature has been dedicated to the characterisation of surface texture on actual manufactured products [17]. The use of test artefacts does allow for easier generation and inspection of a wider array of surface types and orientations and is, therefore perhaps, the preferred choice during manufacturing process development, where the main goal is to understand the manufacturing process and its capabilities, so that the process can be improved and ultimately optimised for the target applications.

Many artefacts have been developed for evaluation of surface texture as generated by different AM processes: within the pool of analysed references for this review, 90% were dedicated to the characterisation of artefacts.

Many artefacts have been developed to study the relationships between surface texture and orientation with respect to the build direction. Horizontal, vertical and tilted planes are generally selected for this purpose. Tilted surfaces in particular are useful to highlight the 'staircase effect', where the edges of individual layers may be observed [73].

A typical artefact configuration is the truncheon [28,49,74–76] (see Fig. 4). The truncheon has a series of progressively rotated square or rectangular sections. A common configuration includes sections rotated in 5° increments from 0° and 90° [49].

Another artefact designed with planar surfaces at different orientations with respect to the build direction is the angled plate [26,29,77]. This consists of a series of individual plates built at a range of angles to the plane of the build plate. The faceted sphere is designed to include a number of measurement surfaces approx-



Fig. 4. A typical truncheon artefact [49].

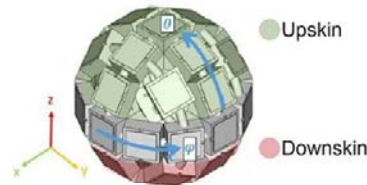


Fig. 5. Faceted sphere artefact. From Ref. [78].

imating a spherical shape [78] and includes a uniform selection of build angles within the build chamber (see Fig. 5).

Plate artefacts with varying spacing between faces have been used to investigate the influence of heat accumulation on surface roughness [19,79]. Some artefacts play a double role, being designed for testing surface texture but also dimensional and geometric accuracy/precision. For example, the National Institute of Standards and Technology (NIST) has included surface roughness measurement areas in their proposed (2012) test artefact [80] (see Fig. 6).

The ASTM F42/ISO TC 261 joint group for Standard Test Artifacts (STAR) is developing a standard for AM test artefacts. One STAR proposed artefact includes seven different artefacts, each designed to check specific AM parameters [81]. One of the seven proposed artefacts is designed for the measurement of surface texture (see Fig. 7).

The surface texture specific STAR artefact is a series of seven platens built at different angles: 0–90° to the horizontal plane, with 15° intervals. The artefact allows for the removal of each platen for easy measurement on optical or stylus instruments. The artefact model would be editable to allow only the construction of those sections required for analysis (perhaps at angles related to the component build angles). Fig. 8 shows the side and top surfaces of an AlSi10Mg SLM component. The layering is not visually apparent in the side surface (a). The hatching lines can clearly be seen on the top surface (b).

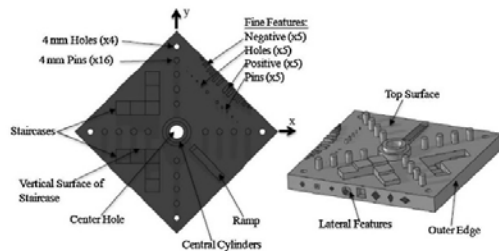


Fig. 6. NIST proposed AM inspection artefact (2012) [80].

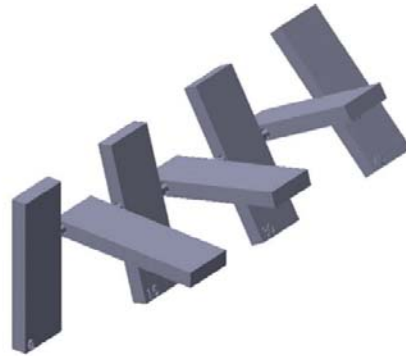


Fig. 7. ASTM F42/ISO TC 261 joint group for standard test artifacts (STAR) proposed surface inspection artefact (2015) [81].

4. Surface measurement technologies and strategies

The spatial frequencies (scales) of interest of the surface to be measured will influence the choice of measurement technology and, in general, technology will govern the metrological quality of the measurement results (for example measurement accuracy and precision).

Both the nature of the material and the structure of the topography influence the choice of measurement technology: contact-based probing (primarily stylus-based measurement) needs to take into consideration the nature of the physical interaction of the probe and the surface, for example whether there is risk of damage to the stylus or work piece during the measurement process. Mechanical and surface properties are heavily influenced by topography and even density: high porosity would lower the strength of the surface layers. The stylus tip radius and cone angle need to be chosen carefully to provide meaningful surface information, with insignificant mechanical filtering of the surface data, and yet be sized to avoid damage when passing over tall, steep sided features that may apply significant lateral loads [82]. Contact techniques should also take into account the accessibility of the surface.

Non-contact techniques, such as focus variation and confocal microscopy, need to take into account the reflective properties of the material being measured. The reflective properties of the AM part may be considerably different from the optical properties of the same material when presented in a polished, flat surface. Non-contact, non-optical techniques (e.g. scanning electron microscopy) and pseudo-contact techniques (e.g. atomic force microscopy) have an array of similar problems when confronted with any specific AM surface.

As the great majority of AM metallic parts are fabricated via powder-based methods, the typical measurand surface is very irregular, and is characterised by sharp protrusions and recesses at multiple scales, with open pores transitioning into closed pores underneath the surface. Some difficult-to-measure surface features are typical of specific AM processes: for example PBF processes produce specific patterns featuring balling, spatter formation, loose or partially melted particles, which are very difficult to measure. Local surface slopes may exceed the maximum measurable limits for measuring technologies, especially optical techniques. Large topographic differences may be observed when comparing an AM metallic surface as generated and the same surface after cleaning. Even more striking is the difference with the same surface after post-processing (typically shot peening [83], laser polishing [84]

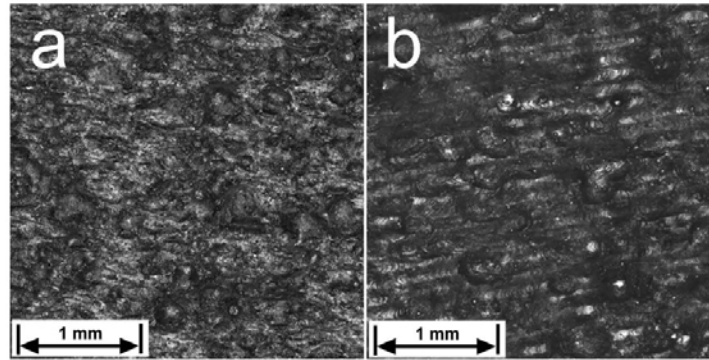


Fig. 8. AlSi10Mg SLM component. (a) Side surface, (b) Top surface.

and/or machining) which essentially produces a new surface. The top surface of a part produced by any layer-based manufacturing process will be influenced by properties, including surface texture, of the previous build layers, contributing to the creation of surface features at multiple spatial wavelengths (scales). Given all the above, the measurement technology should be selected on the basis of the following considerations:

- What are the scales of the features to be characterised?
- What are the sizes and shape properties of the surface features that are more relevant from the standpoint of the function the part?
- What are the sizes and shape of the surface features that, when analysed, lead to a greater understanding of the manufacturing process?

The above questions are linked by the concept of objective-driven measurement; i.e. faced with such a complex geometry, the goals of measurement should be understood first, in order to decide what the priorities should be in capturing information, which in turn should drive the selection of measurement technology together with appropriate measurement settings. Implicit in the above, the most typical objectives are either to analyse how a part conveys function through its surfaces, or to analyse the manufacturing process through the investigation of the surfaces it generates.

In the following, a list of measurement technologies is reported, together with the references that have adopted them for metallic AM surface measurement. The technologies have been divided into sections based on the type of information they can extract from the measured surface.

Profile topography measurement

- Contact stylus [26,27,29,32,45,49,75,76,85–87].

Areal topography measurement

- Confocal microscopy [18,78].
- Focus variation microscopy [26,88].
- Coherence scanning interferometry [89].
- Chromatic confocal microscopy [19].
- Conoscopic holography [86].
- Atomic force microscopy (AFM) [87].
- Elastomeric sensor [90–92].

2D imaging

- Optical microscopy [27,87].
- SEM [18,29,45].

Volumetric

- X-ray computed tomography [25,93].

Other

- Raman spectrometry [85].

It can be seen that the most frequent choice of measurement technology is profile measurement via a stylus-based contact instrument (40% of the examined literature). Profile texture measurement and parameters (see Section 5) are the most ubiquitous industrial surface texture measurement systems. They are generally low cost with a lower (perceived) requirement for operator training and a high comfort level for machinists and inspectors. Historically profile methods have been used for certifying component surface texture complies with drawing and specification requirements and is supported by well-established standards including both ISO and ASME (ISO 3274 [94], ISO 4287 [95], ISO 4288 [96] and ASME B46.1 [97]). Profile techniques are based on scanning and characterising individual profiles traced on the surface. Unless the topography is simple, and characterised by a dominant lay, profile-based measurement is intrinsically limited in its power for capturing topography information, thus making texture parameters limited in terms of the information they can provide relating to part functionality and detailed process feedback [98,99].

The recent shift towards areal topography characterisation is driving the adoption of optical measurement devices based on a range of technologies. The most utilised optical technologies for AM surfaces of metal parts are focus variation microscopy (11% of the examined literature), see Fig. 9, and confocal microscopy (11%). Both technologies can be challenged by the highly irregular nature of the typical topographies being measured, but the acquisition time (at least over a single field of view) is significantly less than raster-scanned techniques. Coherence scanning interferometry, often referred to as vertical scanning interferometry or white light interferometry, is less used (7% of the examined literature) as the highly irregular AM surfaces can present measurement difficulties in terms of local slope and vertical scale of roughness. Similarly, given the highly irregular nature of most AM

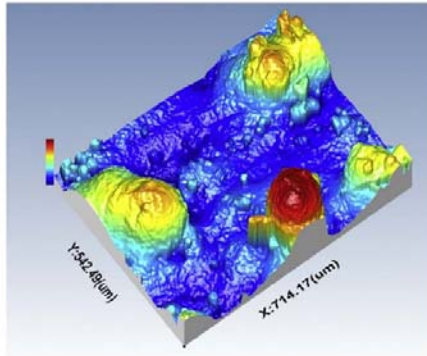


Fig. 9. Focus variation false colour heights map of the top surface of an AlSi10Mg part showing features at various sizes.

metallic surfaces, AFM has been seldom used, both for measurement (vertical) range limitations, and because of the risk of stylus damage. Most researchers involved with the characterisation of AM surfaces will have used some type of conventional 2D imaging, primarily SEM (generally secondary-electron mode) (11%) and optical microscopy (7%). Not being able to provide quantitative information in the vertical (height) direction, 2D imaging techniques have limited use for quantitative surface texture measurement. Thus, 2D imaging is typically reserved for qualitative surface investigation, although in some cases, once calibrated, these instruments have been used for quantitative measurement in the image plane [58]. Despite having been rarely used in the examined literature and initially based on extraction of profile parameter data [25,31,93], X-ray computed tomography (XCT) has potential [100], since, with appropriate data processing methods, surface information can be extracted from volumetric data with no limitations due to vertical walls and undercuts. The most significant advantage of XCT over line-of-sight or contact measurement systems is that surface data can be extracted from the internal surfaces of AM components. Areal surface parameters (per ISO 25178-2) have now been extracted from the XCT volume data of AM components [101]. The main hurdles to widespread adoption of XCT as a means of measuring surfaces of AM parts reside in currently poor spatial resolutions of the measurement, and lack of complete understanding of metrological performance and error sources, necessary for a proper calibration of the surface extraction algorithms (mainly based on thresholding/edge detection) [102].

5. Surface texture characterisation

5.1. Texture parameters

Surface texture characterisation concerns the extraction of texture-related information from the complex topography information obtained through measurement (see Section 4) and producing useful numbers, i.e. quantities that capture salient traits/relevant aspects of the texture such as heights, spacing and distribution of textural features. The ISO specification standards ISO 4287 [95] and ISO 25178-2 [7] define the most frequently adopted parameters in industry and academia: ISO 4287 provides terms, definitions and parameters for profile measurements, while ISO 25178-2 defines areal parameters. ASME B46.1-2009 [97] and JIS B 0601:2013 [103] define analogous sets of texture parameters. How-

ever, the ISO standards were exclusively referenced in the reviewed literature.

Areal texture parameters (adopted in 20% of the cases in the analysed literature) require datasets that describe texture in a three-dimensional Cartesian space. These are generally generated using areal topography measuring instruments (which was the case with all the analysed literature). Areal datasets may be created using a profile lateral scanning system which includes an x -axis drive, a y -axis drive and a z -measurement probe [104]. Datasets may also be generated from volumetric measurements, such as from XCT iso-surfaces [101], or derived from the combination of multiple 2D photographs into 3D data (for example photogrammetry from SEM images, shape from shading), not observed in the analysed references. Profile texture parameters (adopted by 80% of the analysed literature) can be computed from datasets obtained by stylus-based instruments, or extracted from areal topography data, or extracted from XCT analysis, a technique that has been employed to provide profile texture information of AM lattice structures [31,93].

By far, the most frequently adopted texture parameter in the literature is the ISO 4287 profile parameter R_a , the arithmetic mean deviation of the assessed profile [18,27,29,45,49,74,76]. R_a is the arithmetic mean of the absolute ordinate values within a sampling length.

The second-most used texture parameter, again a profile parameter from ISO 4287 is R_q , the root mean square deviation of the assessed profile [25,31,105]. R_q is the root mean square of the ordinate values within a sampling length, thus R_q is the sample standard deviation. Other ISO 4287 profile parameters that have been used to characterise the texture of AM surfaces are R_z (maximum height of the profile) [25,31] and R_t (total height of the profile) [57]. The material ratio curve, which represents the material ratio of the profile as a function of level (also known as the Abbott-Firestone curve), has been used for texture analysis [19].

The predominant use of profile texture parameters (in particular R_a) in the characterisation of AM surfaces is consistent with non-AM surface metrology, where areal texture parameters are still gaining acceptance. While ISO 25178-2 contains a comprehensive selection of areal field, feature, spatial, hybrid and functional parameters, with few exceptions, the height parameters have been chosen in the references. As would be expected, the most widely used areal texture parameter in the analysed literature has been S_a , the arithmetical mean height of the scale limited surface. S_a is the arithmetic mean of the absolute of the ordinate values within a definition area. S_a was used in 90% of the references using areal parameters. The areal S_a parameter corresponds to the profile R_a and thus it has proven easier for users to adopt in those environments where R_a was already utilised.

Areal parameters in general have distinct advantages over profile parameters for surface characterisation: surface topography is three dimensional in nature so any analysis of two-dimensional profiles will give an ambiguous or incomplete description of the real surface; for example, a profile measurement taken perpendicularly to the direction of a scratch may produce the same trace as a profile measurement taken of a single pit, see Fig. 10.

Moylan has recommended the combined use of average roughness (R_a or S_a) mean roughness depth (R_z or S_z), skewness (R_{sk} or S_{sk}) and kurtosis (R_{ku} or S_{ku}) for the characterisation of AM surfaces [81]. S_{sk} and S_{ku} are the areal counterpart of R_{sk} and R_{ku} , respectively the third and fourth-order moments of the probability distribution of heights. In specific configurations, S_{ku} and S_{sk} may provide indications of relative predominance of peaks or pits, and the relationship between the height distribution and a Gaussian distribution. Likewise, S_z is the counterpart to R_z , the maximum height of the scale-limited surface (refer to ISO 4287 [95], ISO 25178-2 [7] and [107] for further details). Fig. 11 shows examples

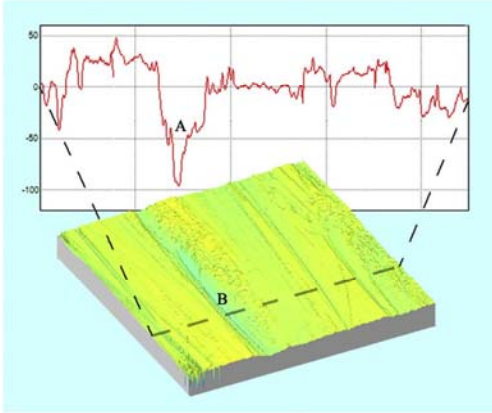


Fig. 10. Profile measurement extracted from an areal measurement, after Ref. [106]. From the profile trace "A" could be a pit or a scratch. From the areal measurement, the same location "B" clearly indicated a scratch.

of SLM Ti6Al4V sample areas before and after vibro-finishing and bead-blasting with Sa values (a–c) together with an SEM image of the post-bead-blasted surface (d) (work performed at The University of Huddersfield).

Results indicated that the following ISO 25178-2 areal parameters were most sensitive to the surface changes during the vibro-finishing process: peak material volume (Vmp), developed

interfacial area ratio (Sdr), reduced peak height (Spk) and skewness (Ssk).

Data created using areal surface measurement techniques may be used to characterise specific surface features using a toolbox of pattern recognition systems [7,108–110]. Significant features can be extracted for analysis based on threshold values. The process defined by ISO 25178-2 includes segmentation of the scale-limited surface based on hills (with peaks), dales (with pits), ridgelines, courses and saddle points. Once segmented a change tree based on these segments is developed. The change tree has scaled height distances between the peaks, saddle points and pits. The segmentation process usually results in over-segmentation, so the tree is then "pruned" by combining segments, commencing with the segments with the least height difference between a pit and a saddle point, or peak and saddle point. The process can be visualised by imagining filling all dales with water to an equal depth until the water overflows from the dale with the least height between the pit and the saddle. The process is repeated until a threshold is reached, such as a specified minimum peak to saddle or pit to saddle height value or a specified number of peaks remains.

The segmentation map may then be used as a mask applied to the original data, permitting analysis of the selected features, or similarly features may be extracted and the underlying surface may be analysed. Segmentation and feature analysis have significant application for additive manufacturing. The partially melted powder asperities on the surface of an as-manufactured component (see Fig. 9) may be removed and characterised. Similarly, extracting the asperity data will allow analysis of the underlying surface texture. Without extraction, the asperity data has the potential to overwhelm information from the underlying surface, making analysis difficult. Analysing the underlying surface after asperity extraction has the potential to provide significant informa-

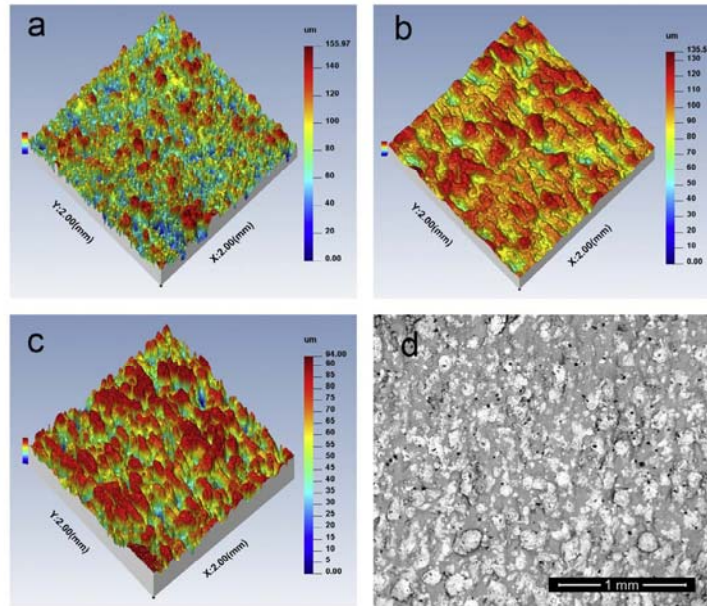


Fig. 11. Ti6Al4V SLM part. Focus variation false colour height maps, (a) No processing, Sa 21 μm , (b) post-bead-blasting, Sa 10 μm , (c) post-vibro-finishing, Sa 12 μm . (d) SEM image of post-bead-blasted surface.

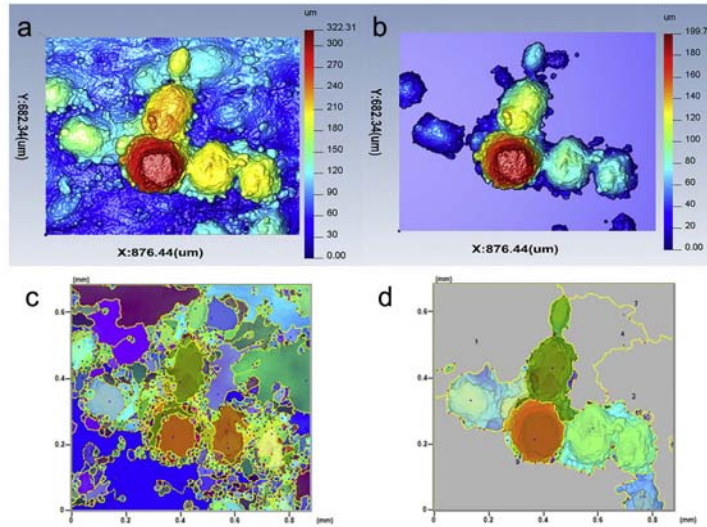


Fig. 12. Feature extraction. (a) False colour height map (original data), (b) After levelling and thresholding, (c) Watershed segmentation followed by 1% Sz Wolf pruning, (d) After 8% Sz Wolf pruning.

tion about the manufacturing process and therefore aid in process improvement and optimisation. Post-processing, such as grit blasting, will remove the asperities but may also destroy information about the surface below. Fig. 12 shows examples for an AlSi10Mg SLM part: focus variation measurement false colour height map (a), a global height thresholding of the levelled surface, showing removed features (b), watershed segmentation followed by Wolf pruning per ISO 25178-2 at 1% Sz threshold (c) and segmentation followed by 8% Sz threshold Wolf pruning showing features that may be extracted for further analysis (work performed at The University of Huddersfield).

5.2. Measurement set-up and processing of acquired data for characterisation

As the values for texture parameters are entirely dependent upon the dataset from which they are computed, attention must be given to the steps that have been taken in order to measure first, and then prepare (process) the topography data for parameter computation. This information is often poorly reported in the literature, making the results typically non-reproducible. Examples of good definition of measurement and analysis include Refs. [27] and [111].

As a general rule of thumb, instruments operating using different principles (contact vs optical) will generate different datasets, even when bandwidth matching has been performed (i.e. the process of making sure the acquired topography datasets cover the same ranges of spatial frequencies) [112]. This is intrinsically related to the measurement technology adopted by each type of instrument and how it interacts with each specific type of surface and material. In most of the analysed references, the type and model of the measurement instrument are appropriately cited. However, only a few references provide all the necessary information needed to replicate the measurement set-up; for example, for optical areal topography instruments, few report the lateral sample spacing or vertical resolution. Once the dataset has been obtained, a

series of additional data modification steps can significantly affect the result of texture parameter computation. For example, non-measured points are common in optical measurement; depending on how these are processed (ignored or padded with interpolated values) the texture parameter results vary. Optical measurement techniques produce specific measurement anomalies (for example, a sequence of characteristic spikes known as “batwings” in coherence scanning interferometry, when a step-like feature is generated). The technique adopted for identifying and removing (or attenuating) measurement anomalies should be reported, as it can influence parameter computation. Comparison of the quantity of voids and missing data produced during measurements has been used to select appropriate AM surface measurement equipment, however, no comparison of the effect of padding or interpolating data on the measurement parameters has been reported and research is needed in this area.

After data capture, the form component is removed. When the measurand surface is planar, form is typically removed by simple subtraction of the heights of the least-squares mean plane computed from the dataset. The majority of the research has been performed using custom designed artefacts, manufactured with planar surfaces for ease of measurement (95% of the analysed references). However, curved or otherwise-shaped surfaces typically need a more careful approach, such as removing a profile measurement along the length of a lattice structure [25]. None of the reviewed references included the removal of complex form from a sample. After form removal, filtering of the spatial frequencies is required.

Reporting the spatial frequencies which have been analysed is important as filtered and unfiltered results will vary considerably. The required measurement length or area and appropriate filtering are defined in the standards (ISO 4288 for profile and ISO 25178-3 for areal data sets). Filtering is based on the roughness or scale of the largest significant feature. Many ISO 4287 roughness parameters, such as Ra, Rq, Rsk, Rku are computed on the scale-limited roughness profile, which is obtained by applying the specific series

of filtering steps on the raw dataset. The most significant filter operation is the separation of waviness and roughness. This separation is performed by application of a high-pass cut-off filter, λ_c . A low-pass filter, λ_s is applied to limit the high frequency component. A value of R_a provided without indication of (at a minimum) the high-pass filter makes comparison of results difficult. The cut-off filter is reported by 90% of the literature works using roughness parameters.

Areal filtering is performed by the application of low-pass and high-pass filters with stated nesting indexes (equivalent to cut-offs), see ISO 25178-3 [113]. In the literature where areal texture parameters have been used, 70% of the references report values for the nesting indexes necessary to reproduce the parameter value. Triantaphyllou et al. [26] investigated the appropriateness of standard cut-off values in AM applications. Ti6Al4V AM components manufactured using SLM and EBM processes had surface R_a values that would require a cut-off (λ_c), of 8 mm per ISO 4288 [96]. The area for optical areal measurements was chosen to be 8 mm \times 8 mm, these lengths corresponding to the cut-off wavelength defined for the profile measurement. The areal L-filter nesting index was established using area-scale analysis [114]. The results obtained showed that the L-filter nesting index (and hence, per ISO 25178-3, the lengths of the sides of the measurement area) needed to be no more than 2.5 mm. This would also suggest that a 2.5 mm cut-off for profile measurements (and not the 8 mm based on the surface R_a per ISO 4288) would be sufficient to capture the data required to characterise the sample SLM and EBM test surfaces. This is significant as it reduces the required profile measurement length by a factor of over three and the required areal measurement area by a factor of ten. The result may also permit areal measurements to be acquired without requiring stitched image fields.

If the textural properties vary between regions of the component then consideration should be given to the size of the observational window, number of windows, relative placement, and treatment of the parameters computed within the windows (averaging for example).

In conclusion, the information currently provided in the literature concerning how topography datasets are processed in order to compute texture parameters varies considerably, often making exact duplication of the results difficult. This scenario may improve with time, with increasing awareness of the data processing steps.

5.3. Texture characterisation in relation to part function

While texture parameters, such as R_a and S_a , quantify the mean deviation of the assessed topography, it has long been recognised that surface texture properties should ideally be related to component function [5]. Characterisation should be preceded by an understanding of which surface features are functionally relevant, and which topographic properties are really responsible for functional performance. Studies have been performed correlating surface texture of AM parts with fatigue resistance [16,71,115]. For example in Ref. [71], Ti6Al4V PBF samples (EBM and SLM) were analysed correlating R_a with fatigue life; it was found that as R_a increases from 3 μm to 1000 μm , fatigue life decreases from 10^5 to 10^4 cycles. In the same work, it was also reported that surface defects had the most significant impact on reducing high cycle fatigue life.

More commonly in the reviewed literature surface texture is analysed to increase understanding of the physics underlying the AM process and the effects of individual process parameters on the AM component. A few examples are reported in the following:

- Grimm et al. [78] found a correlation between the surface orientation of SLM parts and S_{dr} (developed interfacial area ratio),

- Safder et al. [18] researching Ti6Al4V artefacts noted R_a values increased with increasing beam current and decreased with increase in offset focus and scan speed.
- Strano et al. [49] noted upskin surface roughness was influenced by build orientation and layer thickness and downskin surfaces were additionally influenced by laser power.
- Pyka et al. [25] performing chemical etching and polishing of open porous structures, noted that chemical etching primarily removes attached powder grains and electro-chemical polishing decreases the roughness. Hydrofluoric acid was the most effective etching agent.
- Triantaphyllou et al. [26] found that S_a and S_q were suitable measurement parameters for SLM and EBM Ti6Al4V components and that S_{sk} (skewness) differentiated upskin from downskin surfaces.
- Mumtaz and Hopkinson [27] investigating SLM Inconel 625 parts, found that adjusting parameters to achieve minimum top surface and side surface R_a values concurrently was not possible. Parameters that promote a reduction in top surface R_a : increased overlap, reduced scan speed, tend to increase the balling effect and increase side surface R_a . Increasing peak power (to the point of significant material vaporisation) reduces both top and side R_a .
- Beard et al. [85] found that lower scan speed and higher power tend to improve top surface roughness.

Obtaining optimised values for build parameters can be difficult. For example, there is an energy input “sweet spot” below which there is insufficient melting and above which spatter and vaporisation degrade the surface [27]. It was concluded in Ref. [26] that the direction of measurement with respect to lay has little or no effect on the calculated surface texture of SLM and EBM parts. The ASTM F42/ISO TC 261 Joint Group for Standard Test Artefacts (STAR) had found that the effect of the stair-step nature of the layer-by-layer did not dominate the surface texture measurements of PBF platens built at a variety of inclinations [81]. Taylor [4] found that under certain conditions the primary surface lay was not parallel to the laser scan direction.

Research on specific combinations of AM processes and materials, carried out with the help of surface metrology, has led to the determination of optimal configuration parameters for specific process-material combination. However, so far there is a lack of general conclusions of wider applicability.

The relationship between AM process parameters and surface texture is complex and heavily influenced by a multitude of deeply-intertwined physical phenomena; computer-based simulation and predictive modelling has been recognised as a useful method to help understand the relationships between process parameters, and generated topography features [4,116,48,117]. King et al. [118] have modelled the PBF AM process including all factors except the effect of the gas enveloping the build. Currently, due to the process complexity, simulation of one laser pass along a 1 mm laser scan length may take many days on a multi-processor computer system. Commercial companies, such as 3D SIM are working on process solvers that efficiently analyse critical build data and material characterisation to optimise the AM build parameters and process on a part-by-part basis [119].

6. Conclusions

Additive manufacturing (AM) is becoming a strong partner to conventional manufacturing technologies such as casting, forming and machining, for the manufacture of function-critical metallic parts for industrial sectors such as aerospace, medical and automotive.

This review has covered past and current research work on the measurement and characterisation of surface texture for AM metal parts. Amongst AM processes for metallic parts, powder-bed fusion (PBF) has been the subject of the majority of research. As AM technologies experience the transition from prototyping to fabrication of actual parts, a wide array of significant new challenges must be solved. Produced parts must comply to design specifications and standards which include mechanical/thermal/chemical properties, dimensional and surface requirements. These new challenges require a more profound understanding of the AM technology and process, and will ultimately require the development of AM surface texture good practice guidance, specifications and standards.

As the contents of this review have shown, the measurement and characterisation of surface texture for AM processes is challenging. The surfaces of metal PBF components are typically highly irregular, with steep sided and re-entrant features. Relevant surface features exist at a wide range of scales, and care should be taken in selecting instrumentation and measurement scales.

A summary of AM surface texture measurement and characterisation follows:

- Quantitative measurement of surface texture has been predominantly achieved by stylus-based profile measurements. Consequently, the full three-dimensional nature of the topography is not captured.
- Texture characterisation is mostly based on computing ISO 4287 texture parameters on profiles.
- The ISO 4287 Ra parameter is by far the most widely adopted.
- Areal characterisation is increasingly gaining acceptance as the current best solution for obtaining quantitative information about the three-dimensional topography of a surface.
- Areal measurement instrument manufacturers are aware of, and are addressing, the challenges of AM surface texture measurement.
- The majority of existing reference examples where areal characterisation has been used employ ISO 25178-2 texture parameters which are the direct counterpart of the ISO 4287 profile parameters.
- ISO 25178-2 feature parameters, which could help a great deal at isolating surface areas of interest [120] have not been explored in the literature on surface metrology for AM.
- Measurement and characterisation is often not fully reproducible as key information is not reported (for example, void treatment, reduction of measurement anomalies, levelling, filtering and sample spacing).
- In the analysed literature, texture characterisation is mostly performed to gain a better understanding of the AM technology being studied and of its capabilities. This is typical of early-stage development of manufacturing technologies.
- Custom-designed measurement artefacts have generally been used in the research. Artefacts may be optimised for a particular measurement and characterisation scenario.
- There has been limited research into correlation between component functional performance and surface texture.

Metal additive manufacturing presents complex surface metrology challenges, but the significant potential of the process provides incentive to meet these challenges. With the aid of the surface metrology tool box, processes may be understood, improved and optimised. AM-specific surface metrology is in its infancy but will continue to play a vital role as we head toward AM being added to that list of “conventional” manufacturing processes.

Acknowledgements

AT and LB gratefully acknowledge the UK's Engineering and Physical Sciences Research Council (EPSRC) funding of the EPSRC Centre for Innovative Manufacturing in Advanced Metrology (Grant Ref: EP/1033424/1). NS and RKL would like to thank the EC for the MC-IEF-METROSURF grant, RKL would also like to thank the EPSRC for the EP/M008983/1 grant. JT would like to acknowledge that his contribution was prepared by LLNL under Contract DE-AC52-07NA27344 and in collaboration with the Center for Precision Metrology at The University of North Carolina at Charlotte.

References

- [1] Gibson I, Rosen DW, Stucker B. *Additive manufacturing technologies*. Springer; 2010.
- [2] UK Government Office for Science and Department for Business Innovation and Skills. *The future of manufacturing: a new era of opportunity and challenge for the UK*. 2013.
- [3] Markillie P. *A third industrial revolution. The economist special report 2012*. 2012.
- [4] Taylor JS. *Surface characteristics of additive-manufactured components*. In: 15th international conference on metrology and properties of engineering surfaces. 2015.
- [5] Whitehouse DJ. *Surfaces and their measurement*. London: Hermes Penton Science; 2002.
- [6] Stavroulakis P, Leach R. *Review of post-process optical form metrology for industrial-grade metal additive manufactured parts*. *Rev Sci Instrum* 2016;87:041101.
- [7] ISO_25178-2 BE. BS EN ISO_25178-2. *Geometrical product specifications (GPS): surface texture: areal 2: terms, definitions and surface texture parameters*. British Standards Institute; 2012.
- [8] Leach RK. In: Laperrière L, Reinhart G, editors. *CIRP encyclopedia of production engineering*. Berlin: Springer-Verlag; 2014.
- [9] Gu D. *Laser additive manufacturing of high-performance materials*. DE: Springer Verlag; 2015.
- [10] Gu D, Shen Y. *Balling phenomena in direct laser sintering of stainless steel powder: metallurgical mechanisms and control methods*. *Mater Des* 2009;30:2903–10.
- [11] Yin H, Emi T. *Marangoni flow at the gas/melt interface of steel*. *Metall Mater Trans B* 2003;34:483–93.
- [12] Everton SK, Hirsch M, Stavroulakis P, Leach RK, Clare AT. *Review of in-situ process monitoring and in-situ metrology for metal additive manufacturing*. *Mater Des* 2016;95:431–45.
- [13] Gibson I, Shi D. *Material properties and fabrication parameters in selective laser sintering process*. *Rapid Prototyp J* 1997;3:129–36.
- [14] Vandenbroucke B, Kruth J-P. *Selective laser melting of biocompatible metals for rapid manufacturing of medical parts*. *Rapid Prototyp J* 2007;13:196–203.
- [15] Huang NM. *Analyzing the surface finish of knee implants to determine criteria for applications in direct metal laser sintering*. 2012 NCUR 2012.
- [16] Spierings A, Starr T, Wegener K. *Fatigue performance of additive manufactured metallic parts*. *Rapid Prototyp J* 2013;19:88–94.
- [17] Garcia CR, Rumpf RC, Tsang HH, Barton JH. *Effects of extreme surface roughness on 3D printed horn antenna*. *Electron Lett* 2013;49:734–6.
- [18] Saïdar A, He HZ, Wei LY, Snis A, Chavez de Paz LE. *Effect of process parameters settings and thickness on surface roughness of EBM produced Ti-6Al-4V*. *Rapid Prototyp J* 2012;18:401–8.
- [19] Jamshidinia M, Kovacevic R. *The influence of heat accumulation on the surface roughness in powder-bed additive manufacturing*. *Surf Topogr: Metrol Prop* 2015;3:014003.
- [20] Tang H, Qian M, Liu N, Zhang X, Yang G, Wang J. *Effect of powder reuse times on additive manufacturing of Ti-6Al-4V by selective electron beam melting*. *JOM* 2015;67:555–63.
- [21] Beaucamp AT, Namba Y, Charlton P, Graziano AA. *Finishing of additively manufactured titanium alloy by shape adaptive grinding (SAG)*. *Surf Topogr: Metrol Prop* 2015;3:024001.
- [22] Karlsson J, Snis A, Engqvist H, Lausmaa J. *Characterization and comparison of materials produced by Electron Beam Melting (EBM) of two different Ti-6Al-4V powder fractions*. *J Mater Process Technol* 2013;213:2109–18.
- [23] Svensson M, Ackellid U. *Titanium alloys manufactured with electron beam melting-mechanical and chemical properties*. *Proceedings of the materials and processes for medical devices conference: ASM international* 2010:189–94.
- [24] Badrossamay M, Childs T. *Layer formation studies in selective laser melting of steel powders*. In: *Proc SFF Symp*. 2006. p. 268–79.
- [25] Pyka G, Kerckhofs G, Papantoniou I, Speirs M, Schrooten J, Wevers M. *Surface roughness and morphology customization of additive manufactured open porous Ti6Al4V structures*. *Materials* 2013;6:4737–57.
- [26] Triantaphyllou A, Giusca CL, Macaulay GD, Roerig F, Hoebel M, Leach RK, et al. *Surface texture measurement for additive manufacturing*. *Surf Topogr: Metrol Prop* 2015;3:024002.

- [27] Mumtaz K, Hopkinson N. Top surface and side roughness of Inconel 625 parts processed using selective laser melting. *Rapid Prototyp J* 2009;15:96–103.
- [28] Diatlov A, Buchbinder D, Meiners W, Wissenbach K, Büttmann J, et al. Towards surface topography: quantification of Selective Laser Melting (SLM) built parts. In: Bartolo, editor. *Innovative Developments in Virtual and Physical Prototyping*. London: Taylor and Francis Group; 2012. ISBN 978-0-415-68418-7.
- [29] Król M, Dobrzański L, Reimann IC. Surface quality in selective laser melting of metal powders. *Arch Mater Sci* 2013;88:88.
- [30] Slotwinski J, Garboczi E, Stutzman P, Ferraris C, Watson S, Peltz M. Characterization of metal powders used for additive manufacturing. *J Res Natl Inst Stand Technol* 2014;19.
- [31] Pyka G, Burakowski A, Kerckhofs G, Moesen M, Van Bael S, Schrooten J, et al. Surface modification of Ti6Al4V open porous structures produced by additive manufacturing. *Adv Eng Mater* 2012;14:363–70.
- [32] Yasa E, Kruth JP. Application of laser re-melting on selective laser melting parts. *Adv Prod Eng Manage* 2011;6:259–70.
- [33] Yasa E, Deckers J, Kruth JP. The investigation of the influence of laser re-melting on density, surface quality and microstructure of selective laser melting parts. *Rapid Prototyp J* 2011;17:312–27.
- [34] Yang J, Ouyang H, Xu C, Wang Y. Top surface quality research for direct metal laser fabrication. *Rapid Prototyp J* 2012;18:4–15.
- [35] Yadroitsev I, Smurov I. Surface morphology in selective laser melting of metal powders. *Phys Procedia* 2011;12:264–70.
- [36] Spierings A, Herres N, Levy G. Influence of the particle size distribution on surface quality and mechanical properties in AM steel parts. *Rapid Prototyp J* 2011;17:195–202.
- [37] Simonelli M, Tse YY, Tuck C. On the texture formation of selective laser melted Ti-6Al-4V. *Metall Mater Trans A* 2014;45:2863–72.
- [38] Kruth JP, Yasa E, Deckers J. Roughness improvement in selective laser melting. *Proceedings of the 3rd international conference on polymers and moulds innovations 2008*: 170–83.
- [39] Buchbinder D, Schleifenbaum H, Heidrich S, Meiners W, Büttmann J. High power selective laser melting (HP SLM) of aluminum parts. *Phys Procedia* 2011;12:271–8.
- [40] Brinksmeier E, Levy G, Meyer D, Spierings A. Surface integrity of selective-laser-melted components. *CRP Ann Manuf Technol* 2010;59:601–6.
- [41] Badrossamay M, Childs T. Further studies in selective laser melting of stainless and tool steel powders. *Int J Mach Tools Manuf* 2007;47:779–84.
- [42] Ahmed N, Voisey K, McCartney D. Investigation into the effect of beam shape on melt pool characteristics using analytical modelling. *Opt Lasers Eng* 2010;48:548–54.
- [43] Abe F, Osakada K, Shiomi M, Uematsu K, Matsumoto M. The manufacturing of hard tools from metallic powders by selective laser melting. *J Mater Process Technol* 2001;111:210–3.
- [44] Yasa E, Kruth JP, Deckers J. Manufacturing by combining selective laser melting and selective laser erosion/laser re-melting. *CRP Ann Manuf Technol* 2011;60:263–6.
- [45] Calignano F, Manfredi D, Ambrosio EP, Iuliano L, Fino P. Influence of process parameters on surface roughness of aluminum parts produced by DMLS. *Int J Adv Manuf Technol* 2013;67:2743–51.
- [46] Ramos J, Murphy J, Wood K, Bourell D, Beaman J. Surface roughness enhancement of indirect-SLS metal parts by laser surface polishing. In: *Proceedings of the 12th solid freeform fabrication symposium*. 2001. p. 28–38.
- [47] Abe S, Higashi Y, Fuwa I, Yoshida N, Yoneyama T. Milling-combined laser metal sintering system and production of injection molds with sophisticated functions. In: *Towards synthesis of micro-/nano-systems*. Springer; 2007. p. 285–90.
- [48] Patil N, Pal D, Anam M, Gong H, Gu H, Dilip S, et al. Predictive modeling capabilities for dimensional accuracy and surface finish in Metal Laser Melting based Additive Manufacturing. *Dimensional accuracy and surface finish in additive manufacturing*. In: *ASPE 2014 spring topical meeting*. 2014. ASPE.
- [49] Strano G, Hao L, Everson RM, Evans KE. Surface roughness analysis, modelling and prediction in selective laser melting. *J Mater Process Technol* 2013;213:589–97.
- [50] Oreshkin O, Klipper M, Temmler A, Willenberg E. Active reduction of waviness through processing with modulated laser power. *J Laser Appl* 2015;27:022004.
- [51] Brandl E, Heckenberger U, Holzinger V, Buchbinder D. Additive manufactured AlSi10Mg samples using Selective Laser Melting (SLM): microstructure, high cycle fatigue, and fracture behavior. *Mater Des* 2012;34:159–69.
- [52] Van Bael S, Kerckhofs G, Moesen M, Pyka G, Schrooten J, Kruth J-P. Micro-CT-based improvement of geometrical and mechanical controllability of selective laser melted Ti6Al4V porous structures. *Mater Sci Eng: A* 2011;528:7423–31.
- [53] Morgan R, Sutcliffe C, O'Neill W. Experimental investigation of nanosecond pulsed Nd: YAG laser re-melted pre-placed powder beds. *Rapid Prototyp J* 2001;7:159–72.
- [54] Meena VK, Magalhães. Optimization of EDM machining parameters using DMLS electrode. *Rapid Prototyp J* 2006;12:222–8.
- [55] Liu Y, Yang Y, Mai S, Wang D, Song C. Investigation into spatter behavior during selective laser melting of AISI 316L stainless steel powder. *Mater Des* 2015;87:797–806.
- [56] Abd-Elghany K, Bourell D. Property evaluation of 304L stainless steel fabricated by selective laser melting. *Rapid Prototyp J* 2012;18:420–8.
- [57] Rombouts M, Maes G, Hendrix W, Delarbre E, Motmans F. Surface finish after laser metal deposition. *Phys Procedia* 2013;41:810–4.
- [58] Gharbi M, Peyre P, Gorny C, Carin M, Morville S, Le Masson P, et al. Influence of various process conditions on surface finishes induced by the direct metal deposition laser technique on a Ti-6Al-4V alloy. *J Mater Process Technol* 2013;213:791–800.
- [59] Zhu G, Li D, Zhang A, Pi C, Tang Y. The influence of laser and powder defocusing characteristics on the surface quality in laser direct metal deposition. *Opt Laser Technol* 2012;44:349–56.
- [60] Pinkerton AJ, Li L, Lau W. Effects of powder geometry and composition in coaxial laser deposition of 316L steel for rapid prototyping. *CRP Ann Manuf Technol* 2003;5:2:181–4.
- [61] Ding J, Colegrove P, Mehnert J, Ganguly S, Sequeira Almeida PM, Wang F, Williams S. Thermo-mechanical analysis of Wire and Arc Additive Layer Manufacturing process on large multi-layer parts. *Comput Mater Sci* 2011;50:3315–22.
- [62] Wang F, Williams S, Colegrove P, Antonyamy AA. Microstructure and mechanical properties of wire and arc additive manufactured Ti-6Al-4V. *Metall Mater Trans A* 2013;44:968–77.
- [63] Banfeld B, Vd Biest O, Gault R. Additive manufacturing of Ti-6Al-4V components by shaped metal deposition: microstructure and mechanical properties. *Mater Des* 2010;31:5106–11.
- [64] Smith GT. *Industrial metrology: surfaces and roundness*. London: Springer; 2002.
- [65] **Special metals. Inconel alloy 718. n.d.**
- [66] Godino Martínez M. *AISI10Mg parts produced by selective laser melting (SLM) [masters]*. Universidad Carlos III de Madrid; 2013.
- [67] **EOS e-manufacturing solutions. Materials for metal manufacturing. n.d.**
- [68] **AK Steel. 316/316L stainless steel data sheet. 2007.**
- [69] **ASM Aerospace Specification Metals. Titanium Ti-6Al-4V-AMS-4911. 2015.**
- [70] Sidambe AT. Biocompatibility of advanced manufactured titanium implants—a review. *Materials* 2014;7:8168–88.
- [71] Frazier WE. Metal additive manufacturing: a review. *J Mater Eng Perform* 2014;23:1917–28.
- [72] **Sandvik. Metal powders for additive manufacturing. 2010.**
- [73] Strano G, Hao L, Everson R, Evans K. Multi-objective optimization of selective laser sintering processes for surface quality and energy saving. *Proc Inst Mech Eng B: J Eng Manuf* 2011. 0954405411402925.
- [74] Ahn D, Kwon JH, Kwon S, Song J, Lee S. Representation of surface roughness in fused deposition modeling. *J Mater Process Technol* 2009;209:5593–600.
- [75] Ahn D, Kim H, Lee S. Surface roughness prediction using measured data and interpolation in layered manufacturing. *J Mater Process Technol* 2009;209:664–71.
- [76] Campbell RI, Martorelli M, Lee HS. Surface roughness visualisation for rapid prototyping models. *Comput Aided Des* 2002;34:717–25.
- [77] Triantaphyllou A, Giusca CL, Macaulay GD, Leach RK, Milne KA. Surface texture measurement for additive manufacturing. *Dimensional accuracy and surface finish in additive manufacturing*. In: *ASPE 2014 spring topical meeting*. 2014. ASPE.
- [78] Grimm T, Wior G, Witt G. Characterization of typical surface effects in additive manufacturing with confocal microscopy. *Surf Topogr: Metrol Prop* 2015;3:014001.
- [79] Jamshidian M, Kovacevic R. The influence of heat accumulation on the surface roughness in additive manufacturing by electron beam melting (EBM). *Dimensional accuracy and surface finish in additive manufacturing*. In: *ASPE 2014 spring topical meeting*. 2014. ASPE.
- [80] Moylan S, Slotwinski J, Cooke A, Jurens K, Donmez MA. Proposal for a standardized test artifact for additive manufacturing machines and processes. In: *Proceedings of the 2012 annual international solid freeform fabrication symposium*. 2012. p. 6–8.
- [81] Moylan S. Progress toward standardized additive manufacturing test artifacts. *Achieving precision tolerances in additive manufacturing*. In: *ASPE 2015 spring topical meeting*. 2015. ASPE.
- [82] Zecchino M. How to choose the correct stylus for any application. *Veeco*; 2005.
- [83] Uhlmann E, Rethmeier M, Graf B, Kersting R, Bergman A. Flexible manufacturing with an additive process chain design, production and surface finish. *Achieving precision tolerances in additive manufacturing*. In: *ASPE 2015 spring topical meeting*. 2015. ASPE.
- [84] Ross I, Kumstel J, Bremen S, Willenberg E. Laser polishing of laser additive manufactured surfaces made from Inconel 718 and ASTM F75. *Achieving precision tolerances in additive manufacturing*. In: *ASPE 2015 Spring Topical Meeting*. 2015. ASPE.
- [85] Beard M, Ghiya O, Evans KE. Using Raman spectroscopy to monitor surface finish and roughness of components manufactured by selective laser sintering. *J Raman Spectrosc* 2013;42:744–8.
- [86] Galantucci LM, Lavecchia F, Perocco G. Experimental study aiming to enhance the surface finish of fused deposition modeled parts. *CRP Ann Manuf Technol* 2009;5:8:189–92.

- [87] Thomas K, Lukas H, Iris B, Michael M. Nanoimprint Lithography on curved surfaces prepared by fused deposition modelling. *Surf Topogr: Metrol Prop* 2015;3:024003.
- [88] Krolczyk G, Raos P, Legutko S. Experimental analysis of surface roughness and surface texture of machined and fused deposition modelled parts. *Tehnički Vjesnik – Tech Gaz* 2014;21:217–21.
- [89] Temmler A, Willenborg E, Wissenbach K. Laser polishing. *SPIE LASE: International Society for Optics and Photonics*; 2012. p. 82430W–W-13.
- [90] Vetterli M, Schmid M, Wegener K. Comprehensive Investigation of surface characterization methods for laser sintered parts. In: *Fraunhofer direct digital manufacturing conference*. 2014.
- [91] Johnson MK, Adelson EH. Retrographic sensing for the measurement of surface texture and shape. *IEEE Conference on computer vision and pattern recognition*, 2009, CVPR 2009 2009: 1070–7. IEEE.
- [92] Johnson MK, Cole F, Raj A, Adelson EH. Microgeometry capture using an elastomeric sensor. *ACM Trans Graph (TOG)* 2011;46. ACM.
- [93] Kerckhofs G, Pyka G, Moesen M, Van Bael S, Schrooten J, Wevers M. High-resolution microfocus X-ray computed tomography for 3D surface roughness measurements of additive manufactured porous materials. *Adv Eng Mater* 2013; 15:153–8.
- [94] ISO_3274 BE. BS EN ISO_3274. Geometric product specifications (GPS)—surface texture: profile method—normal characteristics of contact (stylus) instruments. *British Standards Institute*; 1996.
- [95] ISO_4287 BE. BS EN ISO_4287. Geometrical product specification (GPS): surface texture: profile method: terms, definitions and surface texture parameters. *British Standards Institute*; 2000.
- [96] ISO_4288 BE. BS EN ISO_4288. Geometric product specification (GPS): surface texture: profile method: rules and procedures for the assessment of surface texture. *British Standards Institute*; 1998.
- [97] ASME. ASME B46.1 (2009) Surface texture (surface roughness, waviness and lay). *New York*; 2009.
- [98] Jiang X, Scott PJ, Whitehouse DJ, Blunt L. Paradigm shifts in surface metrology. Part II. The current shift. *Proc R Soc Lond A: Math Phys Eng Sci* 2007;2071–99. The Royal Society.
- [99] Leach R. Optical measurement of surface topography. *Springer*; 2011.
- [100] Thompson A, Maskery L, Leach RK. X-ray computed tomography for additive manufacturing: a review. *Meas Sci Technol* 2016;27:072001.
- [101] Townsend A, Blunt L, Bills P. Investigating the capability of microfocus x-ray computed tomography for areal surface analysis of additively manufactured parts (in final stage of review). *Dimensional accuracy and surface finish in additive manufacturing*. In: *ASPE 2016 summer topical meeting*. 2016. ASPE.
- [102] Kruth JP, Bartscher M, Carmignato S, Schmitt R, De Chiffre L, Weckenmann A. Computed tomography for dimensional metrology. *CIRP Ann Manuf Technol* 2011;60:821–42.
- [103] JIS Standards. JIS B 0601:2013 Geometrical product specifications (GPS)—surface texture: profile method—terms, definitions and surface texture parameters. 2013.
- [104] ISO. ISO/CD 25178-600. Geometrical product specifications (GPS)—surface texture: areal—part 600: metrological characteristics for areal-topography measuring methods. *ISO*; 2015.
- [105] Turner BN, Gold SA. A review of melt extrusion additive manufacturing processes: II. Materials, dimensional accuracy, and surface roughness. *Rapid Prototyp J* 2015;21:250–61.
- [106] Leach RK, Brown L, Jiang X, Blunt R, Conroy M, Mauger D. *Guide to the measurement of smooth surface topography using coherence scanning interferometry. NPL measurement good practice guide no. 108*. 2008.
- [107] Leach RK. *Characterisation of areal surface texture*. Springer; 2013.
- [108] Senin N, Leach RK, Pini S, Blunt LA. Texture-based segmentation with Gabor filters, wavelet and pyramid decompositions for extracting individual surface features from areal surface topography maps. *Meas Sci Technol* 2015;26:095405.
- [109] Lou S, Jiang X, Scott PJ. Correlating motif analysis and morphological filters for surface texture analysis. *Measurement* 2013;46:993–1001.
- [110] Scott PJ. Pattern analysis and metrology: the extraction of stable features from observable measurements. *Proc R Soc Lond A: Math Phys Eng Sci* 2004;2845–64. The Royal Society.
- [111] Grimm T, Witt G, Wiora G. Characterization of additive manufactured surfaces with confocal microscopy. *Dimensional accuracy and surface finish in additive manufacturing*. In: *ASPE 2014 spring topical meeting*. 2014. ASPE.
- [112] Leach R, Haitjema H. Bandwidth characteristics and comparisons of surface texture measuring instruments. *Meas Sci Technol* 2010;21:032001.
- [113] ISO_25178-3 BE. BS EN ISO_25178-3. Geometrical product specifications (GPS): surface texture: areal: part 3: specification operators. *British Standards Institute*; 2012.
- [114] Brown CA. Areal fractal methods. In: Leach RK, editor. *Characterisation of areal surface texture*. 2013. Springer; 2016. p. 129–53.
- [115] Chan KS, Koike M, Mason RL, Okabe T. Fatigue life of titanium alloys fabricated by additive layer manufacturing techniques for dental implants. *Metallurgical and Materials Transactions A* 2013;44:1010–22.
- [116] Taylor JS. Physical processes linking input parameters and surface morphology in additive manufacturing. *Achieving precision tolerances in additive manufacturing*. In: *ASPE 2015 spring topical meeting*. 2015. ASPE.
- [117] Barari A, Jamiolahmadi S. Estimation of surface roughness of additive manufacturing parts using finite difference method. *Dimensional accuracy and surface finish in additive manufacturing*. In: *ASPE 2014 spring topical meeting*. 2014. ASPE.
- [118] King W, Anderson A, Brown D, Ferencz R, Hodge N, Kamath C, et al. Modelling the metal additive manufacturing process at the scales of the part and the powder. In: *2015 International conference on additive manufacturing and 3D printing*. 2015.
- [119] Stucker B. *Overcoming the computational complexity problem for additive manufacturing. Additive manufacturing and 3D printing*. Nottingham, UK; 2015.
- [120] Tian Y, Wang J, Peng Z, Jiang X. Numerical analysis of cartilage surfaces for osteoarthritis diagnosis using field and feature parameters. *Wear* 2011;271:2370–8.



Areal surface texture data extraction from X-ray computed tomography reconstructions of metal additively manufactured parts



A. Townsend^{*}, L. Pagani, P. Scott, L. Blunt

EPSRC Centre for Innovative Manufacturing in Advanced Metrology, University of Huddersfield, UK

ARTICLE INFO

Article history:

Received 10 November 2016
Received in revised form
17 December 2016
Accepted 20 December 2016
Available online 29 December 2016

Keywords:

Metal additive manufacturing
ISO 25178
Areal surface texture
X-ray computed tomography
Metrology
Internal surfaces

ABSTRACT

Many applications that exploit the manufacturing flexibility of additive manufacturing (AM) produce surfaces, primarily internal features, which cannot be measured using conventional contact or line-of-sight optical methods. This paper evaluates the capability of a novel technique to extract areal surface data from micro-focus X-ray computed tomography (XCT) from AM components and then generate surface parameter data per ISO 25178-2. This non-destructive evaluation of internal features has potential advantages during AM product research and commercial production. The data extracted from XCT is compared with data extracted using a focus variation instrument. A reference dimensional artefact is included in all XCT measurements to evaluate XCT surface determination performance and dimensional scaling accuracy. Selected areal parameters generated using the extraction technique are compared, including S_a , for which the nominal difference between the value obtained using XCT and used the focus variation method was less than 2.5%.

© 2016 The Authors. Published by Elsevier Inc. This is an open access article under the CC BY license (<http://creativecommons.org/licenses/by/4.0/>).

1. Introduction

Additive Manufacturing (AM) has emerged as the new paradigm in manufacturing. AM enables the production of geometrically complex components, by manufacturing them in a layer-by-layer manner using a variety of techniques from powder bed fusion of topologically optimized metal components [1] to the fused deposition modeling of scaffold architecture for tissue engineering applications [2]. AM has the potential for dramatically shorter development cycles and enables previously complex assemblies to be made in one piece. AM is now being used to make production parts in high-value applications such as aerospace, the automotive sector, the energy sector and medical engineering, where part complexity and customizability are key advantages.

Two of the limiting factors of AM however are a lack of precision in terms of achieving many required tolerances on engineering parts [3] and a lack of an infrastructure for the implementation of geometrical product specifications (GPS). In terms of accurate tolerancing and developing the use of metal powder based AM within the wider manufacturing framework, there are significant issues that remain to be answered concerning the optimal traceable metrology techniques used to assess AM parts for geometry

and surface texture. This is especially problematic when parts need to be mated on assembly or require a specific surface roughness. The published information on the development of post-process techniques to measure and characterize complex part surface topography produced by AM are limited and shows a dearth of advanced techniques (e.g. the use of areal topography parameter) to assess the relatively high surface roughness of AM parts.

A recent review has been carried out to highlight the most commonly used surface metrology systems and quantitative topography parameters used to assess part quality [4]. This review showed focus variation, along with confocal microscopy, have become popular methods of measurement of the complex, three-dimensional surfaces of metal AM parts. Areal measurement and characterization (for example, as defined in ISO 25178-2 [5] and ISO 25178-3 [6]) is seeing more widespread adoption as the advantages over contact profile measurements are becoming apparent. Surface topography is three dimensional in nature and areal surface measurements are generally more representative of the functional surface than profile measurements [5]. Similarly, areal measurements will tend to provide greater understanding of AM manufacturing process performance than profile measurements [6].

Additionally, it has become clear that due to the complexity of AM part geometry XCT has an increasingly important role in assessing part geometry [7–10]. XCT has the ability to measure internal and recessed surfaces which would be impossible to access using

^{*} Corresponding author.
E-mail address: a.townsend@hud.ac.uk (A. Townsend).

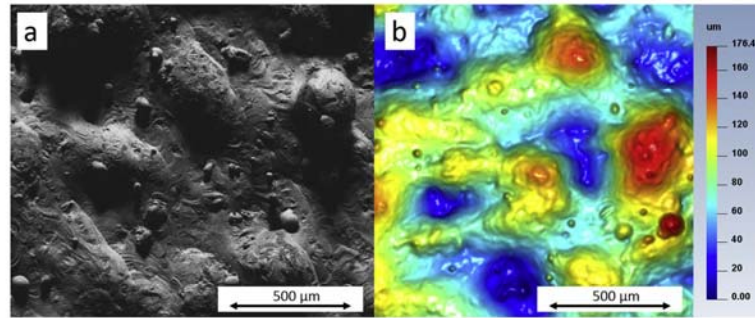


Fig. 1. (a) SEM secondary electron mode micrograph of the AlSi10Mg AM upskin surface (b) Alicona FV surface map of the AM surface.

conventional surface metrology techniques. Unfortunately the data produced by XCT systems is not in the form that is easily useable to enable quantitative surface assessment to be carried out and its accuracy, repeatability and resolution in terms of reproducing useful topography data has yet to be established.

With reference to metal powder based AM techniques, the present paper seeks to address these issues by providing a methodology to capture XCT data and transform it into a format that allows quantitative surface assessment. Additionally the data produced from XCT is verified in terms of its ability to characterize surface topography by comparing the XCT information to surface metrology data captured by a commercial focus variation (FV) surface metrology instrument (Alicona Infinite Focus G4). Issues such as surface determination techniques, scaling errors, instrument stability and repeatability are considered in the context of using an XCT instrument as an effective metrology tool. The aim of the paper is to highlight the efficacy of using XCT systems to produce standard (ISO 25178) surface texture parameter data. This is of particular relevance where the surface topography of internal or recessed surfaces needs to be established without destructively testing the part.

2. Methodology

The methodology used in the present study consists of the measurement and analysis of two artefacts: one additively manufactured artefact with a specific surface zone to be measured for surface texture comparison purposes (AM artefact) and a second artefact, manufactured from a similar material, used to assess and compensate for surface determination [11] and XCT measurement scaling errors (Dimensional artefact).

2.1. Artefact design

2.1.1. AM artefact

The AM artefact is a cube with 10 mm sides. The cube was manufactured on a Renishaw AM250 SLM machine using AlSi10Mg aluminium alloy powder. The AM component top (upskin) surface was used throughout the evaluation. Fig. 1a shows a scanning electron microscope (SEM) micrograph of a part of the surface. Fig. 1b shows a surface map of the same surface captured using an Alicona G4 focus variation instrument.

2.1.2. Dimensional artefact

The dimensional artefact was machined from Aluminium alloy (6082 T6 temper). The material type and overall size, both similar to the AM artefact, were chosen to provide similar X-ray absorp-

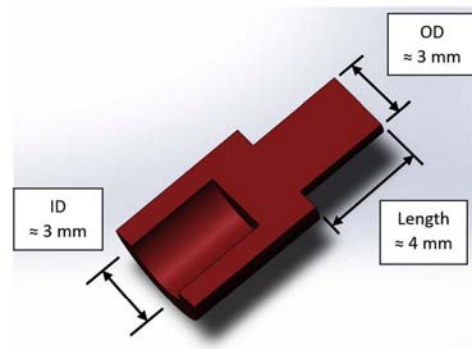


Fig. 2. CAD cross-section view of the dimensional artefact showing the measurement distances.

tion characteristics and surface determination challenges as the AM artefact. Three dimensions were measured during the analysis: An outside diameter (OD) and an inside diameter (ID) of similar size (approx. 3 mm) and a step length between two parallel faces of approximately 4 mm, see Fig. 2.

These measurement dimensions were chosen to highlight possible XCT surface determination problems. If, for example, the surface determination were to position the calculated surface inside the actual part surface, then the OD would tend to be undersized compared to the reference dimension and the ID would tend to be oversized. Surface determination position should have negligible effect on the length measurement because the measurement is between surfaces that are parallel and facing the same direction. Surface determination defines the material boundary based on grey scale (density) values between background and object material. The constructed surface using standard surface determination and iterative local surface determination implemented in commercial software, VGStudio MAX 2.2 [12] are shown in Fig. 3. The result of standard surface determination is a material boundary defined by one grey value applied globally to the object. Iterative local surface determination produces a material boundary based on local surrounding voxels, which largely compensates for any local deviations produced during the acquisition process, such as beam hardening. In this section example it can be seen that the standard surface determination would produce a calculated surface approximately 10–40 μm outside the actual surface. Local iterative surface

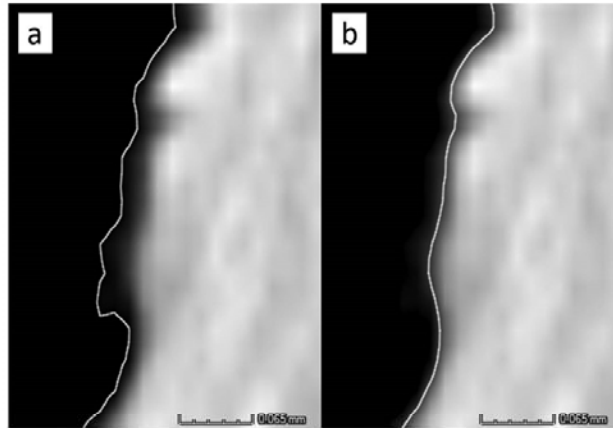


Fig. 3. Surface determination (VGStudio MAX 2.2 [12]) (a) Standard surface determination (b) local iterative surface determination.

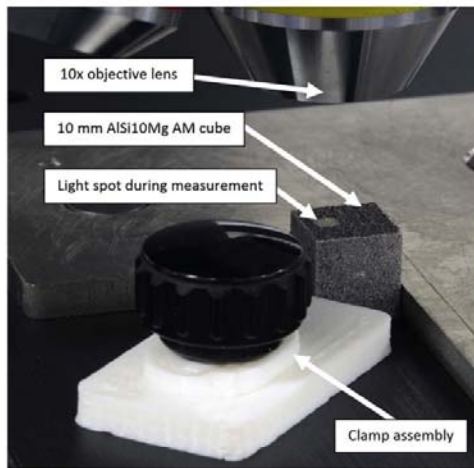


Fig. 4. Focus variation test fixture.

determination was used for all XCT measurements in the current work.

By evaluating these three types of measurements, possible errors due to surface determination can be evaluated and compensated for as necessary. The surface determination evaluation, in combination with information gained by comparing XCT nominal OD, ID and Length dimensions with the measurement results from the CMM, will provide scaling correction factors, as necessary, to be applied to the AM surface texture XCT measurement.

2.2. Measurements

The AM artefact surface reference measurements were taken using a focus variation instrument (Alicona G4) and the dimensional artefact reference measurements were taken using a coordinate measurement machine (CMM) (Zeiss Prismo). Both

artefacts were then assembled into a 3D printed acrylonitrile butadiene styrene (ABS) polymer fixture and were measured together on a Nikon XT H 225 industrial XCT machine.

2.2.1. AM artefact focus variation measurements

All measurements were performed with a 10x objective lens on the Alicona G4. With this lens installed the system step height accuracy, with a 1 mm step, is 0.05%; maximum system lateral resolution is 1.75 μm ; the maximum system vertical resolution is 100 nm with a repeatability of 30 nm. The Alicona focus variation system was chosen for its ability to image surfaces with high slope angles [13], together with its z-axis height range capable of measuring the tall structures present on the AM surface. The reference AM surface was measured 10 times. The component was removed from the fixture between each measurement and then replaced. This removal and replacement protocol was initiated to give an indication of measurement repeatability obtainable in an “industrial” scenario where a series of parts from a batch are measured consecutively using the same instrument, fixture or jig.

The measurement area was approximately 10 mm \times 10 mm (later cropped to 8 mm \times 8 mm for analysis). The measurement consisted of 8 by 10 stitched areas. The lateral sampling distance was 2.33 μm for all measurements. These measurement parameters were chosen based on the roughness of the surface. An initial profile roughness R_a value for the surface obtained was approximately 40 μm . Per ISO 4288 Table 1 requirements [14] this would then require a roughness sampling length and λ_c cut-off wavelength of 8 mm. This would suggest a similar L-filter nesting index (8 mm) and a measurement area of 8 mm \times 8 mm per ISO 25178-3 [15]. The S-filter nesting index value of 0.025 mm was selected from Table 1 of ISO 25178-3. The ratio between the S-filter nesting index value and the measurement sampling distance is required to be a minimum of 3:1 for optical instruments per ISO 25178-3 Table 3. The actual measurement sampling distance of 2.33 μm gives a ratio of greater than 10:1. The Alicona G4 surface data was saved with an STL file format to allow simultaneous processing with the XCT surface data.

2.2.2. Dimensional artefact CMM measurements

The dimensional artefact was measured using a Zeiss Prismo CMM. The CMM maximum permissible error (MPE) is $(1.9 + L/300)$ μm (L in meters). A 1.0 mm diameter ruby probe tip was used for

Table 1
Nikon XT H 225 settings used for all measurements.

Parameter	Value	Parameter	Value
Source to object distance	84.2 mm	Filter material	Copper
Source to detector distance	972 mm	Filter thickness	0.5 mm
Acceleration voltage	150 kV	Number of projections	1583
Filament current	67 μ A	Detector pixels	1008 \times 1008
Exposure time	2829 ms	Voxel size	17.3 μ m

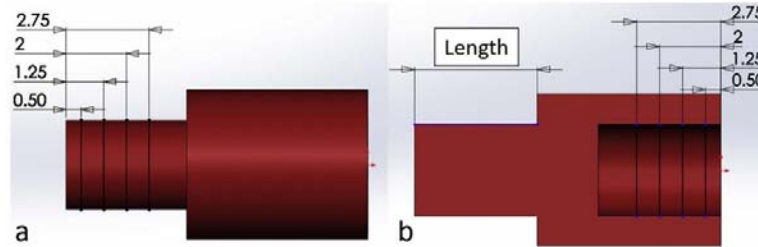


Fig. 5. Location of CMM measurements (a) OD, (b) ID and Length. All dimensions in mm.

all measurements. CMM scanning mode was used whereby the probe traverses the surface, remaining in contact with the surface. The ID and OD were measured at four locations along the length of the artefact; measurements were taken at distances 0.5 mm, 1.25 mm, 2.0 mm and 2.75 mm from the respective end faces, see Fig. 5. 100 measurement points per circle were taken. The dimensional artefact was not removed from the fixture between CMM measurements.

2.2.3. XCT measurements

2.2.3.1. XCT measurement conditions. Fig. 6 shows a CAD cross-section view of the AM artefact and dimensional artefact mounted within the 3D printed fixture. Both artefacts were retained within the fixture using nylon slotted studs. This configuration was used for all of the XCT measurements. The upskin surface of the AM artefact, Fig. 6a, was mounted in the fixture facing downwards, 45° to the horizontal. The fixture was designed such that none of the surfaces of the AM artefact or dimensional artefact to be measured were in direct contact with the plastic of the fixture. This was to optimise surface determination as there is only a two-material interface to consider (artefact to air).

After assembly into the fixture the assembly was mounted on the rotary stage of the Nikon XT H 225, see Fig. 7.

The machine parameter settings were consistent for all XCT measurements, see Table 1.

Reconstruction, from the 1583 TIFF images was performed in Nikon CTPro 3D [16]. Surface determination was performed in VGStudio MAX 2.2. Air was selected and defined as the background material. A volume from the dimensional artefact was selected and defined as the material of interest. An initial surface histogram was generated based on these selections. Iterative surface determination was used, with a (default) search distance of 4.00 voxels for all measurements, with the starting determination based on the initial histogram. Two regions of interest (ROI) were extracted from each measurement: the AM component upskin surface and the entire dimensional artefact. The surfaces of these two ROI were extracted and saved with an STL mesh format, using the VGStudio MAX 2.2 "Super Precise" setting, which provides highest available resolution with no simplification of the mesh.

2.2.3.2. XCT measurement data sets. The XCT measurements consisted of three sets, each of five measurements.

2.2.3.2.1. Set 1. Five measurements were taken with the AM artefact and dimensional artefact in the 3D printed fixture. The fixture was not removed from the rotary stage and the artefacts were not removed from the fixture between measurements.

2.2.3.2.2. Set 2. After the initial five measurements the XCT filament was replaced. Five measurements were taken with the AM artefact and dimensional artefact in the 3D printed fixture. The fixture was not removed from the rotary stage and the artefacts were not removed from the fixture between measurements.

2.2.3.2.3. Set 3. After completion of measurement set 2 the fixture was removed from the XCT rotary stage. The AM component was removed from the fixture and rotated 90° CCW (so the surface-of-interest remained facing downwards at an angle of 45° to the horizontal). Between every subsequent measurement the fixture was removed from the stage, the AM artefact was removed from the fixture, rotated 90° , replaced into the fixture and fixture then replaced onto the rotary stage. This removal and replacement is similar to the protocol followed for the Alicona G4 focus variation measurements and was performed to duplicate an "industrial" lot measurement scenario. The dimensional artefact was not removed between measurements. To allow alignment and cropping of the Alicona and XCT data the data format must be similar, so all files from XCT and Alicona were saved with an STL format.

2.3. Surface data processing for the AM surface

The data processing performed aligns all surfaces to ensure all quantitative data is generated from similar surface areas of the part. The data is converted to a form that allows analysis using standard surface software packages, such as MountainsMap [17] and SurfStand [18]. This processing is a ten-stage sequence incorporating custom computational processing combined with the use of commercially available software. This protocol was used to process all the surface data STL files, from the XCT and the Alicona (this is similar to the process performed in [19]):

2.3.1. Trim data

The STL from the Alicona contains the edges of the top surface and the XCT measurements of the surface also includes the sides

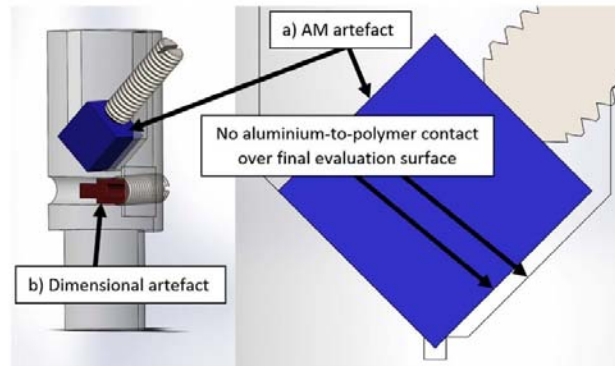


Fig. 6. XCT measurement fixture showing (a) AM artefact (b) dimensional artefact.

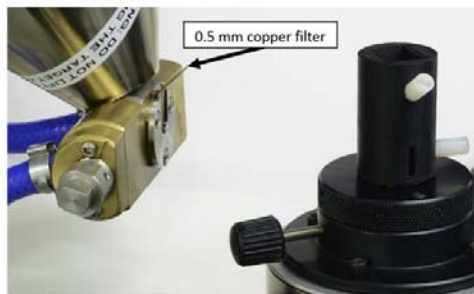


Fig. 7. Fixture containing two artefacts, shown at the measurement position in the Nikon XT H 225.

of the sample. These areas were removed by cropping the surface area to approximately $9\text{ mm} \times 9\text{ mm}$, centred on the middle of the $10\text{ mm} \times 10\text{ mm}$ cube surface.

2.3.2. Convert STL to PLY

PLY file format contains just the vertices and not the triangle information. The file size is approximately a third the size of the STL and allows for faster data computation.

2.3.3. Align surfaces

One surface measurement was chosen as the master for all alignment and cropping purposes. This master was one of the Alicona measurement files. The surface of the master file was not trimmed (per step 1) and so was slightly larger than the files to be aligned to it. This allowed the maximum area of each of the measurement sets to be used for the alignment process. Least squares alignment was performed between all measurement sets and the master surface.

2.3.4. Perform deviation analysis

Deviation analysis is not required during processing but provides verification that alignment has been performed correctly.

2.3.5. Crop to $8.4\text{ mm} \times 8.4\text{ mm}$ PLY

After alignment to the master, each surface was cropped to $8.4\text{ mm} \times 8.4\text{ mm}$, in the same coordinate system as the master so, for example, the XY coordinate values for the corners for all the

samples will be identical. The $8.4\text{ mm} \times 8.4\text{ mm}$ cropped files were saved with a PLY format.

2.3.6. Clean the mesh

This step is only required for the XCT mesh files, not for the Alicona G4 mesh files. Converting the point cloud to a height map (step 7) involves projecting the point cloud onto a plane and assigning a Z height value to each of the height map matrix squares. Errors will occur if there is more than one point cloud surface to be projected onto the plane at the same XY location, such as would be the case with a re-entrant feature. To avoid this the mesh has to be cleaned by removing all non-visible re-entrant features followed by repairing the mesh to make it continuous. This step is performed after alignment to the master (Alicona) mesh because the non-visible areas should correspond to the surface areas not in line-of-site for the Alicona measurement.

2.3.7. Convert to a height map

The $8.4\text{ mm} \times 8.4\text{ mm}$ PLY files (point cloud) were then converted to SDF (height map) format by linear interpolation and projection onto a plane, using a $2.5\text{ }\mu\text{m}$ grid spacing.

2.3.8. Crop to $8\text{ mm} \times 8\text{ mm}$ per ISO 25178-3

The height map was then cropped to $8\text{ mm} \times 8\text{ mm}$ (per ISO 25178-3 requirements, discussed above) and saved as a SDF file format.

2.3.9. Filter per ISO 25178-3

Levelling and filtering was then performed. A Gaussian regression L-filter nesting index of 8 mm and an S-filter nesting index of 0.025 mm, per ISO 25178-3, were applied to each surface.

2.3.10. Generate parameter data per ISO25178-2

Surface parameter data per ISO 25178-2 [20] was then generated.

2.4. Processing of the dimensional artefact data

Best-fit cylinders were generated for the OD and ID using the datum faces used for CMM measurement. Both cylinders extended 0.5 mm to 2.75 mm inward from the respective datum face of the artefact. The Length dimension was calculated as the distance between two planes generated from the small diameter end face and the step face, see Fig. 5.

Table 2
Master sample and copy ISO 25178-2 data comparison.

Parameter per ISO 25178-2	Master	Copy of Master	Percentage difference (in relation to Master) [(Δ) is absolute difference]
Height parameters			
Sq /μm	41.186	41.186	<0.001
Ssk	1.413	1.413	<0.001
Sku	9.297	9.297	<0.001
Sp/μm	342.593	342.601	0.002
Sv/μm	137.346	137.329	−0.012
Sz /μm	479.939	479.93	−0.002
Sa /μm	30.301	30.301	<0.001
Spatial parameters			
Str	0.77	0.77	<0.001
Sa /mm	0.287	0.287	<0.001
Hybrid parameters			
Sdq	0.626	0.626	<0.001
Sdr %	15.895	15.894	(Δ) −0.001
Volume parameters			
Vmp/(μm ³ /μm ²)	3.44	3.44	<0.001
Vmc/(μm ³ /μm ²)	31.70	31.70	<0.001
Vvc/(μm ³ /μm ²)	47.60	47.60	<0.001
Vvv/(μm ³ /μm ²)	3.46	3.46	<0.001
Sk family parameters			
Spk/μm	66.229	66.230	0.002
Sk /μm	90.248	90.253	0.006
Svk/μm	28.196	28.195	−0.004
Material ratio parameters			
Smr1 %	12.8	12.8	(Δ) <0.001
Smr2 %	92	92	(Δ) <0.001

3. AM surface artefact results

3.1. Process verification

3.1.1. Computational alignment and parameter extraction process verification

The primary intention of this research is to investigate the capability of XCT for the measurement and characterisation of AM surfaces. Part of this process is validation of the data extraction and analysis process itself. An initial test was performed to verify the ten-step computation process. This consisted of making a copy of the master surface file then performing iterative closest point (ICP) alignment between the master and its copy with a threshold maximum RMS difference between consecutive iterations of 5×10^{-5} mm. The surface area was approximately $9 \text{ mm} \times 9 \text{ mm}$. A deviation analysis was then performed. The mean distance after alignment was less than 1 nm. The deviation standard deviation was 88 nm. The surfaces were then processed using the ten-stage protocol, resulting in two height maps, $8 \text{ mm} \times 8 \text{ mm}$, levelled and filtered. A set of parameters per ISO 25178-2 were then generated in SurfStand. The difference between the parameter values are reported in Table 2. The parameters highlighted in bold were selected as ones that have been shown in previous research to be sensitive to AM build and post-processing surface variations [4]. The complete parameter set is easily generated using standard software, such as MountainsMap or SurfStand, but just these selected parameters will be reported for the remainder of the paper.

The largest percentage difference between the copy and the master is 0.012% for Sv (the maximum pit height of the scale limited surface) with the majority having a difference of zero to three decimal places. The authors thus consider that this verification of the alignment and extraction process is suitably accurate for this XCT to Alicona G4 AM surface measurement comparison.

3.1.2. Alicona measurement and processing verification

This verification test was performed to verify the precision of the Alicona measurements, in combination with the extraction process verified earlier. All measurements performed on the Alicona were

Table 3
Alicona G4 ten measurement mean and sample standard deviation.

Parameter	Mean	Sample standard deviation
Height parameters		
Sq /μm	41.19	0.0068
Ssk	1.41	0.0012
Sku	9.29	0.0090
Sz /μm	479.61	0.31
Sa /μm	30.31	0.0055
Spatial parameters		
Sa /mm	0.29	0.00050
Hybrid parameters		
Sdr %	15.92	0.012
Sk family parameters		
Sk /μm	90.25	0.025
Material ratio parameters		
Smr2 %	91.98	0.042

processed per the sequence discussed previously, including alignment with the master, conversion to a height map, cropping and filtering per ISO 25178-3. Parameter mean values and sample standard deviations were generated for the ten samples for a selection of parameters, see Table 3.

These numbers, as a typical example Sq mean value $41.19 \mu\text{m}$, with a sample standard deviation of $0.007 \mu\text{m}$, show the good repeatability of the Alicona measurement and data extraction process and repeatability is orders of magnitude better than the expected focus variation to XCT result differences.

3.1.3. Deviation analysis

The results of a deviation analysis between the master sample and another sample from the batch is shown in Fig. 8. The mean distance between the meshes is 4 nm, with a standard deviation of 250 nm. The primary purpose of alignment is to make sure measurements from the same area are compared for ISO 25178-2 parameter extraction. The alignment process performed here is significantly better than required for this purpose.

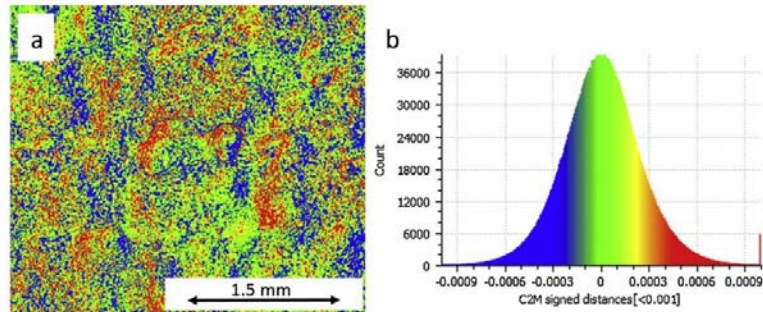


Fig. 8. Deviation analysis between two aligned Alicona measurements (a) deviation map (b) distance histogram (values in mm).

Table 4
XCT five sample mean and standard deviation, Set 1.

Parameter	Mean	Sample standard deviation
Height parameters		
Sq/ μm	40.46	0.030
Ssk	1.35	0.0075
Sku	9.04	0.065
Sz/ μm	479.07	1.76
Sa/ μm	29.84	0.038
Spatial parameters		
Sal/mm	0.298	0.00090
Hybrid parameters		
Sdr/%	13.30	0.17
Sk family parameters		
Sk/ μm	89.76	0.27
Material ratio parameters		
Smr2/%	91.70	0.071

3.2. XCT

All XCT measurements were processed per the ten-step process outlined previously. Data for parameters per ISO 25178-2 were generated for all measurements. The measurement mean and sample standard deviation for the three sets of data is reported as follows.

3.2.1. Set 1: samples not disturbed between measurements

Set 1 consisted of five measurements on the XCT. The fixture was not disturbed between each of the measurements. The parameter mean and sample standard deviation values are shown in Table 4.

3.2.2. Set 2: after XCT filament change, samples not disturbed between measurements

Set 2 consisted of five measurements on the XCT. The XCT filament was changed prior to the first measurement. Automatic focus was performed after the filament change. No other XCT measurement settings were changed. The fixture was not disturbed between each of the measurements, see Table 5. There was a statistically significant difference in mean values measured prior and post filament change; for example, Sq mean 40.46 μm with a standard deviation of 0.03 μm prior to filament change. After the filament change the Sq mean was 40.07 μm with a standard deviation of 0.06 μm . The change was approximately 0.95%. To verify the only parameter that had been adjusted (auto focus) had not produced the difference, an additional test was run with the focus setting returned to the pre-filament change value. The Sq value for this individual measurement was 40.15 μm , which was slightly less than the maximum Sq value, 40.154 μm , obtained from Set 2 (auto focussed post filament change).

Table 5
XCT five sample mean and standard deviation, Set 2.

Parameter	Mean	Sample standard deviation
Height parameters		
Sq/ μm	40.07	0.056
Ssk	1.34	0.0039
Sku	8.98	0.028
Sz/ μm	474.87	1.84
Sa/ μm	29.59	0.045
Spatial parameters		
Sal/mm	0.29	0.00090
Hybrid parameters		
Sdr/%	13.09	0.24
Sk family parameters		
Sk/ μm	89.01	0.18
Material ratio parameters		
Smr2/%	91.74	0.055

Table 6
XCT five sample mean and standard deviation, Set 3.

Parameter	Mean	Sample standard deviation
Height parameters		
Sq/ μm	40.07	0.012
Ssk	1.35	0.0068
Sku	8.99	0.036
Sz/ μm	472.53	1.88
Sa/ μm	29.58	0.013
Spatial parameters		
Sal/mm	0.29	0.00050
Hybrid parameters		
Sdr/%	12.79	0.12
Sk family parameters		
Sk/ μm	88.74	0.11
Material ratio parameters		
Smr2/%	91.74	0.055

3.2.3. Set 3: AM part rotated 90° between measurements

Set 3 consisted of five measurements on the XCT. The fixture was removed from the XCT rotary table and the AM component was removed from the fixture, rotated 90° CCW and replaced prior to the first Set 3 measurement. This removal and replacement process was repeated between each Set 3 measurement. The parameter mean and sample standard deviation values are shown in Table 6. Interestingly, the standard deviations values for this set of measurements is less than the standard deviations obtained for Set 1 and Set 2 measurements – sets for which the artefact was not disturbed between measurements.

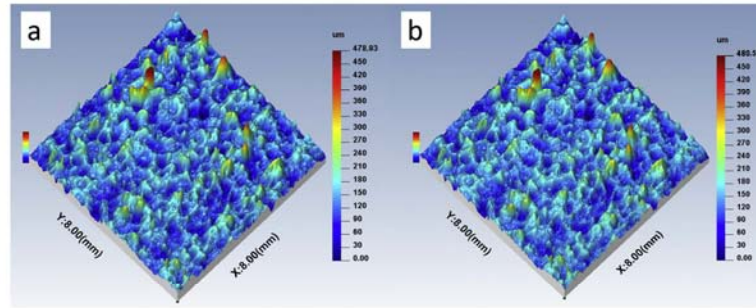


Fig. 9. False colour height maps (a) Alicona master (b) XCT reconstruction from Set 1.

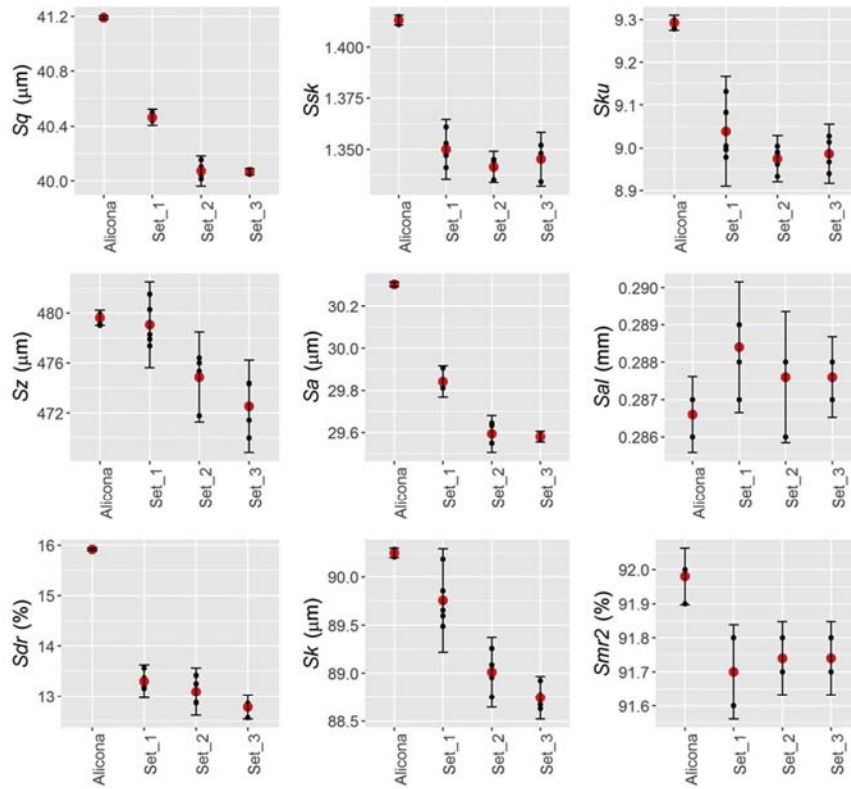


Fig. 10. ISO 25178-2 parameter Alicona to XCT comparison charts with 95% confidence interval.

3.3. XCT to focus variation measurement comparison

Fig. 9 shows false colour height maps for the master Alicona file and one of the measurements from XCT Set 1. The filtering, as with all data presented in this research, was 8 mm L-Filter nesting index and 0.025 mm S-Filter nesting index Gaussian regression filter per

ISO 25178-3. The processed sample size was also 8 mm × 8 mm for all measurements. The surfaces show great visual similarity.

The percentage differences between the Alicona parameter mean value and the parameter mean value for the three sets of XCT data are shown in Table 7. The percentage difference between the mean values of Sa obtained for XCT measurement Set 1, Set

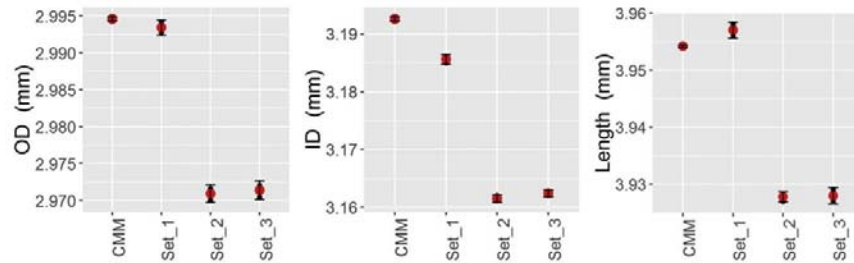


Fig. 11. OD, ID and length CMM and XCT dimensional data.

Table 7
Percentage difference between the XCT mean and the Alicona mean values [(Δ) is absolute difference].

Parameter	Alicona mean value	Set 1 mean value	Set 2 mean value	Set 3 mean value	Percentage difference, Set 1 to Alicona	Percentage difference, Set 2 to Alicona	Percentage difference, Set 3 to Alicona
Height parameters							
$Sq/\mu m$	41.19	40.46	40.07	40.07	-1.8	-2.7	-2.7
Ssk	1.41	1.35	1.34	1.35	-4.5	-5.1	-4.8
Sku	9.29	9.04	8.98	8.99	-2.7	-3.4	-3.3
$Sz/\mu m$	479.61	479.07	474.87	472.53	-0.1	-1.0	-1.5
$Sq/\mu m$	30.31	29.84	29.59	29.58	-1.5	-2.3	-2.4
Spatial parameters							
Sa/mm	0.29	0.29	0.29	0.29	0.6	0.3	0.3
Hybrid parameters							
$Sdr/\%$	15.92	13.30	13.09	12.79	(Δ) -2.6	(Δ) -2.8	(Δ) -3.1
Sk family parameters							
$Sk/\mu m$	90.25	89.76	89.01	88.74	-0.5	-1.4	-1.7
Material ratio parameters							
$Smr2/\%$	91.98	91.70	91.74	91.74	(Δ) -0.3	(Δ) -0.2	(Δ) -0.2

2 and Set 3 and the Alicona G4 measurement set are 1.8%, 2.7% and 2.7% respectively. These differences are remarkably low considering the very different measurement technology employed. As reported previously, the change between 1.8% for Set 1 and 2.7% for Set 2 and Set 3 appears to be caused solely by the filament change.

Charts for the selected areal parameters are shown in Fig. 10. The charts show data for the Alicona and Sets 1, 2 and 3 with the 95% confidence interval (± 1.96 standard deviations of the repeatability measurements).

4. Dimensional artefact results

The dimensional artefact measurement results for the outside diameter, inside diameter and length (Fig. 5) are shown in Table 8. The table includes standard deviation values for each set of measurements, together with percentage differences between the mean value of the XCT data sets and the mean value of CMM data set for OD, ID and Length.

The dimensional change between XCT Set 1 and Set 2 (IE after changing the XCT filament) showed a consistent dimensional change for OD, ID and Length of -0.75%, -0.76% and -0.74% respectively. All dimensional results obtained from the XCT were within 1% of the dimension as measured on the CMM. Charts for OD, ID and length, including 95% confidence interval, clearly showing the XCT measurement change from Set 1 to Set 2, are shown in Fig. 11.

5. Discussion

There is no significant bias in the direction of the dimensional errors for OD, ID and Length that would suggest the iterative local surface determination is incorrect (Table 8). The mean of all the

XCT OD measurement is -0.53% less than the mean CMM OD measurement. Similarly the mean XCT ID and Length measurements are -0.71% and -0.47% less than the corresponding CMM measurements. The filament change effectively resulted in a scaling difference of -0.75%; i.e. the XCT dimensional measurements all reduced by approximately 0.75%. This 0.75% scaling change produced the changes in XCT parameter data given in Table 9. All XCT measurements reported in this paper were taken on the Nikon XT H 225 industrial CT. It should be noted that The Nikon metrology XCT machine, MCT225, includes a protocol, and is supplied with an artefact, for performing post-filament-change calibration.

The initial test of alignment and data extraction for the master surface and a copy, together with the analysis of the ten sample Alicona data showed good repeatability of the Alicona measurements and the described extraction, alignment and parameter data extraction process. The dimensional artefact, easily included during the measurement stage, allows monitoring of the XCT measurement process. The filament change during the measurement process highlighted the need for this monitoring as the change produced differences in the dimensional artefact OD, ID and Length of -0.75%, -0.76% and -0.74% respectively. Correspondingly, statistically significant changes were observed in the areal parameter data sets after the filament change. Using a traceable artefact, manufactured from a similar material to the surface artefact, such as the dimensional artefact used here, as measured on a CMM, will provide valuable verification of scaling and surface determination for the XCT. Measurement uncertainty for AM surface measurements on the XCT (and indeed the Alicona) will be an ongoing area of research – there are a wide variety of AM surfaces and providing traceable calibration information will be difficult. The process used here describes the extraction of areal surface texture data from XCT

Table 8
CMM and XCT dimensional artefact data.

Measurement method	Mean OD (mm) [% dif. c.w. CMM]	Sample std. dev. (mm)	Mean ID (mm) [% dif. c.w. CMM]	Sample std. dev. (mm)	Mean Length (mm) [% dif. c.w. CMM]	Sample std. dev. (mm)
CMM (10 meas.)	2.9946	0.00016	3.1926	0.00019	3.9542	0.00013
XCT Set 1 (5 meas.)	2.9934 [−0.04%]	0.00050	3.1856 [−0.22%]	0.00040	3.9570 [−0.07%]	0.00070
XCT Set 2 (5 meas.)	2.9709 [−0.79%]	0.00060	3.1615 [−0.97%]	0.00030	3.9278 [−0.67%]	0.00040
XCT Set 3 (5 meas.)	2.9714 [−0.77%]	0.00060	3.1624 [−0.95%]	0.00030	3.9280 [−0.66%]	0.00070

Table 9
Percentage change in mean parameter value after changing XCT filament.

Parameter	Set 1 mean value	Set 2 mean value	Percentage difference [(Δ) is absolute difference]
Height parameters			
Sq/μm	40.46	40.07	−0.97
Ssk	1.35	1.34	−0.64
Sku	9.04	8.98	−0.71
Sz/μm	479.07	474.87	−0.88
Sa/μm	29.84	29.59	−0.83
Spatial parameters			
Sa1/mm	0.29	0.29	−0.28
Hybrid parameters			
Sdr/%	13.30	13.09	(Δ) −0.21
Sk family parameters			
Sk/μm	89.76	89.01	−0.83
Material ratio parameters			
Smr2/%	91.70	91.74	(Δ) 0.04

scans, but it should be noted that profile information, such as R_a , or any other parameter per ISO 4287 [21], may be simply extracted and compared from the aligned areal surface data. The authors consider this procedure a valid method for the extraction of areal (and profile) surface texture information from XCT data, applicable to additively manufactured parts but with potential applications beyond the AM field.

6. Conclusions

A method has been developed to extract areal surface information from XCT volume data and generate surface texture parameters per ISO 25178-2. It has been shown that with careful technique and processing the value of parameters obtained using XCT are remarkably similar to those obtained using conventional optical surface texture measurement techniques. Repeatability has been shown to be good, with the AM artefact removed and replaced between XCT measurements the mean S_a value for the sample was 29.6 μm with a sample standard deviation of less than 0.013 μm. The Alicona G4 measurement for the same surface area, also removing and replacing the artefact between measurements, was 30.8 μm with a sample standard deviation of 0.006. This is a difference between the S_a value of less than 2.5%. Additive components with internal features will become more commonplace in industrial applications, such as medical, aerospace and automotive. These industries will all need to have understandable, definable pass-fail requirements for internal surface texture. The methodologies illustrated in the current paper allows quantitative measurement of surfaces per existing areal and profile standards. If and when specific AM related standards are generated, this process will be fully adaptable to these.

7. Future work

The present work will be expanded to cover additional aspects of the XCT data transformation process and will include:

- Further investigation of the effects of surface determination on surface texture parameters.
- Development of stand-alone “one-click” software to perform the analysis and generate parameter data from the XCT volume data, either directly from the point cloud information, or extracted and projected onto a plane as a height map.
- Perform a round-robin investigation to compare XCT capability across different XCT platforms and highlight any potential problems for industry end users of this methodology.
- Map the capability across the XCT chamber.
- Investigate extraction of surface data from re-entrant features and free form surfaces.
- Perform wavelet decomposition of XCT and Alicona data sets to investigate the difference in capability in detecting a range of spatial wavelengths.

Acknowledgement

The authors gratefully acknowledge the UK's Engineering and Physical Sciences Research Council (EPSRC) funding of the EPSRC Centre for Innovative Manufacturing in Advanced Metrology (Grant Ref: EP/I033424/1).

References

- [1] Brackett D, Ashcroft I, Hague R. Topology optimization for additive manufacturing. Proceedings of the Solid Freeform Fabrication Symposium, Austin, TX 2011: 348–62.
- [2] Zein I, Huttmacher DW, Tan KC, Teoh SH. Fused deposition modeling of novel scaffold architectures for tissue engineering applications. Biomaterials 2002;23(4): 1169–85.
- [3] Gibson I, Rosen DW, Stucker B. Additive manufacturing technologies. Springer; 2010. p. 406–7.
- [4] Townsend A, Senin N, Blunt L, Leach RK, Taylor JS. Surface texture metrology for metal additive manufacturing: a review. Precision Engineering 2016 (2016.06.001).
- [5] Stout K, Blunt L. Three-dimensional surface topography, vol. 2. London: Penton; 2000.
- [6] Whitehouse DJ. Surfaces and their measurement. London: Hermes Penton Science; 2002.

- [7] Müller P, Cantatore A, Andreasen JL, Hiller J, De Chiffre L. Computed tomography as a tool for tolerance verification of industrial parts. *Procedia CIRP* 2013;10:125–32.
- [8] Kraemer A, Lanza G. Assessment of the measurement procedure for dimensional metrology with X-ray computed tomography. 14th CIRP conference on computer aided tolerancing (CAT) 2016:267–362.
- [9] Carmignato S. Accuracy of industrial computed tomography measurements: experimental results from an international comparison. *CIRP Annals-Manufacturing Technology* 2012;61(1):491–4.
- [10] Kruth JP, Bartscher M, Carmignato S, Schmitt R, De Chiffre L, Weckenmann A. Computed tomography for dimensional metrology. *CIRP Annals-Manufacturing Technology* 2011;60(2):821–42.
- [11] Borges de Oliveira F, Stolff A, Bartscher M, De Chiffre L, Neuschaefer-Rube U. Experimental investigation of surface determination process on multi-material components for dimensional computed tomography Case Studies in Nondestructive Testing and Evaluation Part B 2016;6(November):93–103.
- [12] Volume Graphics GmbH. *VCStudio MAX*.
- [13] Hiersemazel F, Petzing JN, Leach RK, Helmli F, Singh J. Areal texture and angle measurements of tilted surfaces using focus variation methods; 2012.
- [14] (1996), BS ISO 4288: 1996 Geometrical Product Specifications (GPS) – Surface texture: Profile method – rules and procedures for the assessment of surface texture.
- [15] ISO_25178-3 B.E. (2012), BS EN ISO_25178-3, in Geometrical product specifications (GPS) Surface texture: Areal Part 3: Specification operators. British Standards Institute.
- [16] Nikon metrology NV, *Nikon CT-Pro*.
- [17] Digital Surf., *MountainsMap*.
- [18] The Centre for Precision Technologies U.o.H., *SurfStand*.
- [19] Townsend A, Blunt L, Bills P. Investigating the capability of microfocus X-ray computed tomography for areal surface analysis of additively manufactured parts. Proceedings of dimensional accuracy and surface finish in additive manufacturing, ASPE 2016 Summer Topical Meeting, Raleigh, NC 2016:206–10.
- [20] ISO_25178-2 B.E. (2012), BS EN ISO_25178-2, in Geometrical product specifications (GPS) Surface texture: Areal 2: Terms, definitions and surface texture parameters. British Standards Institute.
- [21] ISO_4287 B.E. (2000), BS EN ISO_4287, in Geometrical product specification (GPS) Surface texture: Profile method. Terms, definitions and surface texture parameters. British Standards Institute.

**INVESTIGATING THE CAPABILITY OF MICROFOCUS X-RAY
COMPUTED TOMOGRAPHY FOR AREAL SURFACE ANALYSIS OF
ADDITIVELY MANUFACTURED PARTS**

Andrew Townsend¹, Liam Blunt¹, and Paul Bills¹
¹EPSRC Centre for Innovative Manufacturing in Advanced Metrology
School of Computing and Engineering
University of Huddersfield
Huddersfield, West Yorkshire, UK

INTRODUCTION

The ability to perform non-destructive areal surface analysis, for example of the internal surfaces of additively manufactured (AM) parts has potential advantages during product development and for production process control. This paper reports on the extraction of areal surface information from microfocus x-ray computed tomography (XCT) data. Using this novel technique a range of areal parameter values were generated from a surface section extracted from XCT scan data of an as-built (no post-processing) AISi10Mg additively manufactured part. This was then compared with the parameter values generated from a focus variation scan of the same surface section. The data comparison method involving normalisation of data format to allow analysis using industry-standard software, such as MountainsMap (Digital Surf, Besançon, France) or SurfStand (The Centre for Precision Technologies UoH) is demonstrated. Importing the extracted surfaces into these powerful software packages allows one-click data filtering per ISO 25178-3 [1] and the generation of a comprehensive suite of areal surface parameter values. These include feature and field parameters, amplitude, spatial, hybrid and functional parameters, as defined in ISO 25178-2 [2]. A method for characterising the capability of XCT for areal surface measurement is demonstrated by comparing results obtained from samples taken from a Rubert comparator test panel, with sample surface R_a values between 0.8 μm and 50 μm .

**XCT AND FOCUS VARIATION AM SURFACE
COMPARISON**

A cube, 10 mm per side, was manufactured using selective laser melting (SLM) on a Renishaw AM250 using AISi10Mg powder. No post-processing, such as grit blasting, was performed after manufacture.

XCT Measurement

The cube was imaged using a Nikon XT H 225 microfocus CT. Nikon CT-Pro (Nikon metrology, Tring, UK) was used to perform reconstruction. Voxel size was 17 μm (x,y,z). Surface determination was performed in VGStudio MAX (Volume Graphics GmbH). Surface extraction (no simplification or downsampling, automatic surface determination) was performed in VGStudio MAX and the data was saved as an STL surface geometry (mesh) file. The surface was then imported into Meshlab (Visual Computing Lab ISTI-CNR), and area of interest (component upskin (top) surface) was aligned with the xyz coordinate system and then extracted and saved with a PLY file format.

Focus Variation

Focus variation (FV) instruments are commonly used to analyse the surface texture of additively manufactured parts and the FV results are used here as reference measurements. The upskin surface of the aluminium cube was measured using an Alcon G4 using a 10x objective lens. Vertical resolution was 0.2 μm and the lateral sampling distance was 2.3 μm . The data was saved as an STL file.

Areal Parameter Comparison

The XCT and FV STL surface sections were both imported into CloudCompare (version 2.6.3beta [GPL software] 2015). The areas were aligned using iterative closest point (ICP) and then both were cropped to give aligned, equal areas. No lateral or vertical scaling was performed during the alignment. Both areas were saved with PLY file formats. The XCT and FV PLY mesh files were levelled, projected onto a grid and converted to SDF (Surface Data Format) in Matlab (The MathWorks, Inc., Natick, Mass, USA. Release R2015b). Projected grid spacing was 2 μm (x and y), 1 nm vertical numerical resolution for both files.

A surface area of 5.6 mm x 5.8 mm, approximately 30% of the top surface area, was used for parameter generation, see Figure 1.

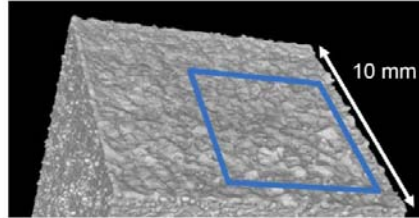


FIGURE 1. Top of AISi10Mg part after XCT reconstruction, showing cropped surface area.

The XCT and FV SDF files were opened in SurfStand (V6.0) software. Based on the surface (no structure of interest with a scale (wavelength) larger than 1 mm) the Gaussian L-filter nesting index was set to 5.0 mm and the S-filter nesting index was set to 0.02 mm, per ISO 25178-3:2012 tables 1 and 3. The FV and XCT false colour height maps, generated in SurfStand, are shown in Figure 2. The correlation between the surface topography of the two height maps can be seen clearly. Areal surface parameter data (per ISO 25178-2), computed in SurfStand from the FV and XCT data for these aligned and cropped areas, are compared in Table 1.

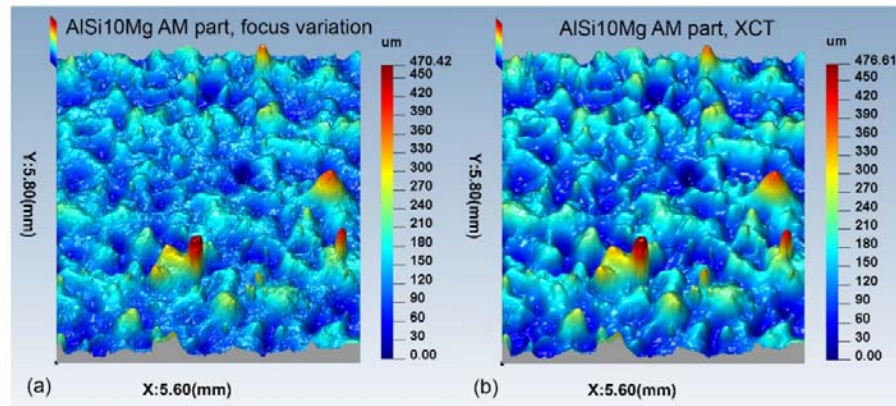


FIGURE 2. AISi10Mg part false colour height map (a) FV, (b) XCT.

TABLE 1. AISi10Mg part, FV and CT ISO 25178-2:2012 parameters.

Parameter	Description	FV	CT	Delta (% of FV)
Amplitude				
<i>Sa</i>	Arithmetic mean height	31.7 μm	40.7 μm	28.4%
<i>Sq</i>	Root mean square height	44.5 μm	53.2 μm	19.6%
<i>Ssk</i>	Skewness	1.72	1.13	-34.3%
<i>Sku</i>	Kurtosis	10.7	6.6	-38.3%
<i>Sz</i>	Maximum height	470 μm	477 μm	1.5%
Spacing				
<i>Sal</i>	Fastest decay autocorrelation length	0.27 mm	0.28 mm	3.7%
Hybrid				
<i>Sdr</i>	Developed interfacial area ratio	21.0%	21.4%	1.9%
Functional				
<i>Smr2</i>	Areal material ratio (dales)	90.8%	93.5%	3.0%

The surface parameters in Table 1 were chosen because they have all been shown to differentiate variations in AM build performance in response to changes in build parameters such as laser and electron beam spot size and power, build orientation and post-processing time [3]. The percentage variation between the XCT and focus variation measurements range between 1.5% for S_z (the sum of the maximum peak value and maximum pit height value) and -38% for S_{ku} (kurtosis). The kurtosis for the XCT measurement is 38% less than that of the focus variation instrument. This is understandable as kurtosis is an indication of "peakedness" of the surface and XCT resolution is considerably less than that of the focus variation instrument and so would tend not to resolve narrow, sharp peaks. S_a and S_q have been the most widely used areal parameters for AM surface measurement [3]. The values of S_a and S_q from the XCT were 28% and 20% greater than the focus variation measurements for this particular AM sample.

Mesh Distance Analysis

The distance (closest points) between the two aligned and cropped meshes was calculated and plotted, see Figure 3. The distance analysis map shows the good lateral scaling of the XCT. The distance distribution was also plotted, showing an approximately Gaussian distribution, and giving a standard deviation of 11 μm , see Figure 4.

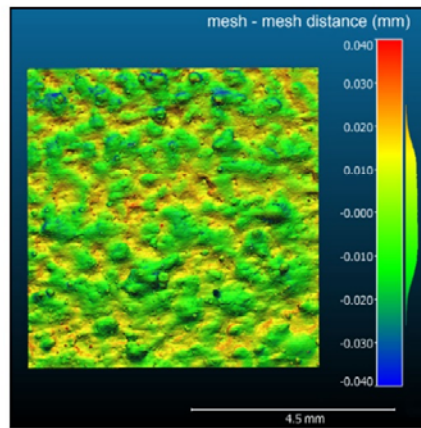


FIGURE 3. XCT to FV mesh difference map.

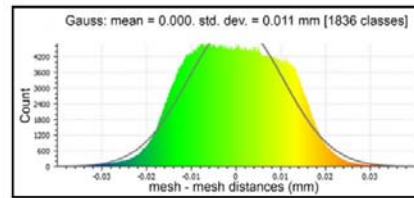


FIGURE 4. XCT mesh to FV mesh distance difference distribution.

XCT AND FOCUS VARIATION ROUGHNESS PLATE COMPARISON

The surfaces of powder bed fusion metal AM parts vary considerably with different manufacturing systems, powder configurations and build parameters. To give an indication of the limits of XCT to produce meaningful areal surface information a series of measurements were performed on test plates with roughness values encompassing those likely to be produced by metal powder bed fusion processes (nominal R_a 0.8 μm – 50 μm).

Rubert roughness comparison specimens

Seven plates, approximately 10 mm x 20 mm, were cut from a Rubert Microsurf 334 (casting) comparator test panel, see Figure 5.



FIGURE 5. Rubert Microsurf 334 comparator test panel.

The casting panel was used as this surface most closely represents the powder bed fusion metal AM surface. No Rubert samples exist for AM surfaces at present.

Measurement and Analysis

XCT results were again compared to those obtained using the focus variation instrument. XCT voxel size for all plates was 12.9 μm (x,y,z). L-filter and S-filter nesting for indexes, based on plate R_a value, were generated using data from ISO 4287-1998 [4], ISO 4288-1998 [5] and ISO 25178-3:2012. The XCT and FV measured areas for each of the seven plates were aligned and

cropped following the same procedure used for the AISi10Mg AM sample. Nine square samples, with sample side lengths based on value of the L-filter nesting index, were extracted from the 0.8 μm – 6.3 μm R_a plates. Four samples were extracted from the 12.5 μm – 50 μm R_a plates (quantity limited by the plate sizes). The files were converted to SDF format, opened in SurfStand and the parameter set was generated. Table 2 shows the nominal R_a value together with the mean S_a value computed from the FV and XCT data for each of the seven plates.

TABLE 2. Rubert plate nominal R_a values, mean FV and XCT S_a values and percentage difference between mean XCT and FV values.

Nominal Rubert Plate R_a (μm)	Mean FV S_a (μm)	Mean XCT S_a (μm)	Difference between mean XCT and FV S_a (% of FV)
50	51.1	55.6	8.8 %
25	27.4	31.3	14.5 %
12.5	12.4	14.6	17.2 %
6.3	6.6	9.0	34.5 %
3.2	4.0	5.6	40.5 %
1.6	2.5	3.5	43.1 %
0.8	0.56	1.09	95 %

Figure 6a shows the four FV and corresponding XCT readings for the nominal 50 μm R_a plate. Figure 6b shows the nine FV and corresponding XCT readings for the nominal 0.8 μm R_a plate.

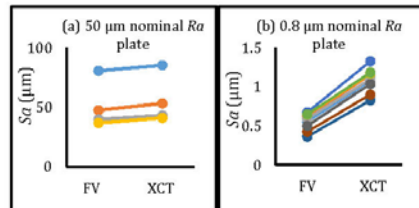


FIGURE 6. Comparison of FV and XCT results (a) 50 μm nominal R_a plate (b) 0.8 μm nominal R_a plate.

The lines on each chart are approximately parallel, illustrative of the correct FV to XCT mesh alignment. The gradients of the lines for the 0.8 μm R_a plate are greater, indicative of the larger percentage difference between the XCT and FV measurements than with the nominal 50 μm R_a plate. For each of the seven Rubert plates a

paired t-test was performed. The null hypothesis being that the difference between the mean S_a as measured on the XCT and on the FV instrument was zero. The 95% confidence level was then generated for the data from each of the seven plates. The mean S_a difference between FV and XCT readings, together with the 95% confidence level of the mean S_a difference were plotted for each of the seven Rubert plates. The values plotted are percentages of the mean FV reading for each plate, see Figure 7.

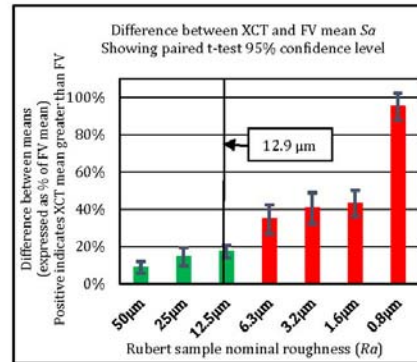


FIGURE 7. Chart of the mean S_a difference between FV and XCT for seven Rubert test plates.

The null hypothesis was rejected: for all seven plates there is greater than 95% probability the XCT measured roughness value is greater than the FV measured roughness value (none of the confidence interval bars cross the 0% line). The percentage difference between the XCT and FV measured roughnesses increases significantly as the absolute plate roughness value reduces (9% at nominal 50 μm R_a and 95% at nominal 0.8 μm R_a). There is a 2x step increase in percentage difference at an R_a value approximately equivalent to the 12.9 μm voxel size of the XCT. Mean differences between XCT and FV S_a measurements were 17% and 35% with sample roughness values (R_a) of 12.5 μm and 6.3 μm respectively. This significant increase in mean difference suggests an initial guideline that XCT areal surface measurements from surfaces with a reconstruction voxel size greater than the surface R_a or S_a should be avoided as errors increase significantly.

CONCLUSIONS

A novel first-step analysis technique has been developed to extract surface information from XCT data and configure this data to allow filtering and parameter generation, per ISO 25178-3 and ISO 25178-2 respectively, using commercially available software packages. Producing standard areal surface data from XCT would be particularly useful for the analysis of internal surfaces of additively manufactured parts, surfaces that up to now could only be analysed using destructive techniques. Initial characterisation of XCT surface measurement capability has been performed. These results show that, dependent upon voxel size and surface roughness, XCT is a viable method for areal surface analysis of AM components. Initial results show a marked decrease in accuracy when the voxel size exceeds the nominal surface R_a value. Additional applications of this technique beyond AM are expected.

FUTURE WORK

Currently there are no AM surface calibration or comparator test panels available and the results obtained for the single test of the AISi10Mg AM surface produced a percentage difference for S_a values computed from XCT and FV (28.4%) higher than that of the approximately comparable Rubert casting plate, 25 μm nominal R_a , (14.5%), see Table 3.

TABLE 3. 25 μm Rubert plate and AISi10Mg AM sample mean FV and XCT S_a values and percentage difference between mean XCT and FV values.

Test sample	FV S_a (μm)	XCT S_a (μm)	Voxel Size (μm)	Percentage difference
25 μm R_a Rubert plate	27.4	31.3	12.9	14.5 %
AISi10Mg SLM	31.7	40.7	17	28.4 %

Future work will include measuring a selection of AM (and non-AM) surfaces to generate a more comprehensive understanding of XCT capability, including the relationship between voxel size and other factors such as surface determination, on measurement accuracy. Generation of a standard AM surface test plate will be investigated. Voxel size and resolution are dependent upon the position of the component being measured in the XCT chamber (in a cone-

beam XCT machine a smaller voxel size will be generated the closer the component is to the x-ray source). The position is dictated by the size of the component. The larger the component is the further away from the x-ray source the component needs to be to be imaged correctly and, subsequently, the larger the voxel size. These factors will be investigated and it is planned to characterise a variety of XCT machines for surface extraction capability.

ACKNOWLEDGEMENTS

The authors gratefully acknowledge the UK's Engineering and Physical Sciences Research Council (EPSRC) funding of the EPSRC Centre for Innovative Manufacturing in Advanced Metrology (Grant Ref: EP/I033424/1).

REFERENCES

- [1] ISO_25178-3 BE. BS EN ISO_25178-3. Geometrical product specifications (GPS) Surface texture: Areal Part 3: Specification operators: British Standards Institute, 2012.
- [2] ISO_25178-2 BE. BS EN ISO_25178-2. Geometrical product specifications (GPS) Surface texture: Areal 2: Terms, definitions and surface texture parameters: British Standards Institute, 2012.
- [3] Townsend A, Senin N, Blunt L, Leach RK, Taylor JS. Surface texture metrology for metal additive manufacturing: a review. Precision Engineering (in press). 2016.
- [4] ISO_4287 BE. BS EN ISO_4287. Geometrical product specification (GPS) Surface texture: Profile method Terms, definitions and surface texture parameters: British Standards Institute, 2000.
- [5] ISO_4288 BE. BS EN ISO_4288. Geometric product specification (GPS) Surface texture Profile method: Rules and procedures for the assessment of surface texture: British Standards Institute, 1998.

Development of an interlaboratory comparison investigating the generation of areal surface texture data per ISO 25178 from XCT

Andrew Townsend¹, Radu Racasan¹, Paul Bills¹, Liam Blunt¹

¹EPSRC Centre for Innovative Manufacturing in Advanced Metrology, School of Computing and Engineering,
University of Huddersfield, Huddersfield, West Yorkshire, UK, e-mail: a.townsend@hud.ac.uk

Abstract

A significant advantage of additive manufacturing (AM) techniques is the ability to design and manufacture parts without the tool-path limitations inherent when using subtractive techniques, such as milling, turning and grinding. This capability of AM enables the production of components with surfaces (such as internal features) that cannot be inspected using standard surface inspection techniques, for example stylus or optical methods. Measurement and characterisation of these surfaces may be vital for component function, whether it be for fluid flow, coating adhesion or bio-attachment. X-ray computed tomography (XCT) has been investigated as a tool for form and dimensional measurement of AM parts; however there has been little research into the ability of XCT for surface texture (particularly areal) measurement and characterization. This paper discusses the initial work performed on producing parameter data per ISO 25173-2 from XCT scans and the rationale employed in the development of a round robin interlaboratory comparison based on this work. Initial round robin data will be discussed.

Keywords: Additive manufacturing, ISO 25178 surface texture, interlaboratory comparison.

1 Introduction - Why AM surface from XCT?

Additive manufacturing (AM) provides the engineer with design flexibility not available when manufacturing is constrained by the tool-path requirements of conventional subtractive techniques such as milling, turning and grinding. Additionally, the ability to use high performance engineering metals, such as titanium Ti6Al4V, 316 stainless steel and cobalt chrome in the AM process provides the aerospace, medical and automotive industries with a new manufacturing toolbox and these industries have seen the potential and are actively engaged with the AM manufacturing industry. However, AM presents many challenges at this early stage of integration into the manufacturing landscape. These quality-driven industries require defined accept-reject requirements for all measurements. A component manufactured using AM is not exempt from the stringent quality requirements that apply to other manufacturing processes. Surface texture requirements will need to be incorporated into drawings and specifications and imposed by customers onto suppliers, using a common language and standards. Verification of compliance with these requirements will be mandatory for AM components.

The exciting design-flexibility of AM will often result in components with sections, such as internal features, that cannot be inspected using standard measurement systems; this applies to dimensional, form and surface texture measurements. Currently, the only practical method available for extracting dimensional and surface texture information from the internal features of metal AM components is X-ray computed tomography (XCT).

The importance of XCT for the measurement of the surface texture of additively manufactured parts has been recognised [1, 2], but, until recently, the extraction of quantitative surface information from XCT scans of AM surfaces has been limited to profile analysis of lattice structures [3, 4]. Recent development of techniques to extract and analyse areal surface texture data and produce quantitative numbers for all surface texture parameters per ISO 25178-2 [5] has the potential to provide industry and the research community with significant analysis and inspection capability [6]. This methodology has shown remarkably good results for the extraction and characterization of AM surfaces from metal AM surfaces. The results presented indicated that, for the surface of the ALSi10Mg selective laser melting (SLM) component evaluated, the difference between the S_a (arithmetic mean height of the scale-limited surface) values obtained from XCT when compared to a focus variation (FV) instrument was less than 2.5%. However, it should be made clear that surfaces that *can* be measured using other techniques (outside surfaces) generally *should* be measured using the standard techniques. The current resolution of XCT, and hence the basic quality of the surface extracted, lags significantly behind other techniques. Additionally, the estimation of measurement uncertainty for XCT is complex and has not been fully addressed in the research community, leading to potential traceability issues. However, just as the AM process itself presents many challenges, XCT surface measurement has challenges that will be faced and hence need to be resolved because of the unique advantages that XCT provides, particularly for the AM sector.

2 Why a round robin?

The results of the referenced research showed that XCT is a viable technique for surface texture measurement. However, all the measurements taken in the reported research were taken on one XCT machine: the Nikon XT H 225 Industrial CT. Because this technique may have industrial and academic research application it is important to assess machine-to-machine variability, and so an interlaboratory comparison (round robin) has been developed: CT-STARR.



CT-SURFACE TEXTURE FOR ADDITIVE ROUND ROBIN

The round robin will consist of two stages: Stage 1 discussed in this paper, is to be a tightly controlled, rigorous and expeditious investigation. The format of Stage 2 will be finalized based on the results and lessons learned from Stage 1. Stage 2 will include a significantly larger number than the four laboratory participants for Stage 1.

3 Round robin Stage 1 methodology

CT-STARR Stage 1 is designed to gauge the repeatability and reproducibility of measurements from closely related XCT machines, using tightly controlled measurement settings and data analysis. The four round robin participants and the XCT machines of each participant are shown in Table 1.

Laboratory	Responsible	XCT machine
University of Huddersfield, UK	Andrew Townsend	Nikon XT H 225 Industrial CT
University of Nottingham, UK	Richard Leach	Nikon MCT225 Metrology CT
National Physical Laboratory, UK	Peter Woolliams	Nikon MCT225 Metrology CT
Nikon Metrology, UK	David Bate	Nikon MCT225 Metrology CT

Table 1: Round robin participating laboratories

3.1 Measurement artefacts

Two artefacts were chosen for the round robin: one AM artifact with a square planar surface area used for all surface measurements and one turned artifact designed for the assessment of scaling and surface determination errors. The same material was used to manufacture both artefacts. This was done to present similar challenges for surface determination during the surface extraction process. Both artefacts were manufactured from titanium Ti6Al4V ELI (extra-low interstitial). This is a high-purity version of Ti6Al4V with lower specified limits on iron, nitrogen, carbon and oxygen. This grade of titanium is commonly used in medical and dental applications because of its excellent bio-compatibility. The ELI grade (Grade 23) has superior damage tolerance (fracture toughness, fatigue crack growth rate) and better cryogenic mechanical properties than Grade 5 Ti6Al4V.

3.1.1 AM artefact

The AM artifact was manufactured on an ARCAM Q10 electron beam melting (EBM) machine. The nominal powder size was 45 -100 μm . A vertical (side) surface was used for all round robin measurements. The required size of the AM surface to be measured was calculated using the profile roughness (Ra) of the surface. Areal standard ISO 25178-3 [7] defines the L-filter nesting index based on the scale of interest. As this is an arbitrary judgment and surface specific, the required filtering and measurement size were based on the profile measurement standard set. The measured roughness (Ra) was approximately 30 μm ; per ISO 4288 table 1 requirements [14] this would then require a roughness sampling length and λ_c cut-off wavelength of 8 mm. This would suggest a similar L-filter nesting index (8 mm) and an areal measurement area of 8 mm x 8 mm per ISO 25178-3 [15]. The artifact was manufactured as a cube of side lengths 10 mm. This provided suitable extra area for aligning and cropping to a "clean" 8 mm x 8 mm surface area.

3.1.2 Surface determination and scaling artifact

The machined artifact used to assess surface determination and dimensional scaling is shown in Figure 1.



Figure 1: Dimensional and surface determination scaling artefact

The overall size of this artefact (13 mm long), manufactured from the same material as the AM surface artefact, was designed to produce similar X-ray attenuation as the AM surface artefact, therefore making it possible to optimise XCT settings for both artefacts simultaneously. Three dimensions were measured during the round robin: The step-length between two parallel faces, one outside diameter (OD) and one inside diameter (ID). The OD and ID were machined to the same nominal dimension (3 mm). These three dimensional configurations were designed to enable the analysis of possible surface determination and global scaling errors. If the surface determination were to calculate and position the generated surface outside the part surface then the ID would tend to be undersized and the OD would tend to be oversized. Surface determination errors would have negligible effect on the length measurement.

3.2 Fixture design

Both artefacts were mounted in an additively manufactured acrylonitrile butadiene styrene (ABS) polymer fixture, see Figure 2. The fixture includes nylon slot-headed set screws to positively retain both artefacts. The surfaces to be measured on both artefacts were not in direct contact with the polymer. The air gap around all these surfaces, producing an air-Ti boundary, was designed to provide optimum surface determination conditions. The fixture design allowed the surface-of-interest of the AM component and the machined artifact to fill the projected image field, therefore maximizing pixel size. The fixture includes a necked-down section that allows line-of-sight between the XCT gun and detector panel at all times during the scan. The flux-normalization area was placed in this area. The brightness within this area for every projected image is compared and normalized to compensate for system variations during the scan.

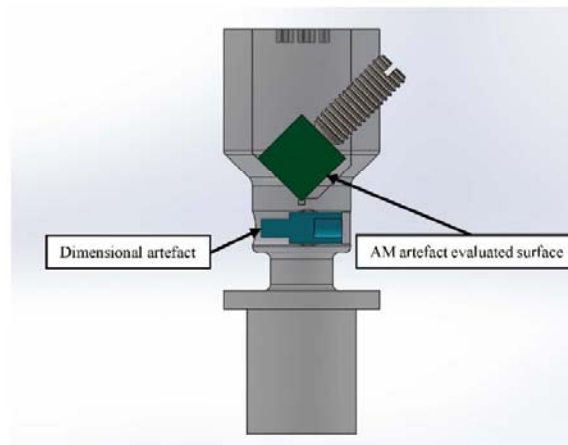


Figure 2: CAD section view of the XCT measurement fixture

3.3 XCT measurement settings

The measurement settings for the XT H 225 are shown in Table 2. These settings were chosen to optimize the exposure contrast while allowing the use of a fully-focused electron beam. The power was kept below 10 W, with the normal focusing setting used on the XCT for all measurements. Above this power the auto-defocus setting is used to keep the energy per unit area of the electron beam target below a safe level, avoiding possible damage to the target. This auto-defocussing effectively blurs the projected images. The artefacts were not removed from the fixture between measurements. The AM surface texture artefact had been removed and replaced in previous work [6] and the results showed no significant difference in the values of extracted surface texture parameters from those obtained when the artifact was not disturbed between scans. Not disturbing the artefacts between measurements will minimize the possibility of damage to the artefacts during the round robin.

Parameter	Value	Parameter	Value
Filter material	Copper	Voxel size	17.3 μm
Filter thickness	1.0 mm	Source to object distance	84.2 mm
Acceleration voltage	160 kV	Source to detector distance	972 mm
Filament current	62 μA	Number of projections	1583
Exposure time	2829 ms	Detector size (pixels)	1008 x 1008

Table 2: Nikon XT H 225 measurement settings

Reconstruction was performed using Nikon CTPro 3D [8] and surface determination was performed using VGStudio MAX 3.0 [9]. Local iterative surface determination was performed with a search distance of 4.0 voxels. Two regions of interest (ROI) were extracted: the dimensional artefact and the AM surface section. The ROI were then converted to a mesh using the VGStudio MAX "Super Precise" setting. A photograph of the fixture within the XT H 225 is shown in Figure 3.

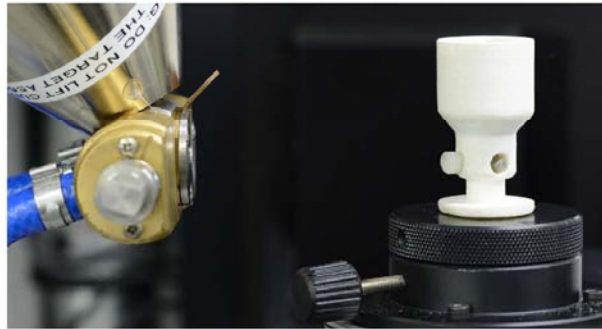


Figure 3: Fixture with artefacts mounted within the XT H 225

3.4 Comparative measurements

Initial results of surfaces and dimensions extracted from the XT H 225 round robin measurements were compared to measurements from an Alicona G4 focus variation instrument and a Zeiss Prismo coordinate measurement machine (CMM) respectively. The extraction and analysis methodology is reported in [6]. The Alicona measurement settings were selected based on ISO 25178-3 requirements. An L-filter nesting index of 8 mm (as discussed in para. 3.1.1) resulted in the selection of an S-filter nesting index value of 0.025 mm per ISO 25178-3 Table 1. The ratio between the S-filter nesting index value and the measurement sampling distance is required to a minimum of 3:1 for optical instruments per ISO 25178-3 table 3. The measurement sampling distance of 2.33 μm used here gives a ratio of greater than 10:1. All XCT data was levelled and filtered using the same filter settings.

4 Surface artefact results

A comparison of the values of areal parameters per ISO 25178-2 from the same surface area measured on the XT H 225 CT and the Alicona G4 is shown in Table 3.

Parameter per ISO 25178-2	Mean Alicona (5 meas.)	Alicona standard deviation	Mean XT H 225 CT (5 meas.)	XCT standard deviation	Percentage difference, XCT in relation to Alicona [(Δ) is absolute difference]
Height parameters					
<i>Sq</i> / μm	32.40	0.001	30.77	0.036	-5.0
<i>Ssk</i>	0.25	<0.001	0.08	0.016	(Δ) -0.17
<i>Sku</i>	3.70	<0.001	3.67	0.009	-0.8
<i>Sp</i> / μm	192.00	0.132	187.20	1.352	-2.5
<i>Sv</i> / μm	138.59	0.186	135.07	2.188	-2.5
<i>Sz</i> / μm	330.59	0.306	322.27	2.889	-2.5
<i>Sa</i> / μm	25.33	0.001	24.05	0.031	-5.1
Spatial parameters					
<i>Str</i>	0.79	<0.001	0.80	0.002	1.3
<i>Sal</i> / mm	0.12	<0.001	0.12	<0.001	0.0
Hybrid parameters					
<i>Sdq</i>	1.00	<0.001	0.81	0.002	-19.0
<i>Sdr</i> / %	39.90	0.013	28.26	0.123	(Δ) -11.64
Volume parameters					
<i>Vmp</i> / (μm ³ /μm ²)	1.93	<0.001	1.73	0.011	-10.4
<i>Vmc</i> / (μm ³ /μm ²)	28.21	<0.001	27.07	0.071	-4.0
<i>Vvc</i> / (μm ³ /μm ²)	38.47	0.005	35.03	0.081	-8.9
<i>Vvv</i> / (μm ³ /μm ²)	34.72	<0.001	35.93	0.027	3.5
Sk family parameters					
<i>Spk</i> / μm	39.95	0.005	36.14	0.198	-9.5
<i>Sk</i> / μm	81.17	0.009	76.36	0.070	-5.9
<i>Svk</i> / μm	30.07	0.009	31.52	0.338	4.8
Material ratio parameters					
<i>Smr1</i> / %	10.00	<0.001	8.96	0.089	(Δ) -1.04
<i>Smr2</i> / %	90.40	<0.001	88.88	0.130	(Δ) -1.52

Table 3: Comparison of mean Alicona and XCT ISO 25178-2 parameter results

Charts for the selected areal parameters are shown in Figure 4. The charts include the data for the Alicona and XCT with the 95% confidence interval for the mean for both.

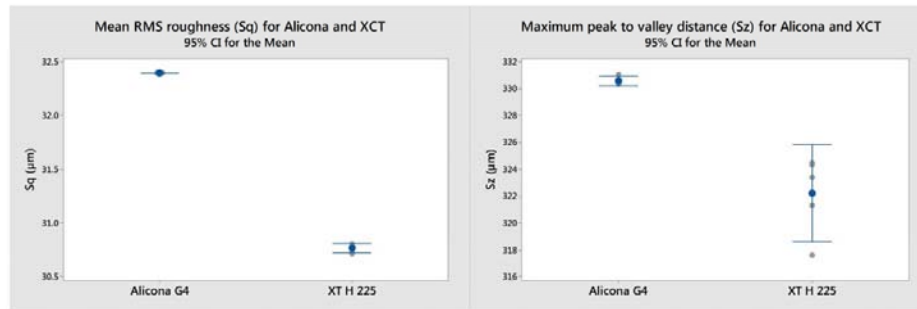


Figure 4: Dimensional and surface determination scaling artefact. The error bars are the 95% confidence interval for the mean. The blue markers are the mean value, the grey markers are each individual value

The false colour height maps for one of the Alicona measurements and one of the XCT measurements are shown in Figure 5. It can be seen that the height maps are visually very similar.

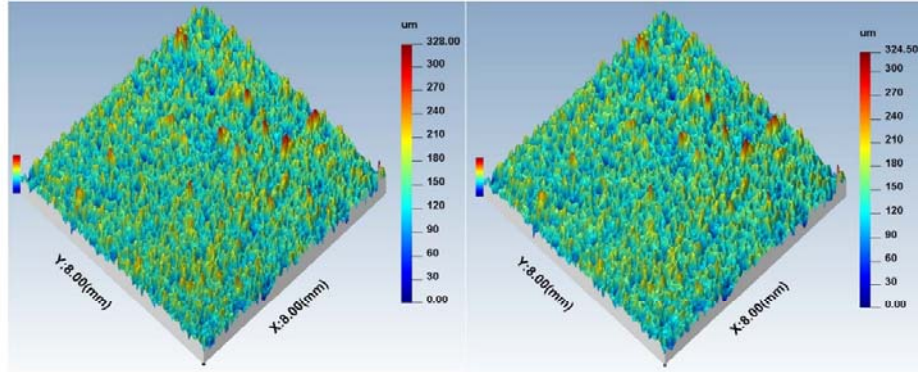


Figure 5: False colour height maps of the extracted surface (a) Alicona, (b) XT H 225

5 Dimensional artifact results

The results of the CMM and XCT measurements of the OD, ID and Length are shown in Table 4 and Figure 6. The mean difference between the XCT and CMM measurements of the OD, ID and Length were -0.27%, -0.83% and -0.54% respectively. A compensation for surface determination can be made for the dimensional artifact. Applying a compensation of 4.1 μm (moving the determined surface toward the part material) makes the OD smaller, the ID larger, the Length dimension remains unchanged. The percentage differences between the XCT measurements and CMM measurements for OD, ID and Length then become -0.55%, -0.55% and -0.54% respectively.

Measurement method	Mean OD (mm) [% dif. c.w. CMM]	Sample std. dev. (mm)	Mean ID (mm) [% dif. c.w. CMM]	Sample std. dev. (mm)	Mean Length (mm) [% dif. c.w. CMM]	Sample std. dev. (mm)
CMM (10 meas.)	2.97345	0.00005	2.98457	0.00005	4.62400	<0.00005
XCT (5 meas.)	2.9654 [-0.27%]	0.00030	2.9599 [-0.83%]	0.00030	4.5990 [-0.54%]	0.00160
After compensating for possible surface determination error by removing 4.1 μm from the XCT surfaces						
XCT (comp.)	2.95724 [-0.55%]		2.96812 [-0.55%]		4.5690 [-0.54%]	

Table 4: Comparison of mean CMM and XCT dimensional results

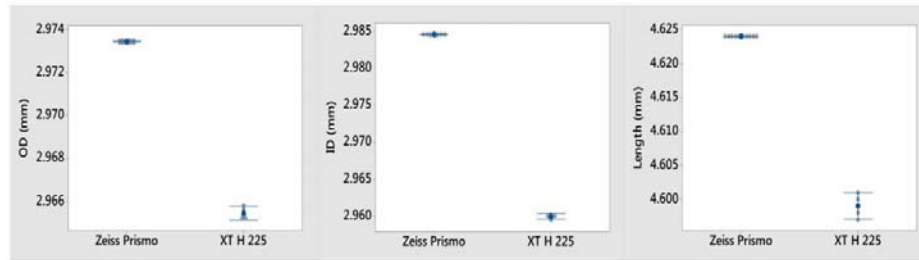


Figure 6: OD, ID and Length from CMM and XCT, showing 95% confidence interval for the mean

6 Discussion

The initial round robin XCT surface texture measurement results show good repeatability; for example, the mean S_q value was $30.77 \mu\text{m}$ with a sample standard deviation of $0.036 \mu\text{m}$ (five measurements). The difference between the mean Alicona measurement and the mean XCT measurement was approximately 5% for S_q . The dimensional artefact was used for analysis of scaling and surface determination and showed that, if compensation for surface determination was applied (by "moving" the determined surface $4.1 \mu\text{m}$ toward the part material), then the ID, OD and Length were consistently 0.54% - 0.55% smaller than the CMM measurements. A global (x,y,z) compensation could then be applied to approximate the measured CMM dimensions. The resultant effect of the AM surface parameter data from the post-measurement scaling will be investigated, but an indication of the difference produced by scaling differences has been reported [6]. In this study the scaling difference was as a result of changing the XCT tungsten filament. The results showed that a scaling difference of approximately -0.75% (x,y,z) produced a difference in S_a for the aluminium AlSi10Mg sample of -0.83% and S_q of -0.97%. One note about scaling changes produced when the XCT filament is changed: the Nikon MCT225 metrology CT includes a measurement artefact and protocol for calibration after each filament change. This Nikon MCT225 metrology CT will be used by the remaining three round robin participants and will be compared to the results presented here for the Nikon XT H 225 industrial CT. The metrology CT will produce reconstructions with a smaller voxel size: the XT H 225 has a 1008×1008 pixel detector, whereas the MCT225 has a 2000×2000 pixel detector. Therefore, with correct magnification adjustments, the voxel size for the metrology CT will be approximately one half the voxel size for the industrial CT. This will produce eight times as many voxels for each scan. The resultant effect on the values of surface texture parameters and dimensional artifact will be reported in the final round robin report.

7 Conclusions

Methodology for an inter laboratory comparison of areal surface texture extraction from XCT has been presented and discussed. Measurement artefacts, fixturing, inspection parameters, comparative measurements and initial results have been presented. The results obtained from one of the four round robin participants using a Nikon XT H 225 industrial CT show good repeatability results for the Ti6Al4V ELI scaling artifact and surface texture surface, with a surface texture S_q value difference between XCT and an Alicona G4 focus variation instrument, of 5%. It is considered that the methodology presented here provides a sound basis for the initiation of the interlaboratory comparison.

Acknowledgements

The authors gratefully acknowledge the UK's Engineering and Physical Sciences Research Council (EPSRC) funding of the EPSRC Centre for Innovative Manufacturing in Advanced Metrology (Grant Ref. EP/I033424/1).

References

- [1] Thompson A., Senin N., and Leach R.K., Towards an additive surface atlas. in Proceedings of dimensional accuracy and surface finish in additive manufacturing, ASPE 2016 Summer Topical Meeting. Raleigh, NC, 2016.
- [2] Townsend A., Senin N., Blunt L., Leach R.K., and Taylor J.S., Surface texture metrology for metal additive manufacturing: a review. *Precision Engineering*. **46**: p. 34-47, 2016.
- [3] Pyka G., Kerckhofs G., Papanthiou I., Speirs M., Schrooten J., and Wevers M., Surface Roughness and Morphology Customization of Additive Manufactured Open Porous Ti6Al4V Structures. *Materials*. **6**(10): p. 4737-4757, 2013.
- [4] Kerckhofs G., Pyka G., Moesen M., Van Bael S., Schrooten J., and Wevers M., High-Resolution Microfocus X-Ray Computed Tomography for 3D Surface Roughness Measurements of Additive Manufactured Porous Materials. *Advanced Engineering Materials*. **15**(3): p. 153-158, 2013.
- [5] ISO_25178-2 B.E., BS EN ISO_25178-2, in Geometrical product specifications (GPS) Surface texture: Areal 2: Terms, definitions and surface texture parameters. British Standards Institute, 2012.
- [6] Townsend A., Pagani L., Scott P., and Blunt L., Areal surface texture data extraction from x-ray computed tomography reconstructions of metal additively manufactured parts. *Precision Engineering*, <http://dx.doi.org/10.1016/j.precisioneng.2016.12.008>, 2016.
- [7] ISO_25178-3 B.E., BS EN ISO_25178-3, in Geometrical product specifications (GPS) Surface texture: Areal Part 3: Specification operators. British Standards Institute, 2012.
- [8] Nikon metrology NV, Nikon CT-Pro.
- [9] Volume Graphics GmbH, VGStudio MAX.

euspen's 17th International Conference &
Exhibition, Hannover, DE, May 2017

www.euspen.eu



Results from an interlaboratory comparison of areal surface texture parameter extraction from X-ray computed tomography of additively manufactured parts

Andrew Townsend¹, Radu Racasan¹, Paul Bills¹, Adam Thompson², Nicola Senin², Richard Leach², Liam Blunt¹

¹ESPRC Centre for Innovative Manufacturing in Advanced Metrology, Centre for Precision Technologies, School of Computing and Engineering, University of Huddersfield, Huddersfield HD1 3DH, UK

²Manufacturing Metrology Team, Faculty of Engineering, University of Nottingham, Nottingham NG7 2RD, UK

E-mail: a.townsend@hud.ac.uk

Abstract

This paper presents the results of the CT-STARR (CT-Surface Texture for Additive Round Robin) interlaboratory comparison. The study compares the results obtained for the extraction of areal surface texture data per ISO 25178-2 from five X-ray computed tomography (XCT) volume measurements from each of four laboratories. To reduce the number of process variables, all participants utilise a Nikon XCT machine, either an XT H 225 industrial CT or an MCT225 metrology CT. Measurement process parameters, such as physical X-ray filtering, acceleration voltage and filament current, are set at similar values for all machines. All data processing and computation to extract, align, crop, filter and generate surface texture parameter information and deviation analysis results from the measurement volumes is performed by one participant. Two Ti6Al4V ELI (extra low interstitial) components are included in each of the XCT acquisitions. The first component is an additively manufactured cube built on an Arcam Q10 electron beam melting machine. Surface texture data is extracted from XCT scans of this part. The second component is a machined artefact designed for XCT scaling and surface determination analysis and verification. The data extracted from XCT measurements of these components is compared with measurements from coordinate measuring machine, focus variation and stylus instruments. The effect of scaling correction and XCT surface determination on extracted surface texture data, as well as measurement repeatability and reproducibility, are discussed.

Additive manufacturing, areal surface texture data, interlaboratory comparison, X-ray computed tomography, metrology, ISO 25178.

1. Introduction

Additive manufacturing (AM) methods enable the manufacture of components with features that are not possible to manufacture using conventional subtractive techniques. However, the freedom to manufacture components with complex internal features presents measurement challenges. Currently the principal method available for imaging the internal features of metal AM components is X-ray computed tomography (XCT). The importance of areal surface extraction from XCT is discussed elsewhere [1, 2] but, until recently, the only reported research detailing the extraction of surface information from XCT was the extraction of profile data from lattice structures [3]. A novel methodology for the extraction of areal surface texture data per ISO 25178-2 [4] from metal AM components has been reported [5]. The results showed a -2.5 % difference between the mean S_a value obtained using XCT when compared to a focus variation (FV) measurement of an AlSi10Mg selective laser melting (SLM) AM component. The potential industrial and research applications of this technique have prompted development of a round robin to assess the variation of results between XCT laboratories. The current work reports on Stage 1 of the CT-Surface Texture for Additive Round Robin (CT-STARR).

Stage 1 is designed to be a tightly controlled, expeditious round robin with a limited number of participant laboratories (four) using similar XCT machines with defined measurement settings. The results of measurements and analysis of Stage 1 data will then be used to guide a second, expanded round robin (Stage 2).

2. Methodology

Two artefacts were manufactured from Ti6Al4V ELI (extra low interstitial) titanium alloy. One artefact was a cube with 10 mm sides additively manufactured using an Arcam Q10 electron beam melting (EBM) system. One side (vertical) surface of this artefact was used for the surface texture analysis. The size of this artefact was dictated by the measurement surface area requirements derived from ISO 4288 (profile) [6] and ISO 25178 (areal) specification standards; with the size and filtering based on the initial surface texture measurements. The second artefact, used for scaling and surface determination analysis, was machined to a similar overall size to enable optimum X-ray attenuation for both artefacts simultaneously. This dimensional artefact includes three measured dimensions: an outside diameter (OD) and an inside diameter (ID) of approximately 3 mm, and a length between two parallel surfaces of approximately 4 mm. Surface determination is the calculation of the surface position during XCT reconstruction; the calculated position of the surface is based on the grey scale values of the XCT images. Inaccuracies in this surface determination would affect these three dimensions differently: if the surface determination were to calculate the surface inside the actual surface the OD would be undersized, the ID would be oversized and the length would be minimally effected by errors, as the surfaces are parallel and facing the same direction. The AM surface and dimensional artefacts were measured using an Alicona G4 focus variation instrument and a Zeiss Prismo CMM respectively prior to the round robin. The two artefacts were mounted within an AM fixture designed to maintain an air gap between all measured surfaces and the fixture (see figure 1).

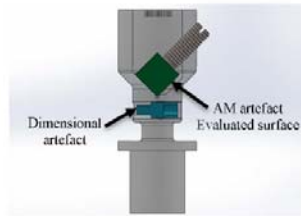


Figure 1. Artefacts within the fixture

The fixture development process is reported elsewhere [7]. The artefacts were not removed from the fixture during five XCT measurements performed by each round robin laboratory. Post round robin measurements included further measurements of surface and dimensions using FV and stylus, together with a repetition of the CMM measurements. The participants and the XCT machines used are shown in table 1.

Table 1. Round robin participant laboratories

Laboratory	Responsible	XCT machine
University of Huddersfield, UK	Andrew Townsend	Nikon XT H 225
University of Nottingham, UK	Richard Leach	Nikon MCT225
National Physical Laboratory, UK	Peter Woolliams	Nikon MCT225
Nikon Metrology, UK	David Bate	Nikon MCT225

All extracted surface data was aligned to one of the FV measurements. The FV and XCT data was processed per the methodology introduced in [5]. The surfaces were levelled and filtered with an L-filter nesting index of 8 mm and an S-filter nesting index of 0.025 mm per ISO 25178-3 [8]. Data was extracted and values for parameters per ISO 25178-2 were generated.

3. Results

Results reported here are for one set of measurements from the University of Huddersfield (XCTHUD) and one set of measurements from the University of Nottingham (XCTNOT). Table 2 shows the mean and standard deviation (SD) values of ISO 25178-2 parameters computed for the FV and XCT measurements.

Table 2. ISO25178-2 parameter values

Parameter	Mean		SD		Mean		SD	
	FV	XCTHUD	XCTHUD	XCTNOT	XCTHUD	XCTNOT	XCTHUD	XCTNOT
Sq/ μm	32.40	0.001	30.77	0.036	32.03	0.252		
So/ μm	25.33	0.001	24.05	0.031	25.07	0.241		
Sz/ μm	330.59	0.306	322.27	2.889	327.80	1.644		
Ssk	0.246	<0.001	0.08	0.016	0.202	0.008		
Sku	3.70	<0.001	3.67	0.009	3.66	0.040		
Sdr/%	39.90	0.013	28.26	0.123	41.92	1.080		

Figure 2 shows the results of the FV, XCTHUD and XCTNOT for Sq and Sz, showing the 95 % confidence interval for the mean. The XTHUD Sq and Sz are approximately 5 % and 2.5 % less than the FV values. The XCTNOT Sq and Sz are approximately 1.1 % and 0.9 % less than the FV values. Figure 3 shows the charts for the dimensional artefact OD, ID and length measurements taken on the CMM and both XCT machines. The OD, ID and length dimensional measurement errors for the XCTHUD were -0.27 %, -0.83 % and -0.54 % respectively. If a surface determination correction of 4.1 μm is applied, moving the calculated surface into the part, the errors become -0.55 %, -0.55 % and -0.54 %.

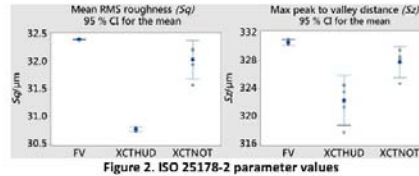


Figure 2. ISO 25178-2 parameter values

A global (x,y,z) dimensional scaling compensation of +0.55 % can then be applied. The effect of these compensations on the AM surface parameters will be investigated as part of future work.

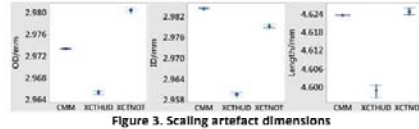


Figure 3. Scaling artefact dimensions

4. Conclusion

The round robin results of ISO 25178-2 areal surface data extraction from XCT scans of a Ti6Al4V ELI component have been reported for two of the round robin participants. The results for Sq for the XCTHUD and XCTNOT measurements are mean 30.77 μm (SD 0.036 μm) and mean 32.03 μm (SD 0.252 μm) respectively; these mean values are within 5 % and 1.1 % of the FV results (FV mean 32.40 μm [SD 0.001 μm]). Analysis of the differences in standard deviation values for the initial XCTHUD and XCTNOT surface parameters, together with the final results for all four participants will be presented at conference and in a later journal. This round robin, an extension of a novel technique to extract quantitative areal surface texture data reported in [5], validates the parameter extraction process, provides useful repeatability and reproducibility data and provides baseline information for an expanded, Stage 2, round robin.

Acknowledgements

AT, RR, PB and LB gratefully acknowledge the UK's Engineering and Physical Sciences Research Council (EPSRC) funding of the EPSRC Centre for Innovative Manufacturing in Advanced Metrology (Grant Ref: EP/I033424/1). AT and RKL would like to thank EPSRC (Grants EP/M008983/1 and EP/L01534X/1) and 3TRPD Ltd. for funding this work. NS and RKL would also like to thank the EC-FP7-PEOPLE-MC METROSURF for supporting this work.

References

- [1] Thompson A, Senin N, Leach R K 2016 *Proc. ASPE 2016 Summer Topical Meeting, Raleigh, NC 156-161*
- [2] Townsend A, Senin N, Blunt L, Leach R K, Taylor J S 2016 *Precision Engineering*, 46 34-47
- [3] Kerckhofs G, Pyka G, Moesen M, Van Bael S, Schrooten J, Wevers M 2013 *Adv. Eng. Mater.* 15 153-158
- [4] ISO 25178-2 2012 *Geometrical product specifications (GPS) – Surface texture: Areal – Part 2: Terms, definitions and surface texture parameters* (International Organization for Standardization)
- [5] Townsend A, Pagani L, Scott P, and Blunt L, 2016 *Precision Engineering* in press
- [6] ISO 4288 1998 *Geometrical Product Specifications (GPS) – Surface texture: Profile method -- Rules and procedures for the assessment of surface texture* (International Organization for Standardization)
- [7] Townsend A, Racasan R, Bills P, Blunt L, 2017 *7th Int. Conf. Industrial Computed Tomography, Leuven, Belgium*
- [8] ISO 25178-3 2012 *Geometrical product specifications (GPS) – Surface texture: Areal – Part 3: Specification operators* (International Organization for Standardization)

Andrew Townsend¹, Radu Racasan¹, Paul Bills¹, Adam Thompson², Nicola Senin², Richard Leach², Liam Blunt¹

¹EPSRC Future Advanced Metrology Hub, School of Computing and Engineering, University of Huddersfield, Huddersfield HD1 3DH, UK

²Manufacturing Metrology Team, Faculty of Engineering, University of Nottingham, Nottingham NG7 2RD, UK

E-mail: a.townsend@hud.ac.uk

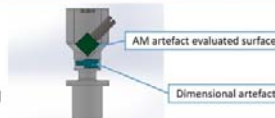
Stage 1: Four Labs

This Stage 1 interlaboratory comparison investigated the extraction of areal surface texture data per ISO 25178-2 from X-ray computed tomography (CT) reconstructions of a titanium additively manufactured (AM) part. Four laboratories were included, using similar machines: one Nikon XT H 225 industrial CT and three Nikon MCT225 metrology CTs. This low number of labs with similar machines were chosen for the purpose of providing knowledge and experience useful for the design and configuration of an expanded Stage 2.

Laboratory	XCT machine	Abbrev.
University of Huddersfield, UK	Nikon XT H 225	XCTHUD
University of Nottingham, UK	Nikon MCT225	XCTNOT
Nikon Metrology, UK	Nikon MCT225	XCTNIK
National Physical Laboratory, UK	Nikon MCT225	XCTNPL

Artefact Design

The CT measurement fixture included two artefacts, both manufactured from Ti6Al4V ELI, a material commonly used in medical and aerospace applications.



- One AM cube, 10 mm per side, manufactured using Electron Beam Melting, for surface texture measurement and analysis. The AM surface was measured five times using an Alicona G4 focus variation (FV) instrument prior to the XCT measurements.
- One machined dimensional artefact, for analysis of scaling and surface determination (results not reported here).

CT Machine Setup

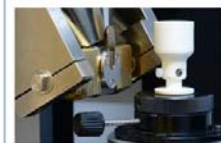
Parameter settings for the CT machines were kept as similar as possible. Five consecutive measurements were performed on each CT machine.

XT H 225 measurement settings. Parameters in bold differ between XT H 225 and MCT225 measurements

Parameter	Value	Parameter	Value
Filter material	Copper	Voxel size	17.3 µm
Filter thickness	1.0 mm	Source to object distance	64.2 mm
Acceleration voltage	160 kV	Source to detector distance	872 mm
Filament current	62 µA	Number of projections	1583
Exposure time	2829 ms	Detector size (pixels)	1008 x 1008

MCT225 measurement settings. Parameters in bold differ between XT H 225 and MCT225 measurements

Parameter	Value	Parameter	Value
Filter material	Copper	Voxel size	8.7 µm
Filter thickness	1.0 mm	Source to object distance	51.0 – 51.2 mm
Acceleration voltage	160 kV	Source to detector distance	1175 – 1180 mm
Filament current	62 µA	Number of projections	3142
Exposure time	2829 ms	Detector size (pixels)	2000 x 2000



Artefact mounted in an MCT225 CT



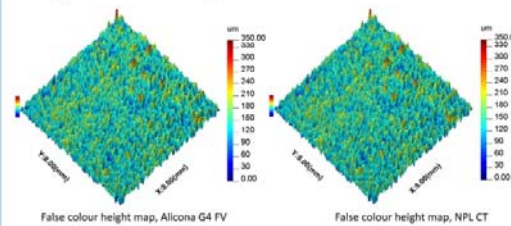
Nikon MCT225 metrology CT

Data Processing

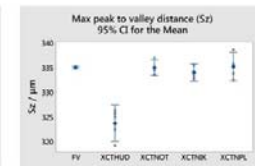
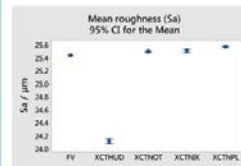
CT reconstruction was performed using Nikon CTPro 3D. Surface determination and extraction were performed using VGStudio MAX 3.0. Local iterative surface determination was performed with a search distance of 4.0 voxels. The AM surface was converted to PLY format using VGStudio MAX "Super Precise" setting. Aligning and cropping of the extracted surface area was performed per Townsend et. Al. [1]. The surface evaluation area was 8 mm x 8 mm, with an L-filter nesting index 8 mm and S-filter nesting index 0.025 mm per ISO 25178-3. Areal surface parameter values per ISO 25178-2 were generated.

Results

False colour height maps for one Alicona G4 and one NPL CT measurement are shown, together with the results table for selected parameters per ISO 25178-2, including sample standard deviation figures (SD). Plots of mean roughness, S_a and maximum peak-to-valley distance, S_z , for the Alicona G4 measurements and all CT machine measurements are shown. There was a **0.5% or less difference between the mean S_a and mean S_z from the extracted surface from all MCT225 machines and the Alicona G4**. The non-metrology XT H 225 machine figures were -5.2% for S_a and -3.4% for S_z .



Parameter	Mean FV	SD FV	Mean ACTHUD	SD ACTHUD	Mean ACTNOT	SD ACTNOT	Mean ACTNIK	SD ACTNIK	Mean ACTNPL	SD ACTNPL
S_a / µm	25.5	0.001	24.3	0.027	25.5	0.011	25.5	0.019	25.6	0.006
S_z / µm	318.8	0.002	30.9	0.032	32.5	0.009	32.5	0.023	32.6	0.007
S_t / µm	335.3	0.199	334.0	2.841	335.2	1.344	334.2	1.433	335.4	2.332
S_{sk}	0.26	<0.001	0.08	0.013	0.20	0.001	0.21	0.001	0.21	0.001
S_{ku}	3.7	<0.001	3.7	0.010	3.6	0.004	3.6	0.005	3.6	0.003
S_{Dr} (%)	40.2	0.014	28.3	0.131	41.9	0.117	42.4	0.137	43.8	0.103



Conclusions

- The results confirm the validity of using CT for the extraction of surface texture data from additively manufactured components.
- The surface extraction methodology and data analysis appears robust.
- These measurements were taken over a period of five months. There appears to have been negligible change of the fixture and artefacts over that time period.
- There is good repeatability and reproducibility of results, providing a good baseline for an expanded, Stage 2 interlaboratory comparison.

Acknowledgements

AT, RR, PB and LB gratefully acknowledge the UK's Engineering and Physical Sciences Research Council (EPSRC) funding of the EPSRC Centre for Innovative Manufacturing in Advanced Metrology (Grant Ref: EP/I033424/1) and EPSRC Future Advanced Metrology Hub (Grant Ref: EP/P006930/1). AT and RKL would like to thank EPSRC (Grants EP/M008983/1 and EP/L01534X/1) and 3TRPD Ltd. for funding this work. NS and RKL would also like to thank the EC-FP7-PEOPLE-MC METROSURF for supporting this work. The authors would like to thank Stephen Brown and Peter Woolliams of the UK's The National Physical Laboratory and Andrew Ramsey and David Bate of Nikon Metrology, UK.

References

[1] Townsend A., Pagani L., Scott P., and Blunt L., (2016), *Areal surface texture data extraction from x-ray computed tomography reconstructions of metal additively manufactured parts*. Precision Engineering, **48**: p. 254-264.

Appendix 6 Chapter 5 CIRP Annals 2017 CT accuracy factors

C. Model
CIRP 1632 1–4

ARTICLE IN PRESS

CIRP Annals - Manufacturing Technology xxx (2017) xxx–xxx



Contents lists available at ScienceDirect

CIRP Annals - Manufacturing Technology

journal homepage: <http://ees.elsevier.com/cirp/default.asp>



Factors affecting the accuracy of areal surface texture data extraction from X-ray CT

Andrew Townsend, Luca Pagani, Liam Blunt, Paul J. Scott, Xiangqian Jiang (1)*

EPSRC Centre for Innovative Manufacturing in Advanced Metrology, School of Computing and Engineering, University of Huddersfield, UK

ARTICLE INFO

Keywords:
X-ray
Metrology
Additive manufacturing

ABSTRACT

The ability to perform non-destructive areal surface analysis of the internal surfaces of additively manufactured (AM) components would be advantageous during product development, process control and product acceptance. Currently industrial X-ray computed tomography (XCT) is the only practical method for imaging the internal surfaces of AM components. A viable method of extracting useable areal surface texture data from XCT scans has now been developed and this paper reports on three measurement and data processing factors affecting the value of areal parameters per ISO 25178-2 generated from XCT volume data using this novel technique.

© 2017 Published by Elsevier Ltd on behalf of CIRP.

1. Introduction

Additive manufacturing (AM) techniques allow the manufacture of parts with geometries and features that cannot be manufactured using subtractive techniques such as milling and turning. This significant advantage of AM is primarily because this technique's layer-by-layer build method is not constrained by the machine tool access requirements of standard machining processes. Correspondingly, access limitations associated with complex geometries prevent standard inspection instruments and techniques from being used to verify dimensions and surface finishes of AM components. The aerospace, medical and automotive sectors have embraced the opportunities presented by AM and additive applications within these industries have seen rapid growth, particularly after the introduction of metals-fed AM machines [1]. These quality-driven industries require traceable verification of all specification and drawing requirements, including surface texture. The primary method used for measuring the internal features of AM components has been X-ray computed tomography (XCT). Significant research has been performed in relation to dimensional metrology using XCT. This dimensional research includes measurement accuracy [2,3], scaling error compensation [4] and development of XCT measurement procedures and workflows [5,6]. Surface texture-from-XCT extraction and characterisation, however, is in its infancy, but if XCT is to be used as an industrial inspection tool for component surface texture acceptance then this measurement and characterisation will need to be performed per accepted reference standards, such as ISO 25178. Surface texture data per ISO 25178-2 [7] has now been

extracted from XCT scans of additively manufactured (AM) components, as described in Townsend et al. [8]. The authors' research forms a foundation for the current paper and the current paper addresses questions that had arisen during the measurement and characterisation work performed: factors affecting the accuracy of the extracted surface texture data. This paper reports on three factors: firstly, the effect of variation in XCT surface determination, which is the process of defining where the surface of an object is based on image grey-scale values. Surface determination was chosen for investigation because the user has to make a non-intuitive choice during surface extraction. The potential effect of this choice is reported here. Secondly, the effect produced by changing the XCT electron-generation filament. This was chosen as an area of investigation as a filament change during a production run will potentially be unavoidable and so the potential effects should be investigated. Thirdly, the differences between results obtained between one surface section measured as an internal and subsequently as an external feature. AM techniques now enable the manufacture of components with complex, critical internal features. It is important to verify that XCT surface data extracted from internal surfaces is *identical* to that extracted from identical external surfaces. Other potential areas of investigation, such as position within the XCT measurement chamber, variation in acceleration voltage, filament current and acquisition time are more measurement component dependent than the three more fundamental areas of investigation reported here.

2. XCT surface determination

XCT surface determination defines the boundary between the component material and the background (usually air) based on the XCT image grey scale (density) values. The surface determination

* Corresponding author.
E-mail address: x.jiang@hud.ac.uk (X. Jiang).

<http://dx.doi.org/10.1016/j.cirp.2017.04.074>
0007-8506/© 2017 Published by Elsevier Ltd on behalf of CIRP.

Please cite this article in press as: Townsend A, et al. Factors affecting the accuracy of areal surface texture data extraction from X-ray CT. CIRP Annals - Manufacturing Technology (2017), <http://dx.doi.org/10.1016/j.cirp.2017.04.074>

65 methods employed to determine which grey scale value is
66 appropriate have been shown to have a significant effect on
67 dimensional information extracted from XCT volume data
68 [6,9]. Here we apply four surface determination techniques to
69 extract the surface (and subsequently generate and compare areal
70 parameter data) from a metal Rubert comparator plate. Using the
71 commonly available Rubert sample plates allows comparison of
72 the effect of surface determination on surfaces with similar
73 configuration but different roughness values when using similar
74 XCT measurement settings and surface characterisation.

75 2.1. Measurement plates

76 Individual rectangular plates, approximately 10 mm × 20 mm,
77 were cut from a Rubert Microsurf 334 (casting) test panel. The
78 casting panel was used as this surface was considered to most
79 closely represent the surface of a powder bed fusion (PBF) metal
80 AM component. The nominal surface Ra values for the plates used
81 for this work were 50 µm and 25 µm as these approximate the as-
82 built PBF metal AM surface roughness [10]. The individual samples
83 were imaged using a Nikon XT H 225 industrial CT machine.
84 Acceleration voltage was 190 kV, filament current was 53 µA, with
85 an acquisition time of 4000 ms. A 1 mm copper filter was used to
86 reduce contrast and beam hardening. Auto-defocus was deacti-
87 vated. The voxel size for all measurements was 12.9 µm (x, y and z).
88 Measurement parameters were identical for both samples.

89 2.2. Surface determination methods

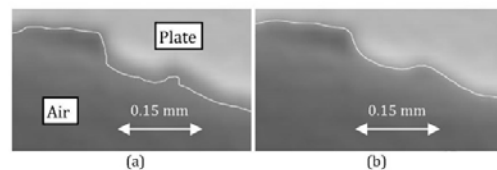
90 XCT surface determination was performed using four different
91 methods, three global and one local.

92 "Manual" in which the global surface determination was set by
93 the user by visually optimizing the surface location, implemented
94 in VGStudio MAX 2.2 [11].

95 ISO 50 surface determination, is also implemented in VGStudio
96 MAX 2.2. The ISO 50 method defines a global threshold which is
97 computed as the mean of two peaks (background and material) of
98 the grey value histogram.

99 The third global surface determination method is the Otsu
100 method [12] implemented in ITK [13]. Otsu surface determination
101 finds two clusters, in the grey value histogram, such that the sum of
102 the within-class variances of the foreground and background is
103 minimised.

104 The local iterative surface determination method, implemented
105 in VGStudio MAX 2.2 performs surface determination based on the
106 local surface grey values. Examples of surfaces created using ISO
107 50 and local iterative surface determination are shown in Fig. 1.
108 The difference between the locations of the computed surface
109 boundary (white line) can clearly be seen.



110 Fig. 1. Rubert 50 plate surface determination (VGStudio MAX 2.2 [11]). (a) ISO
111 50 surface determination (b) local iterative surface determination.

112 Surface conversion to a mesh (STL) format, following surface
113 determination, was performed using the VGStudio MAX 2.2 "Super
114 Precise" setting.

115 2.3. XCT-focus variation comparison

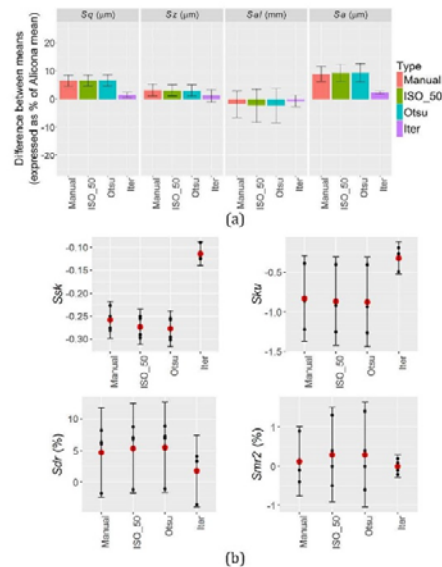
116 The XCT results were compared to those obtained using an
Alicona G4 focus variation instrument. Focus variation (FV) has
been one of the most widely used areal surface measurement

117 technologies for AM research [10]. FV has a large measurement z-
118 range suitable for tall AM structures, has the ability to measure
119 surfaces with high slope angles [14], is well suited to the
120 reflectivity of as-built AM components and is easily adaptable
121 for a variety of roughness levels. The Alicona measurements were
122 performed using a 5× objective lens. Lateral sampling distance was
123 5 µm; lateral resolution was 15 µm. Surface extraction and
124 processing was performed as described in Ref. [8]. The XCT and
125 FV measured areas for each of the Rubert samples were aligned
126 using the ICP (Iterative Closest Point) algorithm and then cropped.
127 Four sample areas, 5 mm × 5 mm were extracted from each of the
128 25 µm and 50 µm Ra samples. Both surfaces were levelled and
129 filtering was performed using an L-filter nesting index (hi-pass
130 filter) of 5 mm and an S-filter nesting index (low-pass filter) of
131 0.020 mm. A surface texture parameter set per ISO 25178-2 was
132 generated using SurfStand [15].

133 2.4. Analysis of results

134 The stated Rubert plate profile Ra values were compared to the
135 Ra values from profiles extracted from the Alicona areal measure-
136 ments. Five measurements, each 5 mm long were extracted. Each
137 of these measurements was the mean of five individual profiles. A
138 λc cutoff of 8 mm was applied, per ISO 4288 (1996) [16]. The mean
139 of the five measured Ra value for the 25 µm nominal Ra Rubert
140 sample plate was 25.3 µm with a sample standard deviation of
141 1.8 µm. The mean measured Ra value for the 50 µm nominal Ra
142 Rubert sample plate was 46.0 µm with a sample standard
143 deviation of 3.7 µm. All subsequent analysis was performed using
144 areal parameters per ISO 25178-2 [7,17].

145 For each of the Rubert sections a paired t-test was performed;
146 the null hypothesis being that the difference between the mean
147 parameter as measured on the XCT and on the Alicona was zero.
148 The 95% confidence interval of the mean was then generated for
149 each of the samples. The percentage difference between the mean
150 FV and XCT readings, together with the 95% confidence interval
151 were plotted for each of the analysed parameters: Sq, Sz, Sal and Sa
152 (Figs. 2(a) [50 µm Ra] and 3(a) [25 µm Ra]). The absolute
153 differences between XCT and FV results for the parameters Ssk, Sku,
154 Sdr and Smr2 are shown in Figs. 2(b) [50 µm Ra] and 3(b) [25 µm



155 Fig. 2. Areal parameters of the Rubert sample, nominal Ra of 50 µm.

Please cite this article in press as: Townsend A, et al. Factors affecting the accuracy of areal surface texture data extraction from X-ray CT. CIRP Annals - Manufacturing Technology (2017), <http://dx.doi.org/10.1016/j.cirp.2017.04.074>

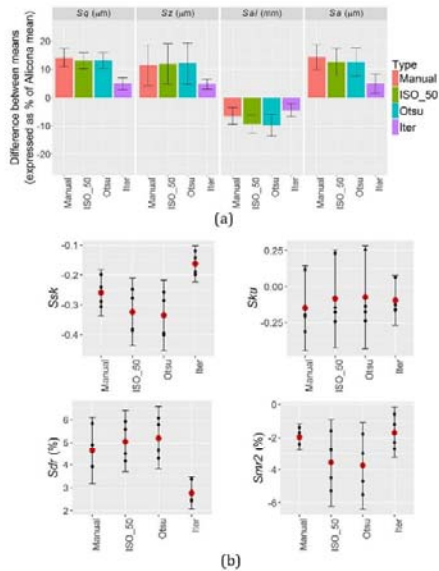


Fig. 3. Areal parameters of the Rubert sample, nominal Ra of 25 µm.

154 Ra]. These selected parameters were chosen because they have
155 been shown to be sensitive to AM build performance and post-
156 processing surface changes [10].

157 The reconstructed surfaces using the global surface determina-
158 tion methods achieve generally similar results, in some instances
159 the manual surface determination has slightly better parameter
160 estimation than the other global methods. Comparing the local
161 with the global surface determination methods for both the 50 µm
162 Ra and 25 µm Ra plates it can be seen that the local iterative
163 method achieves results significantly closer to those obtained
164 using the Alicona G4.

3. Electron-generation filament

166 The filament life for the Nikon machine used for these analyses
167 has historically ranged from 20 h to over 100 h. The situation may
168 arise during an industrial inspection process where the filament
169 fails and has to be replaced mid-batch and so any variation in
170 results due to filament change has the potential influence
171 measurement accuracy, repeatability and batch acceptance.

3.1. Measurement artefacts

172 A 10 mm × 10 mm aluminium AlSi10Mg selective laser melting
173 (SLM) AM cube was scanned five times using the Nikon XT H
174 225. Acceleration voltage was 150 kV, filament current was 67 µA,
175 with an acquisition time of 2829 ms. A 0.5 mm copper filter was
176 used. Auto-defocus was de-activated. Voxel size was 17.3 µm (x, y
177 and z). The filament was then changed and the artefacts were again
178 scanned five times using identical machine parameters. The top
179 surface data was extracted [8]. The same surface was measured on
180 the Alicona G4. The Alicona measurements were performed using a
181 10× objective lens. Lateral sampling distance was 2.33 µm; lateral
182 resolution was 7 µm. The AM surfaces were levelled and filtered
183 with an L-filter nesting index of 8 mm and an S-filter nesting index
184 of 0.025 mm per ISO 25178-3 [18]. The results for the selected ISO
185 25178-2 parameters for the AM artefact surface are shown in Fig. 4.
186

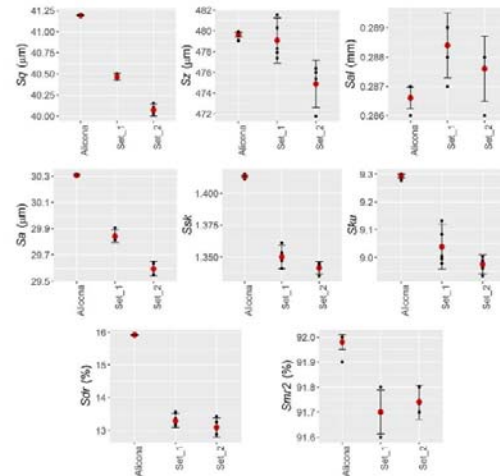


Fig. 4. Areal parameters for the Alicona and pre (Set 1) and post (Set 2) filament change XCT.

3.2. Analysis of results

187 The values of Sq and Sa (mean of five measurements) changed
188 by -0.97% and -0.83% respectively after changing the filament.
189 This change, while not large, may be significant depending upon
190 application and potential issues should be taken into consider-
191 ation. The change in values for the remaining selected parameters
192 is not significant. The XT H 225, the type used for these analyses, is
193 an industrial machine. It should be noted that Nikon produces a
194 metrology XCT machine, the MCT225, which does include a
195 protocol and supplied artefact to be used post-filament change for
196 system calibration.
197

4. Analysis of areal surface parameters of internal features

198 The most significant advantage of XCT over line-of-sight
199 measurement systems is the ability of XCT to measure the internal
200 features of an object, so potentially avoiding costly destructive
201 testing. AM techniques now enable the manufacture of compo-
202 nents with complex, critical internal features. However for the
203 advantages of both XCT and AM to be realised it is important to
204 verify that XCT surface data extracted from internal surfaces is no
205 different to that extracted from identical external surfaces, that
206 there are, for example, no artefacts generated during the XCT
207 measurement process specifically on internal surfaces. This
208 equivalency is important if, for example, a reference measurement
209 is taken on an outside surface using a stylus or optical instrument
210 and then compared to both external and internal surface data
211 extracted from XCT scans of the same component. This investiga-
212 tion assesses whether a surface inside the part reconstructs and
213 analyses differently from the same surface on the outside of the
214 part. Focus variation measurements are not analysed since the aim
215 of this section is to evaluate the reconstruction of the internal
216 features compared to external features, not to quantify the XCT
217 measurement deviations.
218

4.1. XCT measurement

219 A titanium Ti6Al4V 10 mm square section SLM bar, 50 mm long
220 with a 4 mm square internal bore, was imaged using the Nikon XT
221 H 225. The component was then physically sectioned, the
222 "internal" surface now becoming "external", and the component
223 was then re-imaged on the XCT. Measurement settings were
224

Please cite this article in press as: Townsend A, et al. Factors affecting the accuracy of areal surface texture data extraction from X-ray CT. CIRP Annals - Manufacturing Technology (2017), <http://dx.doi.org/10.1016/j.cirp.2017.04.074>

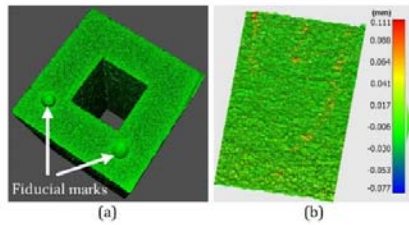


Fig. 5. (a) XCT reconstruction (b) deviation analysis.

identical for both scans. Acceleration voltage was 210 kV, filament current was 48 μ A, with an acquisition time of 4000 ms. A 1.0 mm copper filter was used. Auto-defocus was de-activated. The voxel size of both reconstructed volumes was 15.9 μ m (x , y and z). The surfaces were extracted using local iterative surface determination implemented in VGStudio MAX 2.2. Manual alignment of the surfaces from pre and post-sectioned scans was performed utilising the two fiducial marks, see Fig. 5(a). The ICP algorithm was used for final alignment. Data processing and parameter extraction was performed per Ref. [8]. Fig. 5(b) shows the false colour height map for the deviation analysis between the two extracted surfaces. The deviation ranged from -0.08 mm to 0.11 mm.

After the alignment each mesh was cut into four sub-samples, each with a dimension of approximately 3 mm \times 3 mm. A uniform re-sampling with a nominal resolution of 1.5 μ m was performed. The samples were levelled and Gaussian filtering was applied. The L-filter nesting index and the S-filter nesting index were set, respectively, to 2 mm and 0.005 mm. With a confidence level of 95% the null hypothesis of equality of the means cannot be rejected for all the roughness parameters analysed. Fig. 6(a) shows the bar plot of the percentage differences between the internal and external surface XCT measurements for parameters S_q , S_z , S_{al} and S_a , displaying the 95% confidence interval. Fig. 6(b) shows the absolute differences and 95% confidence interval of S_{sk} , S_{ku} , S_{dr} and S_{mr2} . These results show there was insignificant difference between the same surface as internal and as an external surface.

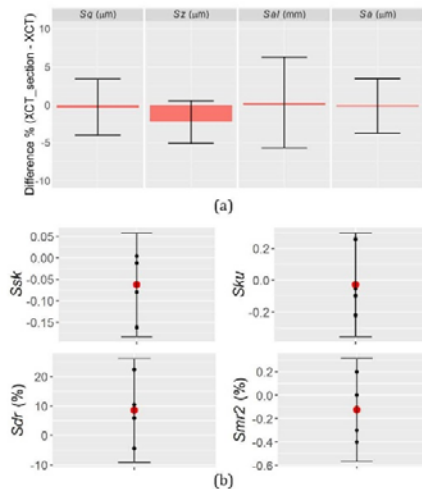


Fig. 6. Areal parameters. Showing difference between internal and external measurements.

5. Conclusions

The effects of three XCT measurement and reconstruction factors on the surface texture data extracted from XCT scans have been investigated. The analysis of scanned Rubert comparator plates has shown that using local iterative surface determination during XCT reconstruction will provide the most accurate results for surface texture parameter generation. Changing the XCT filament had a statistically significant effect on the S_a values extracted from a Ti6Al4V SLM component. A comparison of areal parameters computed on the same surface section of a Ti6Al4V SLM part as an internal and external feature has been performed. The measurements will be expanded to include other materials and wall thicknesses, but these initial results indicate no significant difference between the mean values of the generated parameters for the internal and external measurements. These results will provide valuable information to aid in the optimisation of the XCT surface texture measurement and extraction process for research and industrial applications.

Acknowledgements

The authors gratefully acknowledge the UK's Engineering and Physical Sciences Research Council (EPSRC) funding of the EPSRC Centre for Innovative Manufacturing in Advanced Metrology (Grant Ref: EP/I033424/1) and the funding of the EPSRC Fellowship in Manufacturing: Controlling Variability of Products for Manufacturing (Ref: EP/K037374/1).

References

- [1] The Royal Academy of Engineering (2013) *Additive Manufacturing: Opportunities and Constraints*.
- [2] Carmignato S (2012) Accuracy of Industrial Computed Tomography Measurements: Experimental Results from an International Comparison. *Annals of the CIRP* 61(1):491–494.
- [3] Bartscher M, Hilpert U, Goebbels J, Weidemann G (2007) Enhancement and Proof of Accuracy of Industrial Computed Tomography (CT) Measurements. *Annals of the CIRP* 56(1):495–498.
- [4] Müller P, Hiller J, Dai Y, Andreassen JL, Hansen HN, De Chiffre I (2015) Quantitative Analysis of Scaling Error Compensation Methods in Dimensional X-ray Computed Tomography. *CIRP Journal of Manufacturing Science and Technology* 10:68–76.
- [5] Kraemer A, Lanza G (2016) Assessment of the Measurement Procedure for Dimensional Metrology with X-ray Computed Tomography. *14th CIRP Conference on Computer Aided Tolerancing (CAT)*.
- [6] Kruth JP, Bartscher M, Carmignato S, Schmitt R, De Chiffre I, Weckenmann A (2011) Computed Tomography for Dimensional Metrology. *Annals of the CIRP* 60(2):821–842.
- [7] ISO 25178-2 (2012) *Geometrical Product Specifications (GPS) Surface Texture: Areal Part 2: Terms, Definitions and Surface Texture Parameters*, International Organization for Standardization.
- [8] Townsend A, Pagani L, Scott P, Blunt I (2016) Areal Surface Texture Data Extraction from X-ray Computed Tomography Reconstructions of Metal Additively Manufactured Parts. *Precision Engineering* 48:254–264.
- [9] Borges de Oliveira F, Stolff A, Bartscher M, De Chiffre I, Neuschaefer-Rube U (2016) Experimental Investigation of Surface Determination Process on Multi-material Components for Dimensional Computed Tomography. *Case Studies in Nondestructive Testing and Evaluation* 6:93–103.
- [10] Townsend A, Senin N, Blunt I, Leach RK, Taylor JS (2016) Surface Texture Metrology for Metal Additive Manufacturing: A Review. *Precision Engineering* 46:34–47.
- [11] Volume Graphics GmbH, VGStudio MAX.
- [12] Otsu N (1975) A Threshold Selection Method from Gray-level Histograms. *Automatica* 11(285–296):23–27.
- [13] Yoo TS, Ackerman MJ, Lorensen WF, Schroeder W, Chalana V, Aylward S, Metaxas D, Whittaker R (2002) Engineering and Algorithm Design for an Image Processing API: A Technical Report on Itk-the Insight Toolkit. *Studies in Health Technology and Informatics* 586–592.
- [14] Hierszenzfel F, Petzing JN, Leach RK, Helml F, Singh J (2012) Areal Texture and Angle Measurements of Tilted Surfaces using Focus Variation Methods. *3rd International Conference on Surface Metrology*, Annecy, France, 21–23 March.
- [15] The Centre for Precision Technologies U.o.H., SurfStand.
- [16] ISO 4288 (1998) *Geometric Product Specification (GPS) Surface Texture: Profile Method: Rules and Procedures for the Assessment of Surface Texture*, International Organization for Standardization.
- [17] Jiang XJ, Whitehouse DJ (2012) Technological Shifts in Surface Metrology. *Annals of the CIRP* 61(2):815–836.
- [18] ISO 25178-3 (2012) *Geometrical Product Specifications (GPS) Surface Texture: Areal Part 3: Specification Operators*, International Organization for Standardization.

Joint Special Interest Group meeting between euspen and ASPE
Dimensional Accuracy and Surface Finish in Additive Manufacturing,
KU Leuven, BE, October 2017
www.euspen.eu



Measurement and characterisation of additively manufactured re-entrant surfaces

¹Andrew Townsend, ¹Luca Pagani, ¹Paul J. Scott, ¹Liam Blunt

¹The Future Metrology Hub, University of Huddersfield, UK

A.townsend@hud.ac.uk

Abstract

Additive manufacturing processes simultaneously present manufacturing and measurement challenges and opportunities. The as-built surface may contain *non-intentional* re-entrant (overhanging) features; however the AM process itself presents opportunities to *intentionally* produce re-entrant features. These features may be designed to improve component functionality in areas such as paint and coating adhesion, cell tissue osseointegration, electrical battery design, fluid flow and material cooling systems. These features may prove difficult or impossible to measure using conventional line-of-sight instrumentation. This paper reports on measurement of re-entrant features using X-ray computed tomography and the extraction of surface area and volume information from an additively manufactured planar surface and lattice structure. A parameter, intended to relate directly to functional performance, Sdr_{prime} , is introduced as the percentage of additional surface (including re-entrant surfaces) contributed by the texture as compared to a plane the size of the measurement area.

X-Ray computed tomography
Additive manufacturing
Re-entrant surfaces
Surface texture
ISO 25178

1. Introduction

Additive manufacturing (AM) techniques, particularly powder based processes, often produce surfaces with re-entrant features: undercuts and overhangs. This is an unintentional by-product of the layer-by-layer deposition process. However, one significant advantage AM systems have, when compared to conventional subtractive processes such as milling and turning, is the ability to manufacture components with *intentional*, designed-in, re-entrant features. These features would be tailored to the functional requirement of the component. Manufacturing components with these features will provide advantages based on two properties produced by such features; firstly, an increase in surface area for a given planar area and secondly the ability to mechanically *lock* to the re-entrant surface. Increased surface area for a given planar area may have applications in battery plate design where the surface contact area between liquid or gel electrolyte and the plate may be increased [1]. There may be applications in cooling and fluid flow where an increase in contact surface area provides greater volumetric efficiency [2]. Medical applications may include orthopaedic and dental implants where osseointegration between implant and tissue may be enhanced by the increased surface area [3]. These medical applications may also be enhanced by the second property that can be designed-in, the ability to mechanically *lock* to the surface. Examples of *lock* features due to mechanical design include architectural keystones used in masonry arches, dovetail joints used in woodworking and tooth preparation prior to application of an amalgam filling. During dental amalgam filling preparation the dentist drills a pocket with an internally widening taper or a shelf to prevent the filling loosening and falling out. The dental amalgam fills the pocket and is mechanically locked in place. AM

processes allow generation of similar undercut features of different scales. In addition to medical applications of this *lock* feature, such as osseointegration, there are potential applications for this *lock* feature for paint and coating applications. Conventional measurement techniques, such as optical, stylus or CMM do not have the ability to measure re-entrant features or undercuts. X-ray computed tomography (XCT) has been used successfully for the measurement of internal surfaces [4, 5], dimensions [6, 7] and porosity [8]. There are no line-of-sight restrictions with XCT techniques. This paper reports on the measurement of two AM components: the as-built side surface of an AM medical implant and a section of a small lattice structure with nominally cylindrical lattice "bars". The medical implant was manufactured from Ti6Al4V ELI using a Selective Laser Melting (SLM) system. The lattice was manufactured from Ti6Al4V ELI using an Electron Beam Melting (EBM) system. Methodology for the extraction and analysis of the surface data is reported for both samples. The applicability of areal surface texture data parameter generation per ISO 25178-2 is discussed. The results for generated data from the measured surfaces, including re-entrant features (mesh), is compared and contrasted to generated projected grid data to illustrate errors introduced when re-entrant features are not captured during the measurement and characterisation process. Parameter data for a sample designed re-entrant component will be discussed in section 3.

2. Methodology

The XCT measurement parameter settings and surface extraction procedure for the SLM planar surface and the EBM lattice are discussed in section 2.1. The data processing and parameter value extraction methods are reported in section 2.2.

2.1. Computed tomography measurements

The SLM planar surface and the EBM lattice were both measured using a Nikon XT H 225 CT. Reconstruction for both data sets was performed using Nikon CTPro 3D [9]. Surface determination and surface extraction was performed using VGStudio MAX 3.0 [10]. Local iterative surface determination was performed with a search distance of 4.0 voxels. The surface was extracted using the VGStudio MAX "Super Precise" setting. The XCT settings for the planar surface measurement are given in table 1. The extracted planar surface is shown in figure 1.

Table 1 XT H 225 measurement settings, SLM Ti6Al4V planar surface

Parameter	Value	Parameter	Value
Filter	1 mm Cu	Voxel size	7.1 μm
Acceleration voltage	160 kV	Detector size (pixels)	1008 x 1008
Filament current	62 μA	Number of projections	1583
Exposure time	2829 ms		

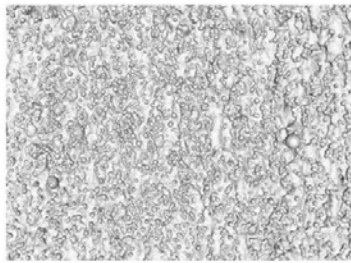


Figure 1. Extracted surface, SLM Ti6Al4V planar surface

The XCT settings for the lattice measurement are given in table 2. The extracted lattice surface is shown in figure 2. The region of interest (ROI) used in the surface evaluation is highlighted. All figures are in mm.

Table 2 XT H 225 measurement settings, EBM Ti6Al4V ELI lattice

Parameter	Value	Parameter	Value
Filter material	None	Voxel size	3.6 μm
Acceleration voltage	60 kV	Detector size (pixels)	1008 x 1008
Filament current	100 μA	No. of projections	1583
Exposure time	1000 ms		

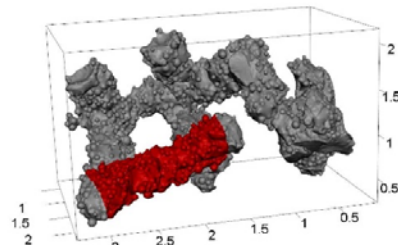


Figure 2. Extracted surface, EBM Ti6Al4V ELI lattice, showing ROI.

2.2. Data processing and parameter extraction

Figures 4 and 5 show, respectively, the complete extracted SLM planar surface and a detail section. The least-squares datum plane can be seen in both figures.

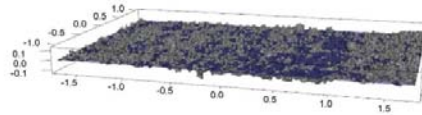


Figure 4. Planar surface showing datum plane

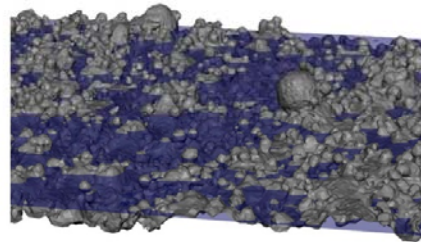


Figure 5. Detail of planar surface showing datum plane

The surface of the lattice section was unwrapped prior to analysis, see figure 6.

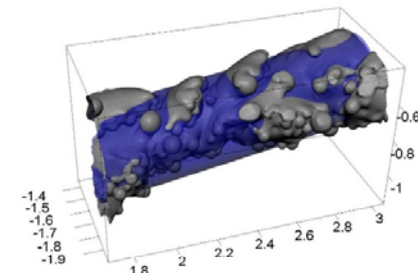


Figure 6. Extracted lattice ROI surface detail showing datum plane

Parameter data was extracted from a projected (grid) data set generated from the planar and lattice surfaces. Figure 7 shows a section of the unwrapped lattice. Projection of the surface onto a grid produces an interpolated surface *curtain* where the features are re-entrant. These areas can be seen in the figure. Surface area and volume data is calculated from the grid projection using this information. The true surface area and volume, that is, including the re-entrant features, cannot be calculated from this projected data. This data set is similar to data sets generated by line-of-sight instruments such as optical focus variation and stylus profilometers. This grid parameter data was compared to values calculated from the mesh surface for both measurement samples. The mesh data analysis does include all surface features, re-entrant and non-re-entrant. In all cases, grid and mesh the primary surface is considered; no filtering has been applied to the surfaces.

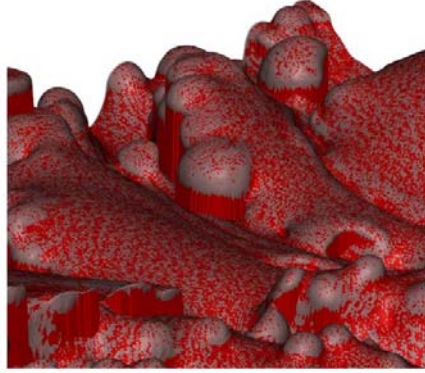


Figure 7. Unwrapped lattice surface, showing interpolated grid curtains

Four parameters were extracted during the analysis: Sdr , Sdr_{prime} , Vmc , Vvc . These parameters were chosen because of their relevance to the functional performances discussed previously. The parameters relate to ISO 25178-2 parameters of the same name but, because of the nature of the mesh surface, are generated differently. The hybrid parameter Sdr is the developed interfacial area ratio. This is the percentage of additional surface area contributed by the texture as compared to a plane the size of the *form* area (not the measurement area). The form area is the total area of all surfaces, including re-entrant surfaces, projected onto the datum plane. The form area is required for the calculation of surface parameters such as Sq , the arithmetic mean of the absolute of the ordinate value within the definition area (A). A parameter Sdr_{prime} is introduced as the percentage of additional surface (including re-entrant surface) contributed by the texture as compared to a plane the size of the *measurement* area. This number can be related directly to the ISO 25178-2 parameter Sdr and provides information directly related to surface function. Volume parameters Vmc and Vvc are core material volume and core void volume respectively. Vmc is defined here as the volume of material between 10% and 80% down from the maximum peak height to the maximum pit height. Vvc is the void volume (i.e. non-material volume) between 10% and 80% down from the maximum peak height to the maximum pit height.

Sdr is computed as

$$Sdr = \frac{1}{A} \left(\iint_{D_s} \|\mathbf{r}_u(u,v) \times \mathbf{r}_v(u,v)\| dudv - \iint_{D_{form}} \|\mathbf{r}_{form,u}(u,v) \times \mathbf{r}_{form,v}(u,v)\| dudv \right)$$

where $\mathbf{r}(u,v)$ is the measured surface, $\mathbf{r}_{form}(u,v)$ is the estimated form surface, A is the area of the form surface, $\mathbf{r}_u(u,v)$ is the partial derivative in u direction, D_s is the domain of the measured surface and D_{form} is the domain of the form surface. Sdr_{prime} is similar to Sdr with exception that area A is replaced by A_{prime} , the projected area. The volume below the surface can be computed as

$$V = \iint_{\Sigma_{form}} \mathbf{r}_{st}(u,v) \cdot \mathbf{n}_{form}(u,v) - Sv \, d\sigma_{form} \quad (1)$$

where Σ_{form} is the form surface, $\mathbf{r}_{st}(u,v)$ represents the scale limited surface, $\mathbf{n}_{form}(u,v)$ is the normal of the form surface and

$$d\sigma_{form} = \|\mathbf{r}_{form,u}(u,v) \times \mathbf{r}_{form,v}(u,v)\| dudv$$

is the infinitesimal area element. From Eq. 1 it is possible to compute the contribution of each height value to the total volume. This density function is expressed as $f_v(h)$. It should be noted that, since the surface in these applications includes re-entrant features this function will not be monotonically increasing, so it is not therefore possible to compute the volume parameter series according to ISO 25178-2. It is proposed to compute these parameters using the percentage of the height instead of area as used in the standard. Let $f_v(h^*)$ the density distribution of the volume as a function of the percentage of the height, a possible definition of $Vm(p)$, with $0 \leq p \leq 1$, can be

$$Vm(p) = \frac{Sz}{A_{max}} \int_p^1 f_v(h^*) dh^*$$

while

$$Vv(p) = \frac{Sz}{A_{max}} \int_0^p f_{v,max}(h^*) - f_v(h^*) dh^*$$

where A_{max} is the maximum section area, $f_{v,max}(h^*)$ is the maximum value of the density function and $h^* = \frac{h-Sv}{Sz}$. The

core volume related parameters can be computed as

$$Vmc = Vm(q) - Vm(p) \quad Vvc = Vv(q) - Vv(p)$$

where p and q are percentages of the distance down from the maximum peak height to the maximum pit height, 10% and 80% respectively.

3. Results

3.1. Structured surface

Figure 10a shows a CAD representation of a sample structured surface, designed with intentional re-entrant features. The surface consists of repeated planar *mushroom* features, figure 10b. Each *mushroom* consists of a *cap* $2 \times 2 \times 2 \text{ mm}^3$ ($H \times W \times D$) attached to a $2 \times 1 \times 1 \text{ mm}^3$ *stem*. For calculation of Sdr from the mesh, for a single *mushroom* feature, including the base area directly below the *mushroom*, the area equivalent to the form area is 10 mm^2 . This includes the top surface, 4 mm^2 , and two horizontal areas of 3 mm^2 each: the underside of the mushroom cap and the base surface. This area is used to calculate Sdr . The plane area equivalent to the measurement area is 4 mm^2 . This area is used to calculate Sdr_{prime} . The total feature surface area, including the base area directly below the *mushroom*, is 34 mm^2 . The Sdr value would be $(34-10) / 10 \times 100 = 240\%$. The Sdr_{prime} value would be $(34-4) / 4 \times 100 = 750\%$. If a grid projection were used for surface reconstruction the *mushroom* would be evaluated to be a block $2 \times 2 \times 4 \text{ mm}^3$ (this includes interpolated side *curtains*). The feature surface area would be calculated as 36 mm^2 , producing an Sdr value of 800%. This result illustrates that

the calculated surface when re-entrant features are included (34 mm²) may be *less* than the calculated surface when they are not included (36 mm²).

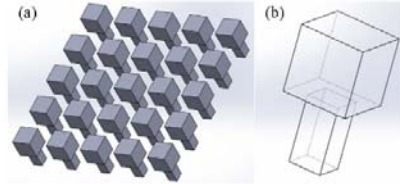


Figure 10. (a) structured surface and (b) single *mushroom* detail

The values for Sdr and Sdr_{prime} for the mesh and grid are shown in table 4, together with the values of volume parameters Vmc and Vvc for a core extending 10% down from the top surface ($p=10\%=0.4$ mm) to 80% down from the top surface ($q=80\%=3.2$ mm).

Table 4. Single planar *mushroom* extracted parameters

Method	Sdr	Sdr_{prime}	$Vmc/$ (mm ³ /mm ²)	$Vvc/$ (mm ³ /mm ²)
Mesh	240%	750%	1.9	0.9
Grid	800%	800%	2.8	0.0

The height vs volume curve is shown in figure 12 and the material ratio curve is shown in figure 13.

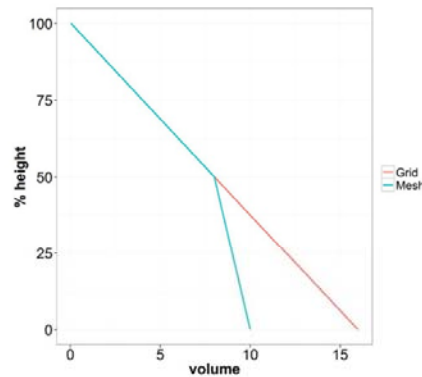


Figure 12. Height vs volume curve, single structured *mushroom*

The knee in the curve for the mesh is located at the 50% height, where the shape transitions from *cap* to *stem*. The grid projection produces a straight line as the transition is not measured. The calculated volumes for the entire feature (100% volume on the material ratio curve) are 10 mm³ for the mesh and 16 mm³ for the grid projection.

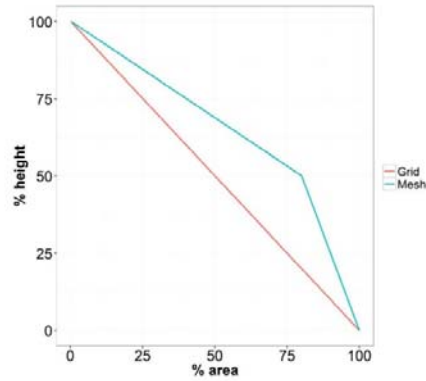


Figure 13. Material ratio curve, single structured *mushroom*

3.2. SLM planar surface

Table 3 shows the values of Sdr , Sdr_{prime} , Vmc and Vvc for mesh and grid for the SLM planar surface.

Table 3 SLM planar surface texture parameters

Method	Sdr	Sdr_{prime}	$Vmc/$ (mm ³ /mm ²)	$Vvc/$ (mm ³ /mm ²)
Mesh	55%	79%	0.076	0.0042
Grid	68%	68%	0.077	0.0038

The material ratio curve for the planar surface is shown in figure 14. The difference in the developed area interfacial area ratio, Sdr between grid and mesh for the SLM planar surface is 13%. The difference for Sdr_{prime} is -11%. The difference between grid and mesh for the volume parameters, Vmc and Vvc , is approximately 1% and -10%.

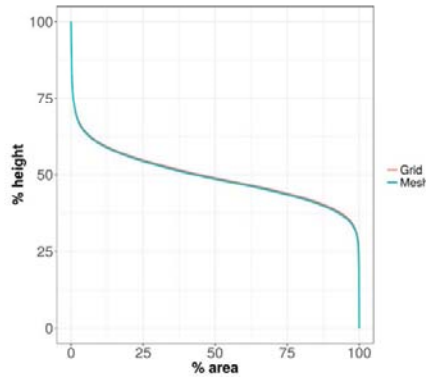


Figure 14. Material ratio curve, SLM planar surface

3.3. Lattice structure

Table 4 shows the values of Sdr , Sdr_{prime} , Vmc and Vvc for mesh and grid for the EBM lattice surface.

Table 4 EBM lattice surface texture parameters

Method	Sdr	Sdr_{prime}	$Vmc/$ (mm^3/mm^2)	$Vvc/$ (mm^3/mm^2)
Mesh	42%	55%	0.064	0.018
Grid	49%	49%	0.077	0.028

The material ratio curve for the lattice structure is shown in figure 15. The difference in the developed area interfacial area ratio, Sdr between grid and mesh for the EBM lattice surface is 7%. The difference for Sdr_{prime} is -6%. The difference between grid and mesh for the volume parameters, Vmc and Vvc is approximately 20% and 56%.

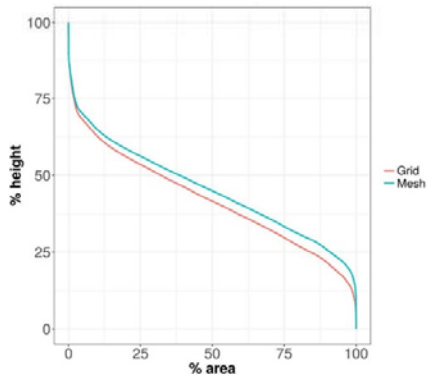


Figure 15. Material ratio curve, EBM lattice

4. Conclusions

AM processes provide the ability to produce complex freeform surfaces and re-entrant features that enhance component functionality, from bio-attachment, battery design, cooling systems, paint and coating adhesion. The ability to measure and characterise these surfaces accurately will be the key to performance optimisation. These surfaces present measurement and data analysis challenges that require the ability to image and extract meaningful data from a complex point clouds or meshes rather than a uniform grid typically generated by line-of-sight instrumentation processes. A method for extraction of surface texture parameters from re-entrant AM surfaces has been demonstrated. XCT measurements scans of two AM surfaces have been made, capturing data for surfaces that would prove difficult or impossible to capture using line-of-sight measurements. Actual surface area and volume data has been extracted and compared to projected (grid) areas and volumes for this data. An example generated structured surface has been discussed. A new parameter, Sdr_{prime} has been suggested. This parameter is the percentage of additional surface (including re-entrant surfaces) contributed by the texture as compared to a plane the size of the measurement area. This new parameter was developed to provide a direct relation to functional performance in applications where the

actual surface area is important. There are significant errors in volume (up to 56% for Vvc) and area (up to 11% for Sdr_{prime}) when re-entrant features of as-built SLM and EBM additively manufactured components are not measured and included in analyses. Including re-entrant features, using the techniques presented here, will provide more accurate data required for analysis and optimisation of the functional performance of AM components.

References

- [1] Gyenge E, Splinter S, Jung J, Snaper A 2002 High-specific surface area, three-dimensional reticulated electrodes for deep cycle lead-acid batteries. in *Seventeenth Annual Battery Conference on Applications and Advances. Proceedings of Conference (Cat. No.02TH8576)*
- [2] Silk E A, Kim J, and Kiger K 2006 Spray cooling of enhanced surfaces: impact of structured surface geometry and spray axis inclination. *International Journal of Heat and Mass Transfer*. **49**(25): p. 4910-4920
- [3] Rungsiyakull C, Li Q, Sun G, Li W, Swain M V 2010 Surface morphology optimization for osseointegration of coated implants. *Biomaterials*. **31**(27): p. 7196-7204
- [4] Townsend A, Pagani L, Blunt L, Scott P J, Jiang X 2017 Factors affecting the accuracy of areal surface texture data extraction from X-ray CT. *CIRP Annals - Manufacturing Technology*
- [5] Thompson A, Korner L, Senin N, Lawes S, Maskery J, Leach R K 2017 Measurement of internal surfaces of additively manufactured parts by X-ray computed tomography. in *7th Conference on Industrial Computed Tomography*. Leuven, Belgium
- [6] Müller P, Cantatore A, Andreasen J L, Hiller J, De Chiffre L 2013 Computed tomography as a tool for tolerance verification of industrial parts. *Procedia CIRP*. **10**: p. 125-132
- [7] Kruth J P, Bartscher M, Carmignato S, Schmitt R, De Chiffre L, Weckenmann A 2011 Computed tomography for dimensional metrology. *CIRP Annals-Manufacturing Technology*. **60**(2): p. 821-842
- [8] Wits W W, Carmignato S, Zanini F, and Vaneker T H, 2016 Porosity testing methods for the quality assessment of selective laser melted parts. *CIRP Annals-Manufacturing Technology*. **65**(1): p. 201-204
- [9] Nikon metrology NV, *Nikon CT-Pro*
- [10] Volume Graphics GmbH, *VGStudio MAX*

CT measurement of re-entrant additively manufactured surfaces

¹Andrew Townsend, Luca Pagani¹, Paul J. Scott¹, Liam Blunt¹

¹The Future Metrology Hub, School of Computing and Engineering,

University of Huddersfield, Huddersfield, West Yorkshire, UK, e-mail: a.townsend@hud.ac.uk

Abstract

Producing components using metal additive manufacturing processes, such as powder bed fusion, presents manufacturing and measurement challenges, but also significant opportunities. The as-built surface may include overhanging (re-entrant) features not intentionally included in the design, but that aid in component functionality. In addition, the additive manufacturing process presents opportunities to design and manufacture re-entrant features intentionally. Re-entrant features increase the specific surface area and, in addition, produce mechanical locking to the surface. These features may be intended to improve surface performance in areas such as biological cell attachment, coating adhesion, electrical capacitance and battery plate design, fluid flow and material cooling. Re-entrant features may prove difficult or impossible to measure and characterise using conventional line-of-sight surface metrology instrumentation, however the correct measurement of these surfaces is vital for functional optimisation. This paper reports on the measurement of re-entrant features using X-ray computed tomography and the extraction of actual surface area information (including re-entrant surfaces) from sample AM surfaces. The proposed new surface texture parameter, Sdr_{prime} , is discussed. This parameter is intended to relate directly to surface function. Sdr_{prime} is the percentage of additional surface (including re-entrant surfaces) contributed by the texture as compared to a plane the size of the measurement area. In addition to Sdr_{prime} , the actual surface area is discussed, together with the percentage of re-entrant surface. The errors produced using line-of-sight instruments and height map parameter generation per ISO 25178-2 are discussed. Measurement results for EBM and SLM additively manufactured components will be presented.

Keywords: X-ray computed tomography, additive manufacturing, ISO 25178 surface texture, re-entrant surfaces.

1 Re-entrant features – functionally significant

Electron Beam Melting (EBM) and Selective Laser Melting (SLM) metal powder bed fusion additive manufacturing (AM) techniques often generate surfaces containing re-entrant features such as overhangs and undercuts (see Figure 1). Re-entrant planar surface features are characterized by two or greater z height values for an (x,y) position, (see Figure 1 (c)).

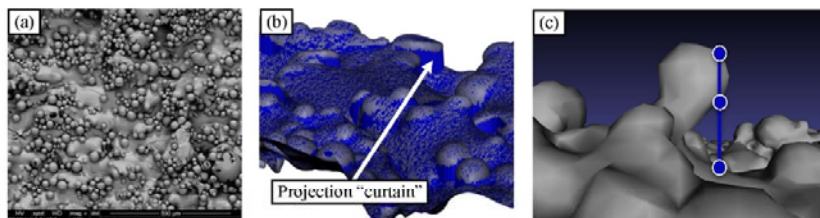


Figure 1: (a) Typical SLM side surface, (b) surface showing projection "curtains", (c) re-entrant surface showing three z positions at one (x,y) location

These as-built features, a by-product of the AM layer-by-layer deposition process, may have functional advantages. Importantly, one significant advantage AM systems have, when compared to conventional subtractive processes such as milling and turning, is the ability to manufacture components with intentional, designed-in, re-entrant features at scales matched to the functional requirements. These features being tailored to the functional requirement of the component. Manufacturing components with these features will provide advantages based on two properties produced by such features: firstly, an increase in surface area for a given planar area or component volume and secondly the ability to mechanically lock to the re-entrant surface. Increased surface area for a given planar area may have applications in battery and capacitor plate design where the surface contact area between liquid or gel electrolyte and the plate may be increased [1]. There may be applications in cooling and fluid flow where an increase in contact surface area provides greater volumetric efficiency [2]. Medical applications such as orthopaedic and dental implants where osseointegration between implant and tissue may be enhanced by the increased surface area [3]. These medical applications, and other applications such as paint and coating adhesion, may also be enhanced by the second property of re-entrant features that can be designed-in: the ability to mechanically lock to the surface. Dovetail joints used in woodworking are an example of mechanical locking due to designed shape.

2 Measurement techniques and data analysis

Conventional surface topography measurement techniques, such as optical focus variation or confocal microscopy, mechanical stylus or CMM probing have a limited ability to measure internal or re-entrant features. Surface data is generally created as a height map, with a single z value corresponding to an (x,y) position. Surfaces between steps are interpolated, producing surface “curtains” at re-entrant features (Figure 1 (b)). X-ray computed tomography (CT), used in this study, has no such line-of-sight restrictions and has been used successfully for the measurement of internal surfaces [4, 5], dimensions [6, 7] and porosity [8]. CT data is true 3D data, consisting of (x,y,z) co-ordinate information. A new surface characterization measurement parameter, Sdr_{prime} is proposed with the ability to extract surface information from true 3D data, such as CT, which includes data for re-entrant surfaces. Sdr_{prime} is the percentage of additional surface (including re-entrant surfaces) contributed by the texture as compared to the area of a plane the size of the measurement area. The parameter is similar to the ISO 25178-2 hybrid parameter Sdr , the developed interfacial area ratio, which has application for height map data, but which cannot account for data from re-entrant features. Characterisation of a re-entrant surface using line-of-sight measurement instrumentation and using height map analysis will produce significant errors in actual surface calculations.

$$Sdr_{prime} \text{ is computed as } Sdr_{prime} = \frac{1}{A_{prime}} \left(\iint_{D_s} \|\mathbf{r}_x(u,v) \times \mathbf{r}_y(u,v)\| \, dudv - A_{prime} \right)$$

where $\mathbf{r}(u,v)$ is the measured surface, $\mathbf{r}_x(u,v)$ is the partial derivative in x direction, D_s is the domain of the measured surface and A_{prime} is the projected area.

3 Designed surface example

A simulated example structured surface, designed to illustrate the errors produced when measuring re-entrant features using line-of-sight instrumentation is shown in Figure 2 (a). Each structure has a 4 mm diameter cap, 1 mm cap height, 1 mm diameter stem with a 4 mm stem height. The calculated values of Sdr_{prime} for a grid projection (similar to the results obtained using line-of-sight measurements) is 600%. The value of Sdr_{prime} for the mesh (which includes re-entrant features not measurable using line-of-sight) is 487.5%. The total surface areas are 75.4 mm² and 61.3 mm² respectively. The error is 23% (see Figure 2 (b)).

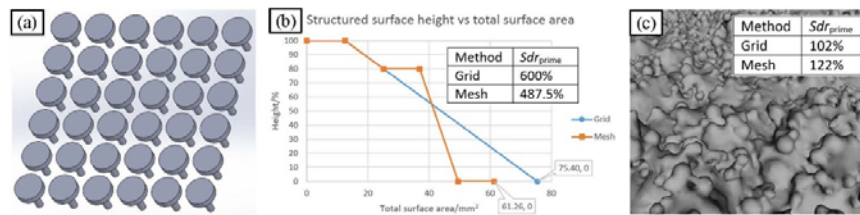


Figure 2: (a) structured surface, (b) graph of percentage height down from top vs total surface area, (c) SLM surface results

4 AM components

An SLM side surface with the values of Sdr_{prime} for grid projection and mesh analysis are shown in Figure 2 (c). Additional results for EBM and SLM additive surfaces, including Sdr_{prime} and total re-entrant surface area, will be presented and functional surface measurement testing will be discussed.

References

- [1] E. Gyenge, S. Splinter, J. Jung, A. Snape, High-specific surface area, three-dimensional reticulated electrodes for deep cycle lead-acid batteries, in Seventeenth Annual Battery Conference on Applications and Advances (Cat. No. 02T118576), 2002.
- [2] E. A. Silk, J. Kim, K. Kige, Spray cooling of enhanced surfaces: impact of structured surface geometry and spray axis inclination, International Journal of Heat and Mass Transfer, **49**(25): p. 4910-4920, 2006.
- [3] C. Rungtanyakull, Q. Li, G. Sun, W. Li, M. V. Swain, Surface morphology optimization for osseointegration of coated implants, Biomaterials, **31**(27): p. 7196-7204, 2010.
- [4] A. Townsend, L. Pagani, L. Blunt, P. J. Scott, X. Jiang, Factors affecting the accuracy of areal surface texture data extraction from X-ray CT, in press, CIRP Annals-Manufacturing Technology, 2017.
- [5] A. Thompson, L. Komer, N. Senin, S. Lawes, I. Maskery, R. K. Leach, Measurement of internal surfaces of additively manufactured parts by X-ray computed tomography, in 7th Conference on Industrial Computed Tomography, Leuven, Belgium, 2017.
- [6] P. Müller, A. Cantatore, J. L. Andreasen, J. Hiller, L. De Chiffre, Computed tomography as a tool for tolerance verification of industrial parts, Procedia CIRP, **10**: p. 125-132, 2013.
- [7] J. P. Kruth, M. Bartsche, S. Carmignato, R. Schmitt, L. De Chiffre, A. Weckenmann, Computed tomography for dimensional metrology, CIRP Annals-Manufacturing Technology, **60**(2): p. 821-842, 2011.
- [8] W. W. Wits, S. Carmignato, F. Zanini, and T. H. Vaneker, Porosity testing methods for the quality assessment of selective laser melted parts, CIRP Annals-Manufacturing Technology, **65**(1): p. 201-204, 2016.

Surface-Specific Additive Manufacturing Test Artefacts

A Townsend¹, L Blunt¹

¹EPSRC Centre for Innovative Manufacturing in Advanced Metrology, Centre for Precision Technologies, School of Computing and Engineering, University of Huddersfield, Huddersfield HD1 3DH, UK

E-mail: a.townsend@hud.ac.uk

Keywords: additive manufacturing, surface texture, quality control, artefact

Abstract Many artefact designs have been proposed for use with additive manufacturing (AM) systems. These have primarily been dimensional and form based artefacts [1-5] with some having included sections designed for surface measurements, such as the (2012) NIST proposed artefact [6]. A series of surface-specific measurement artefacts designed for use in the verification of AM manufacturing processes are proposed here. The surface-specific artefacts can be made more compact because they do not require the large dimensions needed for accurate dimensional and form measurements. The series of three artefacts are designed to provide comprehensive information pertaining to the surface of the parts. Measurement possibilities include deviation analysis, surface texture parameter data generation, sub-surface analysis and build resolution comparison. The artefacts are designed to provide easy access for measurement using standard surface measurement techniques; for example, focus variation, stylus profilometry, confocal microscopy, and scanning electron microscopy. The artefacts may be visually inspected as a simple comparative tool, giving a fast indication of process variation between builds. The three artefacts are small enough to be included in every build and include built-in traceability information, making them a convenient physical record of the build, analogous to a test coupon being included in the furnace with production components during metal heat-treatment processes.

Artefact AMSA1 includes three separate surface evaluation areas on its top face: a flat measurement area parallel to the artefact base plane to allow profile or areal surface measurement and parameter extraction, for example per ISO 4288 [7] or ISO 25178-2 [8], a sloped section with a 1:25 gradient to allow easy visualization and measurement of the layer transition edge, and ten individual raised bosses with a height difference between each boss equivalent to the build layer height which, after suitable preparation, will allow metallographic inspection of sub-surface layers, see Figure 1. To avoid possible operator errors, once the layer height is specified in the design, the layer height is printed on the outside of the artefact and the boss heights are generated automatically, see Figure 2.

Artefact AMSA3 includes a Siemens star on the top face, see Figure 3. Siemens stars are commonly used to determine the resolution of optical instruments, displays and printers and are included in measurement Standards such as ISO 15775 [9] and have been included in AM research [10].

Artefact AMSA4 includes three sections that each have constant amplitude, decreasing wavelength structured sine wave surfaces, see Figure 4 and Equations 1-3. These surfaces may be used for simple visual comparison between builds or a deviation analysis may be performed by measuring the artefact optically or using x-ray computed tomography and then comparing to the artefact CAD design data.

$$Y = \frac{\sin\left(\left(\frac{X}{4}\right)^2\right)}{2.5} \text{ mm} \quad (1)$$

$$Y = \frac{\sin\left(\left(\frac{X}{2}\right)^2\right)}{5} \text{ mm} \quad (2)$$

$$Y = \frac{\sin(X^2)}{10} \text{ mm} \quad (3)$$

Artefact design rationale will be discussed in the paper and the overall efficacy of the adopted approach will be addressed. Build configuration and results obtained using artefacts manufactured using a metal selective laser melting (SLM) process will be compared to those manufactured using an electron beam melting (EBM) process and a polymer SLM process as a means of highlighting the usefulness of the artefacts.

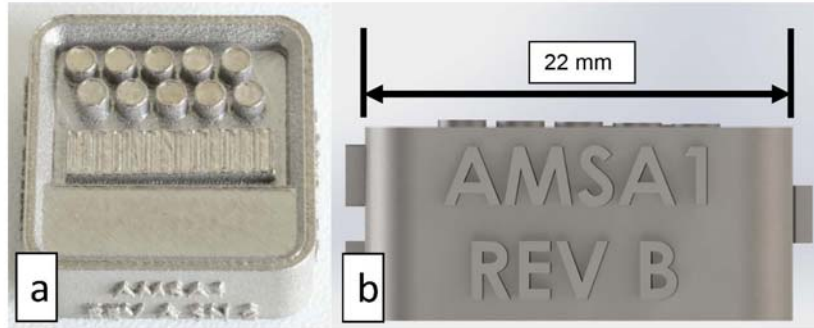


Figure 1. a) Ti6Al4V artefact AMSA1 manufactured using a Renishaw AM250 SLM system b) CAD rendering of AMSA1 showing artefact size.

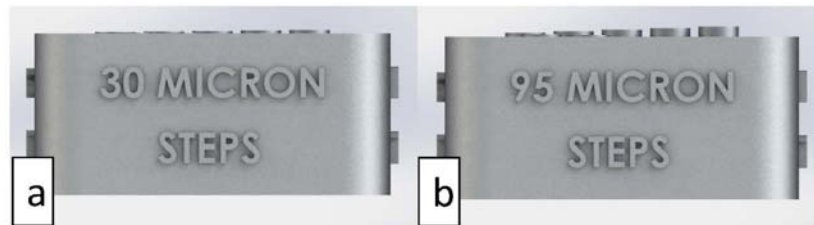


Figure 2. CAD rendering of AMSA1 artefact showing automatically generated bosses and step height notation a) 30 micron layer height, b) 95 micron layer height.

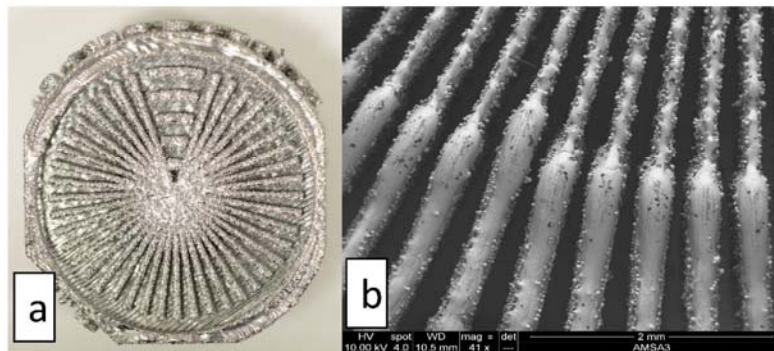


Figure 3. AMSA3 artefact a) Ti6Al4V ELI made using an Arcam Q10 EBM system b) SEM micrograph of a section of Ti6Al4V artefact manufactured using the SLM process.

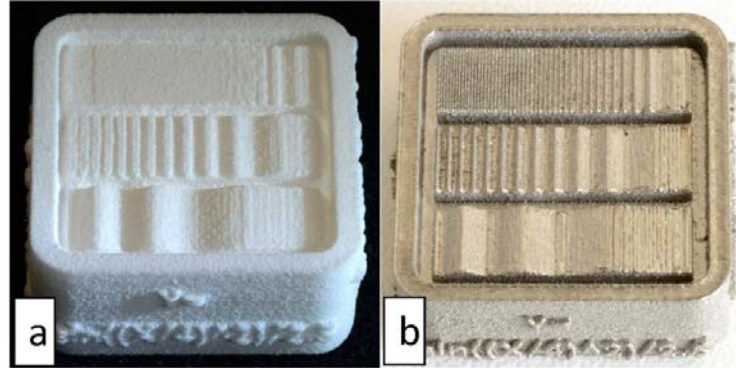


Figure 4. Artefact AMSA4 manufactured using a) an EOS Formiga P 110 (Nylon) SLM system b) Ti6Al4V artefact manufactured using the SLM process.

Main References

- [1] Johnson W., Rowell M., Deason B., and Eubanks M. (2011), *Benchmarking evaluation of an open source fused deposition modeling additive manufacturing system*. in *Proceeding of the 22nd Annual International Solid Freeform Fabrication Symposium*.
- [2] Moylan S., Cooke A., Jurrens K., Slotwinski J., and Donmez M.A., (2012), *A review of test artifacts for additive manufacturing*. National Institute of Standards and Technology (NIST), Gaithersburg, MD, Report No. NISTIR. 7858.
- [3] Santos E.C., Shiomi M., Osakada K., and Laoui T., (2006), *Rapid manufacturing of metal components by laser forming*. *International Journal of Machine Tools and Manufacture*. 46(12): p. 1459-1468.
- [4] Kruth J.-P., Vandenbroucke B., Vaerenbergh v.J., and Mercelis P., (2005), *Benchmarking of different SLS/SLM processes as rapid manufacturing techniques*.
- [5] Mahesh M., Wong Y., Fuh J., and Loh H., (2004), *Benchmarking for comparative evaluation of RP systems and processes*. *Rapid Prototyping Journal*. 10(2): p. 123-135.
- [6] Moylan S., Slotwinski J., Cooke A., Jurrens K., and Donmez M.A. (2012), *Proposal for a standardized test artifact for additive manufacturing machines and processes*. in *Proceedings of the 2012 Annual International Solid Freeform Fabrication Symposium*. The University of Texas at Austin, Austin, TX.
- [7] ISO_4288 B.E., (1998), *BS EN ISO_4288*, in *Geometrical product specification (GPS) Surface texture. Profile method: Rules and procedures for the assessment of surface texture*. British Standards Institute.
- [8] ISO_25178-2 B.E., (2012), *BS EN ISO_25178-2*, in *Geometrical product specifications (GPS) Surface texture: Areal 2: Terms, definitions and surface texture parameters*. British Standards Institute.
- [9] ISO, (2013), *ISO/IEC 15775:1999 Information technology - office machines - method of specifying image reproduction of colour copying machines by analog test charts - realisation and application*.
- [10] Galovskiy B., Flessner M., Loderer A., and Hausotte T. (2013), *Systematic form deviations of additive manufactured parts—methods of their identification and correction*. in *11 th International Symposium on Measurement and Quality Control*.

On characterising surface topography of metal powder bed fusion additive manufactured parts

S Lou¹, A Townsend¹, X Jiang¹, L Blunt¹, W Zeng¹, P Scott¹

¹EPSRC Centre for Innovative Manufacturing in Advanced Metrology, University of Huddersfield, Huddersfield, HD1 3DH, UK

Abstract

Inherent to the somewhat uncontrolled nature of the additive process, the surfaces of metal powder bed fusion additively manufactured components tend to be very rough. Large isolated 'bumps', as one of the major defect features, are often present due to partially melted particles attached to the surface. An enhanced watershed segmentation method is proposed to separate these 'bump' features from the underlying surface texture such that the 'bumps' and underlying surface can be quantitatively analysed. The results show that the amplitude roughness parameters of the underlying surface are significantly less than the un-segmented surface and spatial roughness parameters differ between two surfaces. Characterising the extracted underlying surface and 'bumps' independently allows better correlation between surface measurements and additive system performance and hence aids in process optimization.

Surface metrology, additive manufacture, watershed segmentation

1. Introduction

Additive manufacturing (AM) processes have the potential to produce highly complex, customisable and multifunctional parts at lower material and energy costs and with lower environment pollution than conventional (subtractive) manufacturing techniques. However the commercialisation of AM has been beset by a number of technological issues, wherein uncontrolled process and lack of precision in product are identified as major hurdles [1]. There is an urgent demand for accurate methods of measuring and evaluating AM surface quality.

The complex nature of powder AM processes tends to produce component surfaces that are very rough, showing significant defect features, including large isolated 'bumps' due to partially melted particles attached to the surface, repeating steps generated by successively adding layers, surface pores and re-entrant features. To achieve a good surface finish post-processes, such as grinding, polishing and sand blasting, are performed to remove these protruding 'bumps'. Such processes however will also deteriorate the underlying surface and other defect features which may contain critical evidence concerning the additive process. Thus it is of critical importance to extract the pertinent features in order to facilitate the further study of the origin of individual defects and their relevance to the process optimisation.

As the AM surface topography is often dominated by the presence of 'bump' features, this paper presents the use of the watershed segmentation method for separating the 'bumps' and the underlying surface texture such that they can be quantitatively analysed.

2. Enhanced watershed segmentation

Figure 1a presents a 0.71x0.54 mm² surface measured from the side surface of a solid cube produced by selective laser melting using AISI10Mg powder (no post processing). The surface was measured using an Alicona G4 focus variation instrument with a 20x magnification objective lens. Significant 'bumps' are clearly present on the surface topography while the underlying surface shows relatively better surface quality. To separate the 'bump' features from the underlying surface, an extraction method based on the watershed segmentation technique [2, 3] has been developed.

The 'bump' topography elements feature a high gradient at their geometrical boundary and high surface height in comparison to the neighbouring surface. Edge enhancement is required to reinforce the feature boundary and enable the subsequent segmentation analysis to obtain a more representative extraction. This is achieved by applying the Gaussian filtering to suppress measurement noise and smooth topographical features followed by application of the Sobel

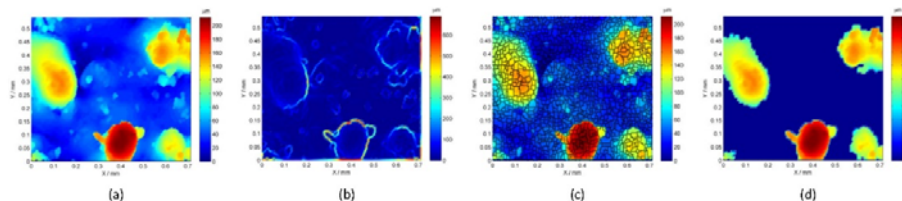


Figure 1. Extraction of 'bump' features from a 0.71x0.54 mm² AM surface: (a) Original surface; (b) Gradient map; (c) Watershed segmentation; (d) Extracted 'bumps'.

operator [4] to yield a gradient map of the processed surface data. Figure 1b shows the resultant gradient map of the surface.

The watershed segmentation is applied to the gradient surface to generate a sequence of small segments. These segmented surface patches designate local surface hills. Figure 1c presents the resulted segments superimposed spatially on the original measured surface. To extract the 'bumps', an estimated threshold $100\ \mu\text{m}$ is applied to the local surface hill height. Those surface patches with their height above this threshold are extracted and regarded as the bump features. See Figure 1d for the extracted 'bumps'.

Figure 2a presents a large surface measured from the same part and by the same measurement instrument but with 10x magnification objective lens. The surface is $6.88 \times 6.98\ \text{mm}^2$, which is a much larger surface area than that shown in Figure 1 and thus is more meaningful for the comprehensive evaluation of the surface topography. The developed method is applied to the measured surface with a systematically defined height threshold of $321\ \mu\text{m}$, which is three standard deviations above the mean height of the underlying surface excluding 'bumps'. Figure 2b illustrates the result of the watershed segmentation

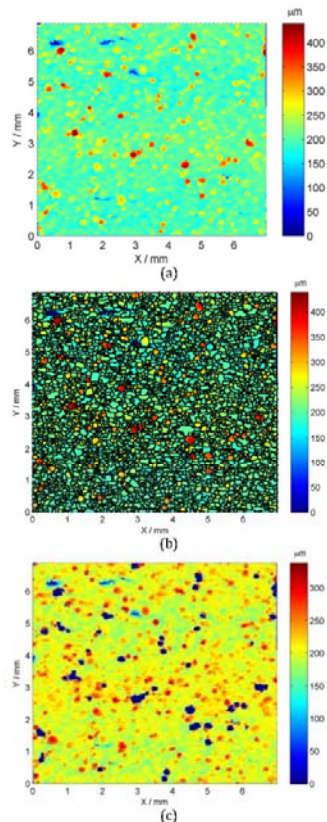


Figure 2. Extraction of 'bump' features from a $6.88 \times 6.98\ \text{mm}^2$ AM surface: (a) Original surface; (b) Watershed segmentation; (c) Underlying surface texture.

and Figure 2c shows the final extracted underlying surface. The 'bump' features are marked by the blue areas.

3. Results and discussion

The values of areal parameters per ISO 25178-2 [3] were extracted from the underlying surface and the un-segmented surface. In the case of the surface presented in Figure 2, the amplitude parameters S_a and S_q and the spacing parameter S_{al} are given in Table 1. It is clearly observed that the values of S_a and S_q for the underlying surface texture are significantly less by around 16% and 17% compared to the un-segmented surface and the S_{al} values of the two surfaces are different as well.

Due to the presence of significant 'bumps', the parameter results of the un-segmented surface evidently differ from that of the underlying surface. Efficient separation of defect features enables independent characterisation of different surface components and thus offers a more accurate analysis of complex AM surface topography.

Table 1 Surface texture parameters of un-segmented surface and the underlying surface.

Parameters	Un-segmented surface	Underlying surface
S_a	22.16 μm	18.72 μm
S_q	37.45 μm	30.88 μm
S_{al}	0.112 mm	0.129 mm

Feature extraction facilitates further characterisation of the 'bump' areas and the result for the surfaces measured is given below, which can also be useful for detecting process malfunction.

- Total 'bump' areas: $0.92\ \text{mm}^2$
- 'bump' area percentage to the whole surface: 1.92%
- Total 'bump' volume: $0.069\ \text{mm}^3$

In the present case the extraction of 'bump' features is determined by thresholding the local surface heights. Other potential judgement criteria include segment volume or the projected segment surface area.

4. Conclusion

The topography of AM surfaces contains various types of defect features pertinent to the additive processes, wherein large isolated 'bumps' are caused by partially melted particles attached to the surface. It is proposed to use the watershed segmentation method with appropriate enhancement to separate the 'bump' features from the underlying surface texture, thus allowing a more accurate analysis of AM surface topography.

Future work includes the improvement of segmentation method and the analysis of other types of defect features, such as step markings and surface pores.

Acknowledgement

The authors gratefully acknowledge the UK's Engineering and Physical Sciences Research Council (EPSRC) funding of the EPSRC Centre for Innovative Manufacturing in Advanced Metrology. The authors would like to thank the University of Nottingham EPSRC Centre for Innovative Manufacturing in Additive Manufacturing for supplying the AM sample.

References

- [1] National Institute of Standards and Technology 2013 Measurement science roadmap for metal-based additive manufacturing
- [2] Scott P J 2004 *Proc. R. Soc. A*, **460** 2845-64
- [3] ISO 25178-2 2012 Geometrical product specification (GPS) - Surface texture: Areal - Part 2: Terms, definitions and surface texture parameters
- [4] Gonzales R et al. 2004 Digital Image Processing Using Matlab

Appendix 11 Referenced areal surface texture parameters

ISO 25178-2 definitions and calculation methods for the areal parameters used in the current research are given here.

Height parameters

Sq

Root mean square height of the scale-limited surface

Root mean square value of the ordinate values within a definition area (A)

$$S_q = \sqrt{\frac{1}{A} \iint_A z^2(x,y) dx dy}$$

Ssk

Skewness of the scale-limited surface

Quotient of the mean cube value of the ordinate values and the cube of Sq within a definition area (A)

$$S_{sk} = \frac{1}{S_q^3} \left[\frac{1}{A} \iint_A z^3(x,y) dx dy \right]$$

Sku

Kurtosis of the scale-limited surface

Quotient of the mean quartic value of the ordinate values and the fourth power of Sq within a definition area (A)

$$S_{ku} = \frac{1}{S_q^4} \left[\frac{1}{A} \iint_A z^4(x,y) dx dy \right]$$

Sz

Maximum height of the scale-limited surface

Sum of the maximum peak height value and the maximum pit height value within a definition area.

Sa

Arithmetical mean height of the scale limited surface

Arithmetic mean of the absolute of the ordinate values within a definition area (A)

$$S_a = \frac{1}{A} \iint_A |z(x,y)| \, dx dy$$

Spatial parameters

Sal

Autocorrelation length

Horizontal distance of the $f_{ACF}(t_x, t_y)$ which has the fastest decay to a specified value s , with $0 \leq s < 1$

$$S_{al} = \min_{t_x, t_y \in R} \sqrt{t_x^2 + t_y^2} \quad \text{where } R = \{(t_x, t_y) : f_{ACF}(t_x, t_y) \leq s\}$$

Hybrid parameters

S_{dr}

Developed interfacial area ratio of the scale-limited surface

Ratio of the increment of the interfacial area of the scale-limited surface within the definition area (A) over the definition area

$$S_{dr} = \frac{1}{A} \left[\iint_A \left(\sqrt{1 + \left(\frac{\partial z(x,y)}{\partial x} \right)^2 + \left(\frac{\partial z(x,y)}{\partial y} \right)^2} - 1 \right) dx dy \right]$$

V-parameters

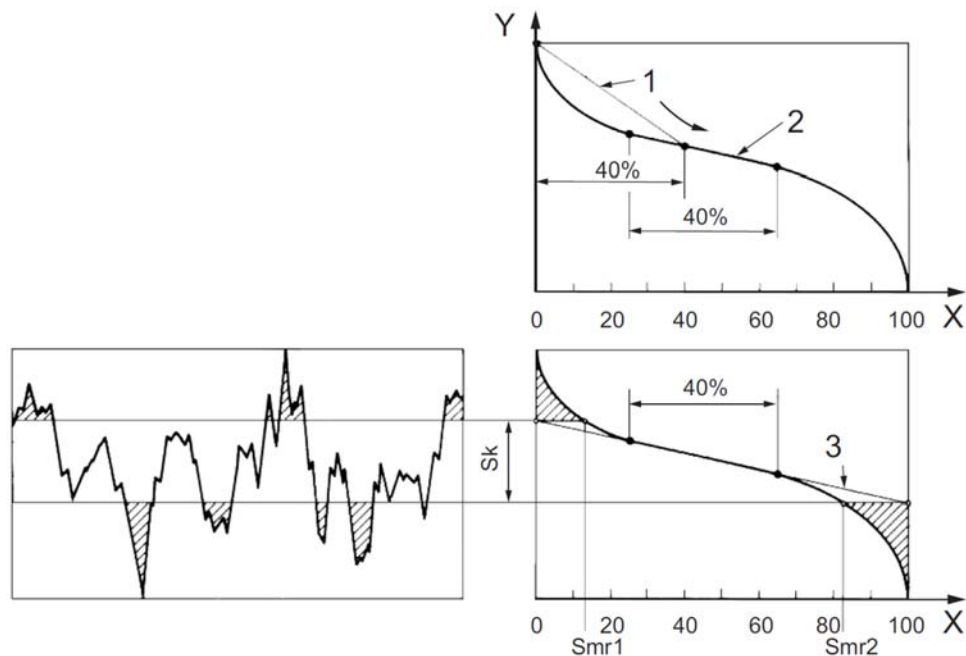


Figure 11-1: Areal material ratio curve and calculation of S_k and S_{mr2}

Key

X areal material ratio

Y intersection line position

1 secant

2 secant with smallest gradient

3 equivalent straight line

S_k core height

S_{mr1} , S_{mr2} material ratios

This figure shows a profile instead of a surface area for ease of illustration. The principle is the same for a surface area.

Sk

Core height

Distance between the highest and lowest level of the core surface, see Figure 11-1:.

Smr2

Material ratio (dales)

ratio of the area of the material at the intersection line which separates the protruding dales from the core surface to the evaluation area (expresses as a percentage).